INVESTIGATION OF SOLAR APPLICABLE GAS CYCLES

A Thesis
Presented to
The Academic Faculty

by

Sandeep Gopalakrishna

In Partial Fulfillment
of the Requirements for the Degree
Masters of Science in the
School of Mechanical Engineering

Georgia Institute of Technology
May, 2013

INVESTIGATION OF SOLAR APPLICABLE GAS CYCLES

Approved by:

Dr. Sheldon M. Jeter, Advisor
School of Mechanical Engineering
Georgia Institute of Technology

Dr. Baratunde A. Cola
School of Mechanical Engineering
Georgia Institute of Technology

Dr. J. Rhett Mayor
School of Mechanical Engineering
Georgia Institute of Technology

Date Approved: 2nd April, 2013

To my lovely wife Manisha and my parents, for their unwavering love and support

ACKNOWLEDGEMENTS

I wish to thank Dr. Sheldon M. Jeter, my supervisor and mentor for his constant support and encouragement through this endeavor. Without his insight and expertise into the subject this thesis would not have seen the light of the day. His penchant for questioning every minute detail of the research made me learn lot more concepts and persevere for perfection.

I would also like to thank my thesis review committee Dr. J. Rhett Mayor and Dr. Baratunde A. Cola for their support and encouragement in my effort to complete my thesis. Their valuable suggestions added great value to the research work.

I wish to also thank my parents and family for their love and support throughout the course of my efforts. Their words always strengthened my resolve to continue in this path to successfully complete my research. Finally, I would like to thank my wife, Manisha for being there with me always and giving me a reason to continue on my path. Her love and support and smile will always inspire me to excel in my efforts.

TABLE OF CONTENTS

LIST OF TABLES

Page

LIST OF FIGURES

Page

LIST OF SYMBOLS AND ABBREVIATIONS

$\boldsymbol{A}$	Area [m^2]
$\boldsymbol{C}$	Cost [$/kW]
$\boldsymbol{c}$	Specific heat capacity [kJ/kg-K]
$\boldsymbol{D}$	Diameter [m]
$\boldsymbol{E}$	Energy [kWh]
$\boldsymbol{G}$	Mass Velocity [kg/s-m^2]
$\boldsymbol{h}$	Specific enthalpy [kJ/kg]
$\boldsymbol{H}$	Heat transfer coefficient [W/m^2-K]
$\dot{I}$	Exergy destruction rate [kW]
$\boldsymbol{k}$	Thermal conductivity [W/m-K]
$\dot{m}$	Mass flow rate [kg/s]
$\boldsymbol{n}$	Number of components [-]
$\boldsymbol{P}$	Pressure [kPa]
$\dot{Q}$	Heat transfer rate [kW]
$\boldsymbol{r}$	Hydraulic radius [m]
$\boldsymbol{S}$	Surface area [m^2]
$\boldsymbol{T}$	Temperature [K]
$\boldsymbol{V}$	Volume [m^3]
$\boldsymbol{w}$	specific work [kJ/kg]

Greek Symbols

$\boldsymbol{\varepsilon}$	Heat exchanger effectiveness
$\boldsymbol{\eta}$	Efficiency

μ	Dynamic viscosity [N-s/m^2]
ρ	Density [kg/m^3]

Subscripts

ann	Annual
c	Cold
comp	Compressor
conv	Convective
h	Hot
hx	Heat exchanger
rad	Radiation
turb	turbine

Abbreviations

CGT	Cold Gas Turbine
CPV	Concentrating Photvoltaic
CRPT	Central Receiver Power Tower
CSP	Concentrating Solar Power
DOE	Department of Energy
DSG	Direct Steam Generation
EES	Engineering Equation Solver
EIA	Energy Information Administration
GT	Gas Turbine
HTF	Heat Transfer Fluid
HTSGT	High Temperature Solar Gas Turbine
LCCF	Life Cycle Cost Factor
LCGT	Lorentz Cycle Gas turbine

LCoE	Levelized Cost of Energy
MPBR	Modular Pebble Bed Reactor
NREL	National Renewable Energy Laboratory
PV	Photovoltaic
SAM	System Advisory Model
SEGS	Solar Energy Generation System
TES	Thermal Energy Storage

SUMMARY

This thesis presents the thermodynamic and economic assessment of gas power cycles for 100 MW solar thermal power generation systems. A gas power cycle for solar power generation is a totally different technology from the current state of the art solar power generation systems. As a result, this thesis provides an assessment of the solar power generation systems with gas power cycles and provides guidance in the selection of design and operating parameters for gas power cycle based solar power generation system.

The gas power cycle based power generation systems are assessed by means of thermodynamic and economic models developed and simulated using commercial thermodynamic analysis software. The gas cycle based power generation systems considered in this study are Cold Gas Turbine, High Temperature Solar Gas Turbine and Lorentz Cycle Gas Turbine. The system models are assessed for their thermodynamic performance using theory based turbo-machinery models with practical performance and loss data. In addition, extensive cost models have been developed for assessing the economic performance of the system models to determine their practical feasibility.

The results from this study indicate that the most economical power generation system is the HTSGT system for a high peak cycle temperature utilizing the central receiver power tower solar collector system. The LCGT system also has a comparable performance at the same operating temperature. The CGT system assessed for operating with parabolic trough solar collector system at a lower peak cycle temperature had an

inferior performance compared to the current state of the art technology for the power generation using parabolic troughs.

CHAPTER 1

SOLAR POWER GENERATION

Introduction

The world energy demand is increasing as also the electricity demand as population increases and the living standards improve. As a renewable source of energy, solar power has come to acquire a new significance in this current world scenario. Solar thermal power technology refers to any technology that generates electricity from thermal energy in sunlight. This study aims to explore a feasible and commercially applicable gas cycle based solar thermal power generation technology that caters to the ever growing demand of cleaner and greener power supply for mankind. This chapter will briefly review the availability of worldwide and regional energy resources and highlight the importance of solar power generation followed by a review of the current state of the art in solar power generation. The later sections of the chapter will present the limitations of the current technology and identify the opportunities to develop new solar power generation technology.

Electricity Demand

According to International Energy Outlook-2010, the world electricity generation in 2007 was 18.8 trillion kWh, with a total installed capacity of 4.5 billion kW (EIA, 2010). EIA estimates that this consumption will rise by 87% by year 2035. The conventional source of energy, coal, will continue to dominate the power generation arena in the foreseeable future. However, the unprecedented increase in energy prices in the current decade along with the rising concerns over the environmental impact of power generation has led to a renewed interest in the alternatives to fossil fuels, nuclear and renewable energy. The long-term prospects for both are positive, fueled by government incentives and rising

fossil-fuel prices (Figure 1.1). In fact, the renewable energy sources are projected to rise above natural gas in power generation in the future.

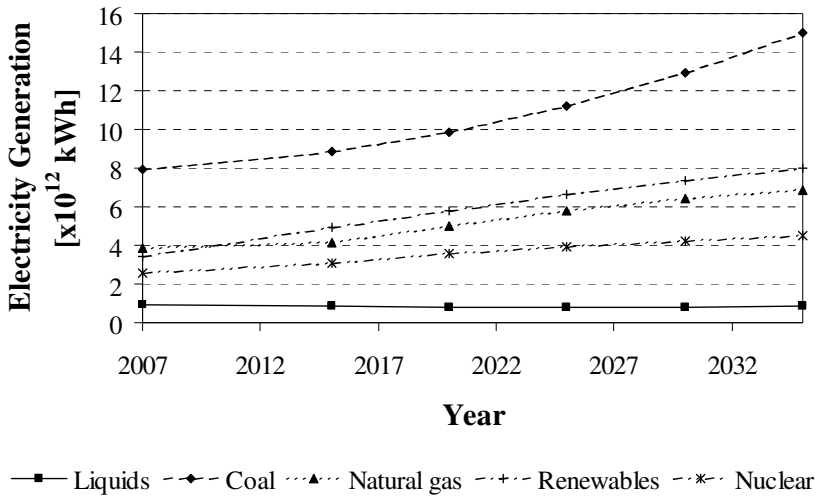

Figure 1.1: World net electricity generation by fuel (Source: USA EIA, 2010)

The major portion of the market for renewable energy is dominated by hydro and wind power currently (~80% share). The other renewable sources, like solar, geothermal, biomass, waste and oceanic energy, although share a small portion of the market; they are supposed to show one of the highest growth rates in the future. The solar power generation specifically is expected by the EIA to rise from almost nothing to about 180 billion kWh by 2035 (Figure 1.2). It is this segment of the energy resource that this project deals with. The potential of solar energy resource presents an opportunity to develop new technologies to improve the performance of the solar power generation systems. But before looking into the current technology for harnessing solar energy, it is necessary to understand the availability of the solar resources and the potential for profitably generating electricity from solar energy.

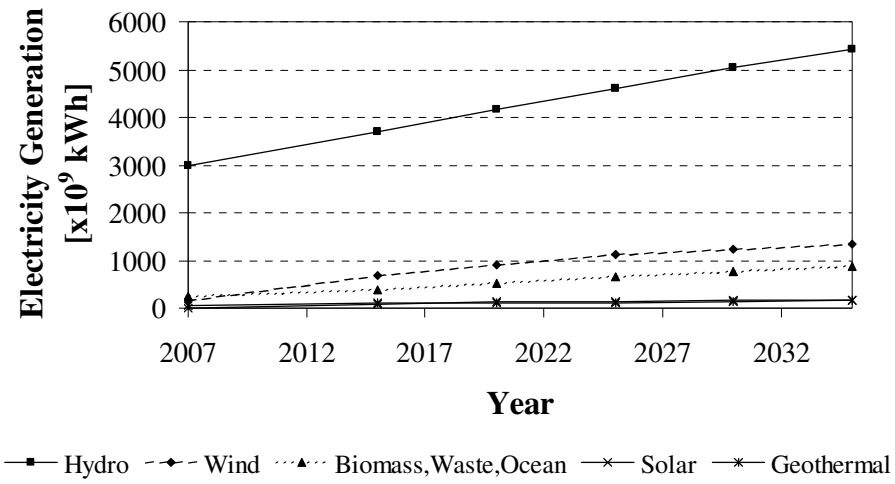

Figure 1.2: World renewable electricity generation by energy source (Source: USA EIA, 2010)

Solar Resource

Although solar energy incident on earth's surface for 40 minutes is equal to all the energy consumed by the human society in a year (James, 2007) with a fairly high amount of incident solar energy on earth's surface (Figure 1.3), the current solar power generation capacity is about 0.5 % of the world's installed electricity generation capacity (Reuters, 2010). This indicates the vast untapped potential of the solar power.

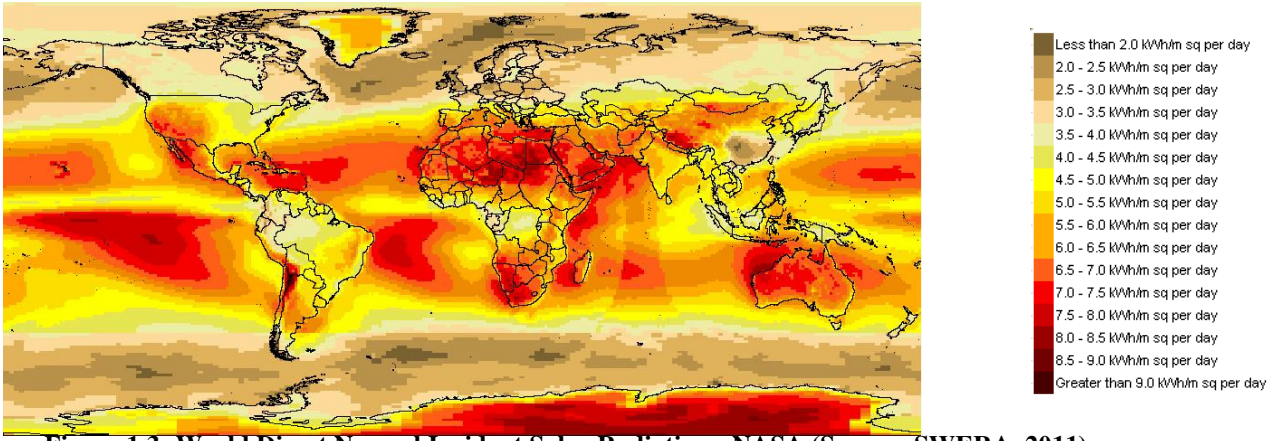

Figure 1.3: World Direct Normal Incident Solar Radiation - NASA (Source: SWERA, 2011)

USA shows an average incident radiation of about 6 [kWh/m^2/day] (Figure 1.4) with the southwest region having above average radiations as high as 8 [kWh/m^2/day].

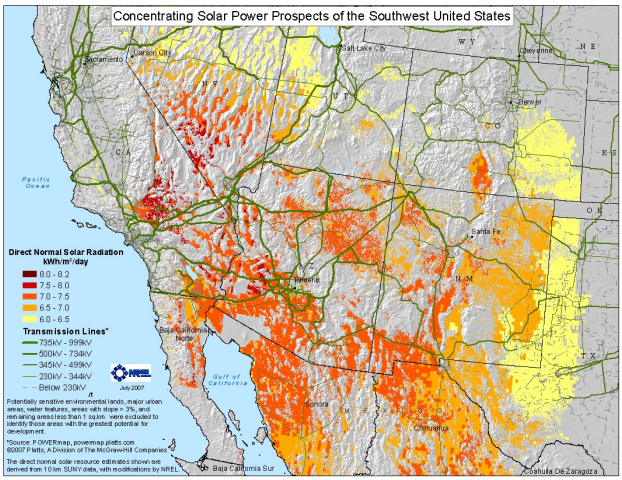

Figure 1.4: US Direct Normal Incident Solar Radiation - NREL (Source: NREL, 2011)

According to NREL, the combined potential of the seven south-western states is about 22,000 GW (Anthony, 2012) as compared to the current nameplate generation capacity of entire US at 1,100 GW (EIA, 2012).

Comparatively, the average incident solar radiation on India is 5 kWh/m^2/day, with a large part of the west and north-west region receiving 6 kWh/m^2/day (Figure 1.5). India is located in the equatorial sun belt of the earth, thereby receiving abundant radiant energy from the sun. The annual global radiation varies from 1600 to 2200 kWh/m^2, which is comparable with radiation received in the tropical and sub-tropical regions but which is qualitatively lower than US where development and deployment of solar technologies is maximum. This makes CSP an export product for India in the near future, while in the long run, it will decide on the choice of solar power technology most economical for Indian market.

All the examples above highlight the existing potential to harness solar energy for power generation. There are currently many technologies available to utilize the solar potential. The next section briefly introduces these technologies and highlights their limitations.

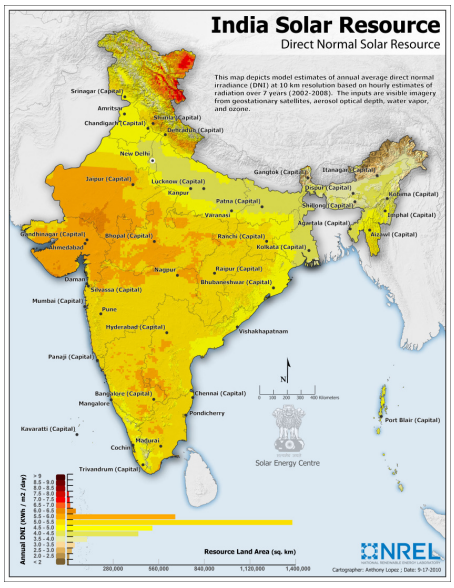

Figure 1.5: India Direct Normal Incident Solar Radiation - NREL (Source: NREL, 2011)

Overview of Solar Power Generation Technologies

Solar power generation is conversion of sunlight into electricity. This section will review the prevalent technologies for generation of electricity from solar energy. The main categories are namely the photovoltaic system (PV) and the concentrating solar power. There are also recent developments in combining these two technologies called as concentrating photovoltaic (CPV). This section presents the details of these technologies.

PV systems directly convert sunlight into electricity using or by indirectly using concentrated solar heat to either act as power source to the conventional power generation systems or to chemically synthesize fuels (DoE, 2011).

PV systems convert sunlight directly into electricity using the photo-electric effect. The first solar cell was constructed by Charles Fritts in the 1880s (Perlin, 1999). In 1931 a German engineer, Dr. Bruno Lange, developed a photo cell using silver selenide. The silicon solar cell was created in Bell Labs in 1954 (SEIA, 2012). These early solar cells cost 286 USD/watt and reached efficiencies of 4.5–6%. Since 1997, PV development has accelerated due to oil and natural gas supply issues and the improving economic position

of PV relative to other energy technologies.PV cells are made of semiconductors such as crystalline silicon or thin-film silicon material. PV can provide tiny amounts of power for watches to large amounts for the electric grid. There has been significant advancement in PV technology in the materials used for making solar cells. Across most PV technologies, the efficiency of commercially available PV modules varies from about 10% (for tandem microcrystalline-amorphous silicon) to 19.6% (for super mono-crystalline silicon) (Alan, 2012). Costs of production have been reduced in recent years for more widespread use through production and technological advances. Crystal silicon solar cells have largely been replaced by less expensive multi-crystalline silicon solar cells, and thin film silicon solar cells have also been developed recently at lower costs of production. The module costs are at $2/kW without adding the cost of support structure, installation, site, tracking etc. (Alan, 2012). The system cost still remains high enough to become a viable option for large-scale power generation. According to a study by North-Carolina Sustainable Energy Association (NCSEA), the levelized cost of solar PV for 2012 is 19 cent/kWh (Miriam, 2012) . Also, CSP with the option of thermal energy storage (TES) has an advantage over the PV system for greater grid penetration due to the premium economic value associated with energy storage (Rick, 2011). Recent developments in concentrating PV technology (CPV) have seen solar cell efficiencies greater than 40% (NREL, 2013).

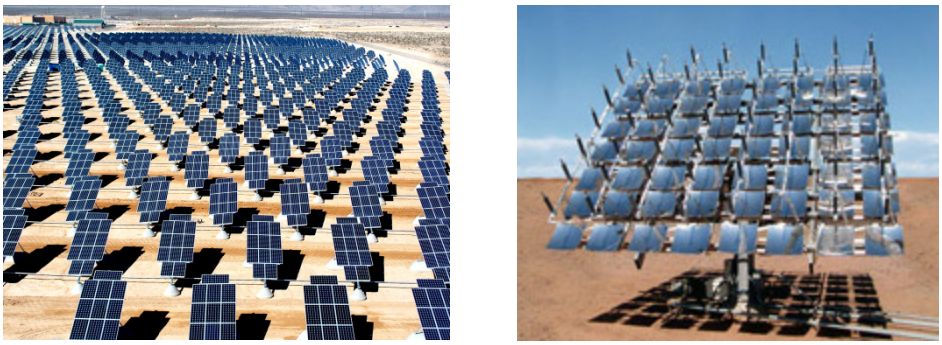

Figure 1.6: Solar Photovoltaic System and Concentrating PV System (Source: NREL)

Concentrating solar power (CSP) technologies use reflective materials to concentrate the solar radiative thermal energy, which ultimately drives a generator to produce electricity. They can also be used to chemically synthesize fuels (DoE, 2011).

Legend has it that Archemedes used mirrors made of bronze to concentrate sunlight on ships of roman fleet and burn them down to repel them from Syracuse (Thomas, 1975). However, the earliest documented work on solar thermal power is by Auguste Mouchout in Paris between 1860 and 1880 where he used parabolic trough to produce steam for solar steam engine (Butti, 1980). John Ericsson built dish concentrator and gas engine towards the end of nineteenth century (Meyer, 2008). Frank Shuman and Charles V Boys developed a 60-70 HP parabolic solar thermal power station in Meadi, Egypt using parabolic troughs (Cutler, 2008). High temperature solar power dish with hemispherical boiler using fused quartz for power generation was invented by R. H. Goddard (Goddard, 1929). In the late 1960s and early 1970s, when it became clear that fossil fuel resources are limited and their unequal distribution lead to strong dependencies, systematic research work was started in a number of industrialized countries on improving solar power concentration technology. Professor Giovanni Francia built the first operational CRPT plant of 1 MW capacity in Sant'llario, Italy in 1968. It had a central receiver in a field of solar collectors (Butti, 1980).

Solar One was the first operational pilot large scale solar-thermal system with a target output of 10 MW built in Mojave Desert in Barstow, California. The plant operated for two years in an experimental assessment phase and for three years in power generation phase. The power generated by the plant was supplied to the grid of Southern California Edison utility. Solar One is a central receiving power tower solar-thermal power plant (CRPT). CRPT plants use mirrors, or heliostats, to focus sunlight at a central receiver. Since many heliostats are focused onto one central receiver, temperatures of 1000^{o}C can be obtained. The heliostat system consisted of 1818 mirrors for a total array area of

71,000 m^2. The receiver was a single-pass superheat boiler, 13.7 m long and 7 m in diameter. The receiver was designed to produce 850 kg/s of steam at 516^o C (961 F). The power generation system included the turbine generator, its auxiliaries and the cooling system for heat rejection (Craig, 1995). Solar One in California was shut down in 1988 after proof-of-concept was established then re-commissioned as Solar Two in 1995 to test improvements to the system including more collection area and different collection fluids for an estimated spending of $ 48.5 million. Solar Two used molten salt, as an energy storage medium instead of oil or water used in Solar One. The molten salt allowed the energy to be stored in large tanks for use such as cloudy days or night time. Solar Two had sufficient capacity to continue running for up to three hours after sun-set. Solar Two was decommissioned in 1999. A commercial power plant, called Solar Tres Power Tower, is being built in Spain by Torresol Energy using Solar One and Solar Two's technology for electrical production of 15 MW. Solar Tres will be three times larger than Solar Two with 2,493 heliostats, each with a reflective surface of 96 m². The total reflective area will be 240,000 m² (2.6 million ft²). They will be made of a highly reflective glass with metal back to reduce costs by about 45%. A larger molten nitrate salt storage tank will be used with the ability to store 600 MWh, allowing the plant to run 24x7 during the summer.

Figure 1.7: PS-10 and PS-20 Concentrating Solar Power Tower Plants (Source: trec-uk.org)

The PS10 Solar Power Plant is the world's first commercial concentrating solar power tower operating near Seville in Spain. The plant was built between 2004 and 2007. The 11 MW solar power tower produces electricity with 624 heliostats with a surface area of 120 m² that concentrates the solar radiation to the top of a 115 meter high, 40-story tower where the solar receiver and steam turbine are located. The solar receiver produces saturated steam at 257 °C which runs the steam turbine with a conversion efficiency of 17% (John, 2009). The PS10 solar power tower stores heat for one hour in tanks as superheated and pressurized water at 50 bar and 285°C. PS10 implements a direct steam generation (DSG) technology, where the solar thermal energy is used to convert water into steam directly. In contrast, a dual loop technology implements a primary heat exchanger with a heat transfer fluid (HTF) which transfers the heat to the working fluid of power cycle in a secondary heat exchanger. The PS10 produces 23.4 GWh of energy with 24% capacity factor. The world's most powerful solar power tower however is the PS20 solar power plant in Seville, Spain with a rated capacity of 20 MW. PS20 produces 48 GWh of energy at a capacity factor of 27% at an earning rate of 36 cent/kWh. It was constructed between 2006 and 2009 as a part of the Sanlucar la Mayor project. PS20 consists of a solar field of 1,255 heliostats designed by Abengoa Solar. Each heliostat has a surface area of 120 m^2 and reflects the solar radiation onto the receiver located on the top of a 165 m high tower. PS20 features a number of significant technological improvements with respect to PS10 including a higher-efficiency receiver, various improvements in the control and operational systems, and a better thermal energy storage system (Spanish News, 2009). The entire Sanlucar la Mayor project will yield a power generation of 300 MW from towers, photovoltaics, parabolic troughs and Stirling engines.

The Solnova 1 station currently under construction uses parabolic troughs to focus sun rays on a linear array of pipes as opposed to point focus for central receiver systems. The pipes containing synthetic oil are heated to 400 C. The dual loop design uses this heat to

generate steam to drive the turbine. Solnova 1 is rated at 50 MW with a conversion efficiency of 19%.

Figure 1.8: Solnova 1 and 3 Parabolic Trough based Solar Thermal Plant (Source: Abengoasolar.com)

According to a SANDIA report, the levelized cost of generating electricity using CSP power tower technology for a 100 MW rated capacity with 0% investment tax credit is about 12 cent/kWh (Gregory, 2011).

Figure 1.9: SEGS-III (Source: NREL)

Solar Energy Generating Systems (SEGS) in California, at 354 MW, is the largest solar thermal energy generating facility in the world. It consists of nine solar power plants in California's Mojave Desert, where insolation is among the best available in the United States. SEGS I–II (44 MW) are located at Daggett, SEGS III–VII (150 MW) are installed at Kramer Junction, and SEGS VIII–IX (160 MW) are situated at Harper Lake (Angela, 2006). The SEGS units have been designed and constructed by Luz International Limited. These plants are based on parabolic trough concentrators providing steam to power

generation plants. They generate peaking power, which is purchased by the Southern California Edison Utility.

The design and economics of these plants depend on US government support for such facilities under Public Utilities Regulatory Policies Act (PURPA), which allows small power producers to supplement their solar output by fossil fuels by as much as 25% of the annual output. The operating strategy of these plants is created to maximize solar energy use and depends on natural gas when solar energy is not available. The solar and natural gas circuits run parallel to optimize output (Figure 1.10).

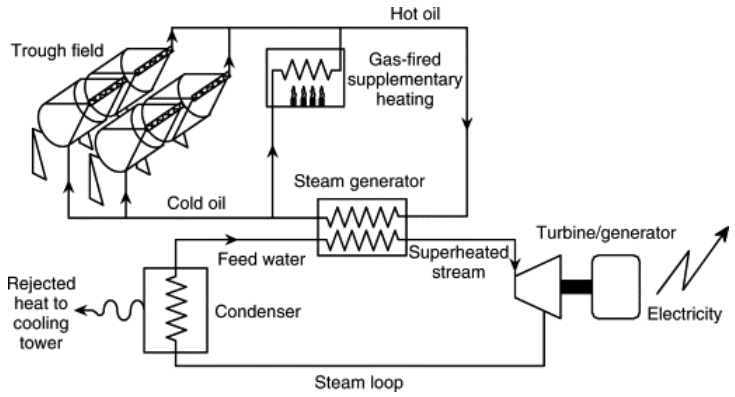

Figure 1.10: Schematic of SEGS Power Plant Layout (Source: Sciencedirect.com)

The major components in the system are the collectors, fluid transfer pumps, the power generation system, the natural gas auxiliary sub-system and controls. The collector system is designed to harness maximum solar energy during summers but leads to lower solar incidence yearly. A synthetic heat transfer fluid (HTF) is heated in the collectors and is piped to steam generation system to produce steam for the turbine. High-temperature pumps circulate this HTF with the fluid leaving the field at 390^{o} C (734 F) and entering at 304 ^{o} C (579 F). The concentration ratio for the reflected sunlight in a parabolic trough is about 80 which is a low value. The thermal efficiency of the heating process in the pipes is about 60-80%.

The annual overall capacity factors have been 30% for SEGS units. The overnight capital cost for the SEGS LS-3 with 6 hours thermal storage was 2340 $/kW with the power-block alone accounting for 440 $/kW (Solarpaces, 2013). The actual levelized cost of delivered energy from SEGS VII in 2001 was 16.4 cent/kWh (John, 2006). The solar to electricity efficiency for all the SEGS units have been around 10-14% (Robert, 2001). No new SEGS plant has been built since 1991 due to declining energy costs and incentives in the past two decades, but research has continued. The next generation SEGS plants will benefit from significant technological developments in materials and manufacturing processes.

Nevada Solar One is another CSP with a nominal capacity of 64 MW and maximum capacity of 75 MW. It is the second solar thermal power plant built in the United States in more than 16 years and the third largest STE plant built in the world since 1991 (ENS, 2007). Nevada Solar One uses proprietary technology to track the sun's location and concentrate its rays during peak demand hours. The plant uses 760 parabolic trough concentrators with more than 182,000 mirrors and 18,240 receiver tubes placed at the focal axis of the troughs and containing heat transfer fluid. The HTF heats up to 391 C (735 F) and is used to produce steam that drives a Siemens SST-700 steam turbine, adapted to the specific requirements of the CSP technology.

Andasol, the first parabolic trough power plant in Europe is the largest solar thermal power plant in collector area. It consists of three different units namely Andasol 1,2 and 3. Andasol 1 went online in March 2009. Each plant has a gross electricity output of 50 MW, producing around 180 GWh annually. The parabolic trough collectors installed have a combined surface area of 51 hectares and it occupies about 200 hectares of land (SolarMillenium, 2008). Andasol has a thermal energy storage system for about 7.5 hours at full-load using molten salts as storage medium.

The recent developments in the trough technology aim at improving the operating limits and cost effectiveness of the system. SkyFuel under the Sunshot initiative is developing an advanced, low-cost CSP collector using higher-concentration, higher-temperature, parabolic trough technology to substantially reduce the cost of baseload utility-scale solar power generation. The parabolic trough collector is being optimized for high-temperature service with a maximum temperature of 100°C above prior state-of-the-art systems (up to 500°C or more). High-temperature design points demand larger apertures and concentration ratios (40%–90% greater than the prior state of the art) with associated improvements in optical accuracy (30%–75% over the prior state of the art). Also, significant reductions in cost is foreseen because of larger aperture, while incorporating additional advancements like the reflective film surfaces being upgraded to improve reflectance and specularity. A surface coat is being developed to provide anti-soiling and abrasion resistance (DoE, 2012).

Figure 1.11: Stirling Energy System's 300 MW commercial solar thermal power plant in California (Source:mtholyoke.edu)

Another CSP technology available for small scale power generation is the dish/Stirling engine. A dish Stirling system uses a large, reflective, parabolic dish. It focuses the incident solar radiation onto a single point above the dish, where a receiver captures the heat and transforms it into a useful form. Usually the dish is coupled with a Stirling engine. The advantage of a Stirling engine is that it can run on any heat source and the cycle efficiency can be theoretically equal to Carnot efficiency. CSP-Stirling is known to

have the highest efficiency of all solar technologies at around 30%. The advantage of a dish system is that it can achieve much higher temperatures due to the higher concentration of light (greater than tower designs). Higher temperatures lead to better conversion to electricity. The first solar powered Stirling Engine, Vangaurd I, was developed by Advanco Corporation in 1984. An 11 m parabolic dish with a concentration ratio of 2100 focused sunlight onto a Stirling engine that reached 800 C with a power output of 25 kW. In January 2010, Stirling Energy Systems and Tessera Solar commissioned the first demonstration 1.5-megawatt power plant - Maricopa Solar, using Stirling technology in Peoria, Arizona (Patrick, 2010). However, the disadvantages are the requirements of heat exchangers for this engine to work, which for the amount of power produced, are large in size. This is due to the low heat transfer coefficients for the gaseous convection, which limits heat-flux. This restriction makes them competitive for a 100kW or lower power segment (Marc, 2005).

Figure 1.12: Compact Linear Fresnel Reflector (Source:kcet.org)

Another solar power concentration technology is the Fresnel concentrators. A linear Fresnel reflector power plant uses a series of long, narrow, shallow-curvature or flat mirrors to focus light onto one or more linear receivers positioned above the mirrors. The receivers can be augmented with a small parabolic mirror for further focusing the light. These systems aim to offer lower overall costs by sharing a receiver between several mirrors with the simple line-focus geometry and single axis tracking. This is similar to the trough design. The receiver is stationary and so fluid couplings are not required. Also,

the support structure is simpler as the mirrors need not support the receiver. With optimized aiming strategies for mirrors aimed at different receivers at different times of day, this configuration allows for a denser packing of mirrors on available land area. Recent prototypes of these types of systems have been built in Australia and by Solarmundo in Belgium (John, 2011).

Impact of Power Cycle on Performance of Solar Thermal Power Plant

The most important factors that affect the selection of power cycle for a solar thermal power plant are:

1) Power Generation System Performance
2) Cost competitiveness
3) Compatibility with adjoining systems and technology

The following section presents the details on each factor

Power Generation System Performance

With so much investment on building of infrastructure for running a solar thermal power plant, the power generation system efficiency is the most important factor as it determines the size of the solar collector system. Power generation system efficiency depends on the solar collector technology chosen to deliver solar power to power generation system working fluid as well as the technology for power generation. The solar collector technology and power generation technology together determine the peak attainable temperature in the power cycle which has a highest impact on the power-block efficiency. Parabolic troughs are scalable to a great extent for a required power generation capacity but are limited by their peak temperatures (Angela, 2006). The power generation technology with the choice of a particular power cycle and working fluid has an impact on the maximum attainable efficiency for a given peak cycle temperature. The net efficiency of the steam turbine generator in the applicable pressure and temperature

range is about 30% -37% for the SEGS (Angela, 2006). This efficiency can be increased by increasing the pressure and temperature of the steam but is constrained either by the solar collector design or the restrictive cost of accommodating a high pressure and temperature steam (Sargent, 2003). There has been an increasing interest in implementing a Brayton Cycle based power generation system i.e. a gas turbine system to harness solar energy (Charles, 2007). The expected advantage of such a system is to achieve higher operating temperatures using a CSP technology (~1000^{o} C) which increases the system efficiency. The present study will focus on the selection of solar collector technology and design of power generation technology to achieve optimum performance from the system.

Cost Competitiveness

The cost of solar thermal power plant is combination of different sub-system costs. In that context, the power cycle has a direct and indirect impact on the cost of the overall system. The direct impact is on the cost of power generation equipment which will implement the selected power cycle. This includes the prime mover and the balance of plant equipment. According to a SANDIA report on power tower technology roadmap, the combined cost of power block and steam generation system for a 100 MW power plant is 1350 $/kW (Gregory, 2011). The indirect impact is on the cost of solar collector system which depends on the efficiency of the power generation system. For large scale power generation, the efficiency of power generation system enhances the economy of operation for the power plant. In 2009, the sunshot program (DoE CSP program) set the goal to reduce the LCoE cost of a hypothetical power plant with 100 MW rated capacity, from today's cost of 15 cent/kWh to below 9 cent/kWh by 2020. This goal was updated in 2011 to 6 cent/kWh (Gregory, 2011).

Another important factor impacting the cost of operation is the availability of resources for the plant operation. For example, availability of water is a constraint that most

Rankine cycle based systems need to account for in their design. The CSP systems are designed to operate more efficiently in areas of abundant sunlight and vast stretches of empty lands like the deserts, and such places have very limited sources of water supply. The present study will focus on the impact of power cycle on cost of the equipment and systems and not dwell on the operating costs of making available resources like water.

Compatibility with Adjoining Systems and Technology

There are multiple systems which interact with the power generation system to impact the feasibility and overall performance of the plant system. The following are the critical few.

Heat Transfer Fluid (HTF)

The HTF absorbs the solar radiation in the receiver system and supplies the energy to the power generation system and the thermal energy storage system. There are many available options of materials based on the operating requirements of the system like organic fluids, synthetic oil, molten salts and sand. The main challenge for the HTF is the stability of the fluid at high temperatures as it dictates the applicability of a particular HTF in a given operating scenario. For example, in Solar Two the power tower can generate very high temperatures (~1000 C) at the receiver surface, but the molten salt HTF used for heat transfer is stable only till 600 C. Similarly, at low temperatures some of the HTFs freeze leading to clogging of the pipes carrying HTFs. SO, the heat input range of temperature for the power cycle has an impact on the feasibility and selection of HTFs.

Thermal Energy Storage (TES)

Any solar power system must cater to the fluctuation in incoming solar radiation due to presence of clouds during daytime and absence of direct sunlight during nighttime operation. The power plant in the absence of sunlight will lose its source of energy and

reduce the capacity factor of the system. This issue is addressed by incorporation of a thermal energy storage system (TES). This system stores the excess energy during daytime operation and utilizes the stored energy during the low sunlight periods and also after sunset. Thermal energy storage technology includes sensible heat storage, latent heat storage and thermo-chemical heat storage (Goswami, 2000). The power cycle implemented has a bearing on the performance of the TES system as the inlet and outlet HTF temperature for the power cycle determine the applicability and efficiency of thermal storage. The present study does not focus on the design of a TES system but assesses the feasibility of its implementation for a given power cycle.

Hybrid Operation

A solar thermal power plant alone has low capacity factor based on the daily and annual fluctuation of solar radiation. TES addresses this issue to some extent by providing stored thermal energy. But the present technology does not allow for storage beyond few hours and also the system will fail to perform for extended periods of "no-sunlight". Another means of improving the availability and capacity factor of the power plant is to use fossil fuel powered backup to maintain the output in a hybrid operation for power generation. SEGS II to IX made use of natural gas back-up fire to augment output during peak demand hours (Angela, 2006). The power cycle selection for a solar thermal plant will have significant influence based on the hybrid operation capability.

Thesis Objective

The purpose of the current study is to assess critically the potential thermodynamic cycles for solar thermal power generation on the following aspects to determine the feasibility of implementing a solar applicable gas cycle:

1. To thermodynamically characterize the potential gas cycles for large scale power generation with the applicable constraints on peripheral technologies

2. To develop cost models to represent the economic performance of the system operating on these potential cycles

3. To compare the thermodynamic and economic performance of the potential cycles with the current state of art to assess the feasibility and establish a suitable guidance for implementation of these cycles.

CHAPTER 2

SOLAR THERMAL POWER CYCLE TECHNOLOGY

Introduction

In a solar thermal power plant, the power conversion system is the second most important system after the solar collector system. This chapter will present the literature review for the recent developments in thermodynamic cycles implemented for solar thermal power generation. We will then proceed to identify the opportunity for assessing the potential power cycles and describe the approach followed for evaluating the new configurations.

Thermodynamic Power Cycles

Thermodynamic power cycles are the basis for the operation of heat engines, which supply most of the world's electricity and run the vast majority of automobiles. Power cycles can be classified according to the type of heat engine they are implemented on. For example, cycles for external combustion engines include the Brayton cycle, which is implemented in gas turbines, and the Rankine cycle, which is implemented in steam turbines. For solar thermal power generation, the cycles implemented in their standard and modified forms are Rankine cycle, Brayton cycle, Stirling cycle and Ericsson cycle or their combinations. The existing literature has been thoroughly reviewed to ascertain the feasibility of the present work and a selected number of papers are being presented in the following section. Since the standard cycles are being modified in their application or choice of working fluid or addition of process steps, a comprehensive discussion of these standard cycles is not presented in this work and readers are referred to a general thermodynamics textbook for additional discussion on the standard cycles (Cengel, 2002).

Rankine Cycle

Although almost all the power generation system implemented in the solar thermal power generation is based on Rankine cycle, not much development has happened in the standard Rankine cycle. However, various thermodynamic cycles based on Rankine cycle such as the organic Rankine cycle, supercritical Rankine cycle, Kalina cycle, Goswami cycle, and trilateral flash cycle have been proposed and studied for the conversion of low-grade heat sources into electricity in the recent past. The organic Rankine cycle (ORC) applies the principle of the steam Rankine cycle, but uses organic working fluids with low boiling points to recover heat from lower temperature heat sources. ORCs yield higher efficiencies than conventional steam cycles at temperatures below 370^{o}C for heat delivery.

Huijuan Chen et al. presented a review of the organic Rankine cycle and supercritical Rankine cycle for the conversion of low-grade heat into electrical power. The study concluded that Organic Rankine cycles do not have a good thermal match with their heat sources, unlike a supercritical Rankine cycle, but a supercritical Rankine cycle normally needs higher operating pressures. The study also concluded that properties of the working fluids play vital role in the cycle performance. The thermodynamic and physical properties, stability, environmental impacts, safety and compatibility, availability and cost are among the considerations when selecting a working fluid (Huijuan et al., 2010).

Christian et. al presented a study on Comparison of sub- and supercritical Organic Rankine Cycles for power generation from low-temperature/low-enthalpy geothermal wells (geothermal fluid temperature of 150 C), considering specific net power output and efficiency (Christian et al., 2013). Organic Rankine Cycles using propane achieved a thermal efficiency of 10.1% at supercritical vapor. Cycles with CO2 used as working fluid achieved thermal efficiency of 8.0%. Compared to subcritical processes with Isopentane, an approximately 30% increase of net power output was achieved with

propane as working fluid. In contrast, CO2 did not seem to be a suitable working fluid under the conditions of this study.

Goswami and Feng proposed a combined power/cooling cycle using ammonia-water mixtures as a working fluid (Goswami, 1999). The cycle was a combination of Rankine and absorption refrigeration cycles. It will not only produce power but also provide a certain amount of cooling. The new thermodynamic cycle proposed to utilize high efficiency flat plate or medium temperature (100- 200°C) concentrators. The proposed cycle achieved a first law efficiency of 23.54% for a turbine inlet temperature of 410 K and 30 bar pressure and exiting at a 2 bar pressure.

Price and Mayor evaluated the feasibility of meso-scale solar thermal power generation (12.5 kW) using various vapor power cycles. Initially, five candidate cycles were analyzed (Price and Mayor, 2008), which was later extended to six candidate cycles (Price and Mayor, 2009 and Price, 2009). Price evaluated the feasibility of meso-scale solar thermal power generation (12.5 kW) using the Rankine cycle, the organic Rankine cycle with toluene, R123 and ethylbenzene as working fluids, the Kalina cycle and the Maloney-Robertson cycle (Price, 2009). The study included economic feasibility through thermo-economic characterization that encompasses a meso-scale cost model for solar-thermal power generation systems. The study indicated that a R123 organic Rankine cycle is the most cost-effective cycle implementation for operating conditions with maximum temperature below 240^{o}C. For temperatures greater than 240^{o}C and less than 375^{o}C, the toluene and ethylbenzne organic Rankine cycles outperformed the other cycles. The highest first law efficiency of 28% of the Kalina cycle exceeded all other cycles at temperatures between 375^{o}C and 500^{o}C. However, when considering cycle cost and overall feasibility, including thermodynamic and thermo-economic performance, the Maloney-Robertson and Kalina cycles had poor performance on a cost-to-efficiency basis.

Pei Gang presented an analysis of low temperature solar power generation using regenerative Organic Rankine Cycle (Pei, 2010). The configuration consisted of small concentration ratio compound parabolic concentrators (CPC) and the regenerative ORC. The system electricity efficiency with regenerative ORC was about 8.6% for irradiance of 750 W/m2 which was higher than that without the regenerative cycle by 4.9%. Daniel et. al. investigated the performance of different types of organic Rankine cycles (ORC) and Kalina cycle and optimized them for low-temperature (100-150 C) geothermal heat sources (Daniel, 2012).

All the development work on the ORCs and other Low grade heat recovery cycles are designed for low power output (< 10 MW), which does not suit the requirement of the present study objective. There have been developments on the use of solar energy as backup to augment the performance of a fossil fired steam turbine unit.

You Ying published a study of using solar energy as an external source to replace the extracted steam to heat the feed-water in the regenerative Rankine plant (You, 1998). Yongping Yang demonstrated the use of medium-or-low temperature solar energy to replace parts of bled-off steam in regenerative Rankine cycle to pre-heat feed-water, in so called solar aided power generation (SAPG) technology (Yongping, 2009).

Zhang presented a numerical study of a solar energy powered Rankine cycle with supercritical CO2 as the working fluid and heat recovery systems (Zhang, 2007). For a turbine inlet temperature range of 137 C and 217 C, the power generation efficiency varied between 20 and 25%.

Brayton Cycle

A significant development has happened in the application of Brayton cycle for solar thermal power generation in the past two decades which included substituting different

working fluids and augmenting additional systems like recuperator and intercooler to enhance the cycle performance.

Yousef carried out performance analysis of closed cycle gas turbine engine with heat recovery using different gases such as air, combustion gases, CO2 and helium (Yousef et al., 1992). He concluded that helium had higher specific work output due to high specific heat but overall system efficiency dropped after a low optimum pressure ratio.

Leonard published a review of test results on solar thermal power modules with Dish-mounted Stirling and Brayton cycle engines (Leonard, 1988). A Stirling module achieved an efficiency of 29.4 percent and a net output of 25.6 kW. The average efficiency over 15 consecutive days was 22.5 percent. Gross efficiency of the receiver-engine subsystem exceeded 34 percent; engine inlet temperature was about 720 °C. A number of malfunctions occurred. Tests of various Brayton subsystems showed receiver efficiencies up to 81 percent and engine efficiencies up to 29.8 percent, at receiver outlet/turbine inlet temperatures of 885-925°C. These were at power levels of roughly 85 kW at the receiver and 25 kW at the engine output. The Brayton engines tested could operate on sunlight, fuel, or both, simultaneously.

Thomas et al. reviewed the status of Dish-Stirling systems that are being developed for commercial markets and presented system specifications along with review of system performance and cost data. The economics, capital cost, O&M costs and the emerging markets for Dish-Stirling systems were also reviewed (Thomas et al., 2003).

Colin and David explored the role of recuperators and regenerators in developing high efficiency gas turbines (Colin and David, 1995). The study projected the use of heat recovery exchangers to address the low emissions requirement on the onset of 21st century. Many potential and upcoming concepts on design and manufacturing of regenerators and recuperators were discussed.

Yousef published a review of a set of research investigations in the field of gas turbine co-generation in power and industry (Yousef, 2000). The study mainly concluded that cogeneration with gas turbines utilized the engine's relative merits and boost its thermal efficiency even at part load.

Uri et al. published a description of tasks involved in solarization of existing power-blocks. The paper reviewed many solar projects and mainly SOLGATE project during 2001 and 2003 (Uri et al., 2004). During 2002–2003 the turbine was operated in Spain, combined with three volumetric receivers. The initial goal of achieving 800°C at the receiver outlet was achieved. The successful tests have encouraged the continuation of work using gas turbines of 10 MW and above.

James et al. developed a dynamic model of a megawatt-scale low-temperature intercooled-recuperated solar gas-turbine power plant to determine its thermodynamic and economic performance (James et al., 2012). The model was then used for multi-objective thermo-economic optimization of both the power plant performance and cost. Detailed performance and cost models were developed for the heliostat field, receiver system, heat exchangers and power system. The optimum performance was reported at peak cycle temperature of 950 C at 12.7 cent/kWh for a 60 MW power plant. However, the receiver losses were ignored, leading to a rise in system performance with peak cycle temperature which looks counter-intuitive. Also, the receiver system was fed with working fluid of the gas turbine and intercooler was air-cooled to reduce water consumption.

Sahil et al. evaluated the use of gas turbine exhaust gas waste-heat powered, single-effect water-lithium bromide (H2O-LiBr) absorption chillers thermo-economically for gas turbine compressor inlet air cooling scheme (Sahil et al., 2013). For an ambient

temperature of 323 K (122 F) and compressor inlet temperature of 283 K, the absorption chiller improved the cycle efficiency by 3.7 percentage points.

Charles et al. reviewed the combined use of fluoride salts for power tower and closed Brayton cycle with helium as working fluid being developed for high temperature nuclear reactors to provide the technology basis for high performance solar power tower system (Charles et al., 2007).

Combined cycles with topping recuperative gas turbines and bottoming ORCs have been reported as an alternative to conventional combined cycles by Chacartegui et al. (Chacartegui et al., 2009) and to low temperature solar thermal electric generation by Gang et al. (Gang et al., 2010).

Chacartegui et al. proposed supercritical and trans-critical cycles based on carbon dioxide for central receiver solar power plants. Two stand-alone closed cycle gas turbines using carbon dioxide and the third is a combined cycle that comprised a topping carbon dioxide gas turbine and a bottoming Organic Rankine Cycle (Chacartegui, 2010). The study compared the thermodynamic performance of the proposed cycles with saturated steam cycle (PS-10) and super-heated steam cycles. Amongst the two closed Brayton cycles considered, the more complex layout L2 working with supercritical conditions at compressor inlet and with improved heat recovery achieves higher cycle efficiency. The improvement with respect to simpler schemes can be as high as 7-12 percentage points, depending on turbine inlet temperature. Combined cycle analysis shows that recuperative ORC systems do not provide a significant advantage due to rather low Heat Recovery Vapor Generator efficiency. There is not a single organic fluid able to optimize combined cycle efficiency independently of turbine inlet temperature of the topping cycle.

Ramon presented a study centered on combined cycle efficiency enhancement by researching the capacity of several working fluids such as N_2, air, or He for the topping

cycle which is a closed Brayton cycle (CBC) and a bottoming cycle which is a Rankine cycle (RC) operating with xenon, ethane or ammonia as working fluids (Ramon, 2012). With nitrogen and air as working fluids for CBC, very similar results in terms of efficiencies are achieved. Pressure ratios of 25 operating with a top temperature of 1300 K, renders a thermal efficiency which approaches 43% in both cases. With helium as working fluid, a pressure ration of 9 for a top temperature of 1300 K renders a thermal efficiency of 43%. However the specific work is much higher than the cycles of nitrogen and air. For the bottoming cycle with different working fluids, the performance is satisfactory in spite of low peak temperature of 700K due to quasi-critical condensation condition. For the combined cycle operation with peak cycle temperature at 1300 K, efficiencies of 66%-68% are achieved for the most favorable cases.

Efforts were also put towards developing the receiver system to enable application of high temperature thermodynamic cycles like Brayton cycle. Nathan et al. presented their effort to provide an experimental basis for the validation of computational models that have been created to support improved designs and further development of the solid particle receiver (Nathan et al., 2010). The experiment demonstrated a single pass temperature increase of nearly 250°C at practical particle mass flow rates and the relative stability of the particle curtain when exposed to wind and buoyant flows. The peak temperature achieved in the cavity was however at 723^{o}C. The study concluded that to achieve temperatures in excess of 900^{o}C, the optical design of the receiver had to be modified as also the recirculation of particles to increase particle residence time.

Kyle and Fletcher investigated several thermodynamic cycles for a small particle heat exchange receiver used in concentrating solar power plants to assess the mechanical loads based on the size of volumetric, pressurized gas-cooled receivers (Kyle and Fletcher, 2011).

Hischier et al. presented an experimental and numerical assessment of a high-temperature pressurized air-based receiver for power generation via solar-driven gas turbines (Hischier et al., 2012). It consisted of annular reticulate porous ceramic (RPC) foam concentric with an inner cylindrical cavity-receiver exposed to concentrated solar radiation. Absorbed heat is transferred by combined conduction, radiation, and convection to the pressurized air flowing across the RPC. Experimentation was carried out using a 3 kW solar receiver prototype subjected to average solar radiative fluxes at the CPC outlet in the range 1870–4360 kW m2 with air and helium as working fluids, heated from ambient temperature up to 1335 K at an absolute operating pressure of 5 bars. Peak thermal efficiencies obtained were 77% for air at 826 K receiver outlet temperature and 78% for helium at 892 K receiver outlet temperature. For the optimized design, thermal efficiencies in the range of 74–90% for air outlet temperatures of 1240–1710 K are predicted.

Hybrid Cycles

Stefano et al. presented an analysis of solar-thermal power plants with thermal energy storage and solar-hybrid operation strategy (Stefano et al., 2011). Selected solar-hybrid power plants were analyzed for base-load as well as part-load operation regarding supply security (due to hybridization with fossil fuel) and low CO2 emissions (due to integration of thermal energy storage). Therefore, those power plants were modeled with different sizes of solar fields and different storage capacities and analyzed on an annual basis. The study concluded that that in comparison to a conventional fossil-fired combined cycle, the potential to reduce the CO2 emissions is high, especially with large solar fields and high storage capacities. However, for dispatchable power generation and supply security, a certain amount of additional fossil fuel was always required. None of the analyzed solar-hybrid power plant showed at the same time advantages in terms of low CO2 emissions and low LEC. While power plants with SHCC (Particle-Tower) show

interesting LEC, the power plants with steam turbine (Salt-Tower, Parabolic Trough, and CO2-Tower) have low CO2 emissions (especially those with large solar fields and high storage capacities). All solar-hybrid power plants showed increasing LEC with increasing solar field sizes and storage capacities. This was mainly caused by the high investment cost of the TES.

Elysia et al. reviewed the hybrid solar–fossil fuel power generation with an emphasis on system integration and evaluation (Elysia et al., 2012).

Summary

A detailed review of available literature on development of thermodynamic cycles and associated systems is carried out with the specific focus on solar thermal power generation. It has been established that although significant development and assessment has happened in the implementation of Brayton cycle for solar thermal power generation, a comprehensive assessment of implementing a gas cycle for solar thermal power generation based on thermodynamic and economic performance of the entire power plant system has not been carried out yet. The following section will now outline the thesis to address this objective.

Gas Power Cycles – Thesis Outline

The current project investigates the concept of CSP with gas cycle power generation with the goal of identifying applicable gas turbine cycles and overall system designs that could provide more cost effective means of providing solar energy based electricity. There are three configurations identified:

1) Cold Gas Turbine (CGT)

2) High Temperature Solar Gas Turbine (HTSGT)

3) Lorentz Cycle Gas Turbine (LCGT)

The CGT system is developed for the parabolic trough configuration and explores the possibility to increase the work extraction from the cycle by lowering the heat rejection temperature. The HTSGT system attempts to increase the heat addition to the power cycle to extract more efficiency from the cycle using a power tower configuration. The LCGT system attempts to increase the GT efficiency by extracting heat from the compressor stage and adding heat in the turbine stage to achieve the Gliding cycle.

Approach for Evaluation of Gas Power Cycles

These gas power cycles need to be designed and evaluated on various aspects of performance and economics and compared against the current system. The power cycle models need to capture performance details of each sub-system in the power block for a certain set of operating conditions. Since the current effort is a first attempt at evaluating alternative gas power cycles applicable for solar thermal power generation, it will be at a conceptual design level and it suffices to evaluate the power cycles at system level. The detailed design can be worked out as a follow on effort once an alternative is deemed feasible at the conceptual level.

A conceptual design is the first step in any design process and requires multiple design iterations to assess the different competing configurations. This requires the modeling tool to be flexible and quick to arrive at a design that is feasible and conceptually optimized. Since, we want to assess conceptual power cycles, a thermodynamic model of the system will provide us the necessary performance details to arrive at a feasible option. Keeping all the above considerations in mind, Engineering Equations Solver (EES) was deemed fit as a modeling tool to assess the power cycle models for performance.

For each configuration assessed, a thermodynamic model of the system is created to represent all the necessary sub-systems. Each sub-system in the power block is modeled

by first principles of thermodynamics. Both energy as well as exergy analysis of the system is performed to assess different aspects of thermodynamics of the design. Finally, a cost model is proposed for the economic assessment of feasible design options.

The following chapters will present the detailed assessment of the identified gas power cycles with their thermodynamic models representing each sub-system and the assessment of their performance using EES.

CHAPTER 3

SYSTEM AND COMPONENT MODELING

This chapter describes the system modeling approach and details of thermo-physical and cost models developed and implemented for the systems and sub-systems towards assessment of power-plant performance. The main purpose of modeling the system is to quantify the power-plant performance based on the performance of individual systems and components and their interactions. The second objective is to perform parametric study on key design parameters to optimize the system performance. The objective of the current study is to perform a conceptual design assessment of the gas cycles applicable for solar thermal power generation system. This chapter describes the thermo-physical model, the associated assumptions for the main components of the system and the cost model for individual components and the overall system cost model which is used to quantify the economic performance of the power-plant system configuration. Most of the components described here are common for all the power-plant configurations considered for assessment. There are a few components specific to a particular configuration. The following chapters will present the system performance assessment based on the models described in the current chapter.

Modeling Approach

The power-plant is a large system with many smaller sub-systems and components interfacing and interacting with each other. For a conceptual design assessment at system level, the entire system is represented by a steady-state system model with individual components modeled to represent their steady-state performance characteristics. The assessment of system dynamics involves a more detailed modeling of the system and components. This assessment is not required at a conceptual design stage and so is out of scope for the current effort. EES (Engineering Equation Solver) is used as a software tool

to develop the system model and assess the steady state performance of the system and perform parametric studies on impact of changing key system parameters on system performance.

Basic Brayton Cycle

Gas Turbines usually operate on an open cycle. Fresh air at ambient conditions is drawn into the compressor, where its temperature and pressure are raised. In a combustion turbine system, the high-pressure air proceeds into the combustion chamber, where the fuel is burned at constant pressure.

The resulting high-temperature gases then enter the turbine, where they expand to the atmospheric pressure through a row of nozzle vanes. This expansion causes the turbine blade to spin, which then turns a shaft inside a magnetic coil. When the shaft is rotating inside the magnetic coil, electrical current is produced. The exhaust gases leaving the turbine in the open cycle are not re-circulated.

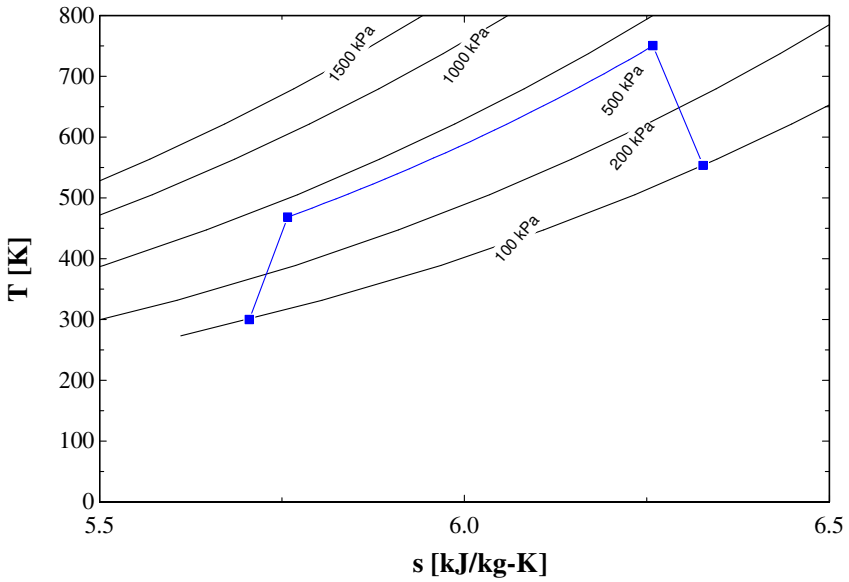

Figure 3.1: Brayton Cycle

The open gas-turbine cycle can be modeled as a closed cycle as shown in Figure 3.1 by utilizing the air-standard assumptions. Here the compression and expansion process

remain the same, but a constant-pressure heat-rejection process to the ambient air replaces the combustion process. The ideal cycle that the working fluid undergoes in this closed loop is the Brayton cycle, which is made up of four internally reversible processes namely; isentropic compression (in a compressor) -state 1 to 2, constant pressure heat addition –state 2 to 3, isentropic expansion (in a turbine) –state 3 to 4, constant pressure heat rejection –state 4 to 1.

Compressor

The object of a good compressor design is to obtain the most air through a given diameter compressor with a minimum number of stages while retaining relatively high efficiencies and aerodynamic stability over the operating range. Compressors contain a row of rotating blades followed by a row of stationary (stator) blades. A stage consists of a row of rotor and a row of stator blades. All work done on the working fluid is done by the rotating rows, the stators converting the fluid kinetic energy to pressure and directing the fluid into the next rotor.

Heat Input System

In the common open-cycle gas turbine, it is a direct-fired air heater in which fuel is burned with the air. In a solar thermal plant this is achieved by heating up the working fluid in a heat-exchanger by the heat transfer fluid heated using solar energy.

Turbine

Gas turbines move relatively large quantities of air through the cycle at very high velocity. The gas turbine in its most common form is a heat engine operating through a series of processes. These processes consist of compression of air taken from the atmosphere, increasing of gas temperature by the constant-pressure combustion of fuel in the air, expansion of the hot gases, and finally, discharging of the gases to atmosphere, in a continuous flow process. The compression and expansion processes are both carried out

by means of rotating elements in which the energy transfer between fluid and rotor is affected by means of kinetic action.

Basic Gas Turbine Schematic

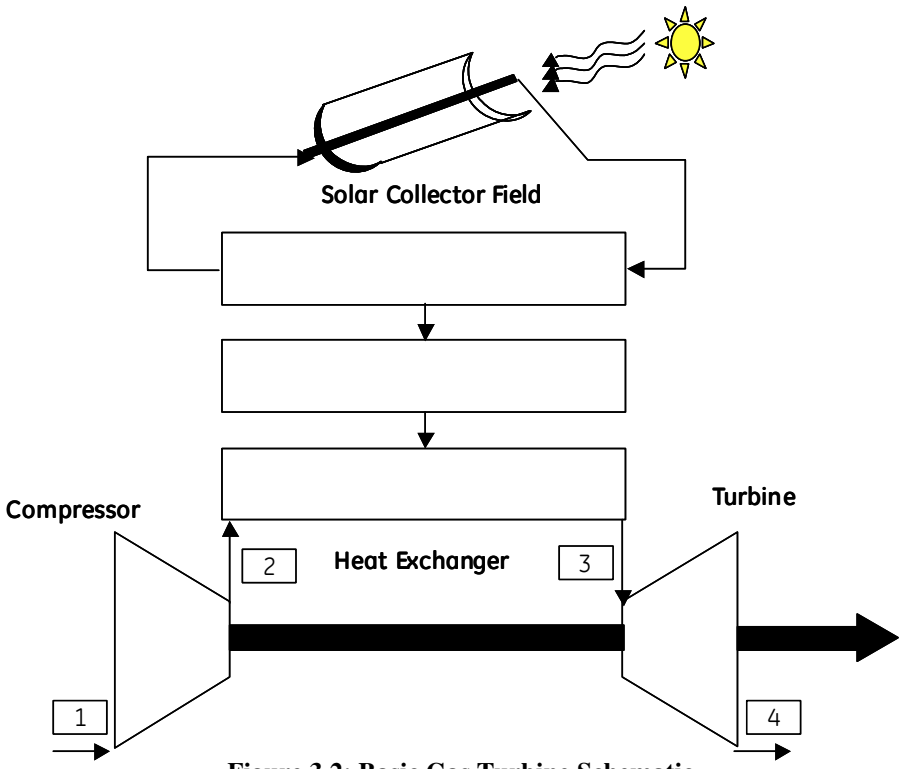

Figure 3.2: Basic Gas Turbine Schematic

The simple gas turbine thermodynamic cycle can be mathematically explained by considering the system as a heat engine. This engine works by taking in the air as working fluid and this fluid is taken through a set of processes, adding and extracting heat as well as work, to deliver net power from the system. For a SFSS system and unit mass of air, the energy equation for the system will be given by:

$$w_{total} - q_{in} = \sum \left(\Delta h + \Delta ke + \Delta pe \right) \tag{3.1}$$

Ignoring the changes in potential and kinetic energies, the system's output is a sum total of the inputs and the change in state of the working fluid through the system. Heat supplied to the system can be expressed as:

$$q_{in} = h_3 - h_2 \tag{3.2}$$

where h is the specific enthalpy of the working fluid and the subscript represents the state of the working fluid in the system based on above schematic. In the above equation, station 2 is the exit of compressor and inlet to heat-exchanger and station 3 is the inlet to turbine

Heat rejected from the system is given by:

$$q_{out} = h_4 - h_1 \tag{3.3}$$

where station 4 is exit of turbine and station 1 is inlet to compressor

The work done by the turbine can be calculated as:

$$w_{\text{turb}} = h_3 - h_4 \tag{3.4}$$

and the work done on the compressor is given by:

$$w_{\text{comp}} = h_2 - h_1 \tag{3.5}$$

The total work output by the system is given from (3.4) and (3.5) as:

$$w_{\text{tot}} = w_{\text{turb}} - w_{\text{comp}} = (h_3 - h_4) - (h_2 - h_1) \tag{3.6}$$

The efficiency for the system is given by:

$$\eta = \frac{w_{\text{tot}}}{q_{in}} \tag{3.7}$$

From (3.2) and (3.7)

$$\eta = \frac{(h_3 - h_4) - (h_2 - h_1)}{h_3 - h_2} \tag{3.8}$$

Re-arranging the above terms, the efficiency for a simple gas turbine can be given by:

$$\begin{aligned} \eta &= \frac{(h_3 - h_2) - (h_4 - h_1)}{h_3 - h_2} \\ &= 1 - \frac{h_4 - h_1}{h_3 - h_2} \end{aligned} \tag{3.9}$$

The above equation also shows that the term in the numerator of second expression is the heat rejected from the system for a unit mass of working fluid as given by (3.3). Eq. (3.9) applies to a generic working fluid.

Now, in real world systems, there are losses and so is the case for compressors and turbines. For compressor, the deviation from ideal is given by:

$$\eta_c = \frac{h_{2s} - h_1}{h_2 - h_1} \tag{3.10}$$

where h_{2s} refers to the enthalpy for an isentropic compression process. For a turbine, this deviation is given by:

$$\eta_t = \frac{h_3 - h_4}{h_3 - h_{4s}} \tag{3.11}$$

The losses in the compressor increase the compressor work and the losses in turbine reduce the work extracted and bring down the overall system efficiency. Figure 3.3 shows the deviation in the compressor and turbine stage.

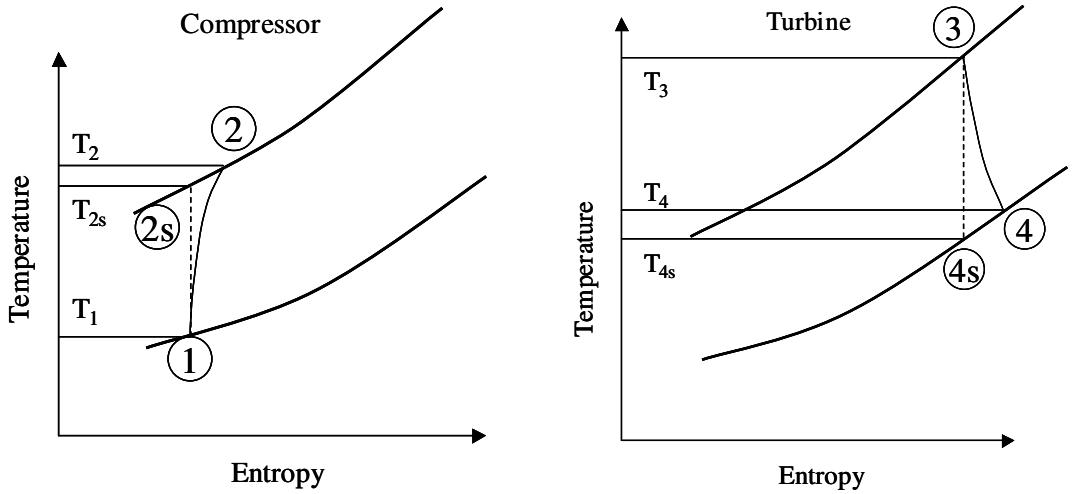

Figure 3.3: Compressor and Turbine Thermodynamic efficiency

Regeneration (Recuperation)

Regeneration is the process of recovering the waste heat in the form of low quality thermal energy to act as input to the other thermal processes. This acts to improve the efficiency of the overall system. In practice, the regenerator is costly, heavy and bulky, and causes pressure losses, which reduce the system efficiency. These factors have to be balanced against the gain in efficiency to decide this system's worth. The effort here is to improve upon the system efficiency by making use of the regenerator. The turbine exhaust is still at a higher temperature and can be used to heat the compressor exhaust, thus utilizing the waste heat.

The regenerator is a heat-exchanger and its performance is quantified by the term effectiveness defined as

$$\varepsilon = \frac{\dot{Q}_{\text{actual}}}{\dot{Q}_{\text{limiting}}} \tag{3.12}$$

This is expressed in hot and cold side, inlet and outlet temperatures as:

$$\varepsilon = \frac{C_{\text{c}}\left(T_{\text{c,o}} - T_{\text{c,i}}\right)}{C_{\min}\left(T_{\text{h,i}} - T_{\text{c,i}}\right)} \tag{3.13}$$

where the subscripts c, h, i, o stand for cold, hot, inlet and outlet respectively and *C* stands for heat capacity rate which is given by:

$$C = \dot{m} \cdot c_{\text{p}} \tag{3.14}$$

The recuperator finds its place in many configurations in the present study and is part of the optimum configuration for each design.

Intercooler & Inlet cooling

The intercooler acts to decrease the fluid temperature after a compressor stage. This causes the downstream compressor stage to raise pressure with lesser effort. Thus the system improves cycle efficiency by reducing the overall work expense in compression.

The typical reduction in temperature achieved in an intercooler stage is of the order of 100K. Inlet-cooling also acts in a similar way but before the working fluid enters the compressor.

Absorption Chiller

An absorption chiller is a system to extract heat from the working fluid to cool it down reducing the amount of compressor work in raising the pressure. This system works on heat input based refrigeration cycle. The working fluid here is a salt solution, which acts as a heat transfer medium by virtue of change in its concentration. This system finds its use in places where process waste heat is available in abundance. This system requires no work input to perform the refrigeration process and thus carries out this task efficiently. A single-effect cycle has a COP (Coefficient of Performance) ranging from 0.6-0.9 whereas the multiple effect cycles can yield COPs beyond 1.0 (Ziegler, 1993)

The single effect absorption cycle uses water as the refrigerant and lithium bromide as the absorbent. It is the strong affinity that these two substances have for one another that makes the cycle work. The entire process occurs in almost a complete vacuum.

A dilute lithium bromide solution is collected in the bottom of the absorber shell. From here, a hermetic solution pump moves the solution through a shell and tube heat exchanger for preheating. After exiting the heat exchanger, the dilute solution moves into the upper shell. The solution surrounds a bundle of tubes which carries either steam or hot water. The steam or hot water transfers heat into the pool of dilute lithium bromide solution. The solution boils, sending refrigerant vapor upward into the condenser and leaving behind concentrated lithium bromide. The concentrated lithium bromide solution moves down to the heat exchanger, where it is cooled by the weak solution being pumped up to the generator. The refrigerant vapor migrates through mist eliminators to the condenser tube bundle. The refrigerant vapor condenses on the tubes. The heat is

removed by the cooling water which moves through the inside of the tubes. As the refrigerant condenses, it collects in a trough at the bottom of the condenser. The refrigerant liquid moves from the condenser in the upper shell down to the evaporator in the lower shell and is sprayed over the evaporator tube bundle. Due to the extreme vacuum of the lower shell [6 mm Hg (0.8 kPa) absolute pressure], the refrigerant liquid boils at approximately 39°F (3.9°C), creating the refrigerant effect. (This vacuum is created by hygroscopic action - the strong affinity lithium bromide has for water - in the absorber directly below.) As the refrigerant vapor migrates to the absorber from the evaporator, the strong lithium bromide solution from the generator is sprayed over the top of the absorber tube bundle. The strong lithium bromide solution actually pulls the refrigerant vapor into solution, creating the extreme vacuum in the evaporator. The absorption of the refrigerant vapor into the lithium bromide solution also generates heat which is removed by the cooling water. The now dilute lithium bromide solution collects in the bottom of the lower shell, where it flows down to the solution pump. The chilling cycle is now completed and the process begins once again.

This system has been implemented as a zero order model in EES to achieve cooling from a single effect absorption chiller. The waste heat from the exhaust is the exergy source. The chilled water is the exergy sink. The ambient air acts as the waste heat sink. Figure 3.4 depicts the schematic of the absorption chiller.

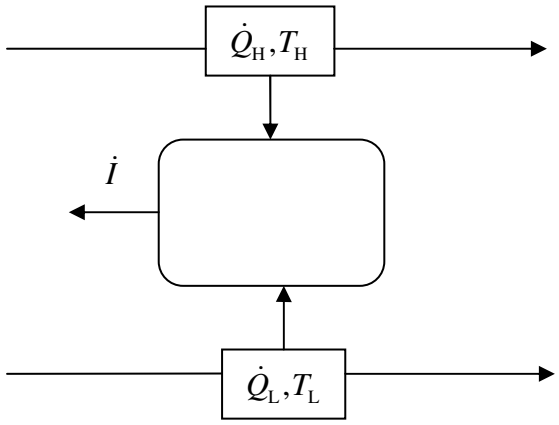

Figure 3.4: Absorption chiller schematic

The performance of a chiller is described by its coefficient of performance (COP). It is defined as the ratio of heat extracted from the chilled sink to the heat input from the waste heat. The COP of an absorption chiller can be arrived at using exergy analysis of the above schematic. The exergy equation describing the control volume enclosing the absorption chiller is given by

$$\dot{Q}_{\mathrm{H}}\left(1-\frac{T_0}{T_{\mathrm{H}}}\right)-\dot{Q}_{\mathrm{L}}\left(1-\frac{T_0}{T_{\mathrm{L}}}\right)-\dot{I}=0 \tag{3.15}$$

Rearranging the terms in Eq. 3.15 to obtain COP

$$COP=\frac{\dot{Q}_{\mathrm{L}}}{\dot{Q}_{\mathrm{H}}}=\frac{\left(1-\frac{T_0}{T_{\mathrm{H}}}-\frac{\dot{I}}{\dot{Q}_{\mathrm{H}}}\right)}{\left(\frac{T_0}{T_{\mathrm{L}}}-1\right)} \tag{3.16}$$

The absorption chiller has been modeled to incorporate the effect of variation in inlet heat temperature on COP of the chiller by characterizing the exergy destruction to input heat ratio to achieve a nominal COP of 0.7 for a single effect absorption chiller.

Thermo-Physical and Cost Analysis Models

It is a known fact that the current state of the art in power generation technology can yield superior systems capable of performing the task with very high efficiency and reliability and capable of delivering in multiple operating conditions. But for every incremental performance improvement, there is a corresponding cost involved. The essence of the current effort is to investigate a system configuration that generates power at a feasible and if possible, at an economical rate compared to the current state of the art. This section analyzes the cost of various design configurations and the auxiliary systems and effect of system parameters on the system cost.

For the proposed design, the system can be divided into following units for cost analysis:

1) Gas turbine
2) Auxiliary Systems (Heat Exchangers)
3) Solar Collector system

Gas Turbine System Cost

A gas turbine is a complex system. Its cost depends on its physical size, cost of manufacturing material and the technology implemented; the most significant out of which is the physical size (Dirk, 2009). For a land based gas turbine, the power output and pressure ratio are indicators of the physical size (Claire, 2008). For a rated power of 100 MW and pressure ratio of 12.7, the baseline gas turbine cost for a simple cycle operation is $227/kW based on the reported cost for a 7EA gas turbine unit of 85 MW rated capacity from GE (Mark, 2010). The cost of the gas turbine system is modeled on the basis of available data of cost, power rating and system pressure ratio on GT (Gas Turbine) systems on offer in the market (Mark, 2010). The data presented in Table 3.1 was used to develop a regression model for gas-turbine system cost based on system rated power and pressure-ratio.

Table 3.1: Gas-Turbine System Cost variation with system parameters

Machine	Manufacturer	Cost ($/kW)	Cost($MM)	Power (MW)	Pressure Ratio
7111EA	**GE**	**$227**	**$19.3**	**85**	**12.7**
9171E	**GE**	**$194**	**$24.5**	**126**	**12.6**
6541B	**GE**	**$267**	**$10.5**	**39**	**12.2**
GT11N2	**ALSTOM**	**$224**	**$24.5**	**109**	**15.5**
6101FA	**GE**	**$258**	**$18.5**	**72**	**15.6**
7221FA	**GE**	**$210**	**$34.0**	**162**	**16.2**

The cost model is represented as

$$\frac{C}{C_0} = \left(\frac{\dot{W}}{\dot{W}_0}\right)^{\alpha} \cdot \left(\frac{P_{\mathrm{R}}}{P_{\mathrm{R}0}}\right)^{\beta} \tag{3.17}$$

where C is system cost, $\dot{W}$ is rated power and P_{R_0} is Pressure ratio

Taking Logarithm

$$\ln\left(\frac{C}{C_0}\right) = \alpha \cdot \ln\left(\frac{\dot{W}}{\dot{W}_0}\right) + \beta \cdot \ln\left(\frac{P_R}{P_{\mathrm{R},0}}\right) \tag{3.18}$$

This reduces the model to a linear equation in 2 variables. Regression analysis was performed whose data is represented in Table 3.2 to arrive at the value of coefficients in Equation 3.18.

Table 3.2: Two Variable Linear Regression Analysis Result

SUMMARY OUTPUT - 2 variable	
Regression Statistics	
Multiple R	0.9977
R Square	0.9955
Adjusted R Square	0.7443
Standard Error	0.0298
Observations	6
	Coefficients
Intercept	0.0000
X Variable 1	0.7345
X Variable 2	0.3665

The regression analysis has a high value for coefficient of determination R^2, which implies that the regression model is able to describe the variation in the GT system cost to a very great extent. Also, the standard error for this regression is much lower compared to

the predicted coefficients, which shows a significant dependence of system cost on independent variables i.e. power rating and pressure ratio. The goodness of fit for the regression model is also seen in the predicted vs. actual cost plot in Figure 3.5.

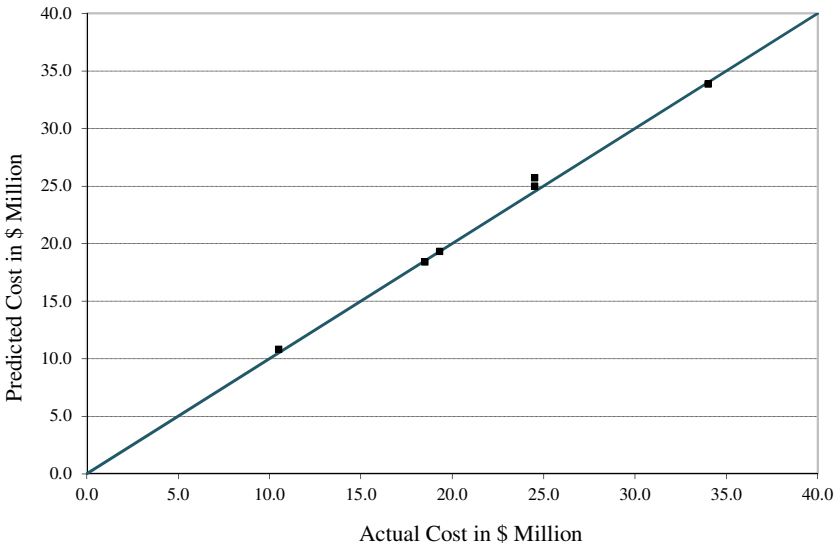

Figure 3.5: Two Variable Linear Regression Analysis Actual vs. Predicted Cost

The gas-turbine system cost model based on the system power rating and system pressure-ratio gives the cost of the GT system as

$$\frac{C}{C_0} = \left(\frac{\dot{W}}{\dot{W}_0}\right)^{0.734} \cdot \left(\frac{P_{\mathrm{R}}}{P_{\mathrm{R},0}}\right)^{0.366} \tag{3.19}$$

The expression derived in Equation 3.19 is utilized in determining the change in gas-turbine system cost.. The GT systems considered in Table 3.1 operated in a limited range of operating conditions, where the inlet condition of working fluid, working fluid properties and fluid power density are all similar for each configuration. Equation 3.19 needs to be modified to account for such variations without changing the output power rating. This can be achieved by replacing the power rating factor with a system size factor. The system power rating varies with the square of system size (Brandt, 1994) represented by its characteristic dimension, the mean system diameter *D* (Dixon, 2005). This can be represented as

$$\frac{C}{C_0} = \left(\left(\frac{D}{D_0} \right)^2 \right)^{0.734} \cdot \left(\frac{P_R}{P_{R,0}} \right)^{0.366} \tag{3.20}$$

The flow cross-section of the GT varies with the square of the mean diameter, so Equation 3.20 can be further modified as

$$\frac{C}{C_0} = \left(\frac{A}{A_0} \right)^{0.734} \cdot \left(\frac{P_R}{P_{R,0}} \right)^{0.366} \tag{3.21}$$

A change in system cross-section will alter the size of the machine. To maintain the same aerodynamic performance of the compressor and turbine systems for a scaled machine size, the GT system should have the same flow velocities across the cross-section. So, the change in GT cross-section in terms of its mass-flow rate and inlet conditions is given by

$$\frac{A}{A_0} = \frac{\dot{m}}{\dot{m}_0} \frac{\rho_0}{\rho} = \frac{\dot{m}}{\dot{m}_0} \frac{P_0}{P} \frac{RT}{R_0 T_0} \tag{3.22}$$

From Equation 1.5 and Equation 1.6, the GT system cost model can be represented as

$$\frac{C}{C_0} = \left(\frac{\dot{m}}{\dot{m}_0} \frac{P_0}{P} \frac{RT}{R_0 T_0} \right)^{0.734} \cdot \left(\frac{P_R}{P_{R,0}} \right)^{0.366} \tag{3.23}$$

This cost represents the cost of the entire GT system including the compressor, the combustor and the turbine. The cost of these individual subsystems mentioned is not necessary as the power plant cost analysis assumes a standard GT system as a single unit. Also, the cost of individual sub-systems is proprietary information and is usually not available in public domain.

Heat-exchanger System Cost

The main auxiliary systems in the power-plant are the heat-exchangers like the intercoolers and recuperator which were augmented into the system to enhance the system performance. To ensure high performance of these systems at lower cost, the compact heat-exchangers were considered as the design option. The criteria for selection

of compact heat-exchanger were based on operating conditions and features including weight, cost, reliability and compactness.

The design details for the heat-exchanger design were based on the heat-exchanger design for the Modular Pebble Bed Reactor (MPBR) heat-exchanger system (Chunyun, 2003). One of the compact heat-exchanger configurations considered for the MPBR system was based on Plate Fin Heat Exchanger (PFHX) concept and was assessed with Helium as the working fluid. For the present work, the basic Plate-Fin design was leveraged with minor modifications and assessed for various combinations of cold and hot fluids for heat exchangers used in intercooling, recuperation or transferring heat from solar collector field. The heat exchangers were assessed and optimized for area while meeting effectiveness and pressure-drop requirements. The heat-exchanger weight and cost were obtained by correlating the MPBR heat-exchanger area, weight and cost and developing transfer function. The following section describes the modeling of heat-exchanger system.

MPBR Heat-exchanger

Plate fin heat exchangers have been widely used as heat exchangers in the field of power generation. Ingersoll Rand Energy Systems (IRES), Portsmouth, NH has developed a plate fin heat exchanger that is well suited to the IHX (Intermediate HX) and recuperator applications. The IRES PFHX is manufactured through a patented approach in which the folded fins are brazed to the stamped plates to form the unit-cells as shown in Figure 3.6. The unit-cells are then stacked to form the totally welded pressure boundary as shown in Figure 3.7. The configuration is specifically designed to accommodate substantial thermal strain and therefore to tolerate the severe temperature gradients encountered during transient operations.

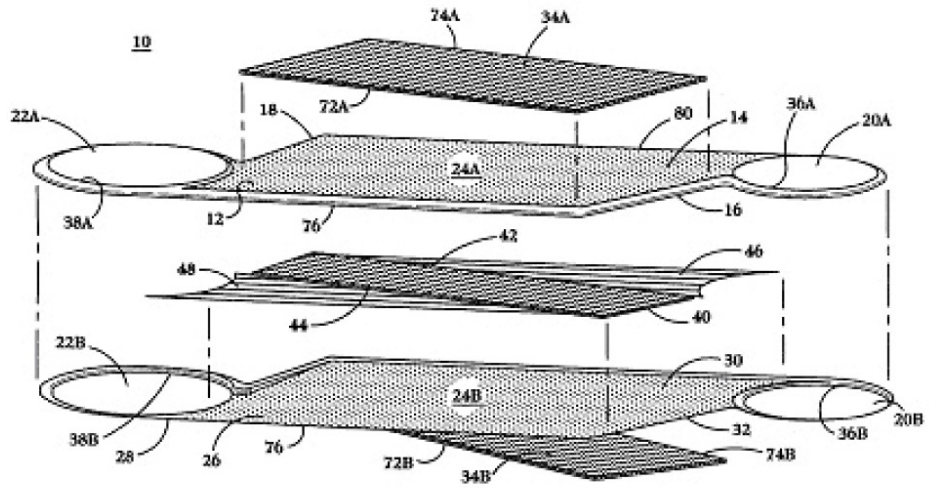

Figure 3.6: IRES PFHX Unit Cell (Chunyun, 2003)

The details of the PFHX design are given in following sections.

Incoloy 800 was selected as the reference material to construct the IHX. The heat-exchangers used in HTSGT such as recuperator and inter-cooler operate at a much lower temperature, they can use conventional and lower cost material such as 300 series stainless steel. For the solar heat exchanger, some of the operating conditions evaluated do approach the high temperatures requiring an Incoloy 800 material for heat exchanger design, but the optimum configuration obtained for the HTSGT, operates at lower peak cycle temperature. The maximum service temperature for 316 SS grade stainless steel is 870^{o}C (1143 K) in dry air operation (ASM Specialty Handbook, 1997). Molten salts do have a detrimental effect on the high temperature performance of stainless steel, but by corrosion resistant coatings, their performance can be improved (ASM Specialty Handbook, 1997). So the assumption of stainless steel as the material of construction for solar heat exchanger holds good in general.

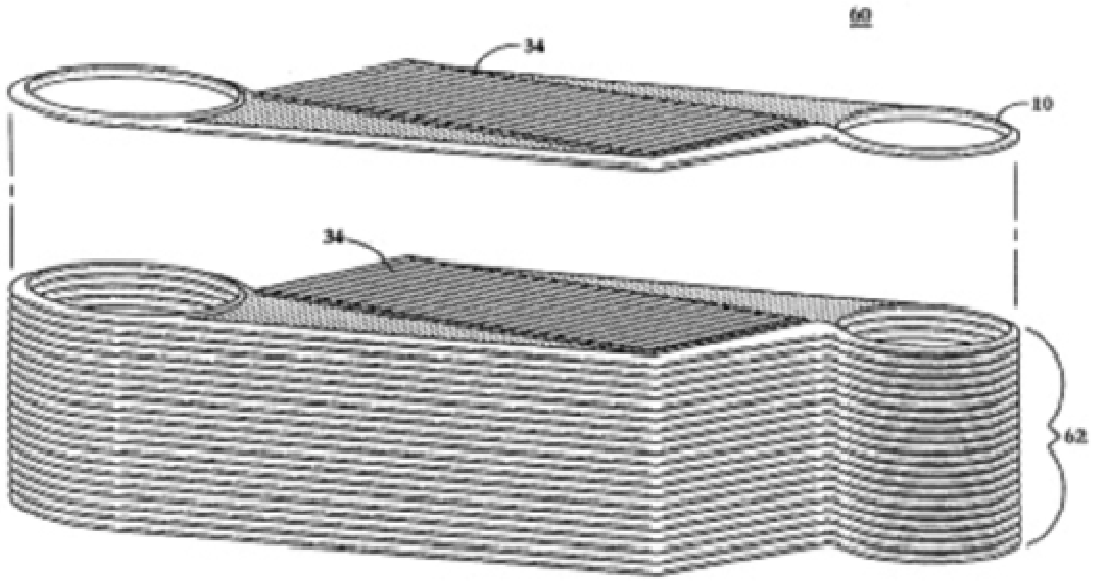

Figure 3.7: IRES PFHX Stack-up

The heat-exchanger design for the MPBR was based on wavy fin compact plate-fin heat exchangers (Kays and London, 1984). The design calculations were based on the friction factor and Colburn factor correlation for the plate-fin surface 11.5-3/8W. The code 11.5-3/8W, for the plate-fin surface describes the geometric details of the surface. 11.5 is the fin spacing per inch, 3/8 is the pitch of the wave in inches, along the length of the fin and W stands for a wavy fin. Figure 5 describes this code.

Heat-exchanger Model

The heat-exchanger model assumptions are:

1. The heat exchanger is adiabatic. The heat exchanger is insulated from the outside surroundings and there is no heat transfer to the environment

2. The weight of the side wall is small in comparison with the amount of weight of the plates separating the flow passages. The side wall is ignored

3. Heat conduction in the longitudinal direction is negligible in both the fluid and the solid walls

4. For both fluid and solid wall, the temperature only varies in the flow direction

5. The header surface is assumed to be small compared to the heat exchanger and so not included in the heat transfer or pressure-drop calculations

The heat-exchanger's core structure is represented in Figure 3.8

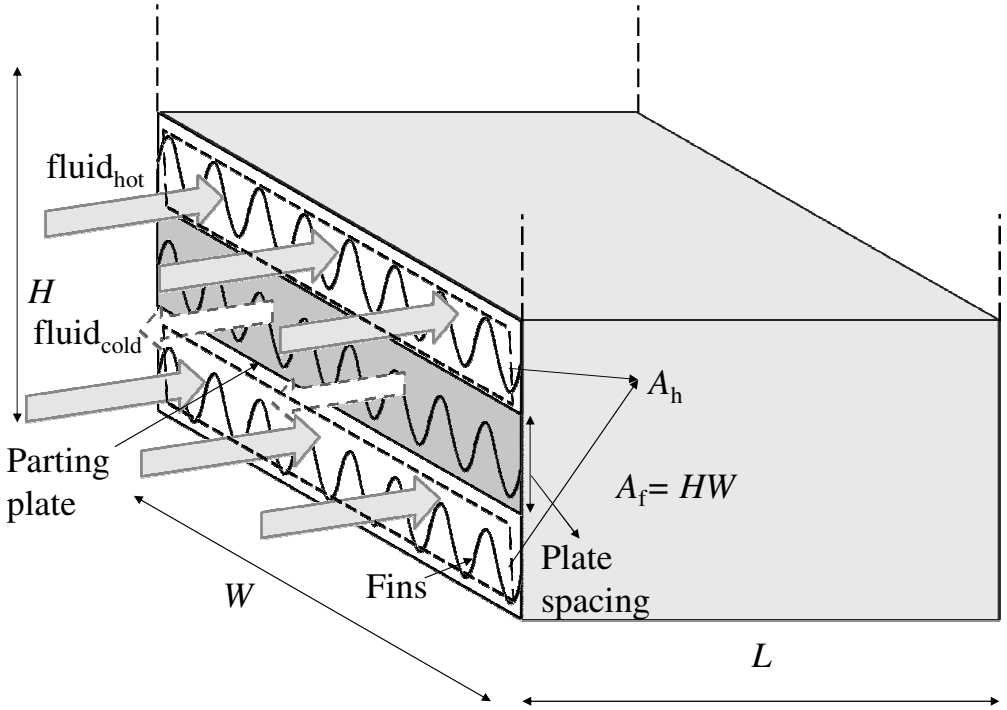

Figure 3.8: Heat-exchanger core schematic

The PFHX design is for a counter-flow heat exchanger. The fluids on the hot and cold side travel in opposite directions through the core. The heat exchanger is a stack-up of finned surfaces for hot and cold side separated by parting plates. The fluids are not mixed and the heat is transferred by conduction through the surfaces. The hotside of the heat exchanger has two layers of finned surface based on the unit cell depicted in Figure 3.6. This leads to a bias in the heat exchanger surface area on hotside compared to coldside. There is a corresponding difference in the free-flow areas and Reynolds numbers for the two surfaces leading to a variation in the flow and heat transfer performance and fin efficiencies between the two sides.

The fin surface is modeled as the wavy fin (Figure 3.9). The wavy fin is characterized by a continuous curvature. The change in flow direction introduced by the waves in the surface tends to interrupt the boundary layer. The wavy fins for IRES PFHX have been

assessed with friction factor and Colburn factor correlations for surface type 11.5-3/8W. This surface has been selected based on its proximity to IRES PFHX plate-fin design specification.

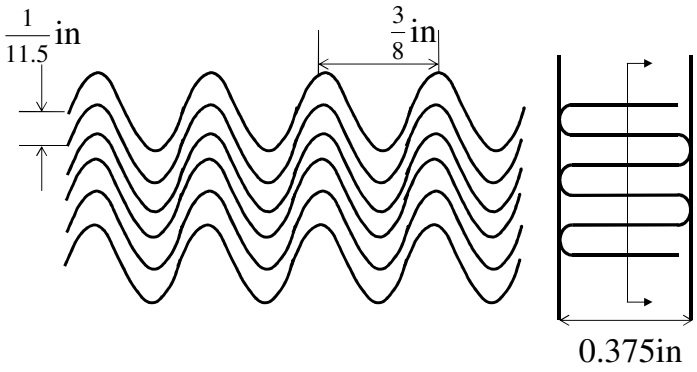

Figure 3.9: Wavy Fin Configuration

The design of the heat exchanger or its performance assessment requires a set of steps to be followed as outlined in Figure 3.10. A core module of the exchanger was chosen and the design process was iterated upon the number of such modules arranged in series and parallel to arrive at a heat exchanger configuration which met the requirements of effectiveness and pressure-drop for the given flow rates and inlet conditions of both hot and cold fluids.

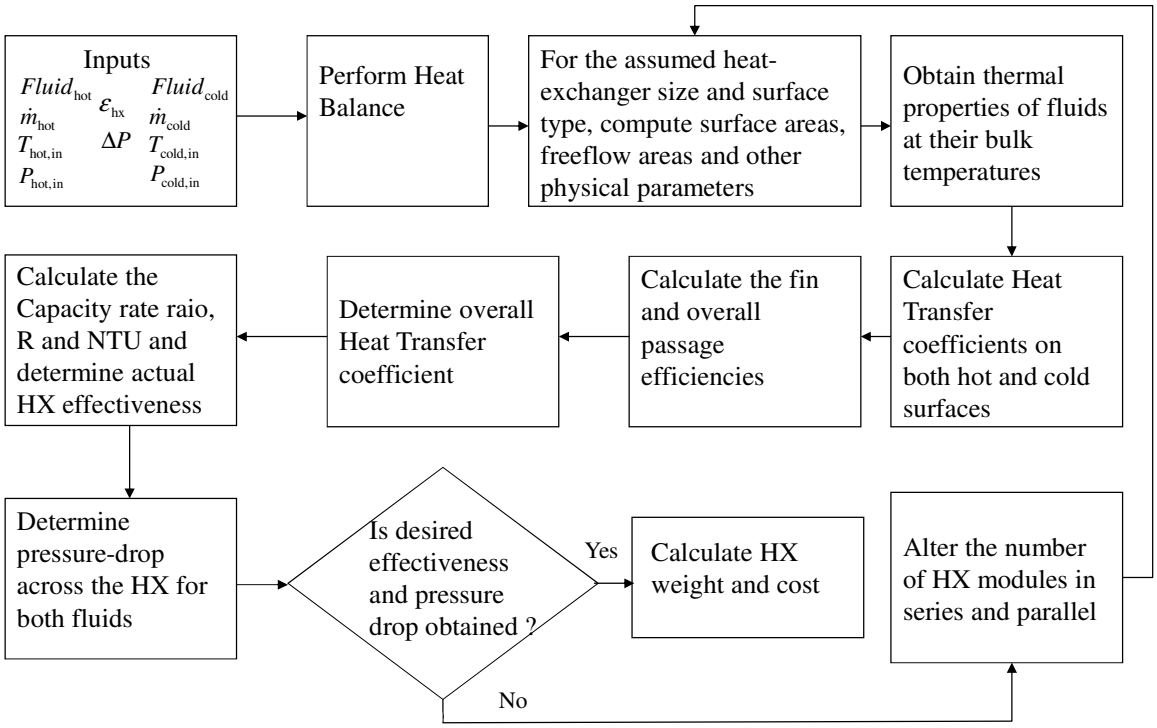

Figure 3.10: Heat-exchanger Design calculation

The inputs for the heat exchanger design calculations are mainly the fluid flow rates and the state of fluids (Pressure and Temperature) as well as the desired effectiveness and pressure loss constraint on the exchanger. The design of the heat exchanger follows the process outlined in Figure 3.10, which will be detailed in the following sections.

Heat Balance

For the given fluids on hot and cold side, the capacity rates are determined as

$$C_c = \dot{m}_{\mathrm{c}} \cdot c_{\mathrm{p,c}}, C_{\mathrm{h}} = \dot{m}_{\mathrm{h}} \cdot c_{\mathrm{p,h}} \tag{2.24}$$

The minimum fluid is obtained from Equation 2.24 (minimum fluid is the fluid with lower capacity rate). If the cold fluid is the minimum fluid ($C_{\min} = C_{\mathrm{c}}$)

$$\varepsilon = \frac{T_{\mathrm{c,out}} - T_{\mathrm{c,in}}}{T_{\mathrm{h,in}} - T_{\mathrm{c,in}}} = \frac{C_{\mathrm{h}}\left(T_{\mathrm{h,in}} - T_{\mathrm{h,out}}\right)}{C_{\min}\left(T_{\mathrm{h,in}} - T_{\mathrm{c,in}}\right)} \tag{3.25}$$

Otherwise ($C_{\min} = C_{\mathrm{h}}$) and

$$\varepsilon = \frac{T_{\mathrm{h,in}} - T_{\mathrm{h,out}}}{T_{\mathrm{h,in}} - T_{\mathrm{c,in}}} = \frac{C_{\mathrm{c}}\left(T_{\mathrm{c,out}} - T_{\mathrm{c,in}}\right)}{C_{\min}\left(T_{\mathrm{h,in}} - T_{\mathrm{c,in}}\right)} \tag{3.26}$$

From Eq. 3.25 and 3.26, we can determine the outlet temperatures of the hot and cold fluids based on the specified heat exchanger effectiveness. The specific heat capacity of the fluids can be obtained for the assumed fluid bulk temperatures based on inlet fluid temperatures and refined later in an iterative manner to arrive at the exact bulk temperatures. The final heat balance is determined for cold fluid as

$$T_{\mathrm{c,avg}} = \frac{T_{\mathrm{c,in}} + T_{\mathrm{c,out}}}{2} \tag{3.27}$$

Obtaining $c_{\mathrm{p,c,avg}}$ for the average bulk temperature $T_{\mathrm{c,avg}}$

$$\dot{Q}_{\mathrm{c}} = m_{\mathrm{c}} \cdot c_{\mathrm{p,c,avg}} \cdot \left(T_{\mathrm{c,out}} - T_{\mathrm{c,in}}\right) \tag{3.28}$$

And for hot fluid as

$$T_{\mathrm{h,avg}} = \frac{T_{\mathrm{h,in}} + T_{\mathrm{h,out}}}{2} \tag{3.29}$$

Obtaining $c_{\mathrm{p,h,avg}}$ for the average bulk temperature $T_{\mathrm{h,avg}}$

$$\dot{Q}_{\mathrm{h}} = \dot{m}_{\mathrm{h}} \cdot c_{\mathrm{p,h,avg}} \cdot \left(T_{\mathrm{h,out}} - T_{\mathrm{h,in}}\right) \tag{3.30}$$

where

$$\dot{Q}_{\mathrm{c}} = \dot{Q}_{\mathrm{h}} \tag{3.31}$$

Having established the heat exchanger outlet temperature for the fluids on both hot and coldside, we can now calculate the heat exchanger performance and derive the surface area and cost of the heat exchanger based on the physical design parameters of the heat exchanger and the properties of the fluids passing through them.

Heat-exchanger Physical Parameters

The heat exchanger physical dimensions and critical parameters are enlisted in Table 3.3. Based on these parameters we determine the physical parameters required for design

calculations. The core dimensions mentioned in the Table below are for a single module of the heat exchanger. To meet the design requirements of the heat exchanger, we require putting these modules in series and parallel to meet the effectiveness requirement and pressure-drop constraints. The modules in parallel split the fluid flow passing through them and have the same state of fluids at their inlets and exits. The modules in series have the same fluid flow through them and the inlet to each module is fed from the exit of the module upstream. The modules in parallel reduce the pressure-drop in the main flow by distributing the flow over a larger cross-section but beyond a limit they reduce the heat transfer capacity of the fluid by slowing it down. The modules in series retain the fluid heat transfer capacity by maintaining the flow velocity but cause greater pressure-drop in the flow. So it requires iteration on the number of modules in series and parallel to arrive at a configuration that satisfies the effectiveness and pressure-drop criteria.

Table 3.3: PFHX Geometric Specifications

Parameter	**Value**	
Core width, W	0.762 [m]	
Core length, L	0.561 [m]	
Core height, H	1.5 [m]	
Parting plate thickness, a	0.38 [mm]	
Fin spacing	1/45 [in]	
Fin thickness, δ	0.076 [mm]	
	Hotside	**Coldside**
Plate spacing, b	3.3 [mm]	1.65 [mm]
Surface to Volume ratio, β	4734	4685
Hydraulic radius, r_h	1.743×10^{-4} [m]	1.761×10^{-4} [m]

Assuming the number of modules in series and parallel are n_s and n_p respectively. The heat exchanger volume, the most important parameter from the cost perspective, is determined based on the core dimensions as represented in Figure 3.8

$$V_{hx} = L \cdot W \cdot H \cdot n_s \cdot n_p \tag{3.32}$$

The next parameter of interest is the frontal area of the heat exchanger. It is calculated for both cold and hot flow. It is the total flow cross-section area seen by the fluid and depends on the heat exchanger dimensions. For parallel or counter-flow heat exchangers, this parameter will be same for both cold and hot flow, for other flow arrangements, it will be different for both sides. The heat exchanger being designed in the present effort is a counter-flow heat exchanger whose frontal area is given by

$$A_{\mathrm{f}} = W \cdot H \cdot n_{\mathrm{p}} \tag{3.33}$$

The surface to volume ratio of the plate fin surface can be utilized to find the available surface area for heat transfer for a given volume. However, since both the cold and hot side of the exchanger share the same volume, another parameter α is required to factor in the surface area occupied by the cold and hot side respectively. This parameter depends on the plate spacing on hot and coldside and the parting plate thickness and is calculated as

$$\alpha_{\mathrm{c}} = \frac{b_{\mathrm{c}}}{b_{\mathrm{c}} + b_{\mathrm{h}} + 2a} \beta_{\mathrm{c}} \tag{3.34}$$

and

$$\alpha_{\mathrm{h}} = \frac{b_{\mathrm{h}}}{b_{\mathrm{c}} + b_{\mathrm{h}} + 2a} \beta_{\mathrm{h}} \tag{3.35}$$

The total surface area of the heat exchanger for the cold and hot fluid flow respectively is then obtained as

$$S_{\mathrm{c}} = \alpha_{\mathrm{c}} \cdot V_{\mathrm{hx}} \tag{3.36}$$

and

$$S_{\mathrm{h}} = \alpha_{\mathrm{h}} \cdot V_{\mathrm{hx}} \tag{3.37}$$

Although the cold and hot fluids see the same frontal area, the actual cross-section area available for flow will determine the heat transfer characteristics and pressure-drop across the exchanger. This parameter is called the free-flow area, which depends on α

and the hydraulic radius, r_h for each side. The hydraulic radius is a geometric characteristic of the flow domain and is determined as

$$r_h = \frac{A}{P} \tag{3.38}$$

where A is the cross-section of flow passage enclosed between two parting plates and two fins and P is the wetted perimeter for that cross-section. The hydraulic radius is four times the hydraulic diameter d_h, another widely used geometric characteristic of the flow passage.

The ratio of free-flow area to frontal area is termed as the factor σ and is determined as

$$\sigma_c = \alpha_c \cdot r_{h,c} \tag{3.39}$$

$$\sigma_h = \alpha_h \cdot r_{h,h} \tag{3.40}$$

The free-flow area is then calculated as

$$A_{ff,c} = \sigma_c \cdot A_f \tag{3.41}$$

and

$$A_{ff,h} = \sigma_h \cdot A_f \tag{3.42}$$

The free-flow area is used to determine the mass-velocity of the cold and hot fluids. Mass-velocity is the mass-flow rate per unit cross-section area. It dictates the heat transfer characteristics and pressure-drop through the exchanger. It is computed as

$$G_c = \frac{\dot{m}_c}{A_{ff,c}} \tag{3.43}$$

and

$$G_h = \frac{\dot{m}_h}{A_{ff,h}} \tag{3.44}$$

The next step is to obtain the fluid thermo-physical properties at their respective bulk temperatures. The properties required for the heat transfer coefficient calculation are

dynamic viscosity μ, thermal conductivity k and specific heat capacity c_p for both cold and hot fluids.

Heat Transfer Coefficient for Cold and Hot Surfaces

To calculate the heat transfer coefficient, we first determine the Reynolds number Re, for the flows as

$$\mathrm{Re}_c = \frac{G_c \cdot d_{h,c}}{\mu_c} \tag{3.45}$$

and

$$\mathrm{Re}_h = \frac{G_h \cdot d_{h,h}}{\mu_h} \tag{3.46}$$

The heat transfer characteristic of the heat exchanger surface is modeled in the form of Colburn factor j_h as a function of Reynolds number for the wavy fin surface (Kays and London, 1984). The data is represented in Figure 3.11. The documented data is for a range of Reynolds number ranging from 300 to 10000. The turbulent region was considered from Reynolds number of 3000 onwards. For lower Reynolds number, the calculation was made considering laminar flow regime.

For flow through the wavy fin cross-section, the Nusselt number for the laminar, fully developed flow through rectangular cross-section is given by

$$\mathrm{Nu}_{FD,Rect} = 7.541 \cdot \left(1 - 2.61 r_a + 4.97 r_a^{\,2} - 5.119 r_a^{\,3} + 2.702 r_a^{\,4} - 0.548 r_a^{\,5}\right) \tag{3.47}$$

where r_a is the aspect ratio of the rectangular cross-section and $r_a < 1$

Then, the heat transfer coefficient is determined as

$$\mathrm{H}_c = \frac{\mathrm{Nu}_c \cdot k_c}{d_{h,c}} \tag{3.48}$$

and

$$\mathrm{H}_h = \frac{\mathrm{Nu}_h \cdot k_h}{d_{h,h}} \tag{3.49}$$

It is interesting to note that in the laminar regime, the heat transfer coefficient for convection on the wall surface is constant and determined by mainly the geometry of the surface and bulk fluid property of thermal conductivity. In this case, Colburn factor *j* varies inversely with Reynolds number.

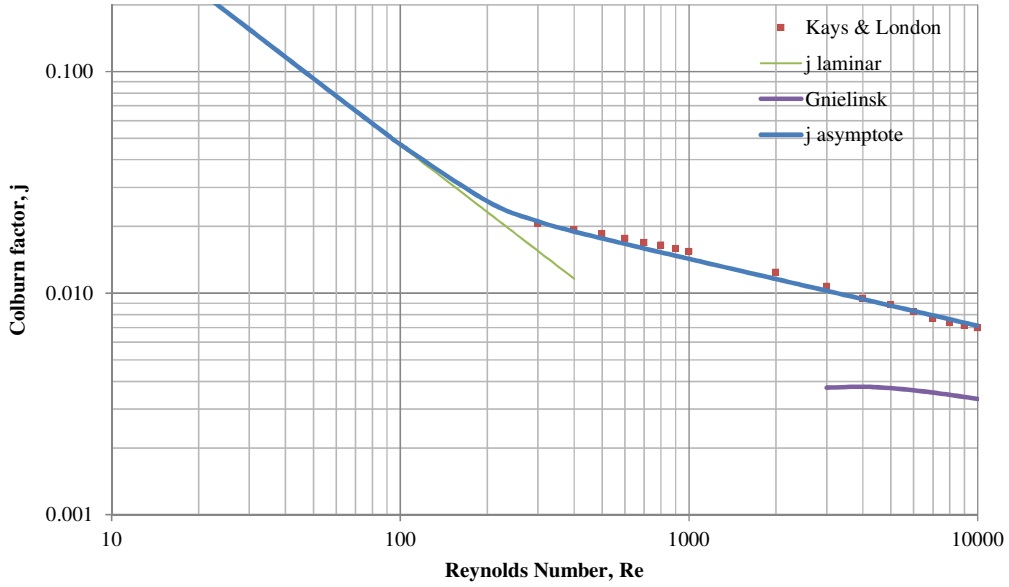

Figure 3.11: Colburn factor vs. Reynolds number

For the flow with Reynolds number greater than 3000 which is in the turbulent regime, the Colburn factor for the heat exchanger surface is known based on data from Kays and London. The heat transfer coefficient can be determined from Colburn factor as follows

$$H_c = \frac{j_{h,c} \cdot G_c \cdot c_{p,c}}{\left(\frac{c_{p,c} \cdot \mu_c}{k_c}\right)^{\frac{2}{3}}} \tag{3.50}$$

and

$$H_{\mathrm{h}} = \frac{j_{\mathrm{h,h}} \cdot G_{\mathrm{h}} \cdot c_{\mathrm{p,h}}}{\left(\frac{c_{\mathrm{p,h}} \cdot \mu_{\mathrm{h}}}{k_{\mathrm{h}}} \right)^{\frac{2}{3}}} \tag{3.51}$$

To account for a gradual transition from the Kays and London data to the laminar regime values for the Colburn factor, the following equation for the asymptotic curve is calculated

$$j_{\mathrm{asy}} = \left(j_{\mathrm{lam}}^{m} + j_{\mathrm{turb}}^{m} \right)^{\frac{1}{m}} \tag{3.52}$$

where the value of *m* is decided based on the minimization of RMS error between predicted values from Equation 1.36 and data from Kays and London. This method of obtaining an asymptotic curve is described in a work on modeling flow friction and heat transfer performance for wavy fins (Awad & Muzychka, 2011). The value of *m* is obtained as 6.2.

Fin and Overall Passage efficiency

The assessment of fin and overall passage efficiency depends on the number of layers of finned surfaces between the parting plates. For the cold fluid, there is only one layer of finned surface between the parting plates. So, the finned surface on the cold side can be considered as single stack with uniform heat transfer on both sides as shown in Figure 3.12.

The fin efficiency for such a configuration is determined in following steps (Allan, 2001). Calculate fin performance parameter as

$$m_{\mathrm{f,c}} = \left(\frac{2H_{\mathrm{c}}}{k_{\mathrm{m}} \delta} \right)^{\frac{1}{2}} \tag{3.53}$$

where k_{m} is the heat exchanger metal thermal conductivity

and fin efficiency as

$$\eta_{f,c} = \frac{\tanh\left(\frac{m_{f,c}b}{2}\right)}{\frac{m_{f,c}b}{2}} \tag{3.54}$$

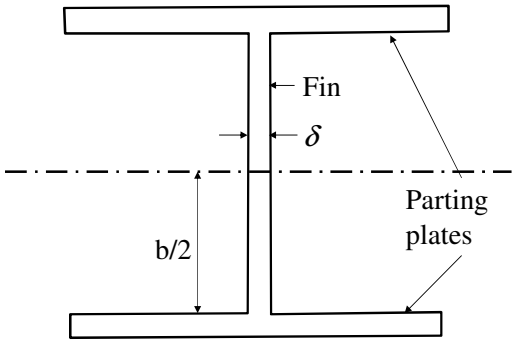

Figure 3.12: Single stack even loading fin configuration

The overall passage efficiency is given by

$$\eta_{o,c} = 1 - \frac{S_{f,c}}{S}\left(1 - \eta_{f,c}\right) \tag{3.55}$$

where $\frac{S_f}{S}$ is the area ratio of finned surface to total surface area.

For the hot side, there are two layers of finned surfaces, so the finned surface can be considered as single stack with even loading but twice the fin length.

The fin performance parameter is then calculated as

$$m_{f,h} = \left(\frac{2H_h}{k_m \delta}\right)^{\frac{1}{2}} \tag{3.56}$$

and fin efficiency as

$$\eta_{f,h} = \frac{\tanh\left(m_{f,h}b\right)}{m_{f,h}b} \tag{3.57}$$

The next design step is to obtain the overall heat transfer coefficient

Overall Heat Transfer Coefficient

The overall heat transfer coefficient is sum total of resistance to heat transfer on both hot and cold surfaces referenced to one side (hot or cold) given by

$$U_c = \frac{1}{\frac{1}{\eta_{o,c} H_c} + \frac{t_w \cdot S_c}{S_w \cdot k_{metal}} + \frac{S_c}{S_h \eta_{o,h} H_h}} \tag{3.58}$$

which is referenced to cold side. S_w is the surface area of the wall surface in contact with the fluid, t_w is the fin thickness and k_{metal} is the thermal conductivity of the metal. Since the thermal conductivity of the fin material is high, the term t_w/k_{metal} is very small, so the middle term can be ignored.

Heat-exchanger effectiveness

To determine the heat exchanger effectiveness, we first determine the capacity rate ratio, R_c and number of transfer units NTU

$$R_c = \frac{C_{max}}{C_{min}} \tag{3.59}$$

and

$$NTU = \frac{U_c \cdot S_c}{C_{min}} \tag{3.60}$$

For counter-flow heat exchangers, the effectiveness then is given by

$$\varepsilon_{hx} = \frac{1 - e^{NTU(R_c - 1)}}{1 - Re^{NTU(R_c - 1)}} \tag{3.61}$$

Pressure-drop across Heat-exchanger passages

The pressure-drop across the heat exchanger is an undesirable but an unavoidable effect. So the intent of the design is to minimize the pressure-drop without significantly increasing the size of the exchanger. The pressure-drop in a heat exchanger can be computed by the following equation (Kays and London, 1984)

$$\frac{\Delta P}{P_{in}} = \frac{G^2 v_1}{2P_{in}}\left[\Phi_1 + \Phi_2 + \Phi_3 + \Phi_4\right] \tag{3.62}$$

where

$$\Phi_1 = 1 + K_c - \sigma^2$$

$$\Phi_2 = 2\left(\frac{v_2}{v_1} - 1\right)$$

$$\Phi_3 = f\frac{S}{A_{ff}}\frac{v_m}{v_1}$$

$$\Phi_4 = \left(1 - \sigma^2 - K_e\right)\frac{v_2}{v_1}$$

v_1, v_2, v_m are specific volume of the fluid at the entrance, at the exit and the mean specific volume respectively

K_c, K_e are the coefficients of contraction and expansion for the fluid respectively

g_c is the acceleration due to gravity

f is the friction factor obtained from the friction factor data documented for the surface type as a function of Reynolds number as shown in Figure 3.13 (Kays and London, 1984).

Similar to Colburn factor, the friction factor data is available from a Reynolds number of 300. The turbulent regime is considered from Reynolds number of 3000 for which the data is taken from Kays and London. For Reynolds number below 3000, the laminar flow correlation for rectangular channel flow is implemented to calculate the friction factor given by:

$$f_{lam} = \frac{24}{\mathrm{Re}}\left(1 - 1.3553r_a + 1.9467r_a^{\,2} - 1.7012r_a^{\,3} + 0.9564r_a^{\,4} - 0.2537r_a^{\,5}\right) \tag{3.63}$$

where r_a is the aspect ratio of the rectangular cross-section and $r_a < 1$

For laminar flow, the friction factor is dependent on the channel aspect ratio and is inversely proportional to Reynolds number. So as the Reynolds number reduces, the friction factor increases.

As in case of the Colburn factor, the friction factor is represented by a single equation for the asymptotic curve

$$f_{asy} = \left(f_{lam}^{n} + f_{turb}^{n} \right)^{\frac{1}{n}} \tag{3.64}$$

where the value of n is decided based on the minimization of RMS error. The value for n is obtained as 1.76

Four terms presented in the Equation of 1.46 respectively denote, the entrance or contraction loss as the fluid approaches the exchanger at a different velocity then changes to exchanger inlet velocity, acceleration loss or gain as the fluid expands or contracts during its passage across the exchanger, flow friction loss and exit loss. Of the four losses mentioned above, the flow friction losses represent the majority of the losses incurred by the flow.

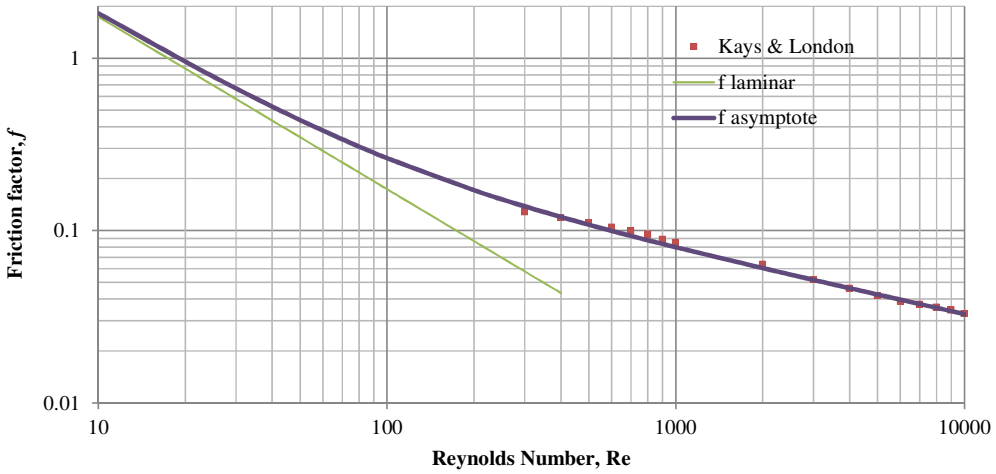

Figure 3.13: Friction factor vs. Reynolds number

The pressure-drop calculations are performed for both hot and cold sides with respective parameters.

Heat-exchanger Cost

After the iterations to arrive at the design configuration which meets the effectiveness and pressure-drop criteria based on the calculations presented above, the heat exchanger weight and cost are calculated based on the MPBR data.

Based on the heat exchanger volume V_{hx}, the total heat exchanger volume with headers in cubic meters $V_{hx,total}$ is derived based on the MPBR data as shown in Figure 3.14

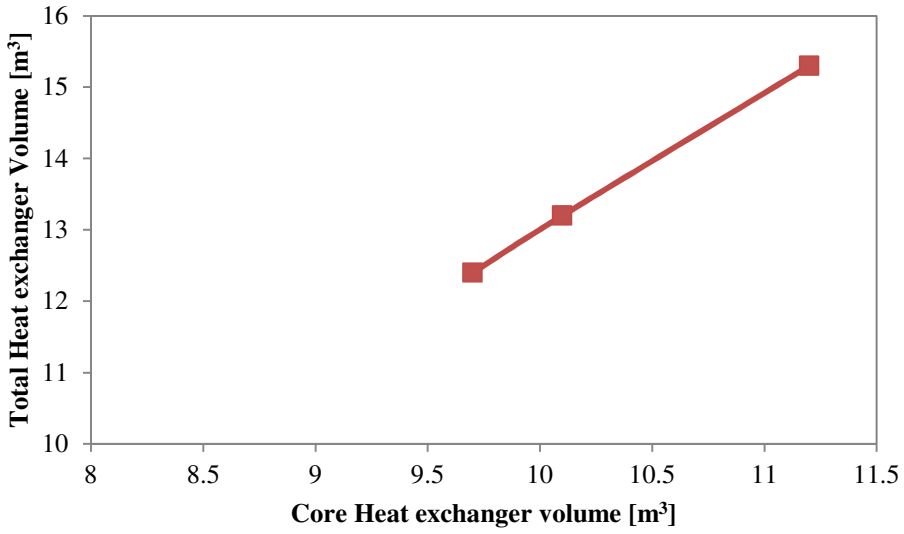

Figure 3.14: Core Heat exchanger volume vs. Total Heat exchanger volume

The total heat exchanger weight in kilograms is then computed by

$$W_{\text{hx,tot}} = 2358.8\left[\frac{\text{kg}}{\text{m}^3}\right]\cdot V_{\text{hx,tot}} \tag{3.65}$$

Finally, the heat exchanger cost in $1,000,000 is obtained by

$$C_{hx} = 1.668\times10^{-5}\left[\frac{\$1000000}{\text{kg}}\right]\cdot W_{\text{hx,tot}} \tag{3.66}$$

Since the heat exchanger cost estimates in MPBR study are for the year 2001(Chunyun, 2003), the cost estimate should be corrected to represent the change in price of heat exchangers till the present date. Figure 3.15 shows the producer price index for heat

exchanger in the recent years (Economagic, 2012). The price index shows an increase of 47% in the price index of heat exchangers. This increase is being adjusted in the cost estimate for heat exchanger presented in Equation 3.66

$$C_{\text{hx,cor}} = 1.47 \cdot C_{\text{hx}} \tag{3.67}$$

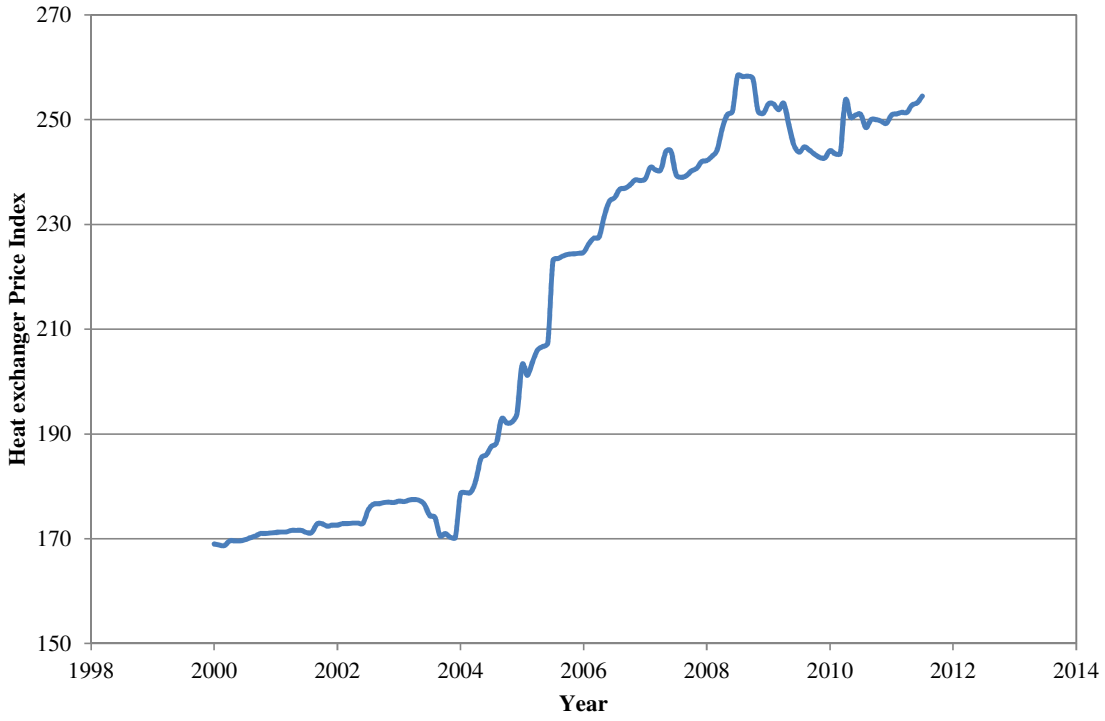

Figure 3.15: Heat exchanger Producer Price Index (Source: Economagic.com)

The advantage of the compact PFHX is in its high effectiveness with very little pressure-loss and a compact design. This is seen very well in the heat-exchanger cost for the HTSGT system.

The model is validated with MPBR calculation data for six different configurations (Chunyun, 2003). These configurations differ from each other in their core dimensions. Table 3.4 provides the specification for each configuration. A sample calculation for

configuration#1 is provided below. The heat exchanger design parameters are presented in Table 3.5

Table 3.4: Heat Exchanger Design Configuration

Configuration	Length [m]	Width [m]	Height [m]
1	0.653	0.254	16
2	0.6	0.254	18.3
3	0.56	0.254	20.6
4	0.325	0.762	16
5	0.3	0.762	18.3
6	0.3	0.762	20.6

Table 3.5: Heat Exchanger Design Parameters

Heat Exchanger Design Parameters		
Parameter	Value	Unit
plate spacing	1.65	[mm]
fin spacing	0.56	[mm]
fin thickness	76	[micron]
parting plate thickness	0.38	[mm]
plates on coldside	1	
plates on hotside	2	
surface area to volume ratio on coldside, β_{cold}	4685	[m^2/m^3]
surface area to volume ratio on hotside, β_{hot}	4734	[m^2/m^3]

The design condition for the heat exchanger is given in Table 3.6

Table 3.6: Heat Exchanger Design Condition for Sample calculation

Heat Exchanger Validation Case Design Conditions		
Parameter	Coldside	Hotside
Fluid	Helium	Helium
Mass Flowrate	119 [kg/s]	119 [kg/s]
Inlet Temperature	659 [K]	1123 [K]
Inlet Pressure	7850 [kPa]	7560 [kPa]

The design calculation with the above design condition for configuration 1 is presented in Table 3.7.

Table 3.7: Heat Exchanger Design calculation

Heat Exchanger Validation Case Design Calculations		
Parameter	Coldside	Hotside
Inlet flow rate, [kg/s]	119	119
Inlet pressure, [kPa]	7850	7560
Inlet temperature, [K]	659	1123
Outlet temperature, [K]	1077	705
Core length, [m]	0.653	
Core width, [m]	0.254	
Core height, [m]	16	
Heat exchanger surface area S, [m^2]	3590	7260
Hydraulic radius r_h, [mm]	0.176	0.174
Frontal area [m^2]	1	2.23
Free-flow to face area ratio σ, [%]	24	55
Mass-velocity G, [kg/m^2-s]	123	53
Reynolds number Re	1700	817
Fanning friction factor f	0.066	0.089
Colburn factor j	0.012	0.016
Heat transfer coefficient h, [W/m^2-K]	10500	5800
Fin efficiency η_f	0.35	0.24
Overall surface efficiency η_o	0.52	0.35
Conductance U, [W/m^2-K]	2350	1160
UA, [kW/K]	843	
Heat transfer rate Q, [kW]	258000	
Effectiveness ε, [%]	93	
Entrance loss coefficient K_c	1.25	1.16
Exit loss coefficient K_e	0.57	0.2
Entrance loss ϕ_1	2.2	1.86
Acceleration loss/gain ϕ_2	0.9	-0.6
Flow friction loss ϕ_3	302	247
Exit loss ϕ_4	0.54	0.35
Pressure loss Δp, [%]	7.2	1.8

The comparison of the model calculations with MPBR data are shown in Figure 3.16

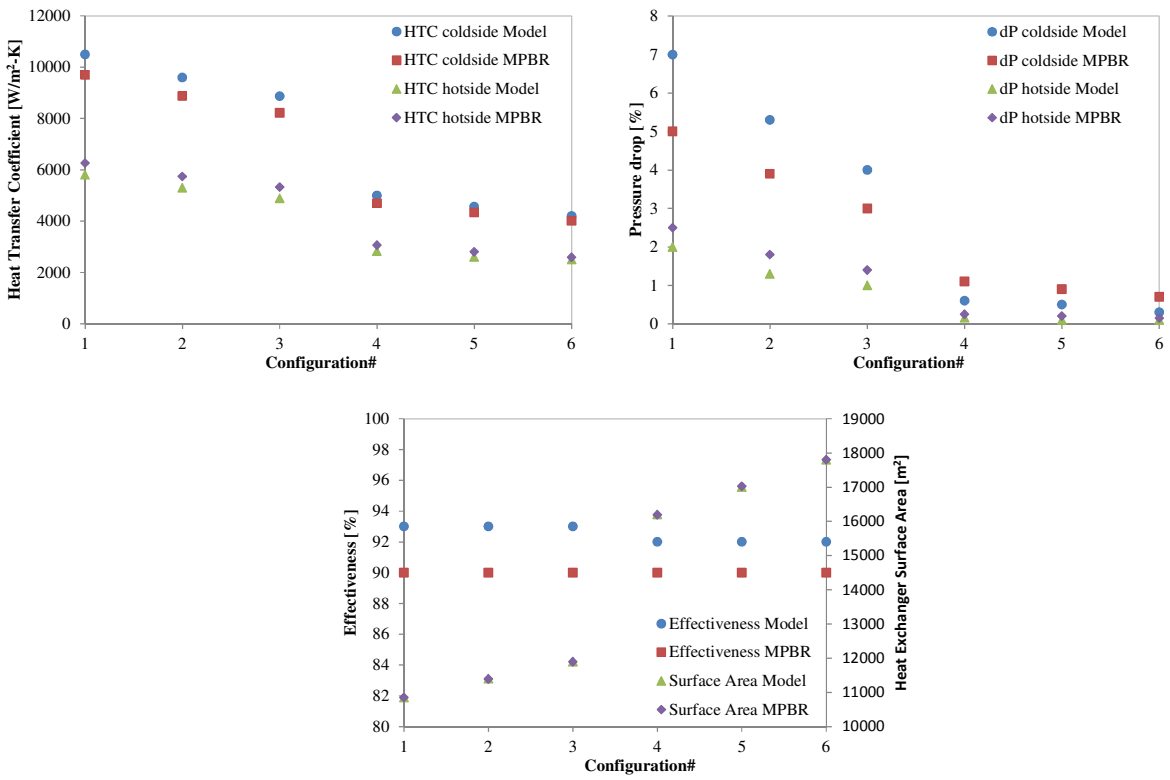

Figure 3.16: Heat Exchanger model validation with MPBR data

The model predictions show a good match with MPBR data. The heat transfer coefficient for both hot and coldside are comparable to MPBR data while the pressure drop prediction is slightly higher. The predicted effectiveness is also higher but the surface area calculation matches well. The higher pressure drop is due to lower Reynolds number prediction for the flows leading to higher flow friction. The same reason increases the heat transfer effectiveness than MPBR. Since pressure drop and effectiveness are contrary requirements, the optimization of heat exchanger surface area for meeting both the requirements will lead to a prediction very close to the actual surface area.

Solar Collector System Cost

The solar collector system for a power tower configuration mainly comprises of solar collector (Heliostat) field and the receiver assembly. The heliostat field has the heliostats

arranged in an optimum pattern to focus the sunlight incident on the mirror surface to the receiver system on the tower. The heat transfer fluid (HTF) running through the receiver system picks-up the heat which is then transferred to the working fluid of GT system through a heat-exchanger.

There are many factors that determine the design and cost of the solar collector system like geographical location of the site, the amount of solar radiation available, the mirror dimensions and optical properties, the receiver technology, the heat transfer fluid (HTF) etc., but the main parameter is the design thermal power to be delivered from solar collector system to the power block based on the GT system performance. The design thermal power required from solar field is determined from the GT system analysis. This input is then used to determine the tower height, receiver area and heliostat field area and also the cost of the solar collector system.

The solar collector system has been designed using the Solar Advisory Model (SAM). SAM is a performance and economic model designed to facilitate decision making for people involved in the renewable energy industry like engineers, technology developers, and researchers etc. SAM makes performance predictions for grid-connected solar, small wind, and geothermal power systems and economic estimates for distributed energy and central generation projects. The model calculates the cost of generating electricity based on information about a project's location, installation and operating costs, type of financing, applicable tax credits and incentives, and system specifications.

SAM is based on an hourly simulation engine that interacts with performance, cost, and finance models to calculate energy output, energy costs, and cash flows.

SAM models system performance using the TRNSYS software developed at the University of Wisconsin combined with customized components. TRNSYS is a validated, time-series simulation program that can simulate the performance of photovoltaic,

concentrating solar power, water heating systems, and other renewable energy systems using hourly resource data.

SAM models parabolic trough, power tower, and dish-Stirling concentrating solar power systems. The dish-Stirling and power tower models are based on research at the University of Wisconsin.

SAM's power tower performance model uses TRNSYS components developed at the University of Wisconsin and described in Simulation and Predictive Performance Modeling of Utility-Scale Central Receiver System Power Plants (Wagner, 2008).

SAM uses weather file that contains hourly data describing the solar resource, wind speed, temperature, and other weather characteristics at a particular location in tmy3, tmy2 and epw formats. This data represents the yearly weather pattern at a location on an hourly basis generated using weather data collected over many years.

Phoenix, Arizona is selected as the reference location for performing the design calculations as it is one of the most promising places to install a solar thermal power-plant. Table 8 lists the reference system details for the solar collector system cost analysis

Table 3.8: Solar Collector System Reference Cost Break-up

Design Parameter	Value
Power Tower reference cost, $C_{tow,ref}$	\$901,500
Tower cost scaling exponent, k_{tow}	0.01298
Receiver reference area, A_{rec}	1110 m^2
Receiver reference cost, C_{rec}	\$59,148,900
Receiver cost scaling exponent, k_{Rec}	0.7
Heliostat field unit area cost, k_{Field}	\$201/m^2

SAM was simulated for varying design thermal power from solar field and the tower height, receiver area and field area were obtained using the optimization tool in SAM.

The solar field optimization algorithm is based on the DELSOL3 model developed at Sandia National Laboratory, and described in A User's Manual for DELSOL3: A Computer Code for Calculating the Optical Performance and Optimal System Design for Solar Thermal Central Receiver Plants (Kistler, 1986). The relation between the tower height and design thermal power is shown in Figure 3.17. The tower height increases with increase in design thermal power.

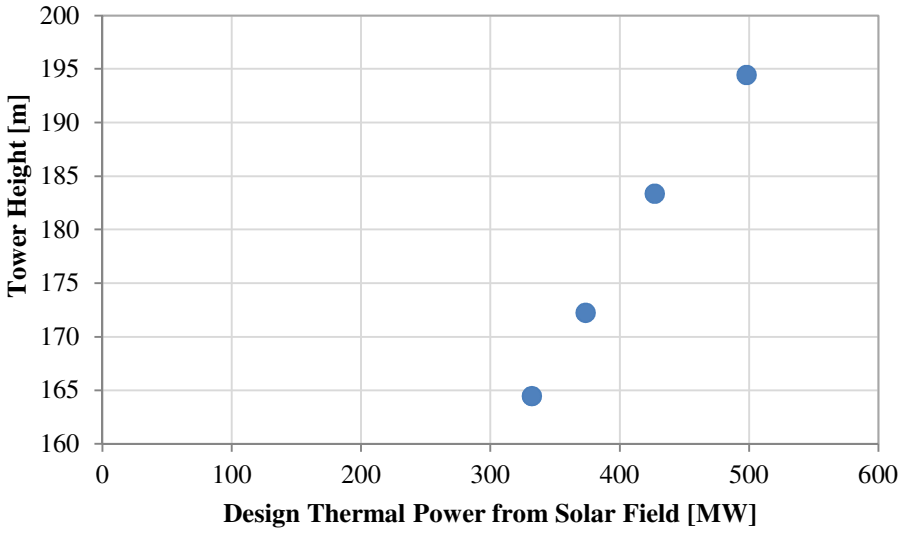

Figure 3.17: Design Thermal Power from Solar Field vs. Tower Height

The tower height h_{tow}, obtained from the relation above is used to calculate the tower cost as

$$C_{tow} = C_{tow,ref} \cdot e^{(k_{tow} \cdot h_{tow})} \tag{3.68}$$

Figure 3.18 shows the variation of the receiver area with design thermal power from solar field.

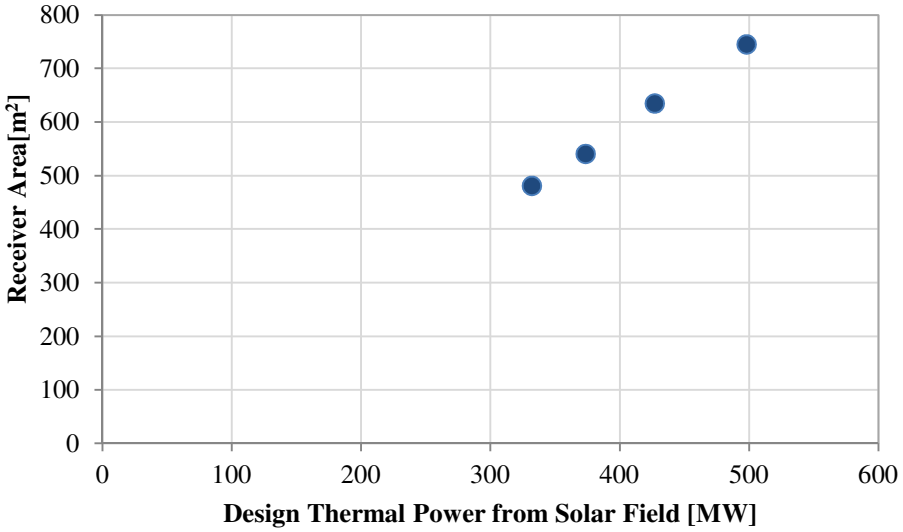

Figure 3.18: Design Thermal Power from Solar Field vs. Receiver Area

The receiver area also scales linearly with design thermal power. The receiver cost is then determined as

$$C_{\text{Rec}} = C_{\text{Rec,ref}} \cdot \left(\frac{A_{\text{Rec}}}{A_{\text{Rec, ref}}} \right)^{k_{\text{Rec}}} \tag{3.69}$$

The relation between the Heliostat field area and design thermal power from solar field is depicted in Figure 3.19. Heliostat field cost depends on the area of the land covered by the heliostats. The land area is representative of the number of heliostats installed. The Heliostat field cost is then calculated as

$$C_{\text{Field}} = k_{\text{Field}} \cdot A_{\text{Field}} \tag{3.70}$$

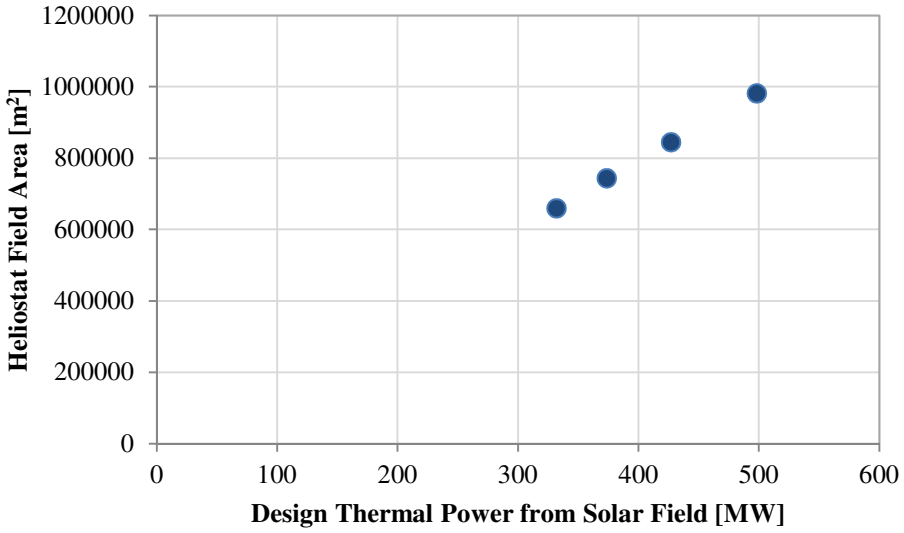

Figure 3.19: Design Thermal Power from Solar Field vs. Heliostat Field Area

The total solar collector system cost is given by:

$$C_{SC,tot} = C_{Field} + C_{Rec} + C_{tow} \tag{3.71}$$

The solar collector system has the largest share of the capital expenditure for a solar energy based power turbine system.

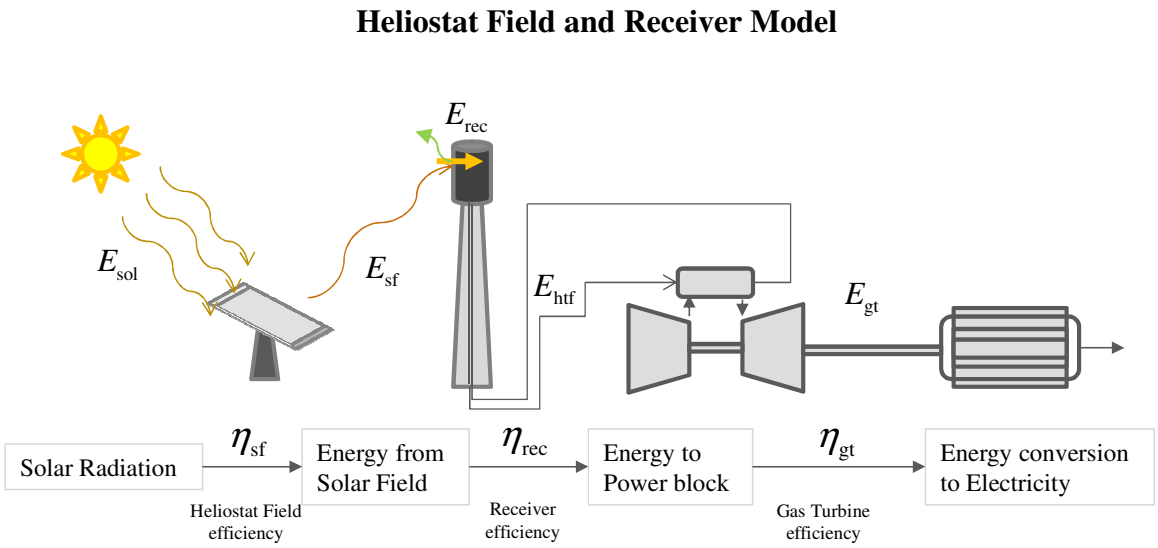

Figure 3.20: Flow of Energy through power plant and various efficiencies involved

The amount of energy converted to electricity in an entire year is calculated based on the plant performance and the amount of solar energy supplied to the GT system. Figure 3.20 shows the schematic of this energy transfer from solar radiation to electricity. The solar energy supplied to the gas turbine system was calculated using SAM (System Advisory Model) based on hourly calculations on performance of the solar collector system for the year using tmy data. The total energy of incident solar radiation annually, E_{sol}, is dependent on the Heliostat field size. A significant portion of this energy is lost in the solar field due to optical losses, losses due to Heliostat field arrangement relative to sun, tracking losses etc. and the remainder is supplied to the receiver as E_{sf}. The solar field efficiency is given by:

$$\eta_{sf} = \frac{E_{sf}}{E_{sol}} \tag{3.72}$$

The major portion of the energy is spent on multiple sources of losses. It depends on the heliostat field layout and geographical location of the power plant site other than the optical properties of the mirror itself and is observed to remain invariant with changes in field size and receiver area and operating conditions (Wagner, 2008). The solar field efficiency varies between 40 and 55% for power tower configuration (Wagner, 2008). Figure 3.21 shows the solar field efficiency for each month at the chosen location for two different design thermal power requirements as calculated using SAM. The solar field efficiency for the present case is calculated as 44% based on the SAM data for the particular site chosen.

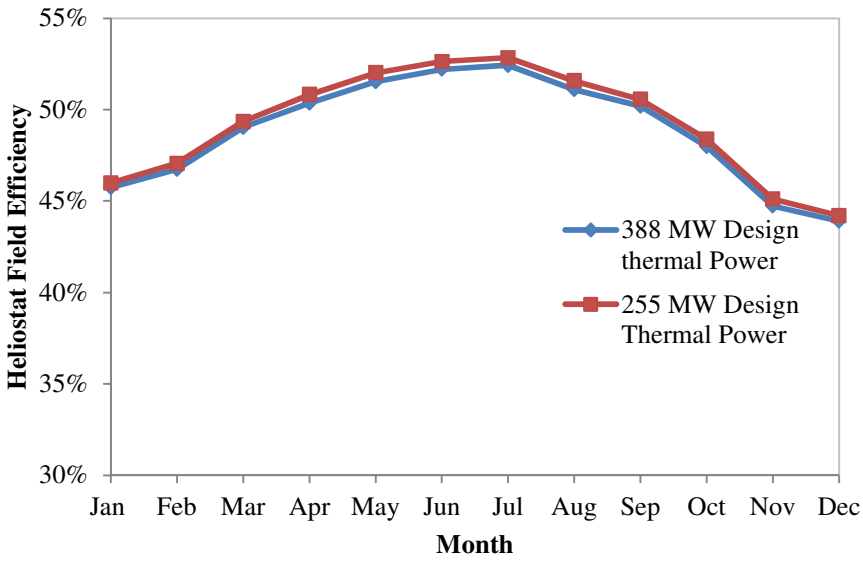

Figure 3.21: Solar Field Efficiency at different Design Thermal Power Ratings (Source: SAM)

The receiver has the HTF circulating through it to absorb the incident radiation on receiver surface. The amount of energy absorbed and supplied to solar heat-exchanger depends on the HTF inlet temperature to receiver and HTF outlet temperature from receiver. A portion of the solar energy incident on the receiver from solar field is lost mainly due to radiative and convective losses which are dependent upon the average HTF temperature through the receiver. The following section describes the receiver model which models the energy absorption by receiver panels and calculates the losses to derive receiver efficiency. The Receiver efficiency is defined as:

$$\eta_{\text{rec}} = \frac{E_{\text{htf}}}{E_{\text{rec}}} \tag{3.73}$$

where E_{rec} is the energy from the solar field absorbed by the receiver.

This is lower than E_{sf} due to some portion (~5%) of the incident radiation getting reflected from the receiver surface. This data is utilized in computing the amount of energy transferred to the power-block annually. The GT system efficiency determines how much of the energy transferred to the power-block is converted to electricity. The relationship is expressed as:

$$\eta_{gt} = \frac{E_{gt}}{E_{htf}} \tag{3.74}$$

The annualized cost of HTSGT and the energy supplied as electricity give the unit cost of electricity generation. This unit cost is then utilized to optimize the system design for the most economical configuration.

Receiver Model

The receiver model's main purpose is to calculate the receiver thermal efficiency to determine the fraction of energy absorbed by HTF from the solar field. The receiver is situated on the tower surrounded by the heliostat field. There are basically two types of receivers- 1) External Receiver and 2) Cavity Receiver. The external receiver spans full 360^{o} for absorbing radiation from solar field, but has higher losses due to exposure to the surrounding. The cavity receiver is shielded from the surroundings, reducing the losses but it also has a smaller field of view, reducing the amount of energy that it can absorb from the solar field. For the present study, the external receiver is modeled for determining receiver efficiency. The external receiver is built-up of many panels. Each of these panels consists of multiple tubes through which the HTF flows. Figure 18 shows the different kinds of receivers. The HTF absorbs the heat from the tube walls based on the flux incident on the panel surface from the solar field.

Figure 3.22: Two different configurations for Receiver 1) External Receiver 2) Cavity Receiver (Source: Wagner, 2008)

These panels are inter-connected to form multiple flow circuits where the HTF enters through some panels, flows through the different interconnected panels and exits from certain panels after picking up heat. Figure 3.23 shows a single receiver panel and the flow pattern through the receiver.

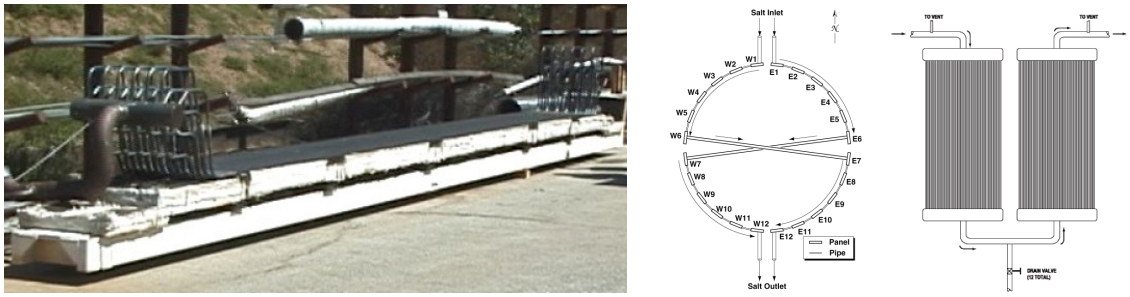

Figure 3.23: 1) Receiver Panel on Solar-II 2) HTF Flow Configuration 3) Flow between two receiver panels (Source: Wagner, 2008)

The receiver walls absorb about 95% of the radiation incident on their surface. However, since the wall surface is exposed to the ambient, a portion of this absorbed energy is lost due to heat transfer through radiation and convection. The schematic of the heat transfer model is represented in Figure 3.24.

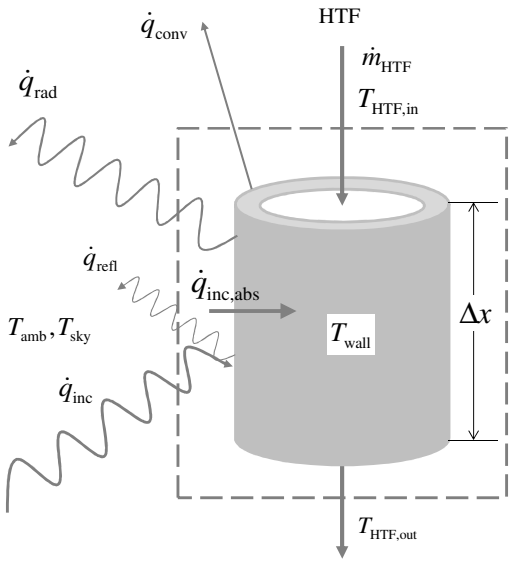

Figure 3.24: Heat Transfer Model Schematic

A control volume is formed around a small section of a tube of length Δx in the receiver panel at temperature T_{wall}. The HTF fluid enters this volume with temperature T_{in} and mass-flow rate $\dot{m}_{HTF}$ and leaves this volume at temperature T_{out}. The radiation incident on the tube wall exterior surface is $\dot{q}_{inc}$. The radiation absorbed by the receiver wall is given by

$$\dot{q}_{inc,abs} = \dot{q}_{inc} - \dot{q}_{refl} \tag{3.75}$$

where $\dot{q}_{refl}$ is the radiation reflected off the wall surface.

$\dot{q}_{conv}$ and $\dot{q}_{rad}$ represent the energy lost to the surrounding due to convection on exterior wall surface and the energy lost due to radiation from exterior wall surface.

The energy absorbed by the HTF is denoted as $\dot{q}_{HTF,abs}$. The model assumes negligible losses due to conduction. The energy balance in the control volume is then given by

$$\begin{aligned} \dot{q}_{HTF,abs} &= \dot{q}_{inc,abs} - \dot{q}_{conv} - \dot{q}_{rad} \\ &= \dot{q}_{inc} - \dot{q}_{refl} - \dot{q}_{conv} - \dot{q}_{rad} \end{aligned} \tag{3.76}$$

The data on the incident radiation flux on the receiver is provided as 12 distinct flux values for the entire 360^o field in the azimuthal direction along the entire vertical length of the receiver. This implies only a single flux value for an entire panel. So, the same flux value will be applicable to multiple tubes in a panel along their entire length. This is accounted for by scaling the heat transfer calculations performed on a single tube as described above by the length of the tube and number of tubes in a panel.

The calculations are performed for each panel and based on the flow pattern of HTF through the receiver panels, the amount of heat absorption by HTF in each panel and the amount of heat loss through each panel is determined.

The incident radiation on a receiver panel is given by:

$$\dot{q}_{inc} = n_{tube} \cdot \int_0^{H_{receiver}} P''_{field}(x) \cdot D_{tube} \cdot dx = n_{tube} \cdot P''_{field} \cdot D_{tube} \cdot H_{rec} \tag{3.77}$$

where P''_{field} is the flux of radiation from the solar field incident on the receiver panel, D_{tube} is the diameter of a single tube on a receiver panel, n_{tube} is the number of tubes on a single receiver panel and H_{rec} is the height of the receiver panel.

The amount of incident radiation reflected off from the surface of the receiver is dependent on the surface absorptivity. The absorptivity α is assumed to be a spectrally independent constant. The reflectivity is then given by 1-α. The reflected radiation is then given by:

$$\dot{q}_{\text{refl}} = (1-\alpha) \cdot n_{\text{tube}} \cdot P''_{\text{field}} \cdot D_{\text{tube}} \cdot H_{\text{rec}} \tag{3.78}$$

The convective losses $\dot{q}_{\text{conv}}$ are proportional to the temperature difference between the receiver panel temperature and the free-stream air temperature flowing around the receiver. The properties of air are evaluated at the average of receiver panel temperature and ambient temperature, T_{amb}. The convective losses are proportional to a mixed convective coefficient which incorporates both natural and forced convection from the receiver surface. The convective losses are then given by:

$$\dot{q}_{\text{conv}} = h_{\text{m}} \cdot n_{\text{tubes}} \cdot D_{\text{tube}} \cdot H_{\text{rec}} \cdot (T_{\text{s}} - T_{\text{amb}}) \tag{3.79}$$

The mixed convective coefficient is determined as:

$$h_{\text{m}} = \left(h_{\text{for}}^{\text{m}} + h_{\text{nat}}^{\text{m}}\right)^{\frac{1}{\text{m}}} \tag{3.80}$$

The value of *m* determines the dominance of larger of the two convective coefficients. As *m* increases, the mixed convection coefficient tends towards the larger of the two components. A value of 3.2 for *m* is chosen based on the recommendations by Siebers and Kraabel (Wagner, 2008).

The convection coefficient for forced convection is dependent on the Reynolds number for the free-stream flow and the surface roughness of the receiver panel surface. A set of correlations for Nusselt number corresponding to different ranges of these two parameters is provided by Siebers and Kraabel (Wagner,2008) as shown in Figure 3.25.

The surface roughness of the receiver is denoted by the term ε and is calculated as the ratio of individual receiver panel tube diameter and receiver diameter $D_{\text{tube}}/D_{\text{rec}}$

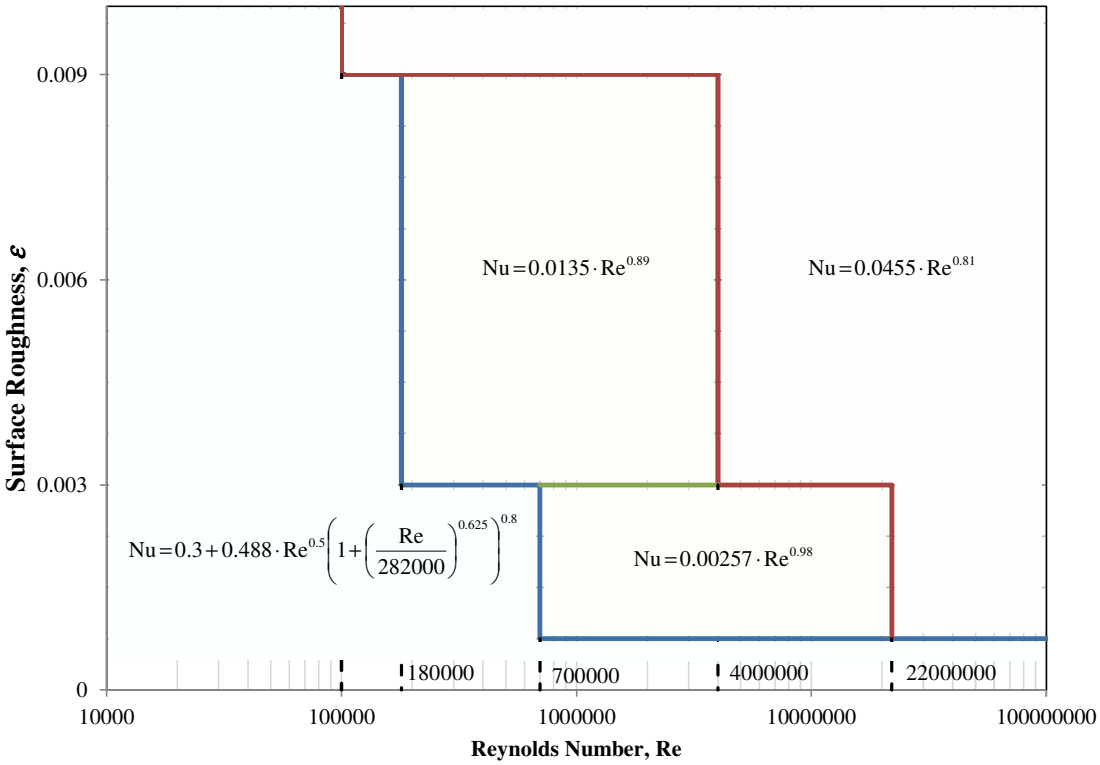

Figure 3.25: Nusselt number correlations for forced convection over receiver surface (Source: Wagner, 2008)

The convection coefficient for forced convection is calculated from the Nusselt number for forced convection as:

$$h_{\text{for}} = \frac{\text{Nu}_{\text{for}} \cdot k_{\text{film}}}{D_{\text{rec}}} \tag{3.81}$$

where k_{film} is the thermal conductivity of the film over the receiver surface which is assumed to be at the average of receiver panel surface temperature and ambient temperature.

For the convection coefficient for natural convection, the large diameter of the receiver lets us consider the flow over vertical flat plate for natural convection over receiver surface. Siebers and Kraabel present the best correlation for this scenario (Wagner, 2008)

$$\mathrm{Nu}_{\mathrm{nat}} = 0.098 \cdot \mathrm{Gr}_{\mathrm{H}}^{\frac{1}{3}} \left(\frac{T_{\mathrm{s}}}{T_{\mathrm{amb}}} \right)^{-0.14} \tag{3.82}$$

where T_s is the average surface temperature of the receiver panel and the Grashof number, Gr is calculated as

$$\mathrm{Gr}_{\mathrm{H}} = g \cdot \beta \cdot \left(T_{\mathrm{s}} - T_{\mathrm{amb}} \right) \cdot \frac{H_{\mathrm{rec}}^3}{\nu_{\mathrm{amb}}^2} \tag{3.83}$$

Where g is the gravitational constant, β is the volumetric expansion coefficient, H_{rec} is the height of receiver panel and ν_{amb} is the kinematic viscosity of the ambient air. The fluid properties are calculated at ambient condition.

The coefficient of natural convection is then calculated as:

$$h_{\mathrm{nat}} = \frac{\mathrm{Nu}_{\mathrm{nat}} \cdot k_{\mathrm{amb}}}{H_{\mathrm{rec}}} \tag{3.84}$$

Of the three major loss components, radiation losses are dominant at high temperatures and are more complex to determine, requiring a careful assessment of their extent. For a proper representation of ambient conditions, the radiation losses are split into two components, radiation losses to the ambient and radiation losses to the sky (Wagner, 2008)

$$\dot{q}_{\mathrm{rad}} = \dot{q}_{\mathrm{rad,amb}} + \dot{q}_{\mathrm{rad,sky}} \tag{3.85}$$

where

$$\begin{aligned} \dot{q}_{\mathrm{rad,amb}} &= h_{\mathrm{rad,amb}} \cdot \left(T_{\mathrm{s}} - T_{\mathrm{amb}} \right) \\ h_{\mathrm{rad,amb}} &= \sigma \cdot \varepsilon \cdot F_{\mathrm{s,amb}} \cdot \left(T_{\mathrm{s}} + T_{\mathrm{amb}} \right) \cdot \left(T_{\mathrm{s}}^2 + T_{\mathrm{amb}}^2 \right) \end{aligned} \tag{3.86}$$

and

$$\begin{aligned} \dot{q}_{\mathrm{rad,sky}} &= h_{\mathrm{rad,sky}} \cdot \left(T_{\mathrm{s}} - T_{\mathrm{sky}} \right) \\ h_{\mathrm{rad,sky}} &= \sigma \cdot \varepsilon \cdot F_{\mathrm{s,sky}} \cdot \left(T_{\mathrm{s}} + T_{\mathrm{sky}} \right) \cdot \left(T_{\mathrm{s}}^2 + T_{\mathrm{sky}}^2 \right) \end{aligned} \tag{3.87}$$

σ is the Stefan-Boltzman constant, ε is the emissivity for the receiver surface, taken as 0.88 (Wagner, 2008), F represents the view factor between the receiver surface and

ambient and sky. F is assumed to be 0.5 for both components (Wagner, 2008). T_s represents the average receiver panel temperature and T_{amb} is the ambient temperature. T_{sky} represents the sky temperature calculated as (Duffie and Beckman, 2006)

$$T_{sky} = T_{amb} \cdot \left(0.711 + 0.0056 \cdot T_{dewpt} + 0.000073 \cdot T_{dewpt}^2 + 0.013 \cdot \cos\left(\left(\frac{180 - hour \cdot 15}{180} \right) \cdot \pi \right) \right)^{\frac{1}{4}} \tag{3.88}$$

T_{dewpt} is the dew-point temperature based on the ambient conditions and relative humidity in the atmosphere and *hour* is the hour of the day ranging from 0 to 24 with 12 representing the solar noon.

All the terms on the right hand side of the energy balance equation have been accounted for in the model. The term on the left hand side is the rate of heat absorbed by the HTF as it passes through the receiver tubes. The change in HTF temperature as it passes through the receiver panel can then be determined by

$$\Delta T_{HTF} = T_{HTF,x+\Delta x} - T_{HTF,x} = \frac{\dot{q}_{HTF,abs}}{\dot{m}_{HTF} \cdot c_{HTF}} \tag{3.89}$$

where ΔT_{HTF} is the temperature change in the HTF fluid as it passes through the receiver panel tube. $\dot{m}_{HTF}$ is the mass-flow rate of HTF through the receiver panel tube and c_{HTF} is the specific heat capacity of the HTF. Figure 3.26 shows the control volume for this scenario.

The only unknown parameter to be obtained is the receiver panel surface temperature T_s. It can be determined by doing an energy balance on the heat transfer across the receiver tube thickness into the HTF flowing through the tube

$$\dot{m}_{HTF} \cdot c_{HTF} \cdot \left(T_{HTF,x+\Delta x} - T_{HTF,x} \right) = \dot{q}_{HTF,abs} = \frac{\left(T_s - T_{HTF,avg} \right)}{\left(R_{cond,wall} + R_{conv,HTF} \right)} \tag{3.90}$$

where $T_{HTF,avg}$ is the average HTF temperature along the length of the receiver tube and $R_{cond,wall}$ and $R_{conv,HTF}$ are the thermal resistance for conduction through receiver tube wall and convection on the inner surface of the receiver tube respectively.

The resistances are in series to conduct the heat from receiver tube surface to the inner tube surface and then the convection from the tube inner surface to the bulk HTF flow inside the tube

The thermal resistance of the receiver tube wall is given by

$$R_{\text{cond, wall}} = \frac{\ln\left(\frac{D_{\text{tube}}}{D_{\text{tube,inn}}}\right)}{2 \cdot \pi \cdot H_{rec} \cdot k_{\text{tube}} \cdot n_{\text{tube}}} \tag{3.91}$$

where $D_{tube,inn}$ is the diameter of the inner surface of the tube and k_{tube} is the thermal conductivity of the tube wall.

The thermal resistance of convection on the inner surface of the receiver tube is given by

$$R_{\text{conv,HTF}} = \frac{1}{h_{\text{inn}} \cdot H_{\text{rec}} \cdot \pi/2 \cdot D_{\text{inn}} \cdot n_{\text{tube}}} \tag{3.92}$$

where h_{inn} is the convection coefficient for the flow on the inner surface of the receiver tube, and can be determined using pipe-flow correlations.

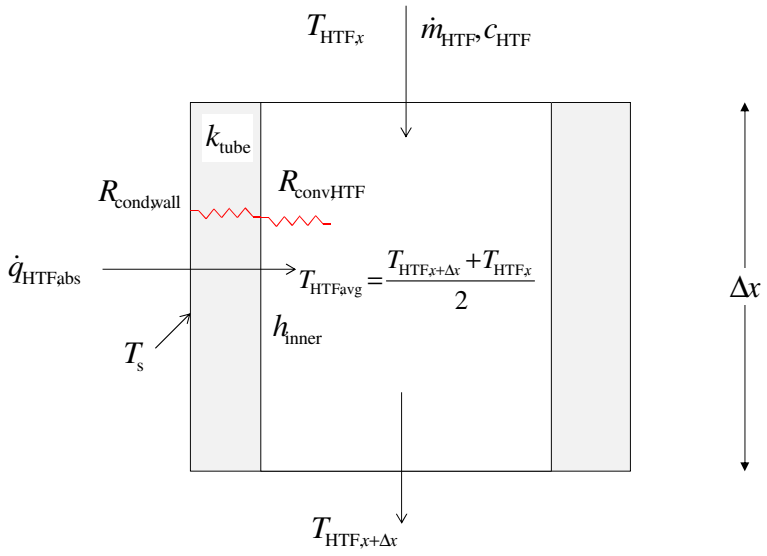

Figure 3.26: Control volume for heat transfer through receiver tube to HTF

Thus the set of equations of individual receiver panels are solved in the sequence of HTF flow pattern through the different panels iteratively with initial guess values for HTF and individual receiver panel surface temperatures till we arrive at a converged temperature distribution across receiver panels and HTF outlet temperature.

Such calculations were performed for each hour of the year for a particular combination of HTF inlet and outlet temperatures to arrive at a receiver efficiency value for that particular combination.

A sample calculation for a particular hour of the year is presented below. Table 3.9 lists the Receiver design parameters for which the assessment was done. Table 3.10 presents the operating conditions for the receiver in that particular hour. Table 3.11 presents the calculated parameters for the receiver based on the model.

Table 3.9: Receiver Design Specifications

Parameter	Value
Receiver Diameter D_{rec}, [m]	13
Receiver Height H_{rec}, [m]	18
Number of Panels N_{panels}	24
Number of Flow-lines n_{lines}	2
Tube Outer Diameter d_{tube}, [mm]	40
Tube Thickness t_{tube}, [mm]	1.25
Receiver surface Absorptivity α	0.95
Receiver surface emissivity ε	0.88

Table 3.10: Receiver Operating Conditions

Parameter	Value
Ambient Pressure P_{amb}, [kPa]	100
Ambient temperature T_{amb}, [C]	13.1
Relative Humidity RH [%]	23
Wind speed V_{wind}, [m/s]	0.75
Azimuth, [deg]	-16.6
Zenith, [deg]	58.3
Direct Normal Incident DNI, [W/m^2]	3380
Solar Field Efficiency η_{SF}	0.428
HTF Temperature at Receiver Inlet $T_{HTF,cold}$, [K]	600
HTF Temperature at Receiver Outlet $T_{HTF,hot}$, [K]	900
Hour of the day $hour$, [0-24, 12 corresponds to noon]	12

Table 3.11: Receiver Model Calculations

Parameter	Value
HTF mass flow rate $\dot{m}_{HTF}$, [kg/s]	381
Solar Radiation Absorbed by Receiver $\dot{Q}_{inc}$, [MW]	365
Radiative Loss by Receiver $\dot{Q}_{rad,loss}$, [MW]	12
Convective Loss by Receiver $\dot{Q}_{conv,loss}$, [MW]	3
Power absorbed by HTF $\dot{Q}_{abs}$, [MW]	350
Receiver Efficiency η_{HTF}, [%]	96
Parameters for Panel 6	
Incident Flux [kW/m^2]	645
Nusselt Number for Forced Convection Nu_{for}	691
Heat Transfer Coefficient for Forced Convection h_{for}, [W/m^{2}K]	2.35
Nusselt Number for Natural Convection Nu_{nat}	6336
Heat Transfer Coefficient for Natural Convection h_{nat}, [W/m^{2}K]	16
Heat Transfer Coefficient for Radiation to Ambient $h_{rad,amb}$, [W/m^{2}K]	32
Heat Transfer Coefficient for Radiation to Sky $h_{rad,sky}$, [W/m^{2}K]	46
Panel Surface Temperature T_s, [K]	740

A table of HTF inlet and outlet temperature with corresponding receiver efficiency for each combination is generated, which is then interpolated upon for any given pair of HTF inlet and outlet temperatures in EES simulation to arrive at the receiver efficiency.

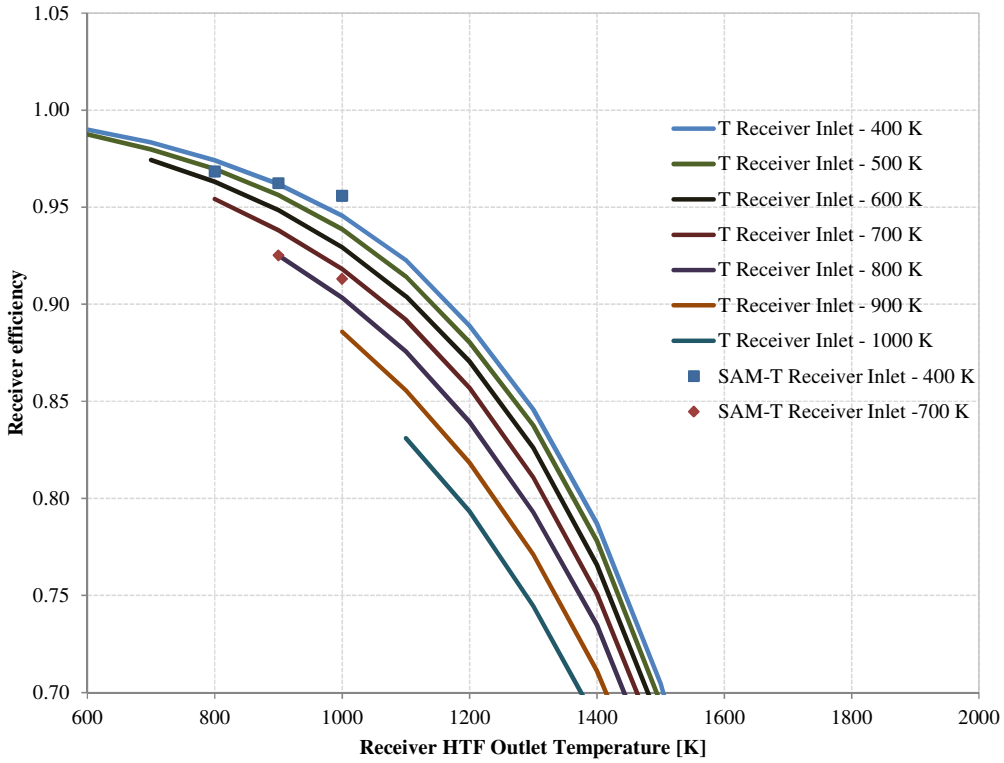

Figure 3.27: Variation of Receiver efficiency with HTF Receiver Inlet and Outlet Temperature

Figure 3.27 shows the variation in receiver efficiency with change in receiver inlet and outlet temperature. This efficiency corresponds to the ratio of energy absorbed by the HTF to energy absorbed by the receiver (energy incident on the receiver surface less reflected by the surface). The efficiency predicted by SAM is also depicted for a few cases. The calculated value is within 2% of SAM predicted values. The difference in value can be attributed to receiver performance being tied to operation of steam turbine which alters the predicted energy transfer to HTF by some extent.

Heat-Transfer Fluid

The efficiency and practicality of a high temperature gas turbine cycle running on solar power depends a lot on the heat-transfer mechanism implemented to transfer the energy from the sun to the working fluid of the gas turbine. The heat-transfer fluid is a part of the heat-transfer system and is integrally related to the choice of the system. The main choice

of fluid depends on its heat carrying capacity and its stability at high temperatures. One of the available options of fluids with such properties is molten salts. The molten salt can include many different molecular groupings its constituents. These salt groups consist of nitrates (NO3), carbonates (CO3), chlorides (Cl), fluorides (F) etc. These ion groups are associated with alkali metal group consisting of Lithium (Li), Sodium (Na), Potassium (K) etc form the constituents of these salts generally. There are heavier elements also involved but are usually avoided due to cost issues. The properties of molten salts can thus vary greatly based on its constitution. Molten salts are often mixed with other salts or compounds forming binary or ternary eutectic mixtures to achieve desired overall properties, and significant effort is underway in this area to improve the performance of heat transfer fluids for solar applications (DOE, 2008). These are very reliable fluids and have been in use for a long time commercially. The main challenges for molten salts are a relatively high freezing temperature, thermal instability at high temperatures and corrosive effects on metal walls containing these fluids. The freezing point ranges from 530K (257°C, 494°F) for the 60% NaNO3, 40% KNO3 mix to 775K (502°C, 935°F) for a salt like 58% KF, 42% ZrF4 (Williams, 2006) which can clog up the piping system if the temperatures go below the melting point during operation or during system shutdown. There are salts which melt at temperatures above 400^{o} C and have a high boiling point beyond 1000^{o} C like Flibe but they are still under development (Peterson, 2008). The main challenge for solar thermal power generation with advanced thermodynamic cycles is the requirement to achieve higher temperature for the HTF in the collector/receiver system. Many of the salts currently available commercially have a maximum temperature capability below our requirement for implementing high temperature cycles, like the solar salt (60% NaNO3, 40% KNO3) whose maximum temperature capability is 870 K beyond which it starts decomposing (Charles, 2007). For a realistic prediction of receiver system performance, the thermal capability of HTF should be beyond 1200 K (927^{o} C). The possibility of replacing molten nitrate salts with mixed carbonates has been identified for

an operating range of temperatures between 700^{o}C and 850^{o}C. At least 15 lithium–sodium–potassium carbonates blends with melting points between 400^{o}C and 410^{o}C and thermal stability between 800^{o}C and 850^{o}C are reported (Wu et al., 2011). However, the thermal stability of the salt is influenced by the atmosphere. It was found that only under a blanket cover of CO_2, the LiNaK carbonate salt showed stability till 1000^{o}C. With argon and air as blanket respectively, the salt decomposed at much lower temperatures. Based on the criteria of thermal stability beyond 900^{o}C, melting point below 525^{o}C and compatibility with high temperature alloys, graphite and ceramics; fluorides, chlorides and alkali fluoroborates are identified as candidate molten salts for high temperature operation (Williams, 2006). Of these, the fluoride salt mixture LiF-NaF-KF was selected as the most promising salt based on superior heat transfer characteristics for nuclear plant loop heat transfer.

Another medium for heat transfer suggested is sand or other such particulates due to their high thermal capacity and thermal stability at high temperature (>1000^{o} C). The mechanism for mobilizing the sand to the heat-exchanger and the system for transferring heat from the sand to the air is currently out-of-scope for the present effort. Direct heating of compressed air from the GT is another option being used in air receiver with volumetric heating. However, it makes thermal energy storage difficult. Also, since air is the medium, it will work well only for small scale power generation with smaller flow rates of air.

A representative model for the HTF is required at two different places for assessment of system performance, one for the assessment of receiver performance and another for solar heat exchanger performance. The requirement is to model the fluid properties of the HTF to carry out the performance calculations. Although the requirement is to represent the high temperature HTF fluid properties, due to lack of proper materials data, as an expedient, the solar salt material property is provided for performance calculation from

SAM (System Advisory Model). The data is available till a temperature of 866 K. For temperatures beyond this limit, the material properties were extrapolated to determine fluid properties. To bind the extent of deviation from real scenario however, we present here the comparison of fluid properties of solar salt with FLiNaK fluoride salt. Table 3.12 shows the comparison of fluid properties at 1200 K for the two fluids. Figure 3.28 shows the comparison of density and viscosity for a range of temperature between these fluids.

Table 3.12: Comparison of fluid properties between Solar salt and FLiNaK fluoride salt

Property	Solar Salt	FLiNaK
Density, [kg/m^3]	1500	1850
Specific heat, [kJ/kg-K]	1.64	1.59
Viscosity, [Pa-s]	0.00036	0.00129
Thermal conductivity, [W/m^2-K]	0.63	0.6

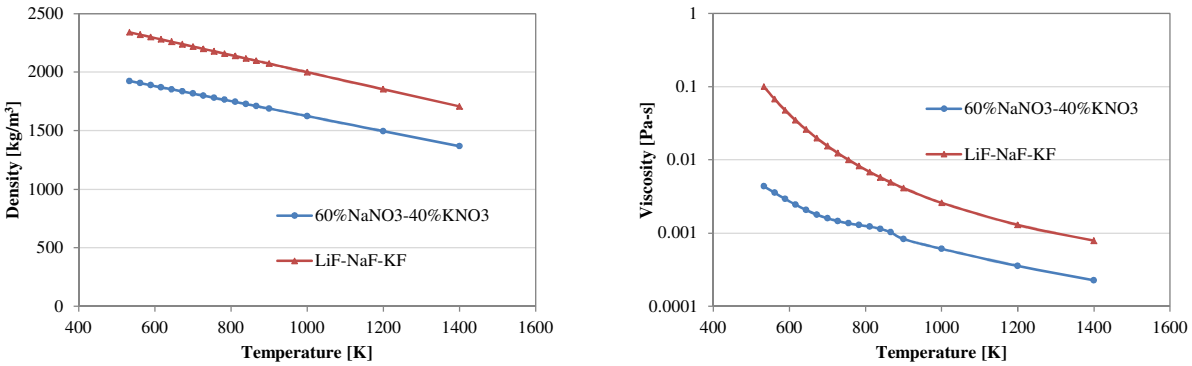

Figure 3.28: Comparison of fluid properties between Solar salt and FLiNaK (a) Density, (b) Viscosity

The values of specific heat and thermal conductivity were almost invariant with temperature, so the values in Table 3.12 suffice for comparison. The higher viscosity for the fluoride salt leads to lowering of Reynolds number for the same mass-flow of the HTF. This can be compensated by increasing the HTF flow rate. The gas cycle performance is not impacted by this deviation. In future, fluid property data for high temperature operation HTFs can be incorporated for more accurate prediction of receiver performance.

Life Cycle Cost of HTSGT System

When a power plant is commissioned, it incurs cost. The construction of the power plant and the purchase and installation of all systems constitute the capital expenditure on the plant. The other cost is to cover for the operation and maintenance of the power plant, referred to as the operations and maintenance (O&M) cost. The capital cost of the entire power-plant for the present study is the aggregate of all the costs described in the sections above. The O&M cost for a standard power-plant has the cost of the fuel as a major component. For a solar energy based power-plant, the fuel is ideally not a requirement and the maintenance interval can be much farther spaced than for a standard plant.

The biggest share of capital expense is taken by the heliostat field and the receiver system. The cost mainly depends on the design thermal power. The costs of the different sub-systems in the power block depend majorly on the volume they occupy or the volume of flow of different fluids that they must accommodate. Empirical data is used to determine the size and cost of these sub-systems, mainly the GT and the Heat-exchangers.

Operations and Maintenance (O & M) costs of the power plant depend on numerous factors like labor, parts replacement, heliostat mirror wash etc. This cost is determined mainly on the basis of rated capacity of the system. For the present analysis, a maintenance cost of 65 $/kW-yr is assumed based on power tower CSP technology cost forecast (Craig, 2010). This assumption will lead to same O & M cost for all configurations as the rated capacity is same for all.

After determining the capital expenditure for the entire power-plant and its O & M cost, Life cycle cost analysis is performed for the chosen economic life and annualized cost of the system is determined. The economic scenario considered for the calculation involves the discount rate, general inflation rate and planning period. The discount rate is kept at

7.5%, general inflation is chosen as 2.5% and a planning period of 30 years is considered based on the NREL estimates for power tower system costs in US market (Craig, 2010). There are other factors affecting cost like contingencies, indirect costs, income tax, insurance, loan, income tax credit. These factors have not been incorporated into the model as they require more detailed and complex calculations which are beyond the scope of this study.

For a CRPT power plant with gas turbine as the prime mover, the total capital expenditure for the plant is given by:

$$C_{\text{pp,cap}} = C_{\text{SC,tot}} + C_{\text{GT}} + C_{\text{BOP}} \tag{3.93}$$

The total capital expenditure is a one-time expense on the plant for its entire economic life and so is the life cycle cost on capital expenditure for the plant, $LCC_{\text{pp,cap}}$. This expense needs to be annualized to determine the unit cost of electricity. The annualized cost of the plant can be determined by calculating the life cycle cost factor. The life cycle cost factor (LCCF) for the plant is determined on the basis of geometric series present worth factor (GSPWF) as

$$LCCF = \frac{1}{(1+d)} + \frac{(1+i)}{(1+d)^2} + \ldots + \frac{(1+i)^{n-1}}{(1+d)^n} \tag{3.94}$$

where d is the discount rate, i is the general rate of inflation and n is the economic life in years

This expression can be simplified as

$$LCCF = \frac{1}{(d-i)}\left(1 - \left(\frac{1+i}{1+d}\right)^n\right) \tag{3.95}$$

The annualized cost is then determined as

$$C_{\text{ann,cap}} = \frac{LCC_{\text{pp,cap}}}{LCCF} \tag{3.96}$$

The other component of the annual cost is the O & M cost of the power plant. So the total annualized cost of the power plant is

$$C_{\text{ann,tot}} = C_{\text{ann,cap}} + C_{\text{ann,O\&M}} \tag{3.97}$$

The annual system cost and the annual electricity generation together determine the unit cost of electricity for the system.

$$C_{\text{unit}} = \frac{C_{\text{ann,tot}}}{W_{\text{ann}}} \tag{3.98}$$

The unit cost of electricity determines the economic feasibility of a system to justify its design and operation. A sample calculation for determination of life cycle cost of the power plant is represented in Table 3.13

Table 3.13: Sample Calculation for Life Cycle Cost Analysis of Power plant

Cost Parameters	Values
Powerplant Capacity [MW]	100
Powerplant Capital cost [$]	200,000,000
Powerplant Capital cost [$/kW]	2000
O&M Cost $C_{\text{ann,O\&M}}$,[$/kW-yr]	65
discount rate d, [%]	5
inflation rate i, [%]	2.5
Economic Life n, [years]	30
$LCC_{\text{pp,cap}}$	200,000,000
$LCCF$	20.6
Annual Cost, $C_{\text{ann,cap}}$	9700000
Total Annual Cost, $C_{\text{ann,tot}}$ [$]	16200000
Annual Power Generation W_{ann}, [kWh]	180,000,000
Unit cost of Electricity C_{unit}, [cents/kWh]	9

CHAPTER 4

COLD GAS TURBINE

Introduction

The energy regime for solar thermal power is mostly dominated by systems that harness solar energy at relatively low temperatures when compared to the temperature ranges applicable for a combustion gas turbine. The solar collector system for a typical trough based solar thermal power-generation unit spans a large network of piping and relay systems like the SEGS (Angela, 2006). These systems typically have a fluid inlet temperature of 280^{o}C and an outlet temperature of 380^{o}C (Thorsten, 2002), which are relatively low temperatures. The present chapter assesses the feasibility of a gas-turbine operating at temperature ranges applicable for a trough based solar power generation system. This GT system is called the Cold Gas Turbine (CGT).

There have been attempts at designing high efficiency systems utilizing solar power in the past. Attempts have been made to develop a feasible and competitive solar energy based gas turbine system with augmentation of recuperation system or a combination of Brayton and Rankine cycles and with improvisations in the solar collector system (Peter et al, 2005). In another instance, a gas turbine system implementing the HAT (Humid Air Turbine) cycle incorporated the solar energy to achieve an improved performance (Hongbin, 2009).The use of solar energy in both these instances has been mainly to act as an additional low temperature source of energy to assist in the output of the main cycle, with the primary source of energy as fossil fuel to generate power.

The need for implementing a gas-turbine system with solar energy as the primary source requires assessing the feasibility of it being applicable in the low temperature regime for the working fluid. The peak cycle temperature is the most important factor to determine

the efficiency of a heat engine. The cycle efficiency increases with the peak cycle temperature. However, the maximum possible temperature is limited by the material capability for most engines. But for the current state of the art gas turbines, this limit is much higher than the peak temperature achievable for a parabolic trough. With solar collector system, the material capability is based on the conversion technique implemented to transfer solar energy onto the working fluid. The maximum possible temperature of the heat transfer fluid (HTF) in the parabolic trough concentrators for the class of organic and synthetic fluids used in the SEGS systems is 655 K (382^{o} C) (Angela, 2006). With molten slats, this temperature can be increased to 773 K (500^{o} C) (Kearney, 2002).

Basic Gas Turbine - Advantages

According to an assessment of CSP technology for the state of California, the capital expenditure cost on a gas turbine is ~40% lower than that of a steam based system (Black and Veatch, 2006). The operating cost of gas turbines however, is higher compared to steam based system due to the cost of fuel for conventional gas turbines. With the primary source of heat as solar energy, the operating cost for the gas turbine reduces drastically. The gas turbine currently available in the market are designed to work at very high temperature ranges and so a low operating temperature will increase the system reliability and durability with the components loaded thermally below their design limits. The conventional gas turbine without a combustion system further improves the durability of the system by avoiding any corrosive effects that the fuel and exhaust gases would have on the turbine components and also makes the system emission free and thus a green option for power generation. In addition, at small scale the gas-turbine system is a less complex system than a Rankine cycle based unit and so more robust. All these advantages make it a potential candidate for solar power generation at small scale.

Basic Gas Turbine Model

In the proposed application the gas turbine will be an open cycle heat engine. The most important parameter for thermodynamic performance evaluation of the system is the peak cycle temperature. Based on the discussion in the previous section, the design peak cycle temperature for the CAT system is specified as 750 K.

The system efficiency is calculated with constant compressor and turbine efficiencies at 0.86 and 0.85 respectively based on the system performance for a 6FA gas turbine unit (Jay, 1996). The pressure loss in heat exchanger is at 2% based on achievable pressure loss demonstrated in MPBR study (Chunyun, 2003). The system performance varies with both compressor pressure-ratio and turbine inlet temperature or the peak cycle temperature as shown in the Figure 4.1 below.

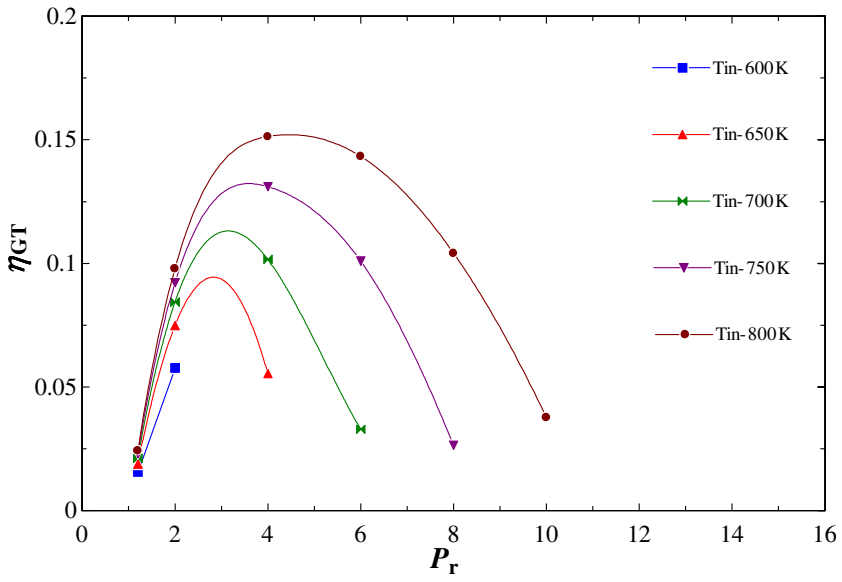

Figure 4.1: System efficiency vs. Pressure ratio for different Turbine inlet temperature

The system efficiency rises with the pressure-ratio at a constant turbine inlet temperature till a certain peak value and then falls down again to impractical levels. This trend results from differential rate of change in compressor and turbine work as depicted in Figure 4.2 at a constant turbine inlet temperature of 750 K.

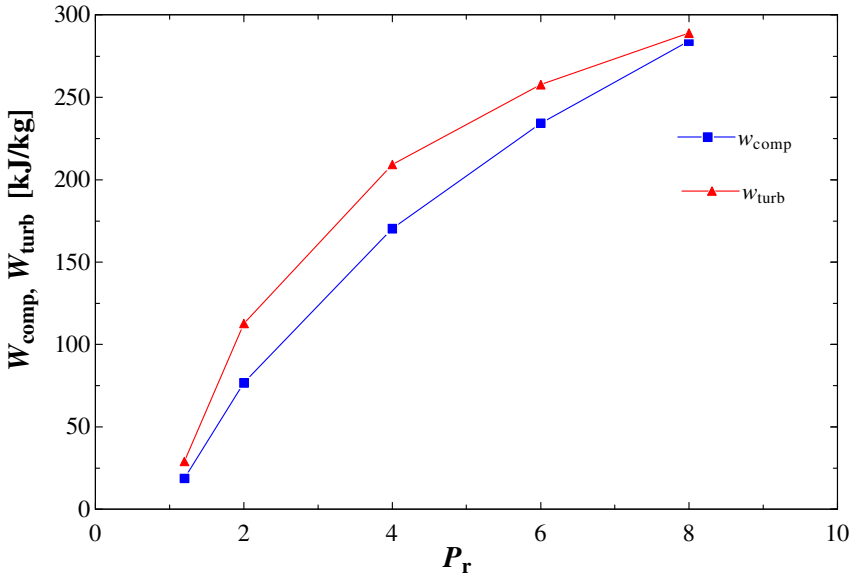

Figure 4.2: Change in Compressor and Turbine Work with Pressure ratio

With increasing turbine inlet temperatures, this trend continues with higher system efficiencies being achieved and the peak efficiency achieved at higher pressure-ratio.

For the turbine inlet temperature of 750 K, the peak cycle efficiency is 13.1%, achieved at a pressure ratio of ~4.

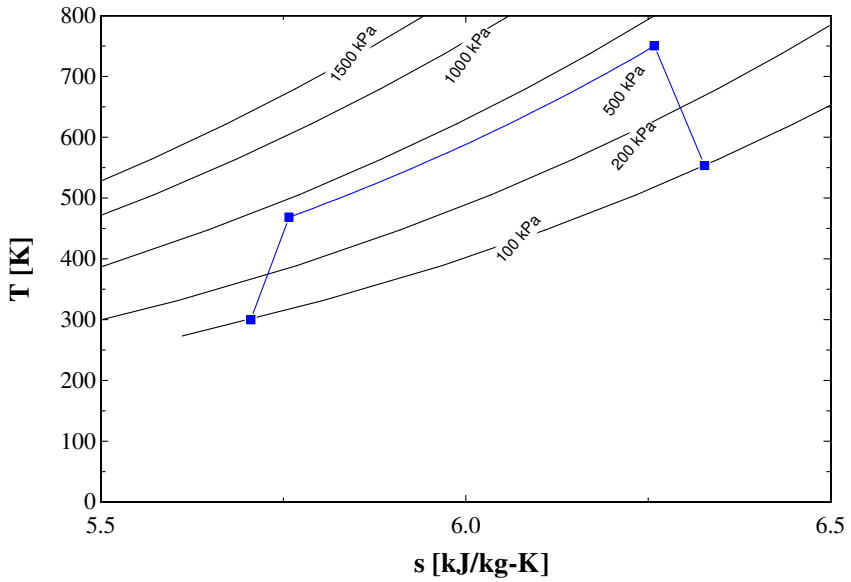

Figure 4.3: Thermodynamic cycle for Basic Gas Turbine (Brayton cycle)

The thermodynamic cycle for the system at peak cycle temperature of 750 K and pressure ratio of 4 is represented in the Figure 4.3

For a peak cycle temperature of 750 K, the efficiency of 13.1% is low. With the consideration of additional losses of a real system, the power generation efficiency will reduce further. The direct implementation of this schematic in power generation for CGT will not be economical. So the above basic system is augmented with additional systems namely recuperator, inlet-cooling, intercooler and absorption chiller to make use of the waste heat from the turbine exhaust and improve upon the system efficiency with the lower peak cycle temperature.

Exergy Flow Analysis

The exergy flow analysis for a system provides a detailed picture of the system performance and helps in identifying the areas, which can be modified to result in an improved performance. Figure 4.4 shows the exergy analysis for the simple-cycle configuration.

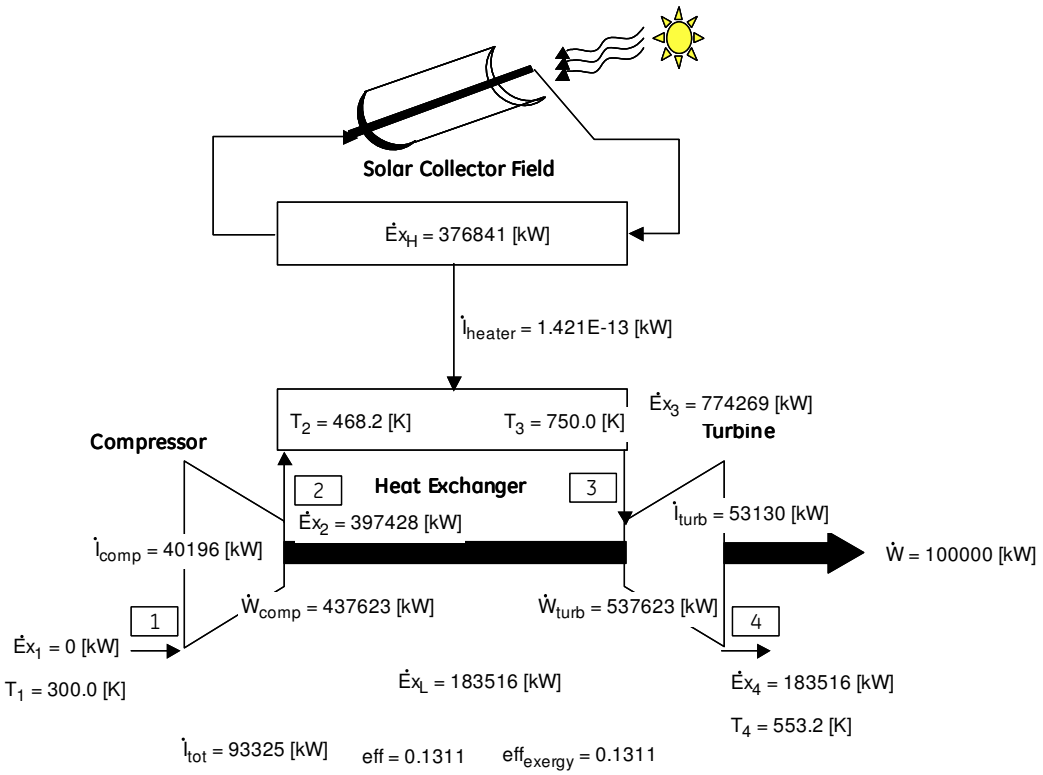

Figure 4.4: Exergy Flow Diagram for Simple Cycle Gas Turbine system

The main observation from the above figure is that we lose a good portion of exergy in the compressor and turbine sections but more importantly, we exhaust an even greater amount of useful energy i.e. energy out of the system. Theses losses, if reduced, will lead to a more efficient system for power generation.

Basic Gas Turbine – Improvement opportunities

The advantages of implementing a simple gas turbine were enumerated in the previous section. However, for low peak cycle temperatures, the GT efficiency is low (13% at 750K). This is because the heat discharged from the cycle is a significant portion of the heat input required. There are known solutions to this problem- 1) Regeneration and 2) Inlet cooling and inter-cooling.

Regeneration

It makes use of the waste heat from turbine exhaust to preheat the compressor discharge before it enters the heat-exchanger unit, lowering the requirement on heat-input for the

same work and thus improving system efficiency. However, at higher pressure ratios, the compressor discharge temperature might be higher than turbine exhaust temperature to make this option ineffective.

Inlet cooling and Inter-cooling

It reduces the temperature of the working fluid before the compressor stage to reduce the specific volume of the fluid and thus a decrease in the amount of work required to compress the fluid. However, it also increases the heat input required and lowers the effective temperature for heat input which can reduce the system efficiency.
In the following section we will see the incorporation of both these concepts into the CGT and its impact on performance.

Gas Turbine with Recuperator

To improve the system efficiency for the GT system the system is augmented with a recuperator. Figure 4.5 shows the schematic for the recuperated system. The recuperator will utilize the thermal energy of exhaust gases to heat the compressor discharge air before passing it onto the solar heat exchanger.

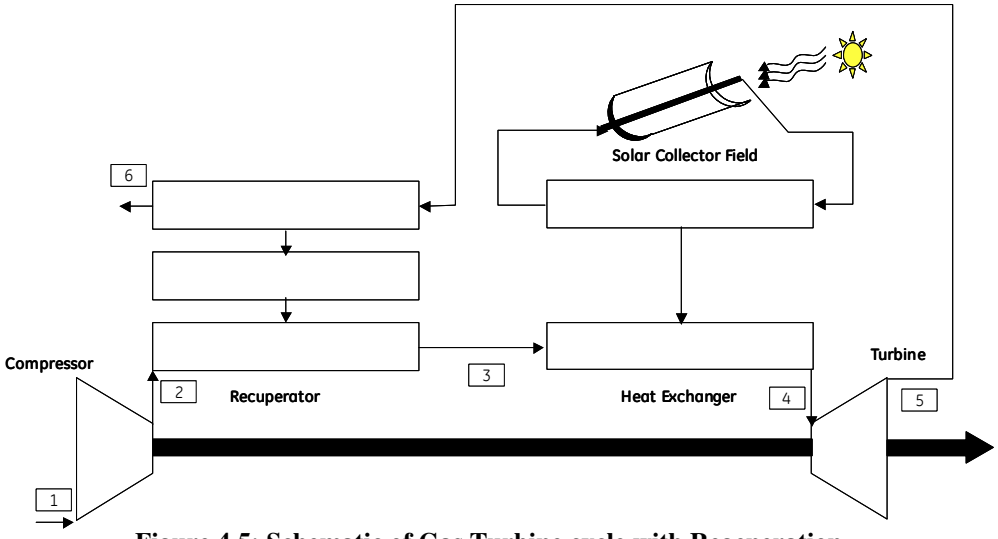

Figure 4.5: Schematic of Gas Turbine cycle with Regeneration

For a 95% heat transfer effectiveness based on MPBR design (Chunyun, 2003), at a pressure ratio of 1.74, the system efficiency is 28%. The T-s plot for the thermodynamic system is given in Figure 4.6

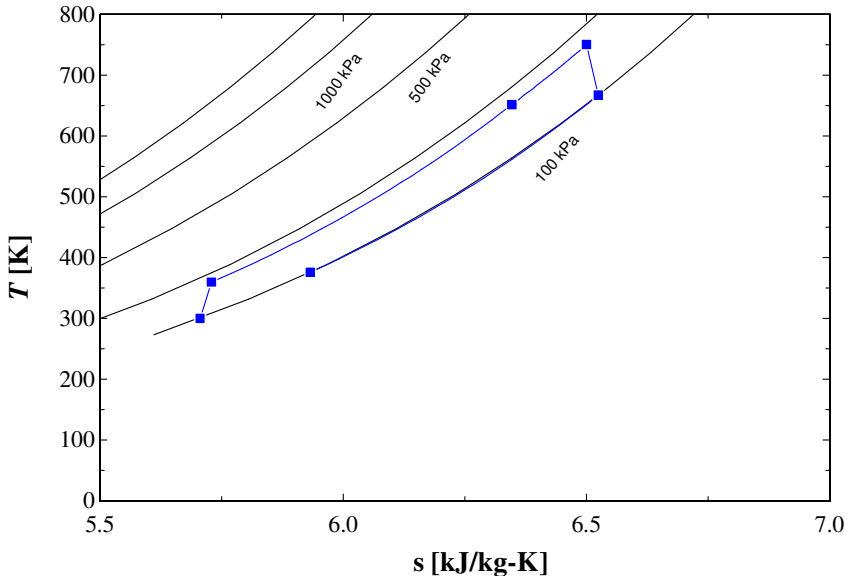

Figure 4.6: Thermodynamic cycle for CGT with Regeneration

The cycle shows the effect of incorporating the recuperator. The heat-input from the exhaust gas increases the enthalpy of compressor exhaust gas, reducing the heat input required from the solar collector system which improves the GT efficiency. The waste heat recovery improves with lower pressure ratio for a particular peak cycle temperature.

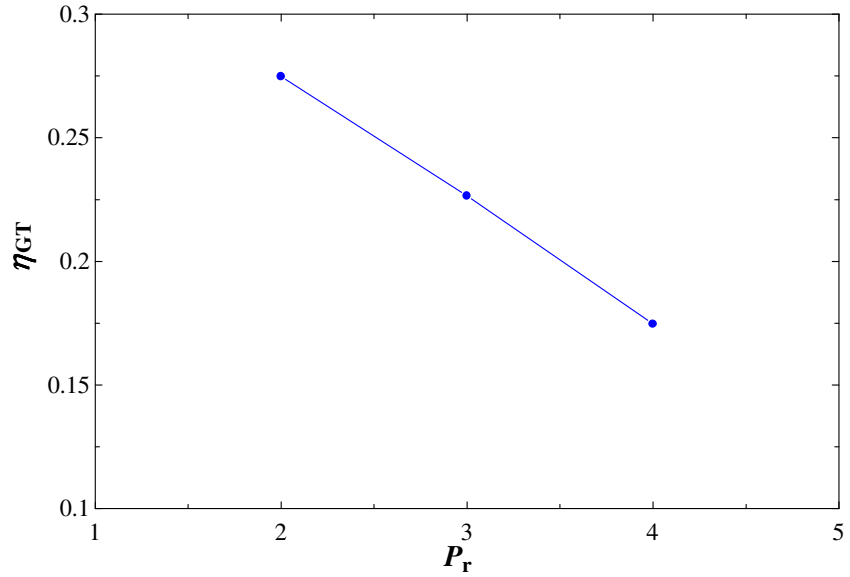

Figure 4.7: System Efficiency vs Pressure ratio

This happens because with lowering of pressure ratio, the turbine exhaust has more heat compared to temperature of compressor discharge fluid and the heat input from main heat-exchanger reduces, thus improving the system efficiency. Figure 4.7 shows the variation of GT efficiency with pressure ratio.

Exergy Flow Diagram

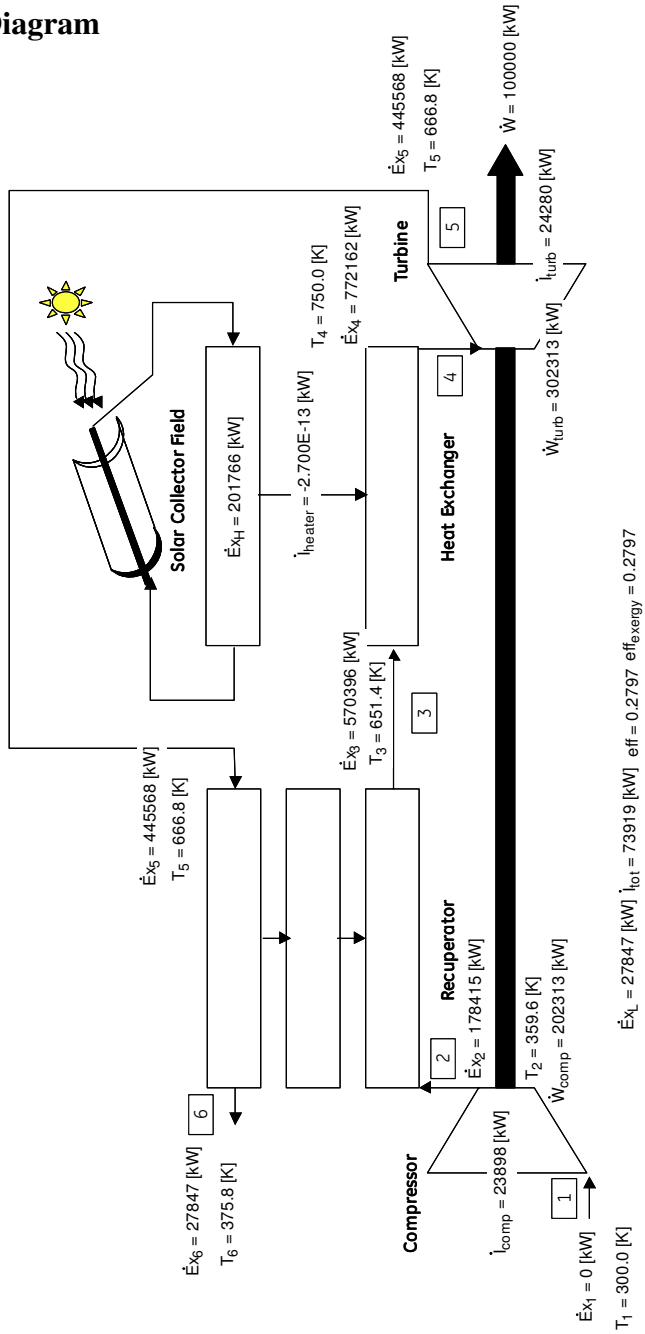

Figure 4.8: Exergy Flow Diagram for Simple Cycle GT with Recuperator

The exergy input and the exergy exhausted are favorably different from the simple cycle gas turbine. The recuperator utilizes the exhaust heat well to achieve a high system performance.

The next session augments the cooling system to cool the working fluid and reduce compressor work to enhance the system performance and analyze how that benefits our design.

Gas Turbine with Recuperator, Inlet Cooling and Intercooling

We are constrained in our system by the peak cycle temperature. To gain on the efficiency for the system, we need to look at the lowest cycle temperature. The advantage of lowering the temperature of working fluid before compression is that the work input required for raising the fluid pressure to the same pressure level goes down. This is supposed to improve the system efficiency. The drawback of this approach is that, lowering the temperature at compressor inlet will bring down the compressor exhaust temperature as well, which adversely affects the mean temperature of heat-input for the system.

This lowering of temperature could be achieved by augmenting the system with inlet-cooler and intercooler. Both these systems act as heat-exchangers to extract heat from the working-fluid. The inlet-cooler lowers the working fluid temperature at the inlet to the compressor whereas the inter-cooler lowers the working fluid temperature during the process of compression. This requires the compression to be achieved in multiple stages wherein the exhaust of the low-pressure compressor will be cooled by the inter-cooler and then introduced into the high-pressure compressor.

The system, although being designed for low temperature operation, still has a reserve of waste gas, which has ample heat content, although at lower quality. This waste process heat could be utilized with the aid of a system to provide us the required cooling for the working fluid. A system that suits our requirements as stated above is the Absorption chiller. An absorption chiller is a system that works on heat input based refrigeration cycle. The working fluid here is a salt solution, which acts as a heat transfer medium through a change in its concentration. This system finds its use in places where process waste heat is available in abundance. This system requires no work input to perform the

refrigeration process and thus carries out this task efficiently. This system has been described in detail in the system modeling chapter (Chapter 3).

The following section describes the new sub-systems added into the simple cycle gas turbine and how it impacts the system:

Power Generation System

The modified schematic has the following augmentations

1) Inlet Cooling System
2) Low Pressure Compressor
3) Inter-cooler
4) High Pressure Compressor
5) Absorption Chiller
6) Recuperator

Gas Turbine System

The working fluid passes through the inlet cooling section to lower its temperature. Then it is compressed in the low-pressure compressor. The exhaust from the low-pressure compressor is passed through a series of heat-exchangers, all part of the inter-cooling system. The working fluid then enters the high-pressure compressor. The exhaust from the high pressure compressor then enters the recuperator. After the compressor discharge air is preheated in the recuperator, it enters the main heat-exchanger to extract heat from the solar energy collector system. This heated fluid then enters the turbine section. After exiting the turbine, the exhaust gas is passed first through the recuperator and then through a heat-exchanger to supply process heat to the absorption chiller unit. The fluid in the main unit thus completes the cycle.

Absorption Chiller System

The Absorption Chiller absorbs heat from two sources 1) Gas turbine exhaust 2) Low-pressure compressor exhaust. Both these sources have the working fluid at a fairly high temperature and acting as a good quality heat source.

The absorption chiller unit uses this heat input to work its system and refrigerate the working fluid both in the inlet-cooling system as well as the intercooler after the mid-section cooling system. The absorption chiller has been modeled to incorporate the effect of variation in inlet heat temperature on COP of the chiller by characterizing the exergy destruction to input heat ratio to achieve a nominal COP of 0.7.

Cooling System

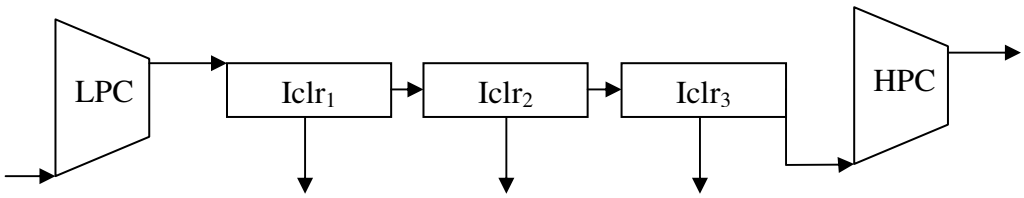

Figure 4.9: Intercooler schematic

The main constituent of the cooling system is the intercooler. Figure 4.9 shows the schematic for the intercooler. The intercooler is divided into three different heat exchanger units on the cold-side. The first heat-exchanger unit in the inter-cooler system extracts heat from the LP compressor discharge to act as input to the absorption chiller system.

$$\dot{Q}_{\text{iclr, abch, ip}} = h_{\text{iclr1, in}} - h_{\text{iclr2, in}} \tag{4.1}$$

The mid-section cooling system gets the working fluid from the first unit after it supplies heat to the absorption chiller. This fluid is then cooled to atmospheric temperature in the mid-section cooling unit.

$$\dot{Q}_{\text{iclr,atm,op}} = h_{\text{iclr2,in}} - h_{\text{iclr3,in}} \tag{4.2}$$

The absorption chiller refrigeration unit is the third heat-exchanger in the inter-cooler system. Here the working fluid is cooled below ambient temperature before it enters the high-pressure compressor.

$$\dot{Q}_{\text{iclr,atm,op}} = h_{\text{iclr3,in}} - h_{\text{hp,in}} \tag{4.3}$$

The total heat extracted from the intercooler is

$$\dot{Q}_{\text{iclr,tot}} = \dot{Q}_{\text{iclr,abch,ip}} + \dot{Q}_{\text{iclr,atm,op}} + \dot{Q}_{\text{iclr,atm,op}} \tag{4.4}$$

The total heat input to the absorption chiller is

$$\dot{Q}_{\text{abch,H}} = \dot{Q}_{\text{iclr,abch,ip}} + \dot{Q}_{\text{iclr,atm,op}} \tag{4.5}$$

The total heat extracted from the chilled water using the absorption chiller is

$$\dot{Q}_{\text{abch,L}} = COP \cdot \dot{Q}_{\text{abch,H}} \tag{4.6}$$

where

$$\dot{Q}_{\text{abch,L}} = \dot{Q}_{\text{ic}} + \dot{Q}_{\text{iclr3}} \tag{4.7}$$

The chilled water from the absorption chiller is used for inlet cooler and the third unit of intercooler as shown in Eq. 4.7. The schematic of the absorption chiller is presented in Figure 4.10.

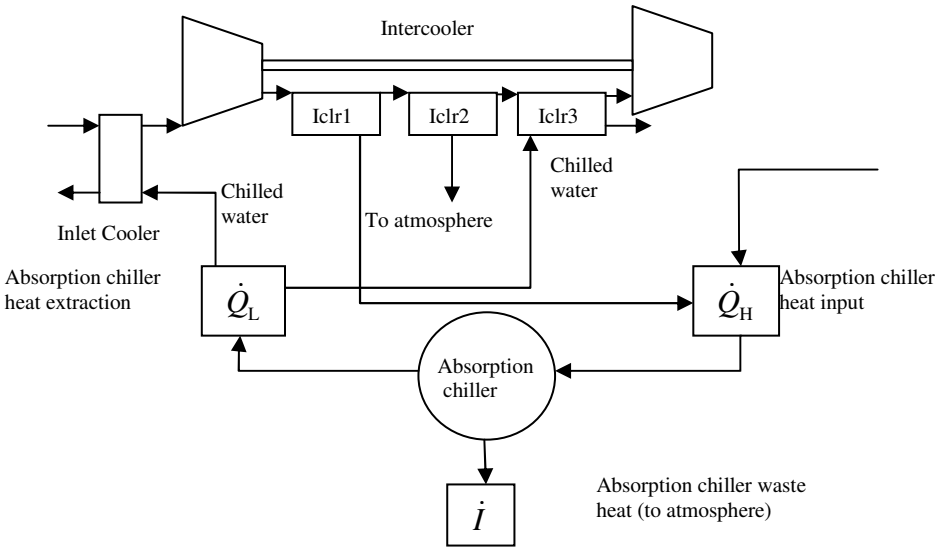

Figure 4.10: Absorption chiller schematic

Effect of Recuperation and Cooling

The combined effect of recuperation and cooling, making use of the energy from the waste heat in the system has lower system efficiency than with only recuperator system. Figure 4.11 shows the thermodynamic cycle for this system. The system pressure ratio is 2.6 and the resulting system efficiency is 27.1%

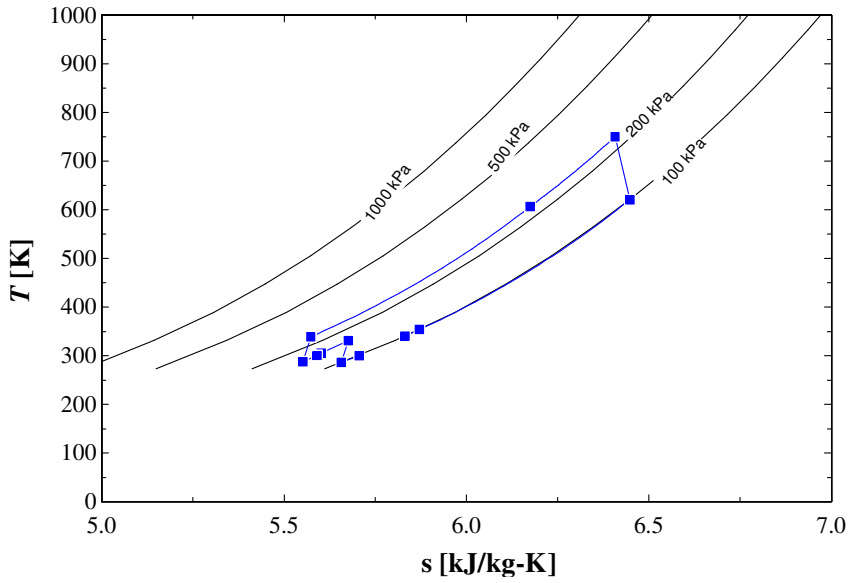

Figure 4.11: T-s diagram for Recuperation and Cooling system augmented CGT

The exergy flow diagram below shows the interaction between different systems.

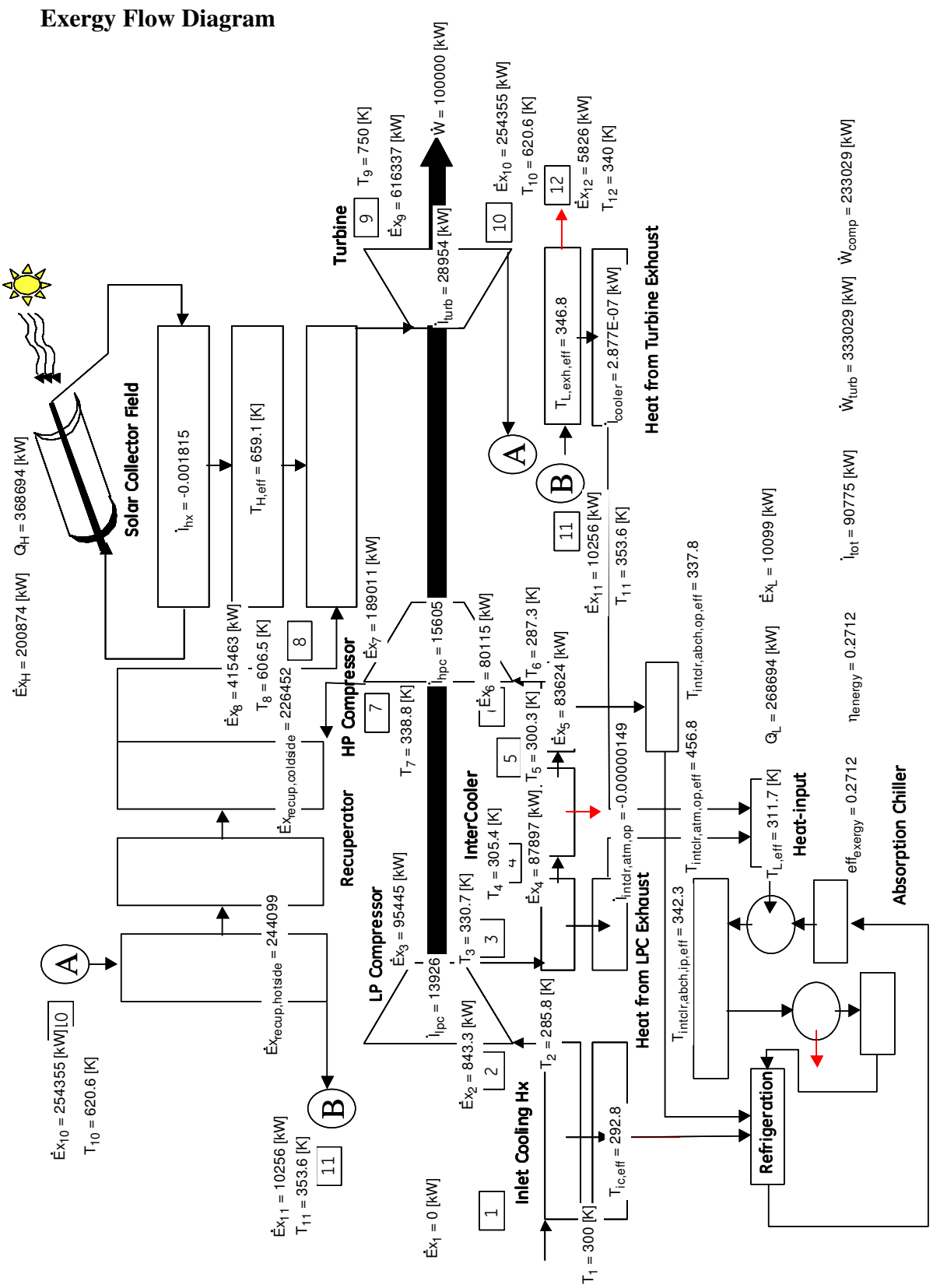

Figure 4.12: Exergy Flow Diagram for Recuperator and Cooling system augmented CGT

Recuperator and Cooling System Performance

The cooling system is required to bring down the compressor work. This advantage increases with higher pressure ratio as the turbine work increases. However, coupled with regeneration which favors a lower pressure ratio, the advantage of the cooling system was not realized and the overall system efficiency came down at the specified peak cycle temperature.

The Recuperator reduces the requirement on the solar heat-exchanger to raise the working fluid temperature. It also raises the effective temperature of heat addition, improving the overall quality of heat-addition. This performance is better at lower pressure. The cooling system will be able to lower the compressor discharge temperature which helps in making the recuperator perform more effectively and the overall system performance is improved. However, this phenomenon is observed at higher peak cycle temperatures as shown in Figure 4.13.

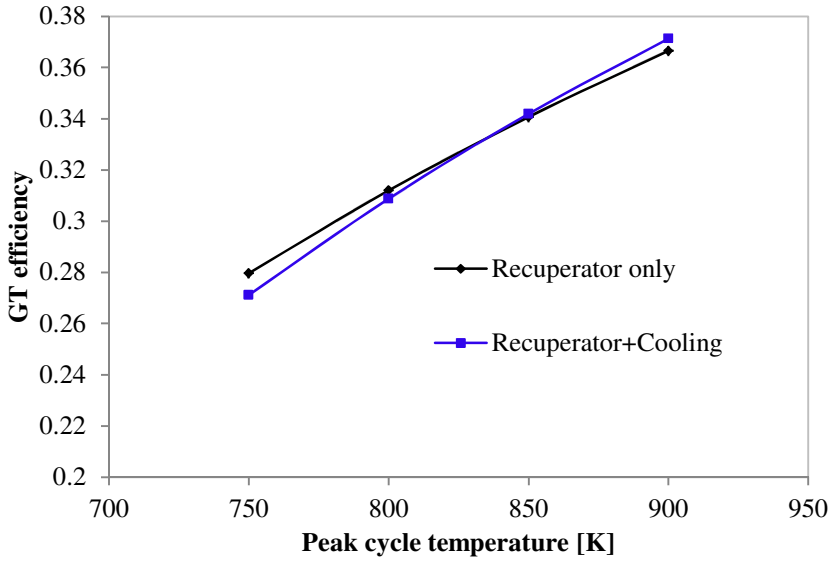

Figure 4.13: Comparison of Recuperator only system with Recuperator + Cooling system

Conclusion

The CGT as a concept is a good alternative to many existing solar energy conversion technologies. However, from thermodynamics point of view, the system has an upper limit on the maximum achievable power cycle efficiency. This is lower than the quoted efficiency of currently available power generation systems for large-scale power generation, and so is not a viable option for a solar energy based power-generation system using parabolic trough solar collector system technology. The proposed configuration will become viable with the increase in maximum achievable temperature for the power cycle. As the GT efficiency falls below the current industry standards for the steam turbine based power generation system, the economic analysis for this configuration was not performed. For future efforts, concepts like inverse Brayton cycle can be explored or alternate working fluid can be explored to make this configuration feasible.

CHAPTER 5

HIGH TEMPERATURE SOLAR GAS TURBINE

Introduction

This chapter presents the design, optimization and evaluation of high temperature solar gas turbine performance and economics. This chapter specifically illustrates the design process to optimize the performance of a high temperature solar gas turbine (HTSGT) power plant while meeting the challenges for operating a solar gas turbine at high temperatures and assesses the system performance within the design and operation constraints. There is good amount of literature and textbooks on the gas cycles (Dixon, 2005), but very few assessments done in the context of solar power generation considering realistic operational constraints and compatibility with technologies like TES and the associated economics. The aim of the chapter is to develop an economically optimum conceptual design of a gas turbine that is compatible with a high temperature Central Receiver Power Tower (CRPT) and thermal energy storage (TES). The performance model is evolved from a basic Brayton cycle and augmented with sub-systems such as intercooler and recuperator to assess the impact on performance. The later sections of the chapter will also provide a comparative analysis of the HTSGT model with the gas-fired Brayton cycle and helium based closed-loop Brayton cycle to assess the HTSGT cycle against the current industry standards and future trends in power generation.

Central Receiver Power Tower System

The power tower arrangement consists of a large array of double-axis sun-tracking heliostats on the ground, which reflect and concentrate the incident solar energy onto a central tower-mounted receiver. Figure 5.1 shows a typical power tower system.

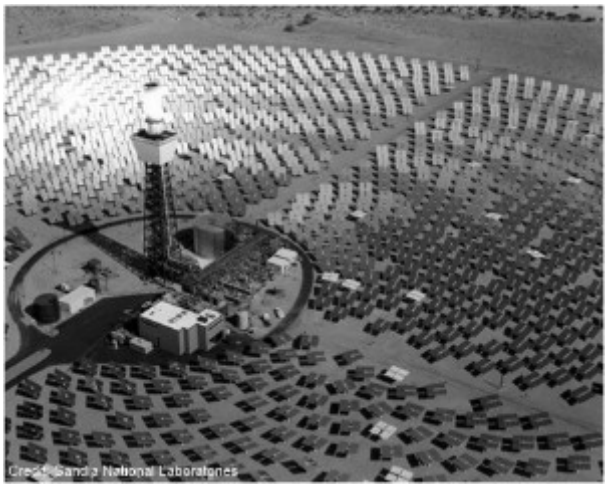

Figure 5.1: Solar Tower Concentration System (Source: www.solartowersystems.com)

The concentration ratio is typically about 800 (Sandia, 2011), with operating temperatures ranging from 500^{o} C to 800^{o} C (Garg, 2006). The working fluid is usually molten salt, synthetic oil, or liquid sodium.

The CSP technology can achieve very high temperatures (~1500^{o} C) and has better efficiency than PV solar cells. PV cells are getting cheaper but similarly are heliostats. So, CSP is more economical and furthermore, only CSP has the capability for thermal energy storage (EIA, 2010). Also, a larger area can be covered by using relatively inexpensive mirrors rather than using solar cells. There are two main challenges for this technology, firstly, the concentrating systems require sun tracking to maintain sunlight focus at the collector and secondly, power generation in diffused light conditions using thermal energy storage, which is often done by underground tank storage of heated fluids, like molten salts (Sargent & Lundy, 2003).

High Temperature Solar Gas Turbine Model

The discussion on solar energy conversion always revolves around the systems mentioned above. But the main focus of this chapter is to evaluate the performance of the gas turbine cycle with a high peak cycle temperature. The following section describes the thermodynamic cycle applicable to an HTSGT. At higher temperatures, the system

performance improves thermodynamically but the system cost will increase with superior materials required for sustaining performance in higher temperatures.

The HTSGT is evaluated as simple Brayton cycle and with sub-system augmentation like intercooler and recuperator are to estimate the system performance.

For the most complex system augmentation designed for the present effort, gas is compressed in an axial compressor with intercooling in a single or two stages followed by directing it through a recuperator for preheating before going to the cold end of the solar power conversion heat exchanger. The compressed gas absorbs the solar energy in the heat exchanger. This gas then enters the turbine and expands producing shaft power to drive the compressor(s) and the generator for electric energy production. The turbine exhaust then passes through a recuperator to preheat the compressed gas. Finally, the gas is exhausted, in an open cycle using air, to complete the cycle.

The design iteration of the system to achieve the best performance is executed in a sequential manner involving addition of subsystems to a simple cycle system to convert more of solar energy into electricity.

System Scale and Design Parameters

The HTSGT system is stipulated to be the most suitable for the low to medium power generation range. Therefore, the system has been designed for 100 MWe at 80 F (300 K) ambient temperatures and standard atmospheric pressure at sea-level of 100 kPa.

Solar Collector Field and Receiver Area

The solar collector system (heliostats and central receiver) sizing depends mainly on the required thermal power input to the power-block. The field and receiver area is a direct scaling of the thermal power input. The power tower height is also dependent on the

thermal power requirement, but is not a direct scale. The details of the CRPT model are represented in the system modeling chapter (Chapter 3).

Incident Solar Radiation and Energy to Receiver

The incident solar energy which is the source of all power generated by the plant, is dependent on the heliostat field area. This solar radiation varies continuously based on the time of the day and with seasons, so the system performance was calculated using SAM (System Advisory Model) based on hourly calculations for the year using tmy data. This data shows a direct correlation to the field area. The energy to receiver is the energy incident on the receiver from the heliostat field. This energy is in fact less than half the amount of solar energy incident on the field. The major portion of the energy is spent on multiple sources of losses (Wagner, 2008). The efficiency of heliostat field is derived based on the aggregate of the hourly variation of heliostat field efficiency in SAM for the entire year. It depends on the heliostat field layout and geographical location of the power plant site other than the optical properties of the mirror itself and is observed to remain invariant with changes in field size and receiver area and operating conditions.

Receiver Efficiency

The receiver operates as a heat exchanger with the HTF acting as the working fluid and absorbing the heat incident on the receiver surface based on its temperature at the inlet and the exit. The HTF itself loses some amount of this heat due to different modes of heat loss. These losses are represented by the receiver efficiency which is calculated by data from SAM for different operating conditions of the receiver and a model of the receiver which evaluates the heat transfer across receiver panel accounting for the different modes of heat loss. Figure 5.2 shows the different modes of heat loss from the receiver. The details of the modeling are discussed in chapter 3.

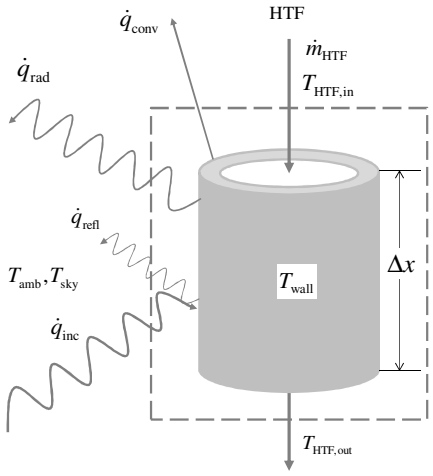

Figure 5.2: Receiver Model Schematic

Gas Turbine System

The system efficiency is calculated for an assumed constant compressor and turbine efficiencies of 0.86 and 0.85 respectively based on the system performance for a 6FA gas turbine unit (Jay, 1996). The heat exchangers have been designed for an effectiveness of 95% and pressure loss at 2% of the heat-exchanger pressure based on the heat exchanger design results for MPBR (Chunyun, 2003).

The design iteration is carried out with two critical design variables – overall system pressure ratio and peak cycle temperature. The overall system pressure ratio is the ratio of peak cycle pressure to the GT inlet pressure. For a system with multiple compressors, it is the product of individual pressure ratios. The peak cycle temperature is the peak temperature attained in the solar collector field. The turbine inlet temperature, which is the most critical design parameter for the GT, is lower than the peak cycle temperature due to heat transfer from the solar collector field to the GT working fluid in a heat exchanger with finite surface area.

System Cost Calculation

Power plant system performance cannot be assessed in isolation to arrive at the optimum configuration. Cost of the system is an important aspect of the system design. The costs of the different sub-systems in the power block depend majorly on the volume they occupy or the volume of flow of different fluids that they must accommodate. Empirical data is used to determine the size and cost of these sub-systems, mainly the GT and the Heat-exchangers. Operations and Maintenance (O & M) costs of the power plant depend on numerous factors like labor, parts replacement, heliostat mirror wash etc. This cost is determined mainly on the basis of rated capacity of the system. For the present analysis, a maintenance cost of 65 $/kW-yr is assumed based on power tower CSP technology cost forecast (Craig, 2010). This assumption will lead to same O & M cost for all configurations as the rated capacity is same for all. After determining the capital expenditure for the entire power-plant and its O & M cost, Life cycle cost analysis is performed for the chosen economic scenario and annualized cost of the system is determined. The details of the cost calculation for individual components are presented in the section on system modeling (Chapter 3).

The economic scenario considered for life cycle cost assessment involves three economic parameters, the discount rate, the general rate of inflation and the economic life of the plant. The annualized cost of the system is computed considering the discount rate at 7.5%, general inflation at 2.5% and a planning period of 30 years based on the NREL estimates for power tower system costs in US market (Craig, 2010). There are other factors affecting cost like contingencies, indirect costs, income tax, insurance, loan, income tax credit. These factors have not been incorporated into the model as they require more detailed and complex calculations which are beyond the scope of this study. The annual system cost and the annual electricity generation together determine the unit

cost of electricity for the system. The unit cost of electricity determines the economic feasibility of a system to justify its design and operation.

The system performance is represented in terms of the critical parameters like system efficiency, solar field area and HTF temperature etc. The calculations for different aspects of the design are represented by means of a block diagram. The calculation for a representative case is presented in Table 1. The performance trends for each of the critical parameters are then presented to draw inferences.

The main intent of the chapter is to assess how much electrical energy is produced for a given design and what is the cost incurred in its production and based on the assessment, determine the optimum design condition. The following sections describe the system performance for various design configurations considered and determination of the optimum design configuration overall.

System Design Assessment

The assessment of the system is being performed to estimate the economy of generating electricity using a GT from solar energy for a particular design configuration. The calculation procedure for simple cycle configuration is depicted in a block diagram in Figure 5.3.

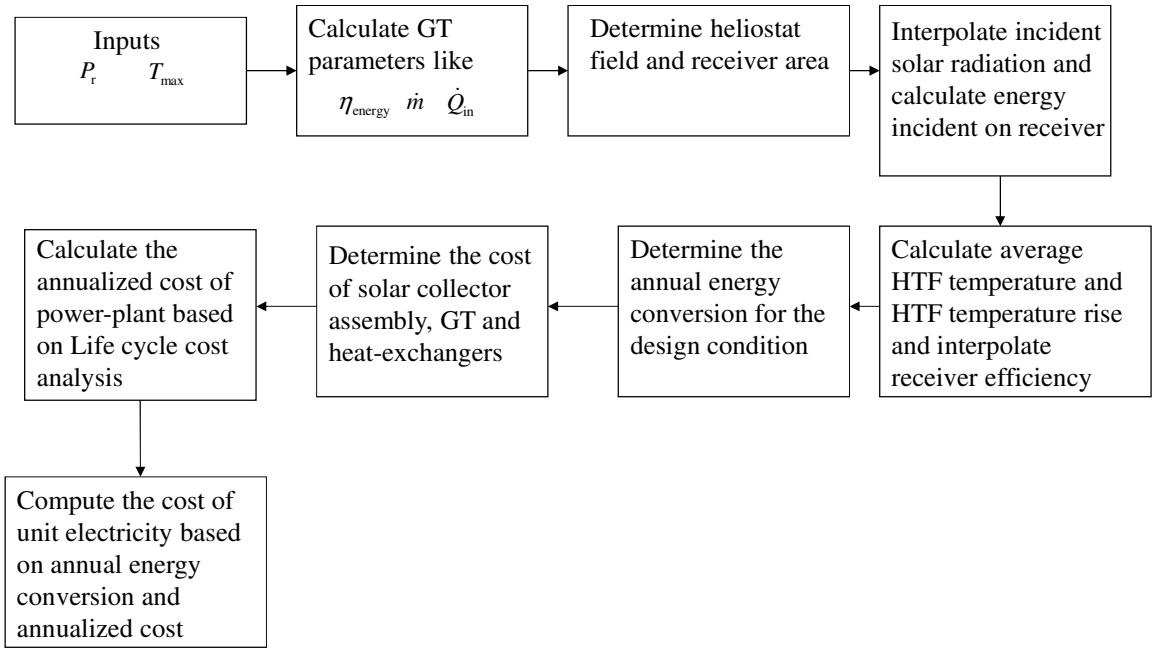

Figure 5.3: Process Map for System Performance Calculation- Simple Cycle

The GT pressure ratio and peak cycle temperature (turbine inlet temperature) characterize the GT system's thermodynamic cycle (Frank, 2000). The thermodynamic cycle determines the GT performance and size, which determines the sizing of the rest of the systems in the power plant and the associated cost. So, all the system parameters mentioned in the section above are assessed as dependent parameters for the variation in GT overall pressure ratio and turbine inlet temperature. The gas cycle efficiency indicates the thermodynamic performance of the power block. The mass-flow rate of working fluid aids in determining the size of gas turbine and heat exchangers associated with the gas turbine. The largest and most expensive system is the solar collector system (heliostat field and central receiver). The cost of this sub-system is directly related to the area it

occupies. The area of solar field and the receiver surface area are dependent on the thermal power input to power block operating at its full capacity (design condition). The thermal power input is determined based on GT system efficiency.

The solar collector field area directly determines the amount of solar energy incident on the heliostat field. Based on the efficiency of the heliostat field, the amount of energy incident on the receiver can be determined. The gas cycle calculations help determine the average HTF temperature and the temperature rise in the HTF. These parameters are used to obtain the receiver efficiency based on the compilation of hourly data for receiver performance under different operating conditions. This determines the energy input to power block after accounting for receiver losses. The GT system efficiency finally determines the amount of energy converted to electricity annually. Figure 5.4 shows flow of energy through various sub-systems of the power-plant to generate electricity and the efficiencies of different systems involved as described above.

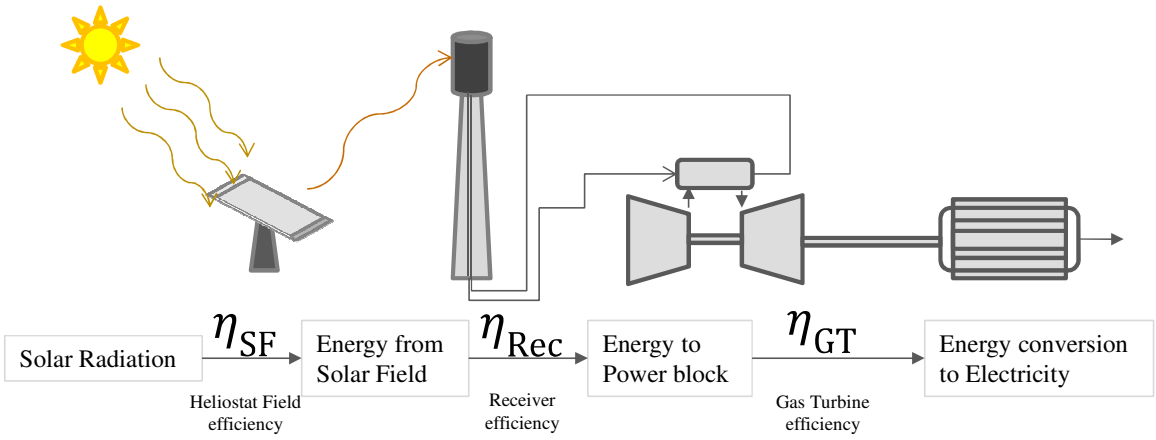

Figure 5.4: Flow of Energy through power plant and various efficiencies involved

The next step is to determine the capital expenditure for the entire power-plant based on its individual component cost estimation. The annualized life-cycle cost of the power plant is then determined using the capital expenditure and the O&M cost. The unit cost of electricity is calculated based on the annualized life cycle cost for the total annual energy conversion. The following section describes the performance trends for each design

configuration assessed and the trends for each of the system parameters for all design configurations.

Results: Simple Cycle

The simple cycle is the most basic of all the configurations assessed. The power block comprises of a GT and a solar heat exchanger. The EES model calculates the system performance for each design point characterized by overall pressure ratio and peak cycle temperature. The calculation procedure is depicted in a block diagram in Figure 5.3.

Table 5.1: Power-plant system parameters for a representative operating condition (represented to three significant digits)

System Parameters	T_{max} = 1200 [K] P_r = 10
GT System Efficiency [%]	28
Mass-flow rate [kg/s]	553
Thermal Power Input [MW]	360
Solar Collector Field Area [m^2]	715000
Receiver Surface Area [m^2]	521
Tower Height [m]	170
Incident Solar Radiation [GWh]	1800
Energy to Receiver [GWh]	793
Average HTF Temperature [K]	942
HTF Temperature Rise [K]	576
Receiver Efficiency [%]	85.1
Energy to Power-block [GWh]	641
Energy Converted to Electricity [GWh]	180
Solar Collector System Capital Cost [$/kW]	1800
GT System Capital Cost [$/kW]	438
Heat Exchanger Capital Cost [$/kW]	7
Power-plant Capital Cost [$/kW]	2240
Annualized Life-cycle Cost [$Million]	21
Annual O&M Cost [$Million]	6.5
Unit Electricity Cost [¢/kWh]	11.8

The performance trend for the key system parameters is shown in Figure 5.5. The simple cycle GT efficiency increases with increase in peak cycle temperature. For a given peak

cycle temperature, the GT efficiency initially raises then falls with increase in GT overall pressure ratio.

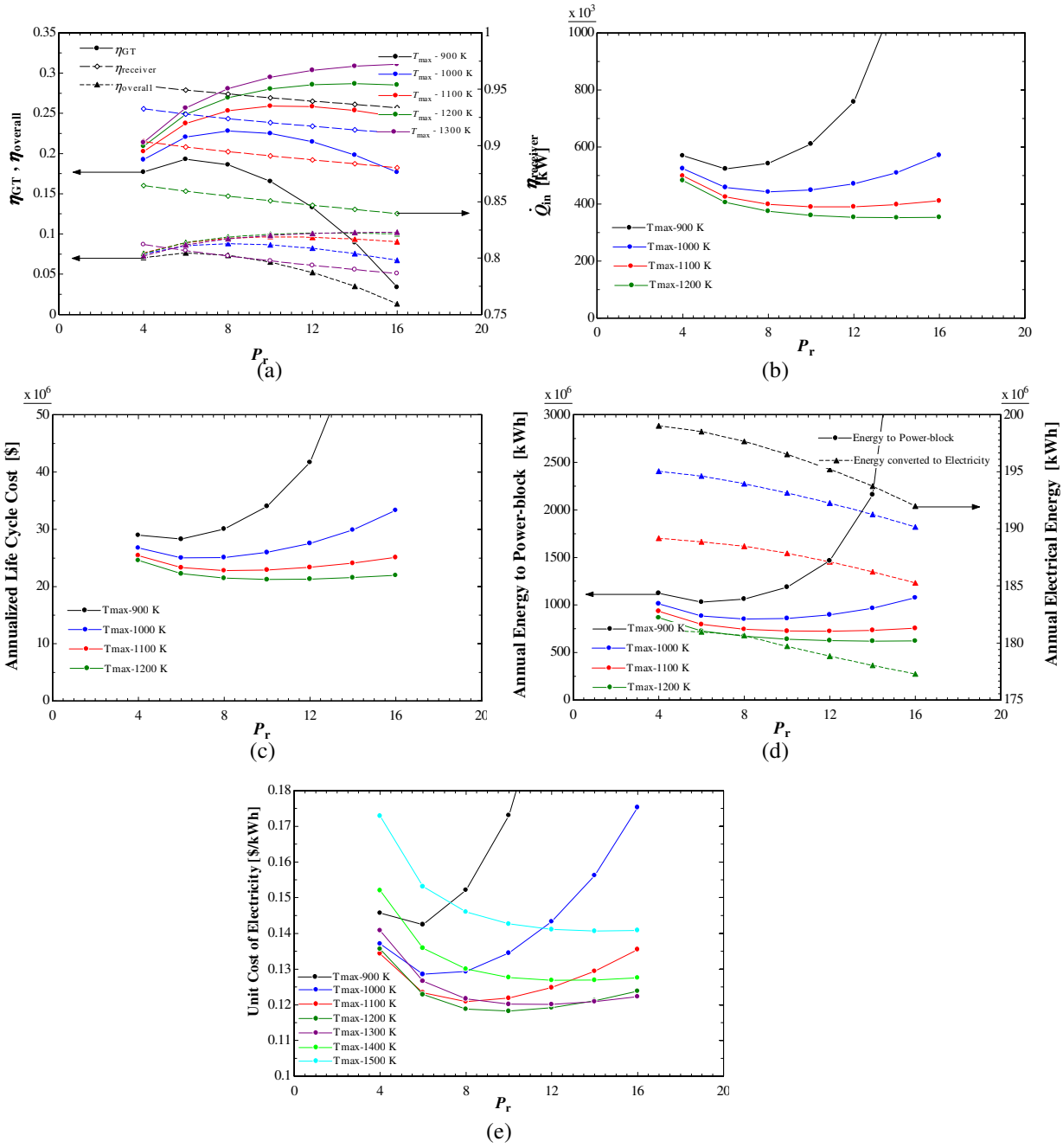

Figure 5.5: Power plant system performance in terms of key design parameters: (a) *System efficiency*, (b) *Thermal power input*, (c) *Annualized life-cycle cost*, (d) *Annual electricity generation* and (e) *Unit cost of electricity* - Simple Cycle

The required thermal power input is the inverse of the GT system efficiency and as the design power output is fixed, the trend shows the inverse relation when Figure 5a is

compared to Figure 5b. At higher pressure ratio and peak cycle temperature, the thermal power requirement reduces. The variation is more sensitive to change in peak cycle temperature.

The solar collector system size and consequently cost is directly proportional to design thermal power input. This is the largest sub-system of the power plant and hence has the maximum impact on the life-cycle cost which looks very similar in trend as the design thermal power input.

The simple cycle configuration has higher efficiency at high peak cycle temperature and pressure ratio. However, the overall energy conversion depends on both, GT and solar collector system efficiency as well as the solar collector field area. Figure 5d shows the annual energy conversion variation with peak cycle temperature and pressure ratio. Ideally, as the solar field area is determined on the basis of GT efficiency, the energy conversion should be same for all configurations. However, the energy conversion varies with configuration. It reduces with increase in peak cycle temperature. This is due to reduction in solar collector efficiency for higher peak temperature. For a particular peak cycle temperature, the temperature rise reduces for the HTF with increasing pressure ratio, which reduces the receiver efficiency and consequently the energy conversion. The peak overall efficiency reaches to about 10% of the incident solar radiation.

Figure 5e shows the variation in unit cost of electricity with peak cycle temperature and pressure ratio. The unit cost initially reduces then increases with increase in pressure ratio. The rate of increase is greater at lower peak cycle temperature. The optimum peak cycle temperature for the most economical simple cycle system is 1200 K and the optimum pressure ratio is 10. The minimum unit cost is 11.8 cents/kWh. As the peak cycle temperature increases, the lower GT efficiency combined with reduced receiver efficiency make the unit cost rise significantly for lower pressure ratio.

The efficiency predicted with minimum unit cost for simple cycle configuration is 28%.

The exergy flow diagram for the optimum configuration is depicted in Figure 6. An exergy flow diagram depicts the flow of exergy into and out of the system, as the working fluid passes through each component of the system changing its state following the gas cycle for which the system is designed. The exergy flow indicates the efficiency and effectiveness of different sub-systems and can be used to improve the system. For a simple cycle, the exergy flow diagram is simple. The exergy flows through the compressor into the solar heat exchanger and out of it into the turbine, from where it exits into the atmosphere. The exergy rises in the compressor due to the compression process. Then it increases significantly in the solar heat exchanger where the heat from the solar collector system is transferred to the working fluid. In the turbine section, the exergy drops down as the flow expands and imparts the exergy to turbine. The turbine drives the compressor with about two-third of the exergy it gained from the working fluid and utilizes the remaining one-third to drive the generator. The leftover exergy is spent to the atmosphere. Some amount of exergy is destroyed in the process inside the compressor and turbine due to their non-ideal operation. The exergy flow diagram for larger systems is more complex and requires much detailed observation.

Exergy Flow Diagram – Simple Cycle

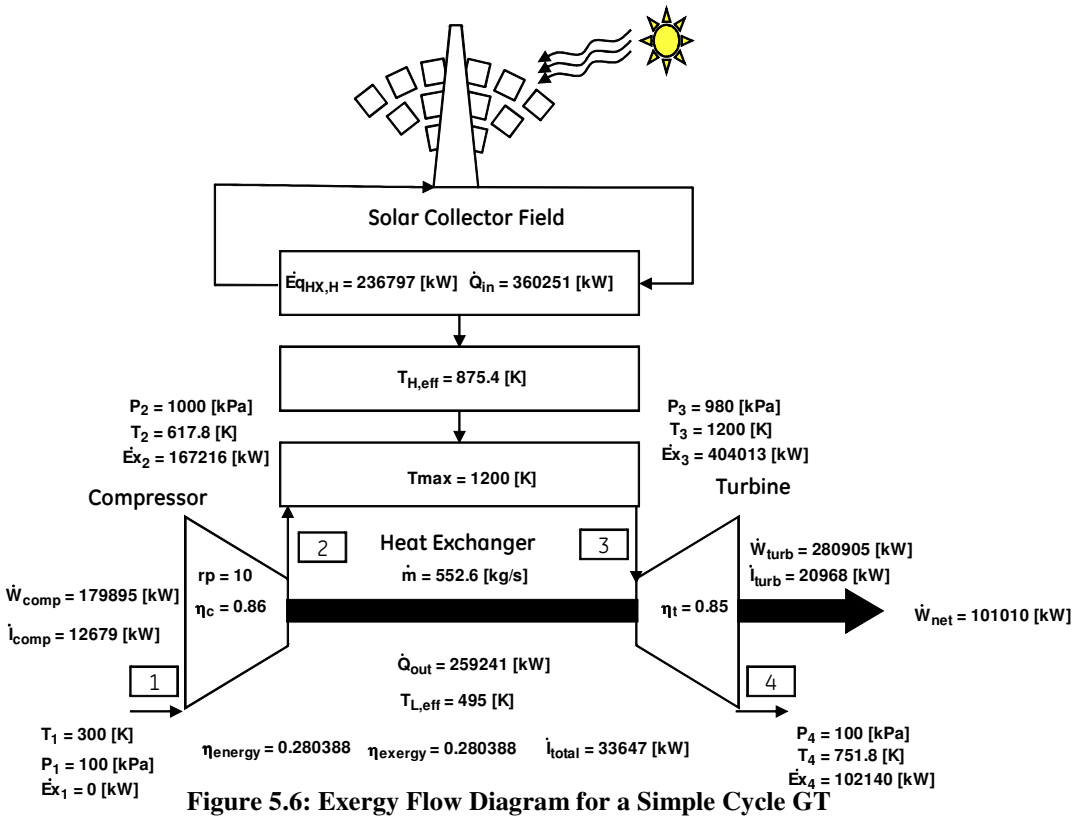

Figure 5.6: Exergy Flow Diagram for a Simple Cycle GT

Figure 5.7 shows the T-s diagram for one of the configurations. The diagram shows graphically how the working fluid changes its state while passing through the system to represent the gas cycle.

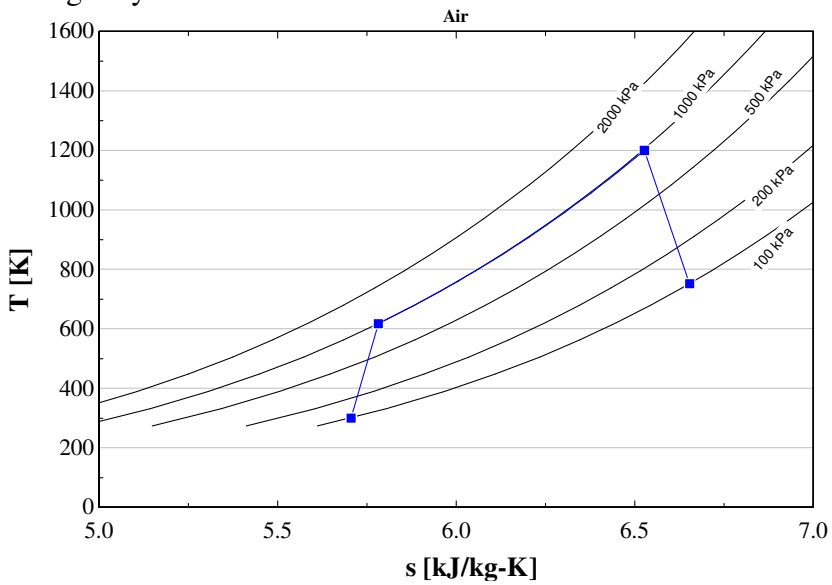

Figure 5.7: T-s Diagram for a Simple Cycle GT

Results: Intercooled HTSGT

The first augmentation to the simple cycle configuration is an intercooler (Figure 30). The intercooler aids in removing the heat generated in the compressor due to compression process. The high temperature of the fluid increases its specific volume and makes compression difficult and requires more effort to raise the pressure. Reducing the fluid temperature by intercooling reduces compressor work and more of turbine work can be used for power generation. Also, intercooling reduces the inlet temperature of the working fluid into the solar collector system which increases the amount of energy extracted from the solar collector field and lowers the effective temperature of heat input. Intercooling is effected by passing the compressed working fluid through a compact heat exchanger which has water as the cooling fluid. The amount of water pumped through the exchanger coldside and the exchanger effectiveness determine the degree of intercooling. The typical reduction in temperature achieved in an intercooler stage is of the order of 100 K. The heat exchanger is designed to maintain the pressure loss below 2% of heat exchanger inlet flow pressure based on the heat exchanger design results for MPBR (Chunyun, 2003).

Single stage Intercooler

Single stage intercooler has one intercooler and two compressors, a low pressure compressor and a high pressure compressor. The configuration is studied for system performance as illustrated in Figure 5.8.

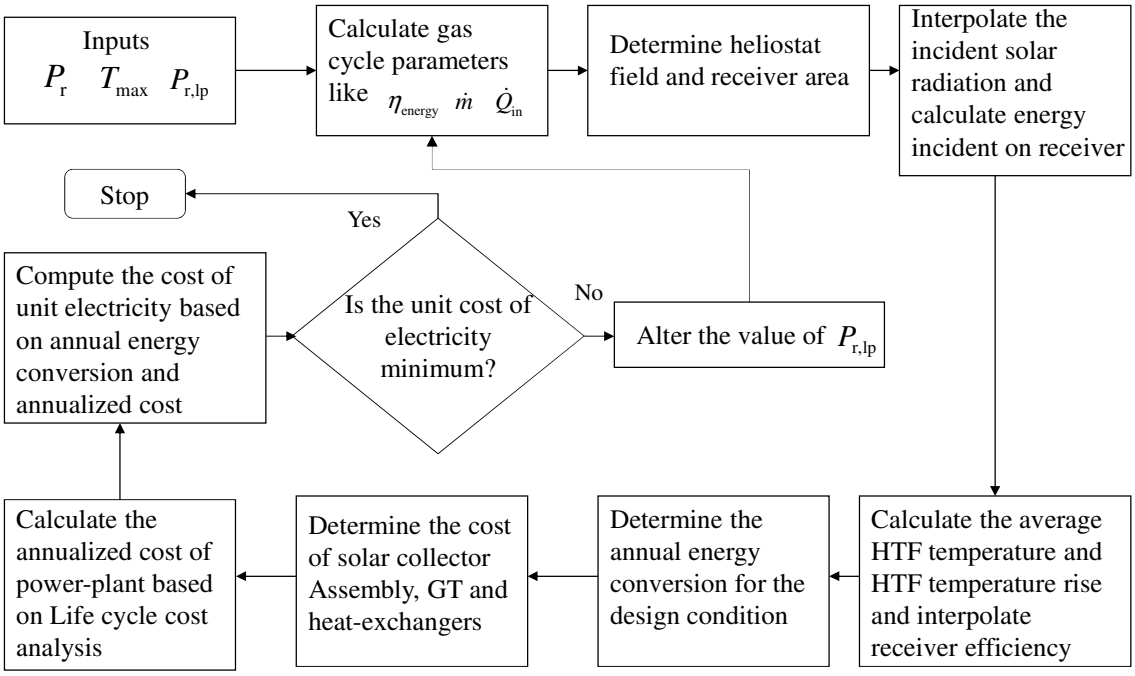

Figure 5.8: Process Map for System Performance Calculation-Single Stage Intercooler

Optimum LP compressor pressure ratio

The GT performance for a specific overall pressure ratio and peak cycle temperature varies with change in LP compressor pressure ratio. The LP compressor pressure ratio will determine the HP compressor's outlet temperature and the overall compressor work. Both these parameters affect the GT efficiency and annual energy conversion into electricity. Since the paramount quantity of interest is the economy of the power plant, the LP compressor pressure ratio is optimized for minimum cost of unit electricity. Figure 5.9 shows the GT system efficiency and receiver efficiency with single intercooling stage for varying LP compressor pressure ratio for a specific overall pressure ratio and peak cycle temperature. The GT efficiency peaks at about a LP pressure ratio of 2 whereas the receiver efficiency increases monotonously with higher LP compressor pressure ratio. This happens because as LP pressure ratio rises, the HP compressor outlet temperature reduces, which increases required specific heat input for power generation. Initially, the

rate of increase in specific heat input is lower than the rate of reduction in compressor work which increases GT efficiency, but for higher LP compressor pressure ratio, there is a very little gain in net work done by the system for an increase in heat input which lowers the GT efficiency.

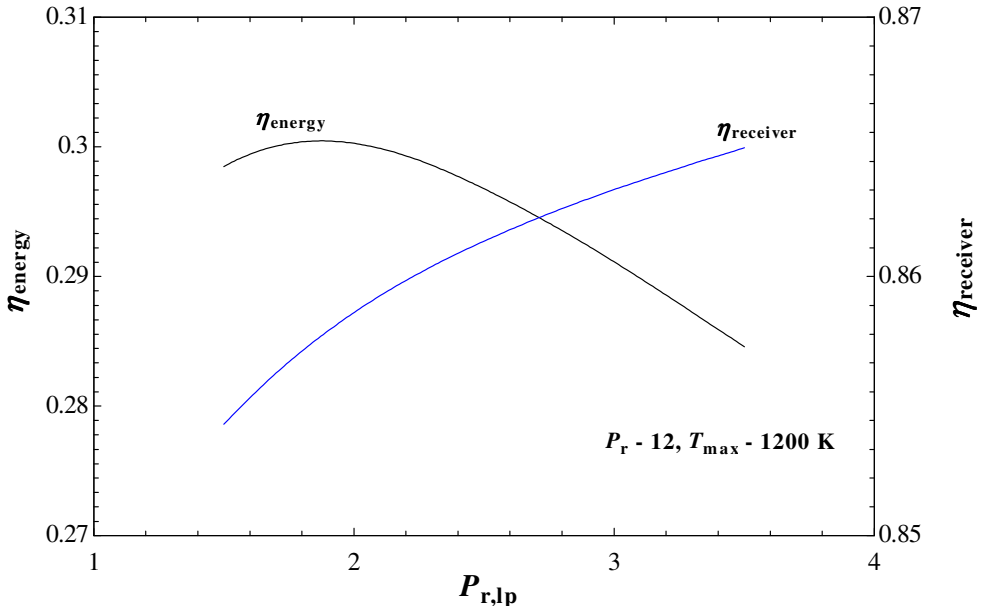

Figure 5.9: GT Efficiency and Receiver Efficiency variation with LP Compressor Pressure ratio- Single Stage Intercooler

With the reduction in HP compressor outlet temperature, the average HTF temperature reduces and the HTF temperature rise increases, both of which are favorable towards increasing the receiver efficiency. The GT efficiency decides the heliostat field area and so a major portion of the capital cost, whereas the receiver efficiency decides the amount of energy converted to electricity. Since, these parameters show opposing patterns, the optimum system configuration with minimum unit cost will be an intermediate point for the LP compressor pressure ratio as shown in Figure 5.10. The optimum LP compressor pressure ratio is computed for each operating point and the system assessment is performed at this LP pressure ratio.

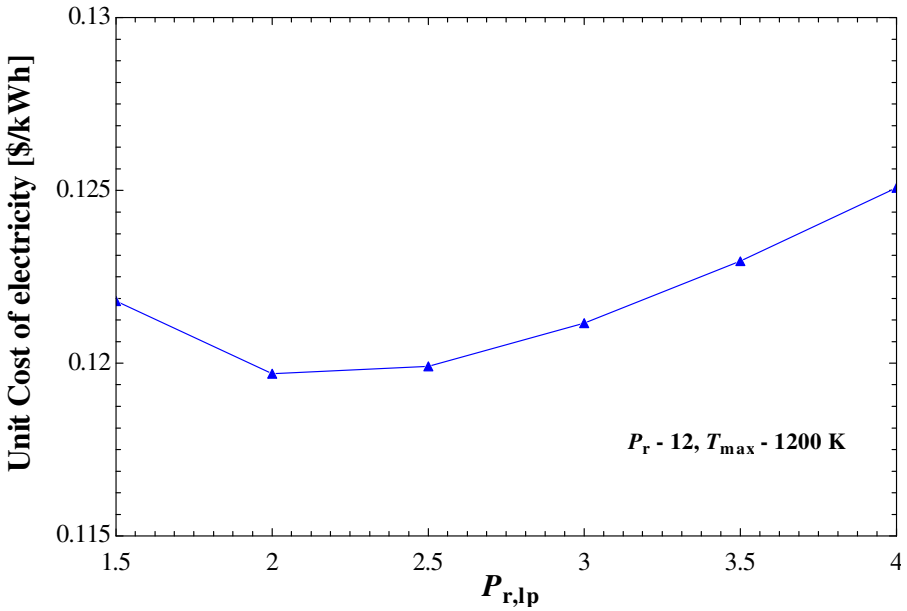

Figure 5.10: Optimum LP Compressor Pressure ratio variation with Overall Pressure ratio and Peak Cycle Temperature-Single Stage Intercooler

The design configuration is then analyzed with optimum LP compressor pressure ratio. The performance trend for the single stage intercooler augmented GT is shown in Figure 5.11. Compared to simple cycle configuration (Figure 5.5), the single stage intercooler gives higher GT efficiency for all peak cycle temperatures and pressure ratios. Also, for a given peak cycle temperature, the peak efficiency is attained at a higher pressure ratio. The peak GT efficiency is 31.4% at a peak cycle temperature of 1200 K, which is higher than simple cycle peak of 28%.

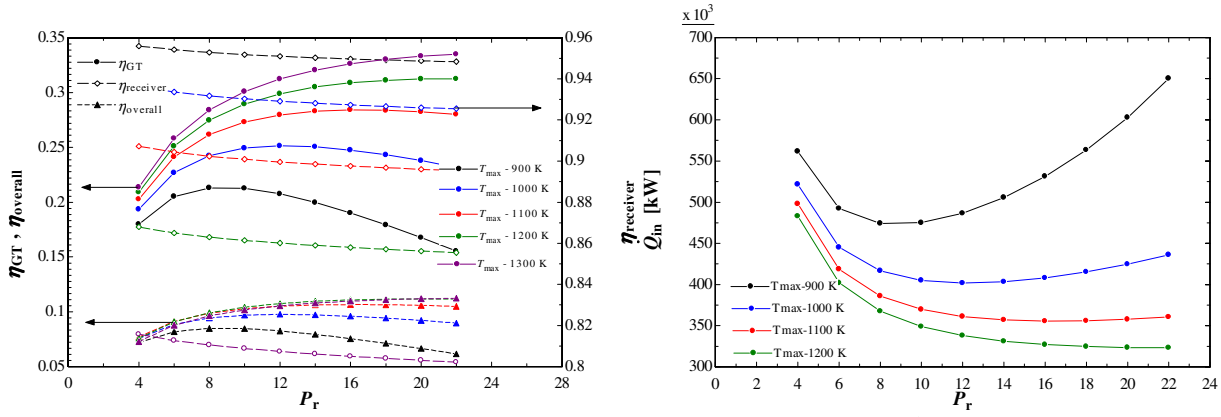

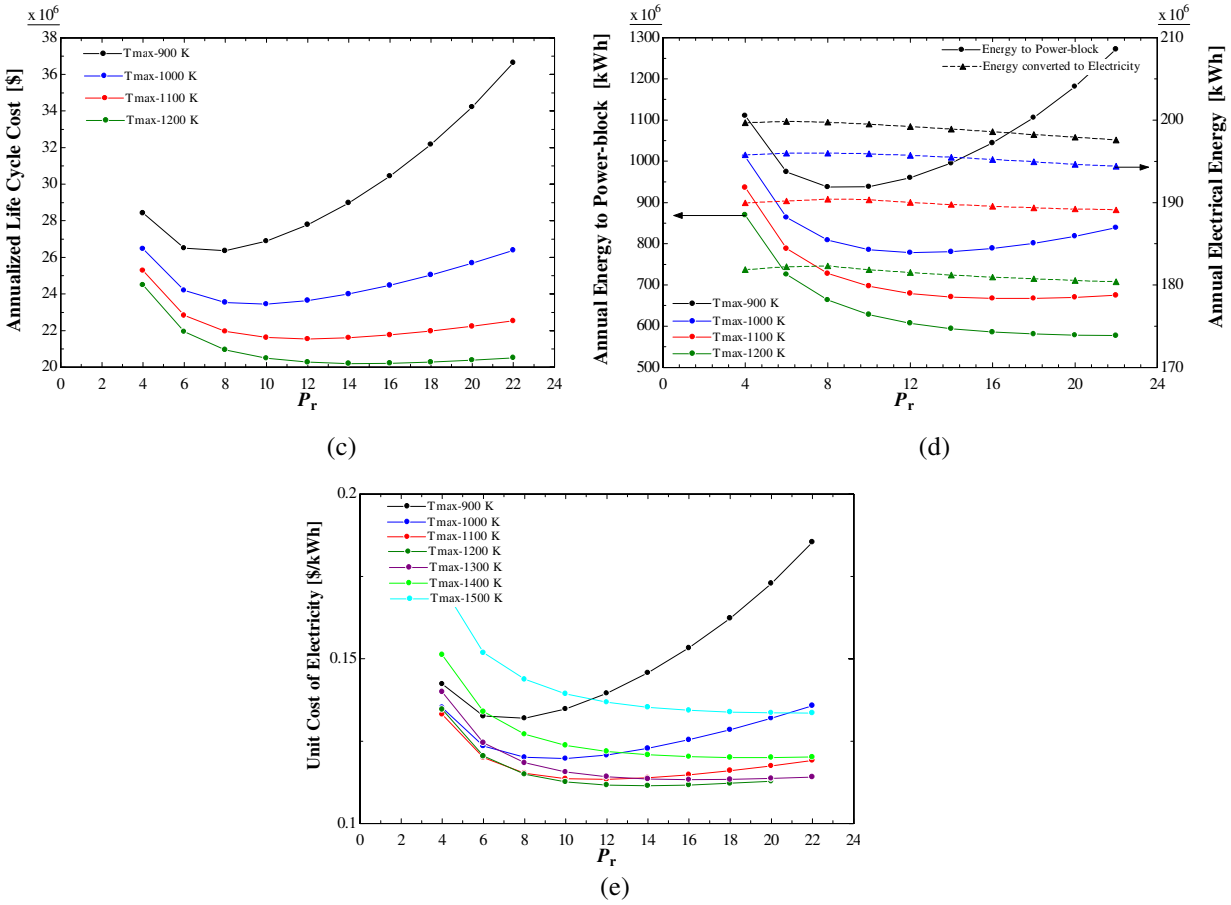

Figure 5.11: Power plant system performance in terms of key design parameters: (a) *System efficiency*, (b) *Thermal power input*, (c) *Annualized life-cycle cost*, (d) *Annual electricity generation* and (e) *Unit cost of electricity* - Single Stage Intercooler

The trend for required thermal power input is the inverse of the GT system efficiency as described in the case of simple cycle configuration. At higher pressure ratio and peak cycle temperature, the thermal power requirement reduces. The variation is more sensitive to change in peak cycle temperature at higher pressure ratio but at lower pressure ratio, the thermal power input changes more rapidly with pressure ratio than peak cycle temperature.

The life-cycle cost is almost the same trend as the thermal power input. However, at high pressure ratio, the life-cycle cost rises more rapidly than the thermal power input due to the increase in cost of other sub-systems compared to the solar collector system.

Figure 5.11d shows the amount of energy delivered to power-block and the electricity generated annually. The single stage intercooler has higher energy conversion compared to simple cycle configuration owing to higher receiver efficiency (Figure 5.5d). Also, for a particular peak cycle temperature, the energy conversion rate varies very little with overall pressure ratio.

Figure 5.11e shows the variation in unit cost of electricity with peak cycle temperature and pressure ratio. The trend is similar to simple cycle configuration. The optimum peak cycle temperature for the most economical simple cycle system is 1200 K and the optimum pressure ratio is 14. The minimum unit cost is 11.1 cents/kWh, which is lower than simple cycle configuration. Also, the trend for unit cost of electricity for peak cycle temperature of 1100 K and 1200 K at lower pressure ratio is almost identical. The efficiency predicted with minimum unit cost for single stage intercooler configuration is 30.5%.

The exergy flow diagram for the optimum configuration is depicted in Figure 5.12. The exergy flows through the LP compressor into the intercooler. Then it goes into the HP compressor followed by solar heat exchanger and out of it into the turbine, from where it exits into the atmosphere. The exergy rises in the LP compressor due to the compression process. Then the exergy reduces inside the intercooler as the heat is taken away from the working fluid. The flow the goes into the HP compressor where its exergy rises again. Then it increases significantly in the solar heat exchanger where the heat from the solar collector system is transferred to the working fluid. In the turbine section, the exergy drops down as the flow expands and imparts the exergy to turbine. The turbine drives the compressor with about 40% of the exergy it gained from the working fluid and utilizes the remaining 30% to drive the generator. The leftover exergy is spent to the atmosphere. Some amount of exergy is destroyed in the process inside the compressor and turbine due to their non-ideal operation.

Exergy Flow Diagram – Single stage Intercooler

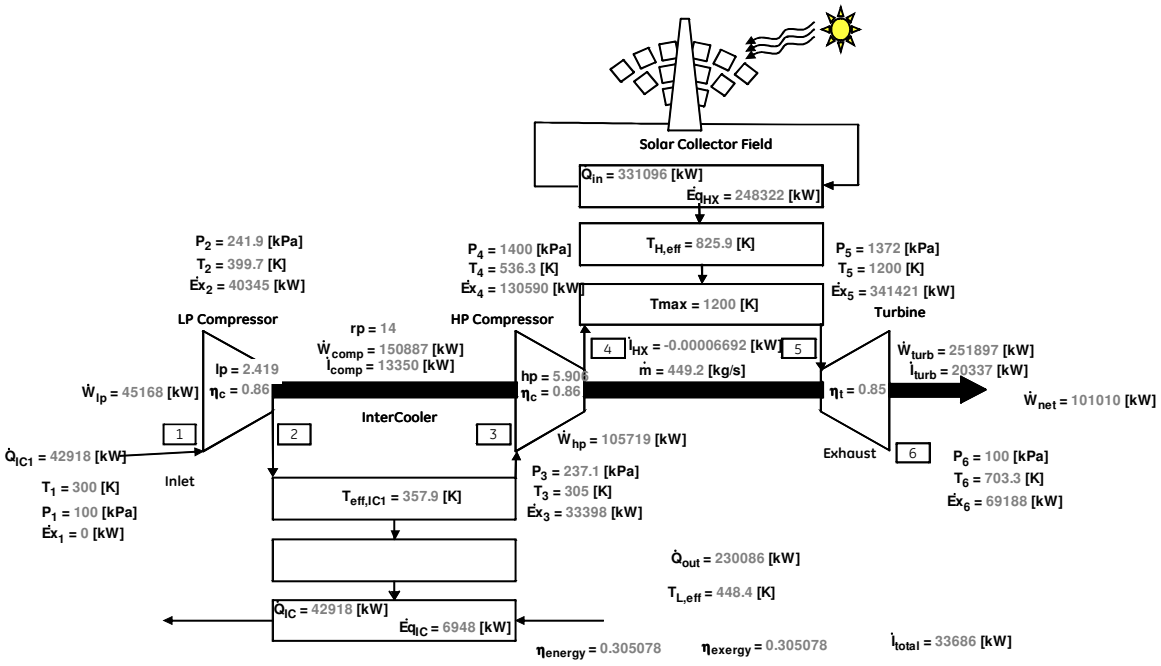

Figure 5.12: Exergy Flow Diagram for a Single stage Intercooled GT

The T-s diagram for the configuration is plotted in Figure 5.13. The temperature rise shown in the figure below is greater than the temperature rise in a simple cycle configuration. Such high temperature difference is challenging for the present thermal energy storage technology which works best with a 200 K to 300 K temperature difference.

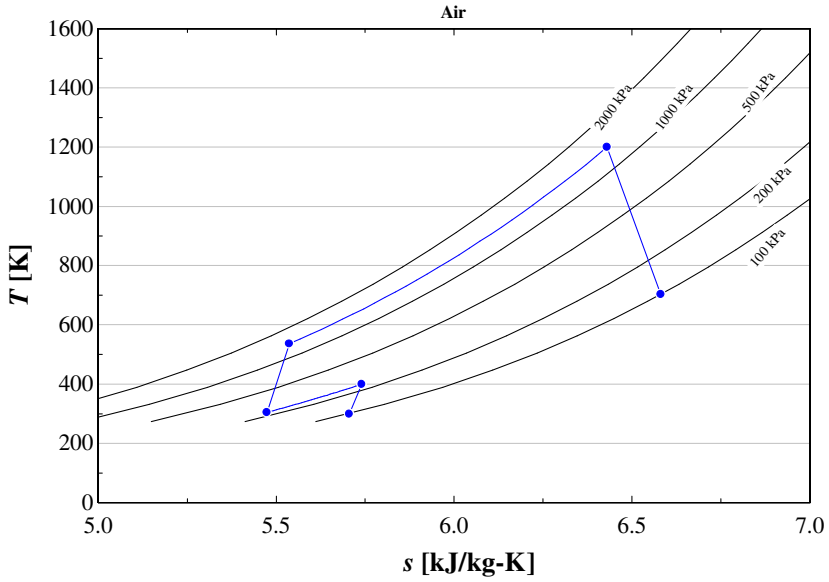

Figure 5.13: T-s Diagram for a Single stage Intercooled GT

Two stage Intercooler

Intercooling can also be done in multiple stages as well. The purpose is to reduce compressor work for attaining higher pressure ratio. The advantage of two intercooling stages, however, needs to be assessed for its viability.

Two stage intercooler augmented system has two intercoolers and three compressors, a low pressure (LP) compressor, an intermediate pressure (IP) compressor and a high pressure (HP) compressor. The configuration is studied for system performance as illustrated in Figure 5.14.

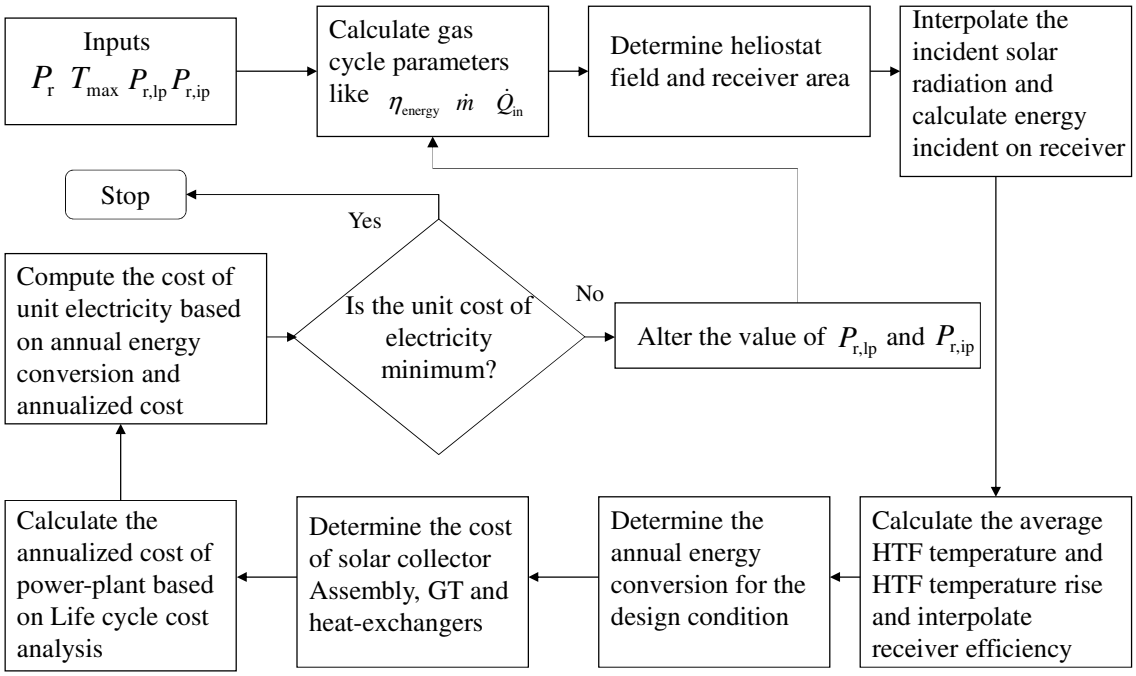

Figure 5.14: Process Map for System Performance Calculation-Two Stage Intercooler

Optimum LP compressor and IP compressor pressure ratio

As with the single stage intercooler, the GT performance for a specific overall pressure ratio and peak cycle temperature varies with change in LP and IP compressor pressure ratio. The LP and IP compressor pressure ratio determine the HP compressor's outlet temperature and the overall compressor work, both of which affect the GT efficiency and annual energy conversion into electricity. Again, the LP and IP compressor pressure

ratios are optimized for minimum cost of unit electricity. Figure 5.15 shows the GT system efficiency and receiver efficiency with two stage intercooler for varying LP and IP compressor pressure ratio for a specific overall pressure ratio and peak cycle temperature. A similar trend is observed compared to single stage intercooling, wherein the GT efficiency rises and falls whereas the receiver efficiency increases monotonously with increase in LP and IP compressor pressure ratio. The reason for this trend is also same as for the single stage intercooler. As the LP and IP pressure ratios rise, the HP compressor outlet temperature reduces, which increases required specific heat input for power generation. Initially, the rate of increase in specific heat input is lower than the rate of reduction in compressor work which increases GT efficiency, but for higher LP and IP compressor pressure ratio, there is a very little gain in net work done by the system for an increase in heat input which lowers the GT efficiency.

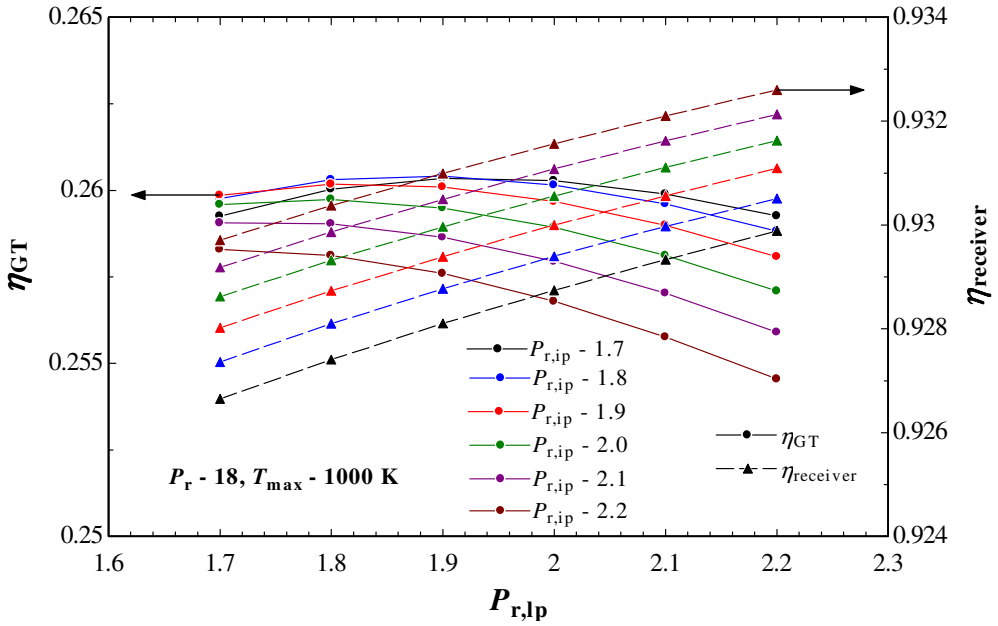

Figure 5.15: GT Efficiency and Receiver Efficiency variation with LP Compressor Pressure ratio- Two Stage Intercooler

With the reduction in HP compressor outlet temperature, the average HTF temperature reduces and the HTF temperature rise increases, both of which are favorable towards increasing the receiver efficiency. Both GT efficiency and receiver efficiency are

favorable to reduction in cost. Since, these parameters show opposing patterns, the optimum system configuration with minimum unit cost will be an intermediate point for the LP and IP compressor pressure ratio as shown in Figure 16. The optimum LP and IP compressor pressure ratios are computed for each operating point and the system assessment is performed at these LP and IP pressure ratios.

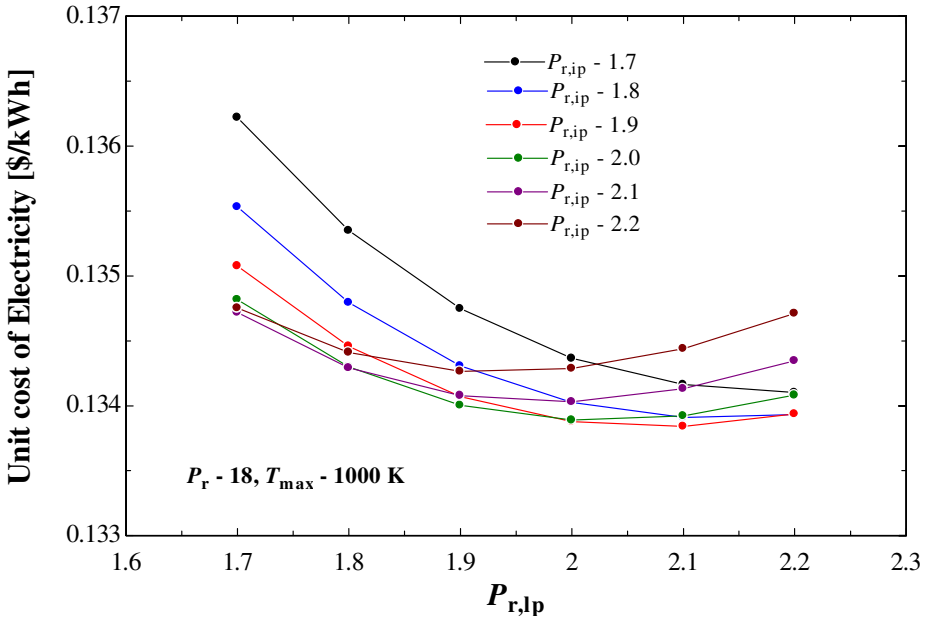

Figure 5.16: Optimum LP Compressor Pressure ratio variation with Overall Pressure ratio and Peak Cycle Temperature- Two Stage Intercooler

Figure 5.17 shows the performance trend for the two stage intercooler. Compared to single stage intercooler configuration (Figure 5.11a), the two stage intercooler gives marginally higher GT efficiency. Also, for a given peak cycle temperature, the peak efficiency is attained at a higher pressure ratio. The peak GT efficiency is 32.4% at a peak cycle temperature of 1200 K, which is slightly higher than single stage intercooler configuration peak of 31.4%.

The thermal power input shown in Figure 17b is similar in trend to the single stage intercooler. The second intercooler stage had a larger impact at lower pressure ratio in improving GT efficiency and so the corresponding reduction in thermal power input is seen at lower pressure ratio.

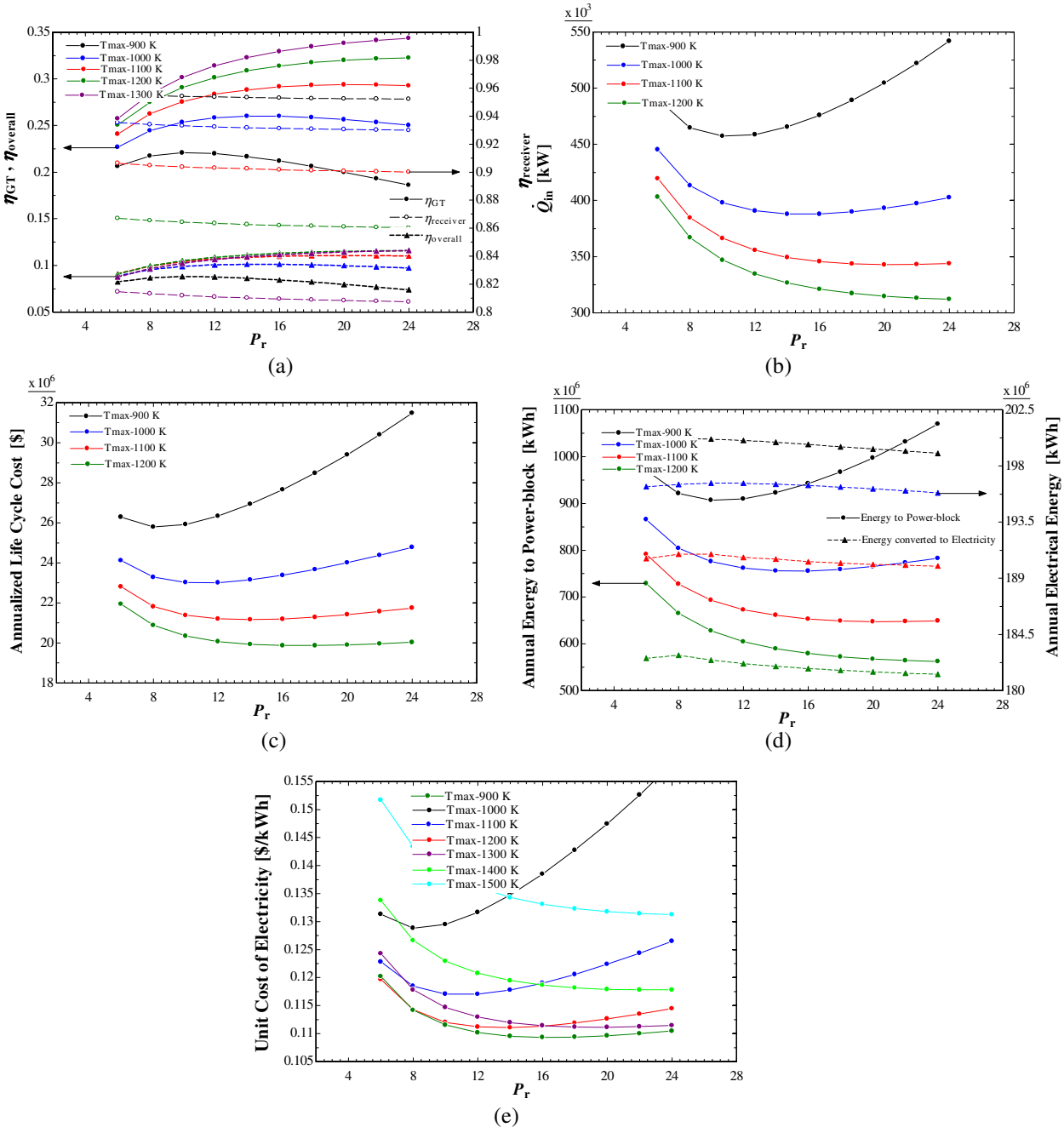

Figure 5.17: Power plant system performance in terms of key design parameters: (a) *System efficiency*, (b) *Thermal power input*, (c) *Annualized life-cycle cost*, (d) *Annual electricity generation* and (e) *Unit cost of electricity* – Two stage Intercooler

The life-cycle cost is similar in trend to the single stage intercooler. The life-cycle cost shows very little variation with change in operating conditions at high pressure ratio and peak cycle temperature.

Figure 5.17d shows the amount of energy delivered to power-block and the electricity generated annually. The two stage intercooler has almost the same annual energy conversion compared to single intercooler configuration (Figure 5.11d).

The optimum peak cycle temperature for the most economical simple cycle system is 1200 K and the optimum pressure ratio is 16. The minimum unit cost is 10.9 cents/kWh as seen in Figure 5.17e, which is slightly lower than single stage intercooler configuration.

The efficiency predicted with minimum unit cost for two stage intercooler configuration is 31.4%.

The exergy flow diagram for the optimum configuration is depicted in Figure 5.18.

Exergy Flow Diagram – Two stage Intercooler

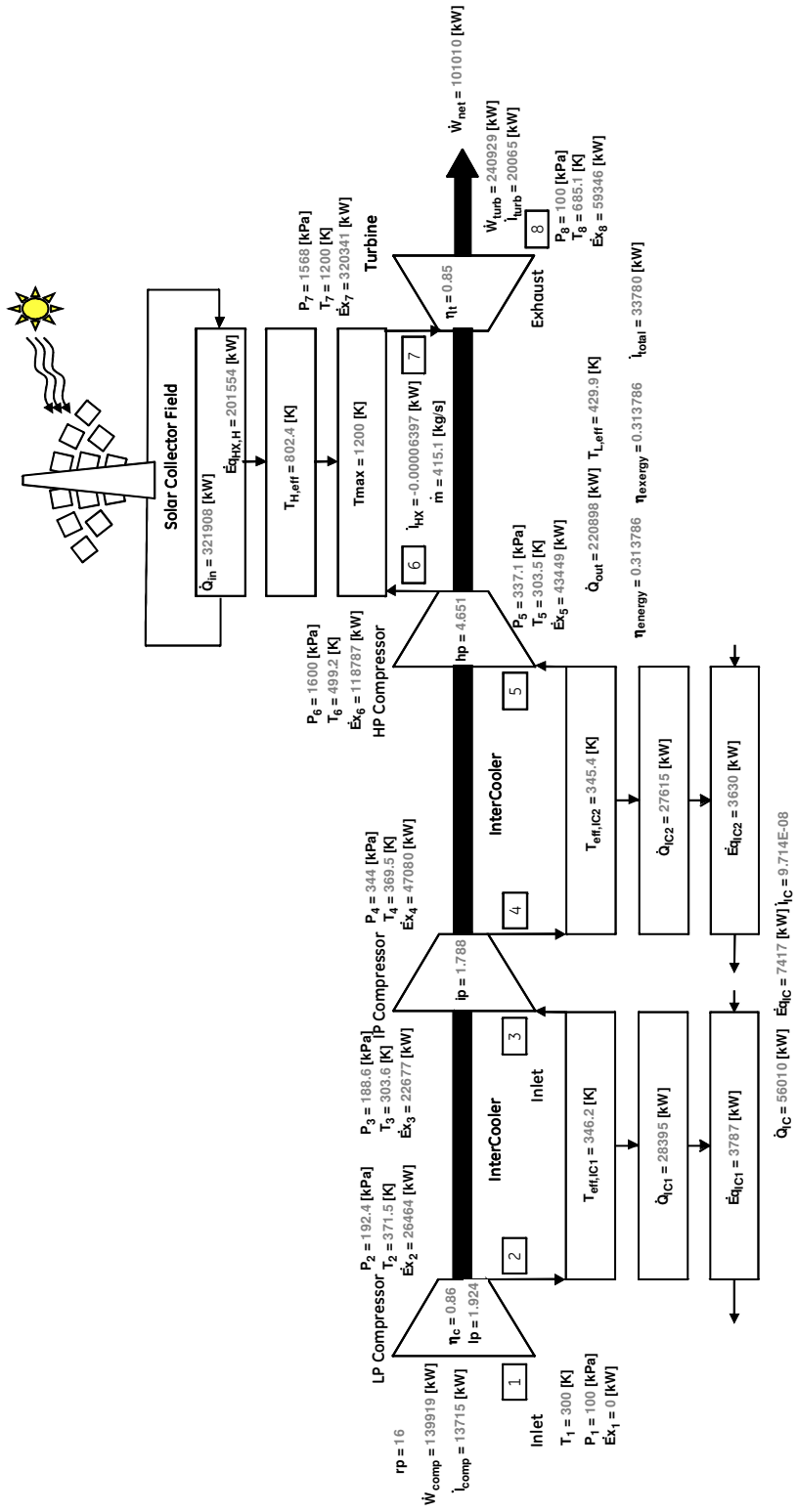

Figure 5.18: Exergy Flow Diagram for a Two stage Intercooled GT

The T-s diagram for the configuration is plotted in Figure 5.19. The temperature rise shown in the figure below is similar to the temperature rise in a single stage configuration.

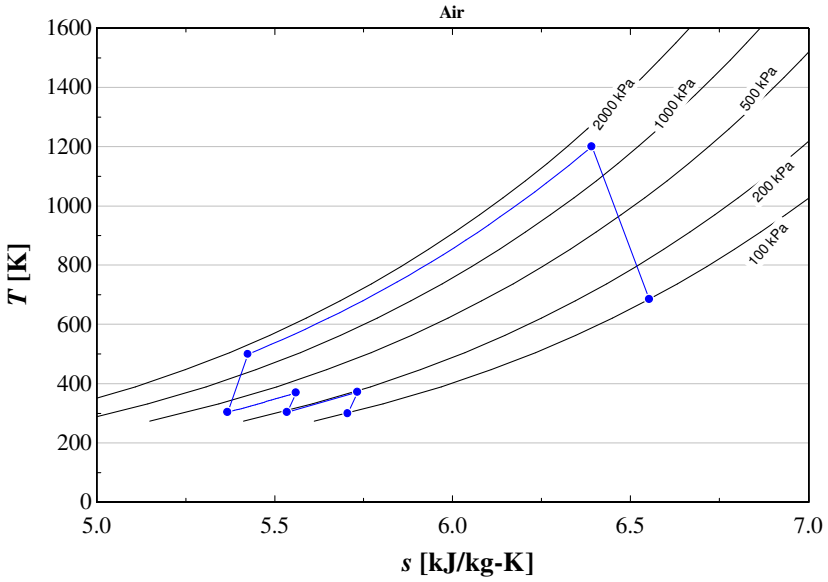

Figure 5.19: T-s Diagram for a Two stage Intercooled GT

Results: Recuperated HTSGT

The next augmentation which is one of the most common systems is the recuperator. The recuperator is expected to not only increase the system efficiency but also increase the effective temperature of heat transfer from the solar heat exchanger.

Recuperator

The temperature of the exhaust gases at the turbine exit is typically higher than the gas temperature at heat-exchanger inlet. This indicates a loss of potential heat source with degraded performance. A recuperator is a special purpose counter-flow energy recovery heat exchanger used to recover waste heat from exhaust gases. This system acts to bring up the gas temperature at heat-exchanger inlet causing less intake of solar heat per unit mass, correspondingly, the exhaust temperature of the gas vented into the atmosphere comes down leading to lesser wastage of useful heat. The performance of the recuperator is estimated in terms of how close the temperature rise was to the turbine exhaust temperature. The typical range of effectiveness is at 85-95%. Also, the flow through the recuperator, incurs a pressure loss across the heat transfer surfaces in the order of 2-5% based on the heat-exchanger design.

For a particular peak cycle temperature, a lower pressure ratio reduces the compressor discharge temperature and increases the turbine exhaust temperature. So the recuperator performs better at lower pressure ratio.

In the current system, the recuperator has been designed for an effectiveness of 95% and pressure loss at 2% of the heat-exchanger inlet flow pressure based on the heat exchanger design results for MPBR (Chunyun, 2003)..The configuration is studied for system performance as illustrated in Figure 5.20.

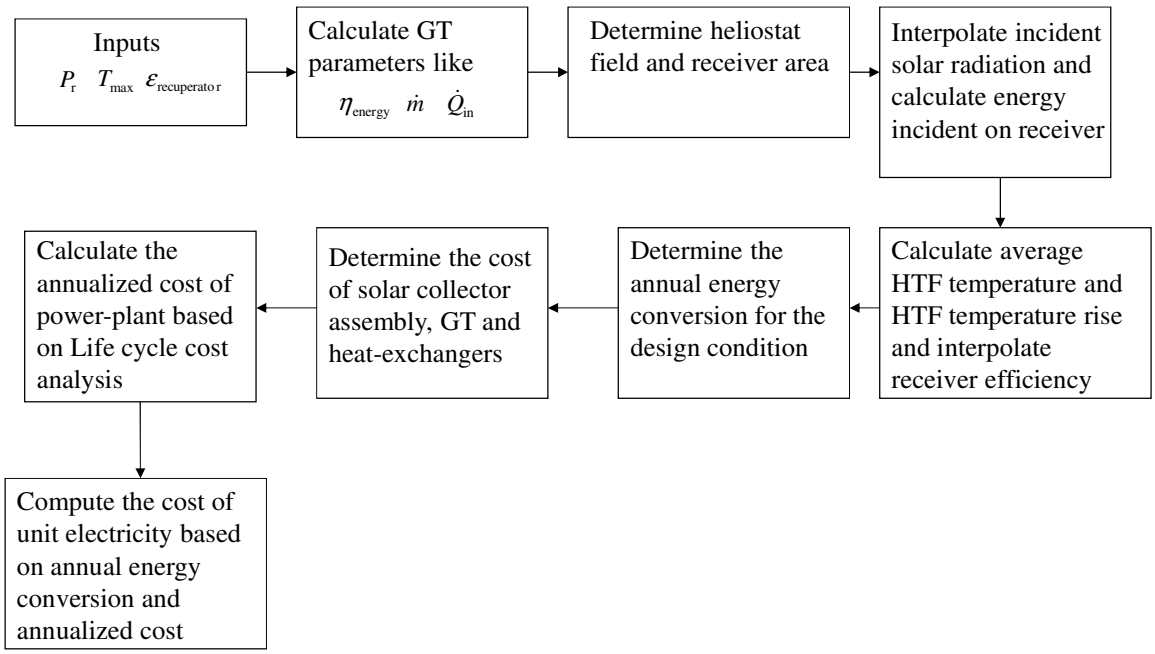

Figure 5.20: Process Map for System Performance Calculation-Recuperator

The system performance for the recuperated GT configuration is presented in Figure 5.21.

There are two main differences in the trend compared to earlier configurations. The first and main difference is that recuperator gives significantly higher GT efficiency for all peak cycle temperatures and pressure ratios. Secondly, for a given peak cycle temperature, the peak efficiency is attained at lower pressure ratio. The peak GT efficiency is 45.1% at a peak cycle temperature of 1200 K and pressure ratio of 4.

The thermal power input still follows the trend of reducing with increase in peak cycle temperature (Figure 5.21b). However, at a particular peak cycle temperature, the thermal power input from receiver shows a reverse trend compared to previous configurations. This is due to the recuperator making up for a greater contribution to enthalpy rise at lower pressure ratio than at higher pressure ratio. At higher pressure ratio, the heat transferred through recuperator reduces causing the thermal power transferred from receiver to rise.

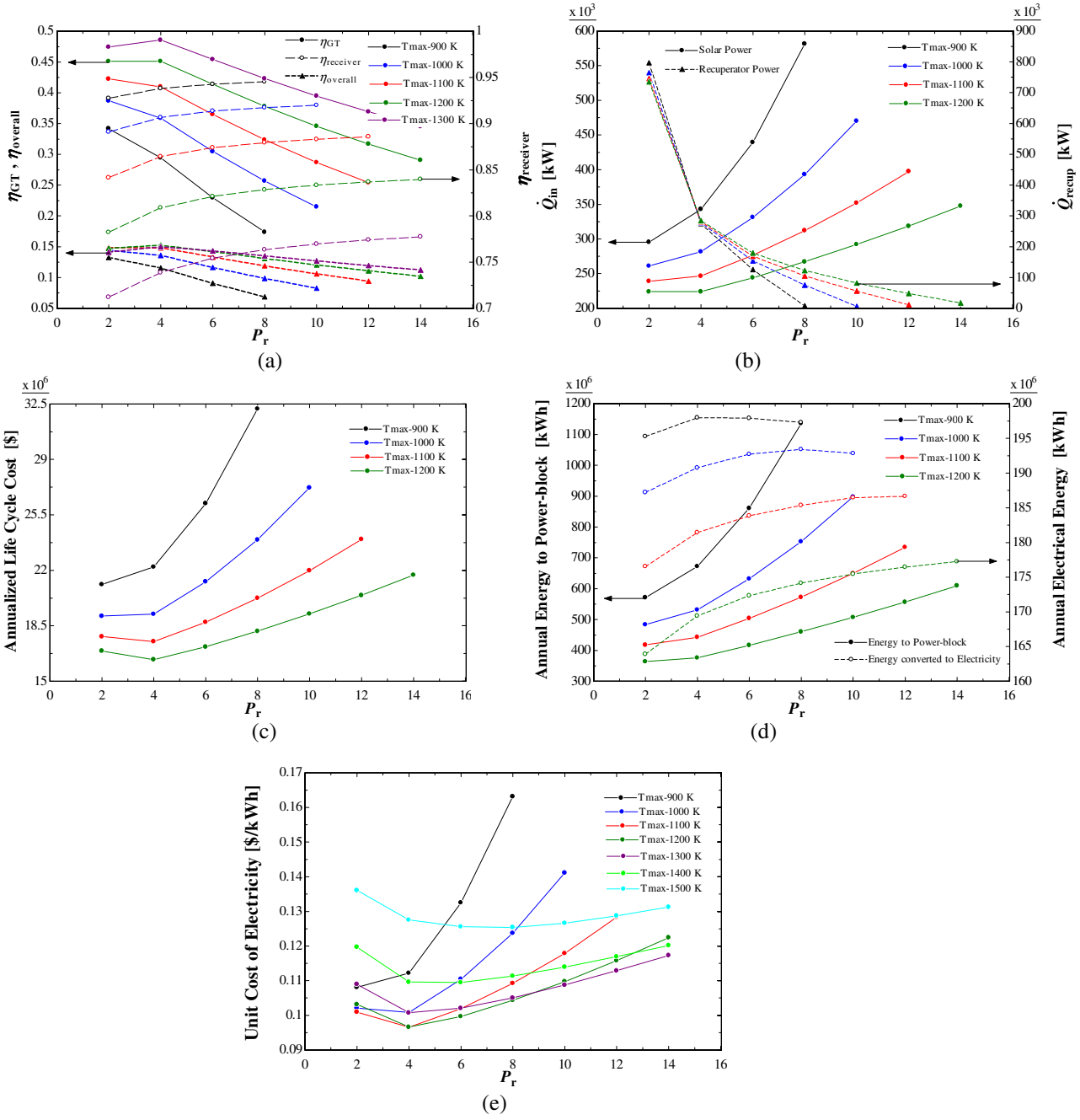

Figure 5.21: Power plant system performance in terms of key design parameters: (a) *System efficiency*, (b) *Thermal power input*, (c) *Annualized life-cycle cost*, (d) *Annual electricity generation* and (e) *Unit cost of electricity* – Simple Cycle

The life-cycle cost varies significantly with both peak cycle temperature and overall pressure ratio other than at lower pressure ratio where the life-cycle cost reduces with increase in peak cycle temperature.

Figure 5.21d shows the amount of energy delivered to power-block and the electricity generated annually. The recuperated system has lower energy conversion compared to previous configurations, especially at lower pressure ratios owing to lower receiver efficiency.

The unit cost of electricity is depicted in Figure 5.21e. At lower peak cycle temperature, the unit cost of electricity is at the lowest overall pressure ratio. As the peak cycle temperature rises, the optimum unit cost is obtained at higher pressure ratio. The optimum unit cost at a particular peak cycle temperature initially reduces with increase in peak cycle temperature, then increases. The optimum peak cycle temperature for the most economical simple cycle system is 1100 K and the optimum pressure ratio is 4. The minimum unit cost is 9.6 cents/kWh.

The efficiency predicted with minimum unit cost for recuperated configuration is 41%. The exergy flow diagram for the optimum configuration is depicted in Figure 5.22. The exergy flows through the compressor into the recuperator followed by solar heat exchanger and out of it into the turbine, from where it exits into the atmosphere. The exergy rises in the compressor due to the compression process. Then the exergy increases inside the recuperator as the heat is added to the working fluid. The flow then goes into the solar heat exchanger where it increases significantly due to the heat from the solar collector system. In the turbine section, the exergy drops down as the flow expands and imparts the exergy to turbine. The turbine drives the compressor with about 26% of the exergy it gained from the working fluid and utilizes 24% to drive the generator. Afterwards, the flow enters the recuperator to give-up the 38% residual exergy to the flow from the exit of the compressor. The remaining exergy is spent to the atmosphere. Some amount of exergy is destroyed in the process inside the compressor, turbine and recuperator.

Exergy Flow Diagram – Recuperator

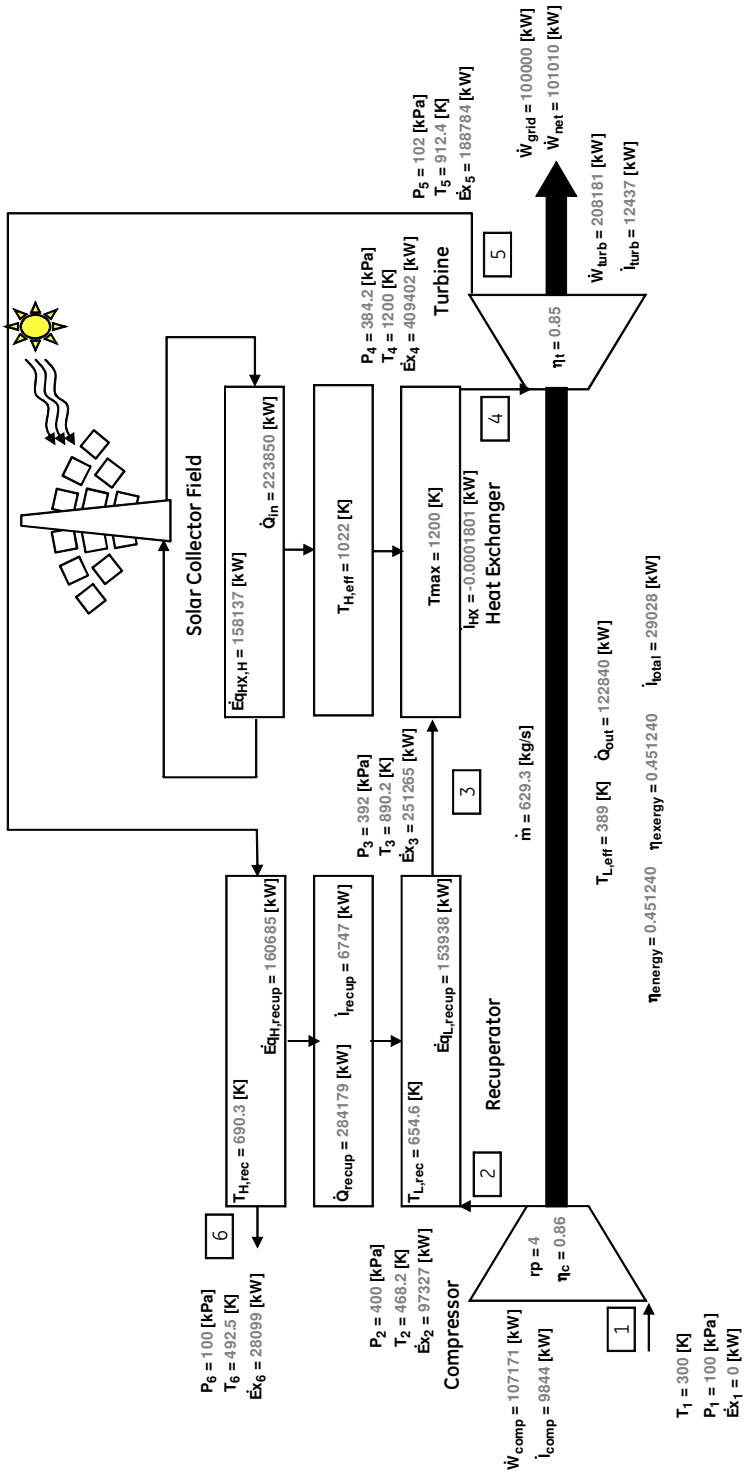

Figure 5.22: Exergy Flow Diagram for a Recuperated GT

The T-s diagram for the configuration is plotted in Figure 5.23. The temperature rise through the receiver is about 300 K which is more suitable for thermal energy storage.

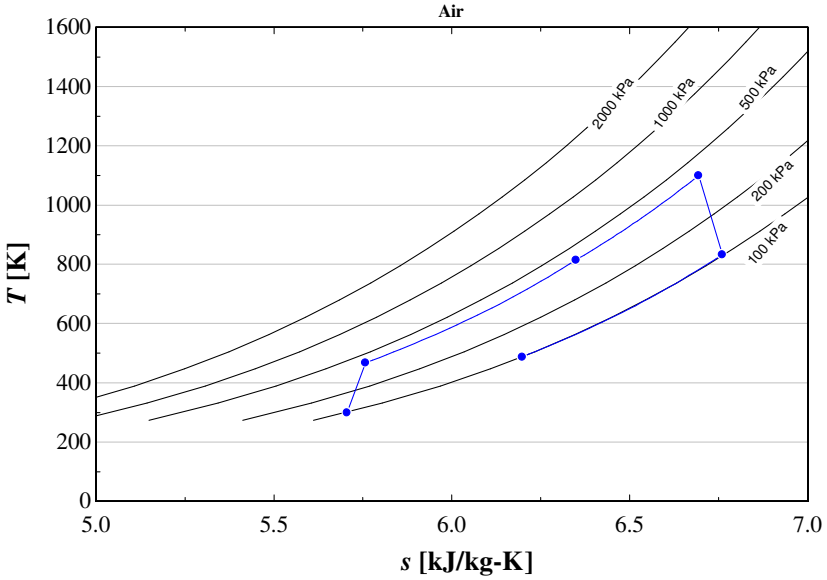

Figure 5.23: T-s Diagram for a Recuperated GT

Results: Single stage Intercooler with Recuperator HTSGT

Another way to make recuperator a feasible option is by reducing the compressor discharge temperature using intercooling. It might also allow us to go for a higher pressure ratio. However, the system complexity as well as cost increases with both the intercooler and recuperator present.

Single stage Intercooling and Recuperation

The system has one intercooler and two compressors, a low pressure (LP) compressor and a high pressure (HP) compressor and a recuperator. In the current system, the intercooler and recuperator have been designed for an effectiveness of 95% and pressure loss at 2% of the heat-exchanger inlet flow pressure based on the heat exchanger design results for MPBR (Chunyun, 2003)..The configuration is studied for system performance as illustrated in Figure 5.24.

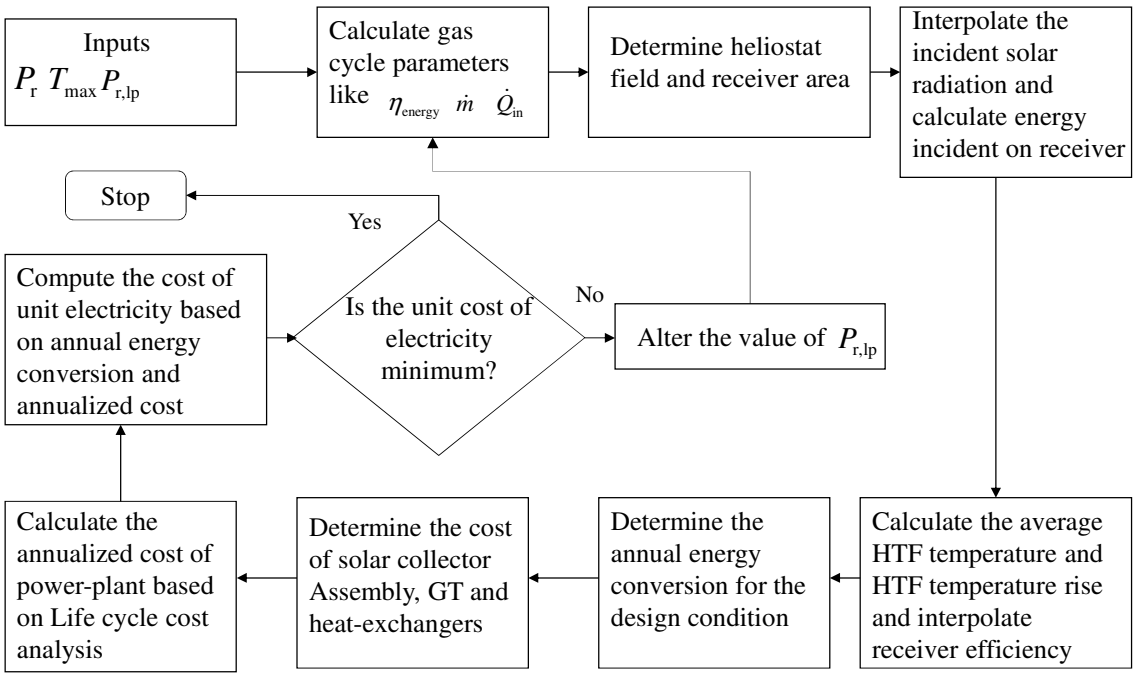

Figure 5.24: Process Map for System Performance Calculation-Single stage Intercooler with Recuperator

The system performance for the single stage intercooler with recuperator is shown in Figure 5.25. The trend for GT efficiency is similar to the recuperator only configuration. The peak GT efficiency is 48.2% at a peak cycle temperature of 1200 K, which is higher than the recuperator only system.

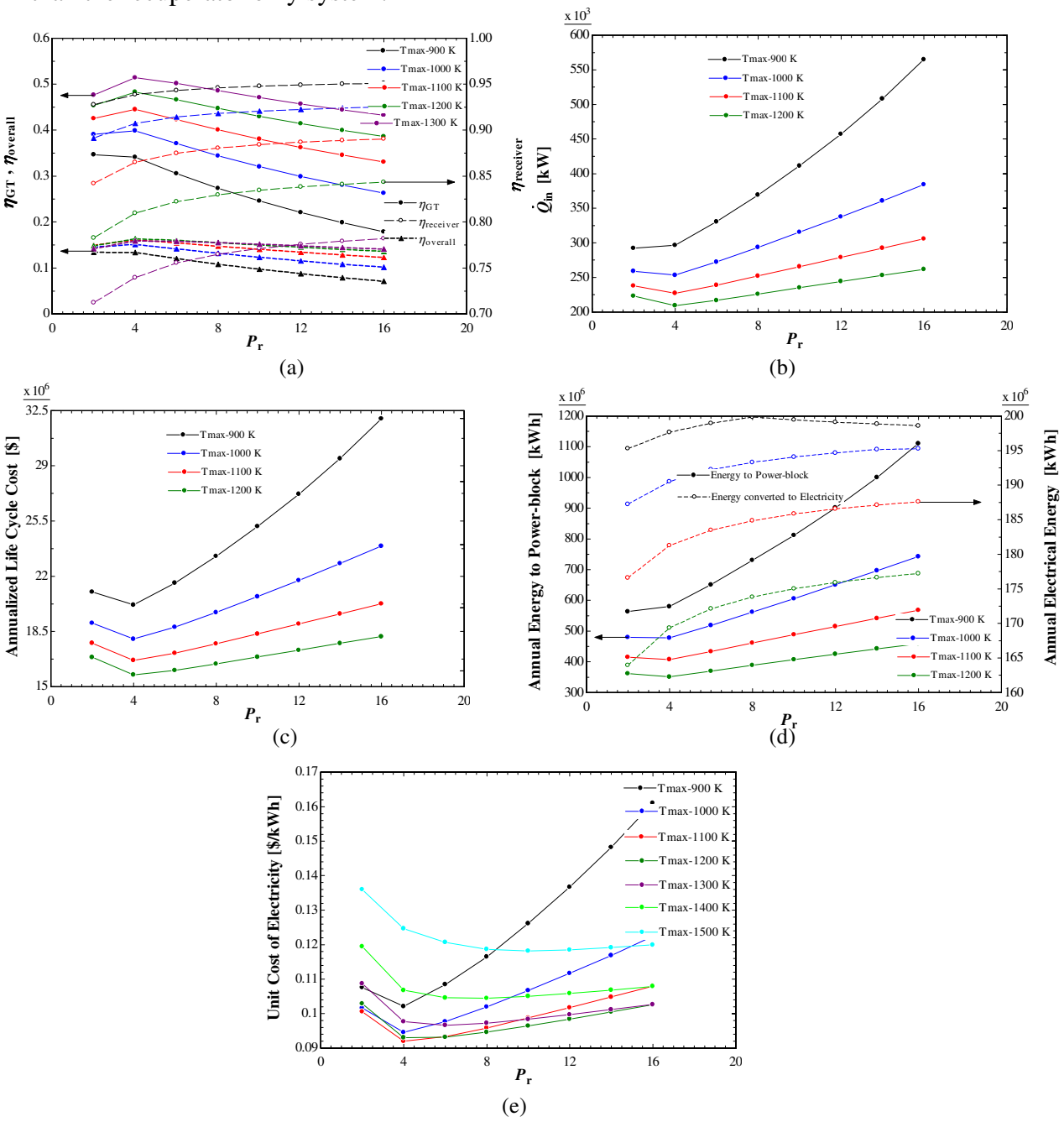

Figure 5.25: Power plant system performance in terms of key design parameters: (a) *System efficiency*, (b) *Thermal power input*, (c) *Annualized life-cycle cost*, (d) *Annual electricity generation* and (e) *Unit cost of electricity* - Single stage Intercooler with Recuperator

The optimum efficiency is achieved at low pressure ratio for all peak cycle temperatures. The thermal power input follows the trend of recuperated system (Figure 5.21b). At higher pressure ratio, the heat transferred through recuperator reduces causing the thermal power transferred from receiver to rise.

The life-cycle cost is low at low pressure ratio in line with the thermal power input variation. The annual electricity generation however drops towards the low pressure ratio (Figure 5.25d). This is due to the lowering of receiver efficiency at low pressure ratio where the recuperator causes the average HTF temperature to rise.

The unit cost of electricity initially drops then rises with pressure ratio at all peak cycle temperatures (Figure 5.25e). The optimum peak cycle temperature for the most economical simple cycle system is 1100 K and the optimum pressure ratio is 4. The minimum unit cost is 9.2 cents/kWh, which is higher than recuperated only system. The efficiency predicted with minimum unit cost for recuperated configuration is 44.5%. The exergy flow diagram for the optimum configuration is depicted in Figure 5.26. The exergy flows through the LP compressor into the intercooler. It then goes into the HP compressor then recuperator followed by solar heat exchanger and out of it into the turbine, from where it exits into the atmosphere. The exergy rises in the LP and HP compressors due to the compression process. The intercooler reduces the exergy by taking away heat. Then the exergy increases inside the recuperator as the heat is added to the working fluid. The flow then goes into the solar heat exchanger where it increases significantly due to the heat from the solar collector system. In the turbine section, the exergy drops down as the flow expands and imparts the exergy to turbine. The turbine drives the compressor with about 28% of the exergy it gained from the working fluid and utilizes 26% to drive the generator. Afterwards, the flow enters the recuperator to give-up the 37% residual exergy to the flow from the exit of the compressor. The remaining

exergy is spent to the atmosphere. Some amount of exergy is destroyed in the process inside the compressor, turbine and recuperator.

Exergy Flow Diagram – Single stage Intercooler with Recuperator

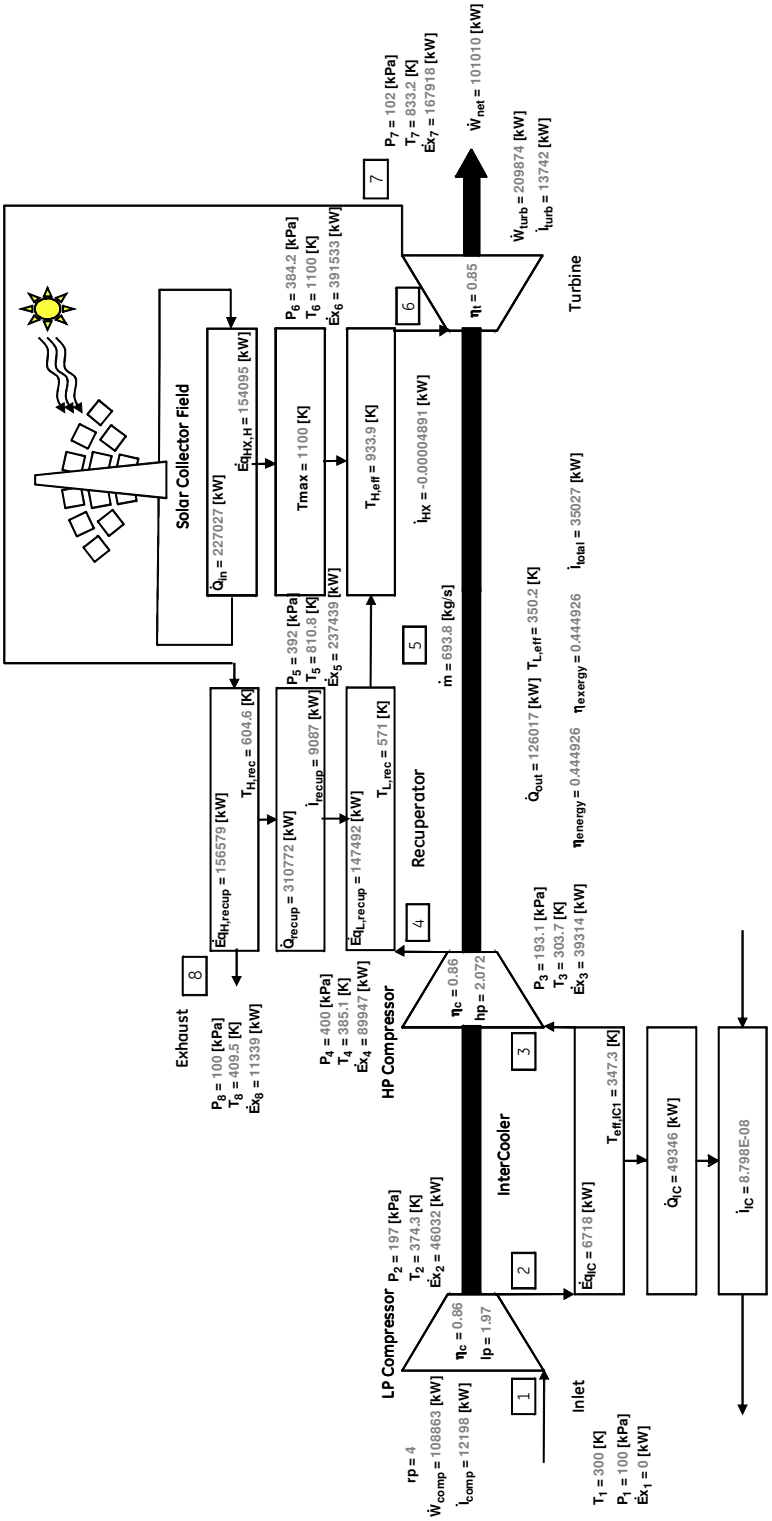

Figure 5.26: Exergy Flow Diagram for a Single stage Intercooler with Recuperated GT

The T-s diagram for the configuration is plotted in Figure 5.27. The temperature rise across the receiver section is about 300 K, which is slightly higher for thermal energy storage system to work.

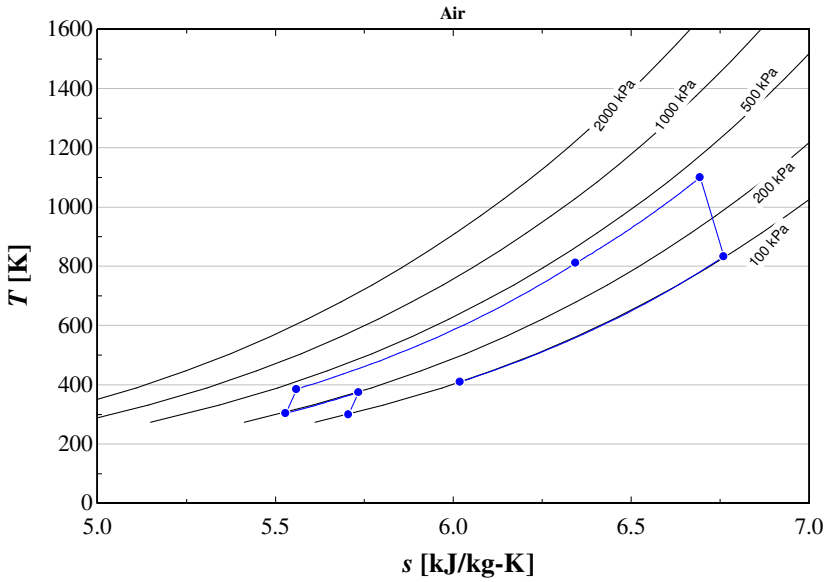

Figure 5.27: T-s Diagram for a Single stage Intercooler with Recuperator GT

Results: Two stage Intercooler with Recuperator HTSGT

The compressor discharge temperature can be reduced even more by using two-stage intercooling. It might allow us to go for a higher pressure ratio. However, the system complexity as well as cost will increase further.

Two stage Intercooling and Recuperation

The system has two intercooler and three compressors, a low pressure (LP) compressor and a high pressure (HP) compressor and a recuperator. In the current system, the intercooler and recuperator have been designed for an effectiveness of 95% and pressure loss at 2% of the heat-exchanger inlet flow pressure based on the heat exchanger design results for MPBR (Chunyun, 2003). The configuration is studied for system performance as illustrated in Figure 5.28.

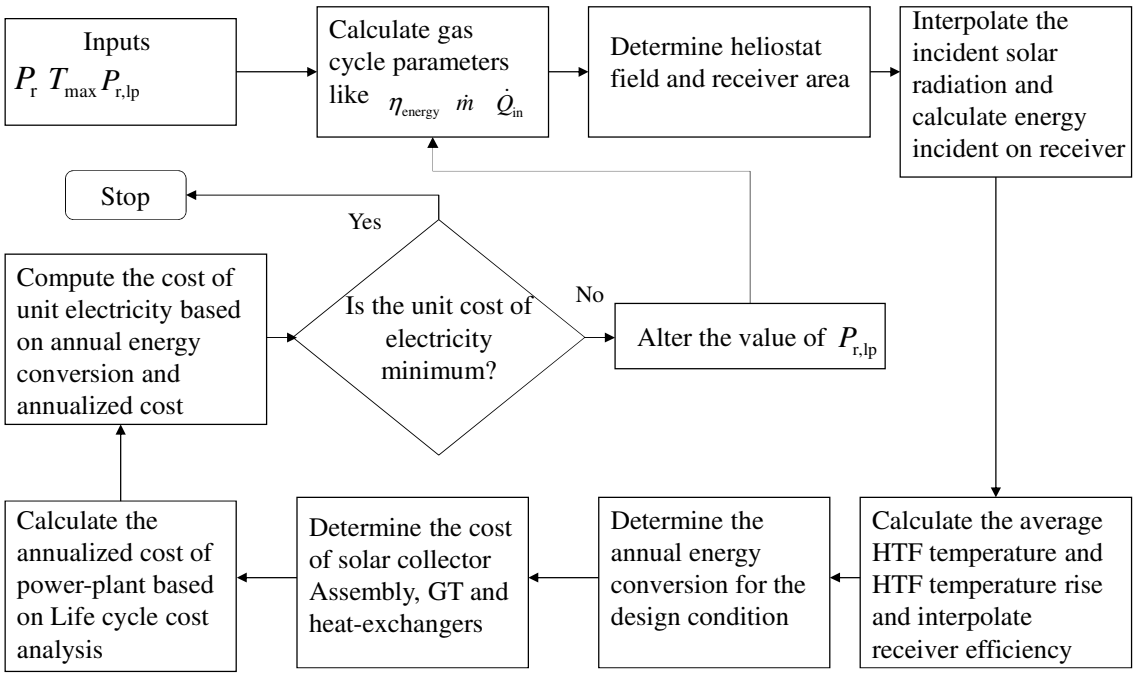

Figure 5.28: Process Map for System Performance Calculation-Two stage Intercooler with Recuperator

Figure 5.29 shows the system performance for the system with two-stage intercooler and recuperator. The trend is similar to the earlier recuperator configurations. The peak GT

efficiency is 48.9% at a peak cycle temperature of 1200 K, which is the highest GT system efficiency achieved in all configurations.

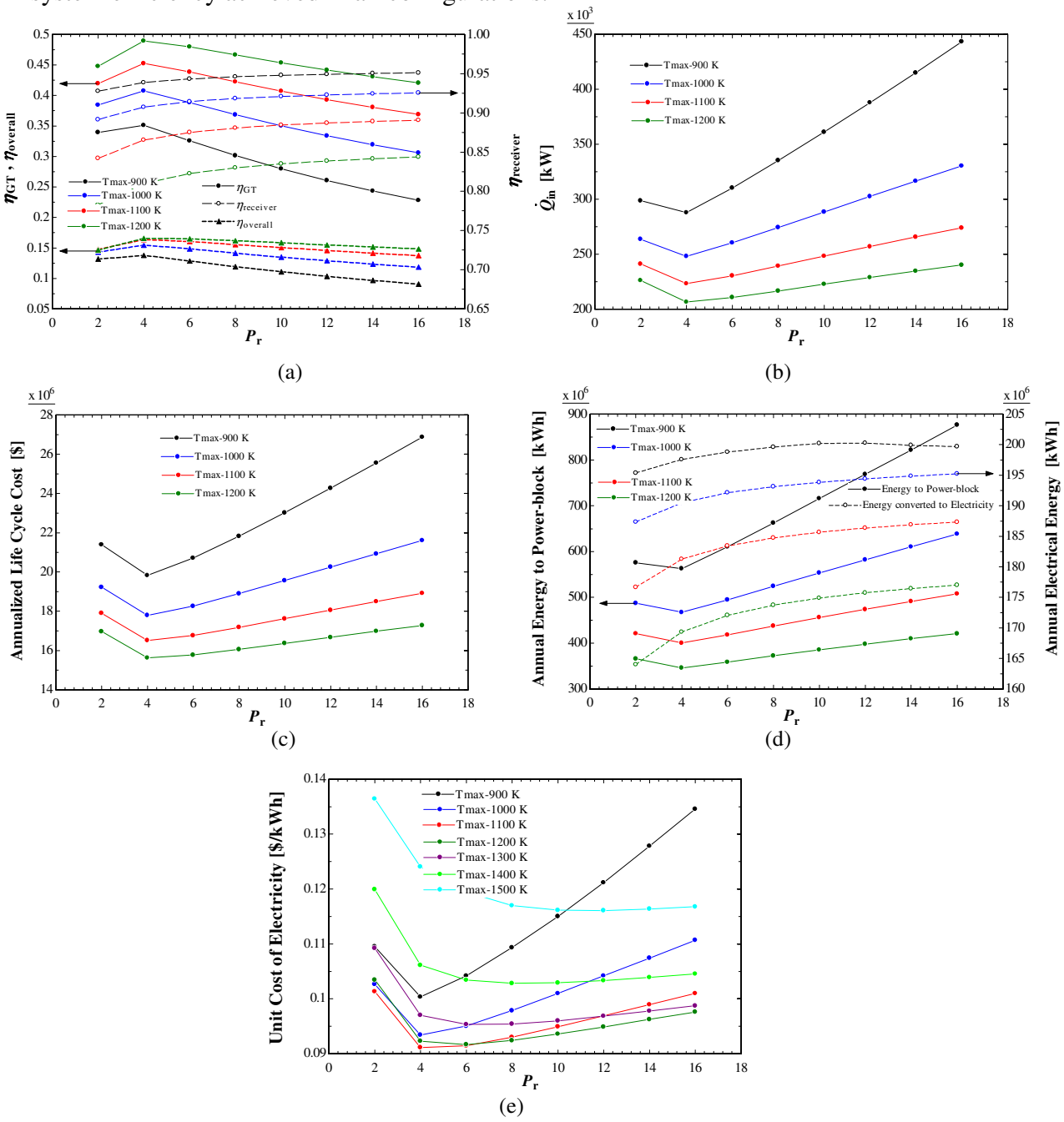

Figure 5.29: Power plant system performance in terms of key design parameters: (a) *System efficiency*, (b) *Thermal power input*, (c) *Annualized life-cycle cost*, (d) *Annual electricity generation* and (e) *Unit cost of electricity* - Simple Cycle

The thermal power input, annualized life-cycle cost and annual electricity generation trends are very similar to the single stage intercooler with recuperator configuration. The

optimum peak cycle temperature for the most economical system is 1100 K and the optimum pressure ratio is 4. The minimum unit cost is 9.1 cents/kWh, which is the lowest cost for all the configurations assessed.

The efficiency predicted with minimum unit cost for recuperated configuration is 45.2%. The exergy flow diagram for the optimum configuration is depicted in Figure 5.30. The exergy flows through the LP compressor into the intercooler. It then goes into the HP compressor then recuperator followed by solar heat exchanger and out of it into the turbine, from where it exits into the atmosphere. The exergy rises in the LP and HP compressors due to the compression process. The intercooler reduces the exergy (about 2%) by taking away heat. Then the exergy increases inside the recuperator as the heat is added to the working fluid. The flow then goes into the solar heat exchanger where it increases significantly due to the heat from the solar collector system. In the turbine section, the exergy drops down as the flow expands and imparts the exergy to turbine. The turbine drives the compressor with about 27% of the exergy it gained from the working fluid and utilizes 26% to drive the generator. Afterwards, the flow enters the recuperator to give-up the 38% residual exergy to the flow from the exit of the HP compressor. The remaining exergy (about 1.8%) is spent to the atmosphere. 9% of exergy is destroyed in the process inside the compressor, turbine and recuperator.

Exergy Flow Diagram – Two stage Intercooler with Recuperator

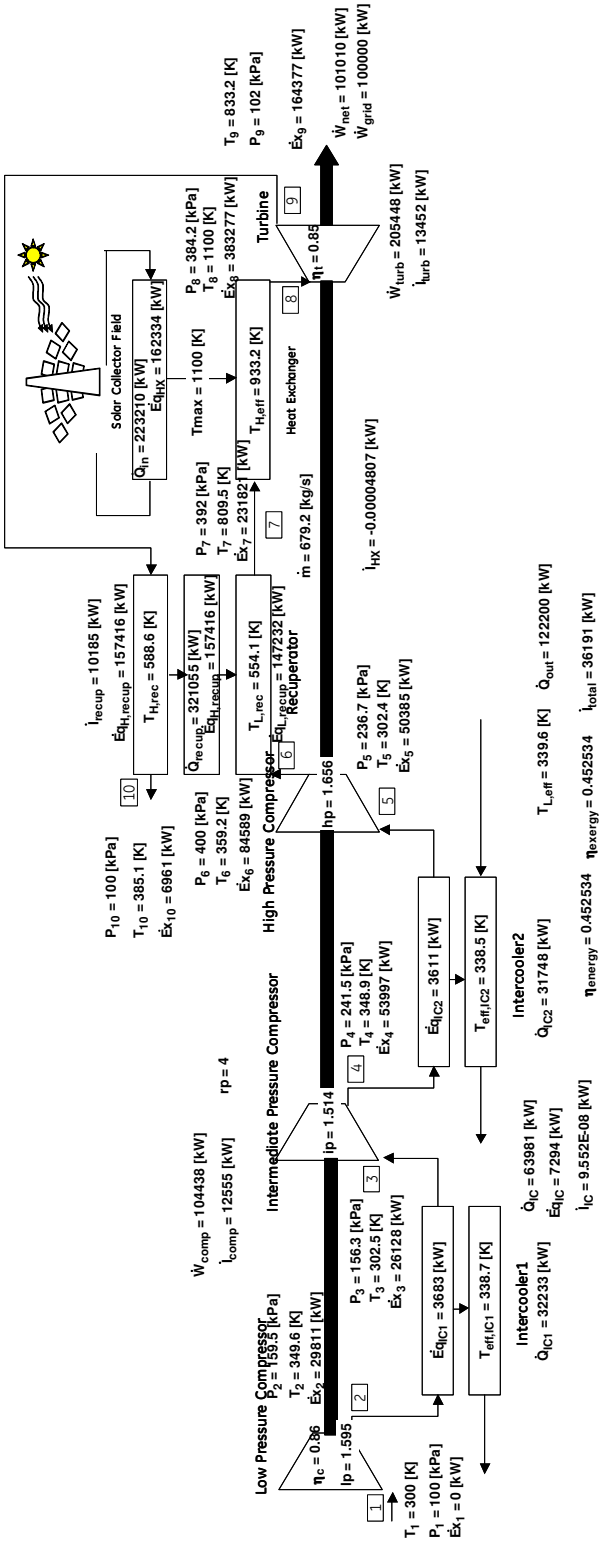

Figure 5.30: Exergy Flow Diagram for a Two-stage Intercooler with Recuperator GT

The T-s diagram for the configuration is plotted in Figure 5.31. The temperature rise across the receiver section is similar to single-stage intercooler with recuperator configuration.

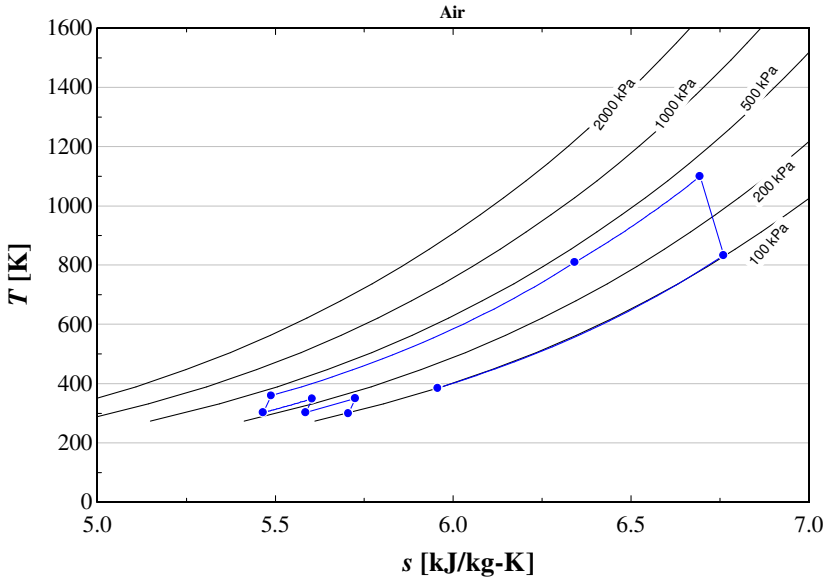

Figure 5.31: T-s Diagram for a Two-stage Intercooler with Recuperator

System Parameter Variation with Configurations

The present section details the variation of individual system parameters for different design configurations assessed. These parameters represent the performance and cost of individual sub-systems which add-up to represent the overall power-plant system performance and cost.

Gas Turbine Efficiency

The GT efficiency is at the core of determining a suitable HTSGT system for power generation using Brayton cycle. The GT efficiency determines the required thermal power input to generate a rated output of electricity. Figure 5.32 shows the variation in GT efficiency for different design configurations. The effect of augmenting intercooler and recuperator sub-systems can be readily seen in the trends.

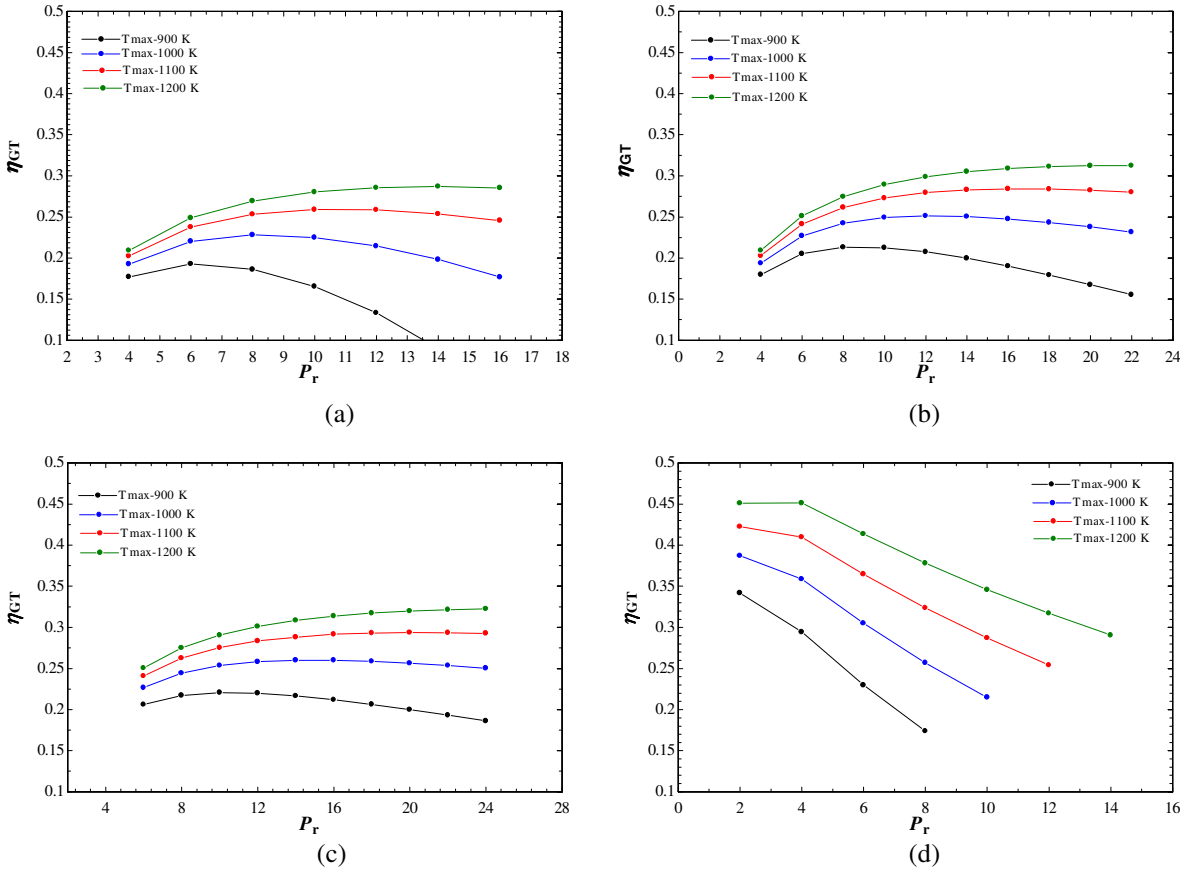

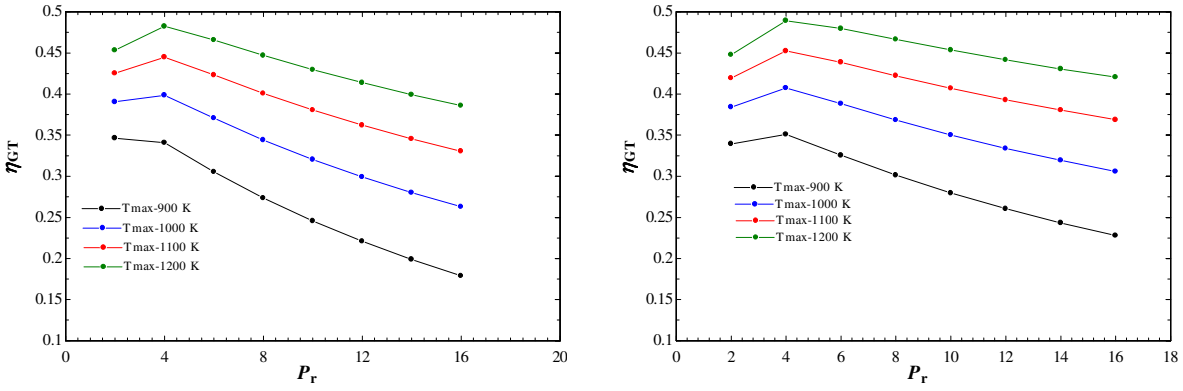

Figure 5.32: GT efficiency variation for different configurations: (a) Simple cycle, (b) Single-stage Intercooler, (c) Two-stage Intercooler, (d) Recuperator, (e) Single-stage Intercooler with Recuperator and (f) Two-stage Intercooler with Recuperator

The GT efficiency for simple cycle (Figure 5.32a) increases with the peak cycle temperature and for a given peak cycle temperature, it has an optimum pressure ratio for maximum GT efficiency. This optimum pressure ratio increases with increasing peak cycle temperature as shown in Figure 5.5. This trend is caused by the change in net specific work with increase in overall pressure ratio. At lower pressure ratio, the compressor specific work increases less rapidly than the turbine specific work increase. But as pressure ratio increases, the compressor specific work increases at a greater rate than turbine specific work. The heat input to the system reduces continuously with pressure ratio. Table 5.2 shows the comparison of the above mentioned parameters at two different pressure ratios for a specific peak cycle temperature.

Table 5.2: GT system parameters at two different pressure ratios

GT System Parameters	T_{max} = 1000 [K]	
	$P_r = 8$	$P_r = 16$
Compressor Specific Work, w_{comp} [kJ/kg]	284	422
Turbine Specific Work, w_{turb} [kJ/kg]	389	479
Net Specific Work, w_{net} [kJ/kg]	105	57.3
Specific Heat Input, q_{in} [kJ/kg]	462	324
Mass-flow rate, $\dot{m}$ [kg/s]	959	1760
GT Efficiency, η [%]	22.8	17.7

The single stage intercooler gives higher GT efficiency compared to simple cycle for all peak cycle temperatures and pressure ratios. Also, for a given peak cycle temperature, the peak efficiency is attained at a higher pressure ratio. The optimum pressure ratio increases with increase in peak cycle temperature. This is because as the peak cycle temperature rises, greater work can be extracted at higher pressure ratio. At a particular peak cycle temperature, as the pressure ratio increases, the heat input to the system as well as the net work done decrease. The optimum pressure ratio is decided by the fact that the heat input to the system initially reduces rapidly then gradually whereas the net work done initially reduces gradually then falls off rapidly. Table 5.3 shows this trend for a particular operating condition.

Table 5.3: Single stage Intercooled GT system parameters at three different pressure ratios

GT System Parameters	T_{max} = 1000 [K]		
	$P_r = 6$	$P_r = 12$	$P_r = 18$
Compressor Specific Work, w_{comp} [kJ/kg]	213	311	372
Turbine Specific Work, w_{turb} [kJ/kg]	347	444	493
Net Specific Work, w_{net} [kJ/kg]	134	133	121
Specific Heat Input, q_{in} [kJ/kg]	590	529	496
Thermal Efficiency, η	22.70%	25.10%	24.30%

The two-stage intercooler performs very similar to the single stage intercooler but with marginal improvement in GT efficiency. The effect of the second intercooler stage is seen to improve the GT efficiency for lower peak cycle temperatures significantly than at high peak cycle temperatures.

The recuperator gives significantly higher GT efficiency for all peak cycle temperatures and pressure ratios (an increase in GT efficiency by almost 50%). Also, for a given peak cycle temperature, the peak efficiency is attained at lower pressure ratio.

At a particular peak cycle temperature, as the pressure ratio increases, the heat input to the system as well as the net work done increase. The optimum pressure ratio is decided

by the fact that the heat input to the system rises more rapidly than the net work done. Table 5.4 shows this trend for a particular operating condition.

Table 5.4: Recuperated GT system parameters at three different pressure ratios

GT System Parameters	T_{max} = 1000 [K]		
	$P_r = 2$	$P_r = 4$	$P_r = 6$
Compressor Specific Work, w_{comp} [kJ/kg]	77	170	234
Turbine Specific Work, w_{turb} [kJ/kg]	143	274	341
Net Specific Work, w_{net} [kJ/kg]	66	104	106
Specific Heat Input, q_{in} [kJ/kg]	170	290	349
Specific recuperator heat transfer, q_{rec} [kJ/kg]	499	286	162
Thermal Efficiency, η	38.7%	35.9%	30.5%

The trend for the recuperator with single-stage and two-stage intercooler is similar to the recuperator-only configuration. However, the variation in GT efficiency with pressure ratio reduces with augmentation of intercooler stages. Also, the GT efficiency at lower peak cycle temperatures improves with the augmentation of intercooler stages.

GT Mass-flow rate

For a given operating condition for the GT and a given working fluid, the mass-flow rate will determine the size of the GT. For higher mass-flow rate, the GT size has to increase to accommodate the flow. This will determine the capital expenditure on the GT.

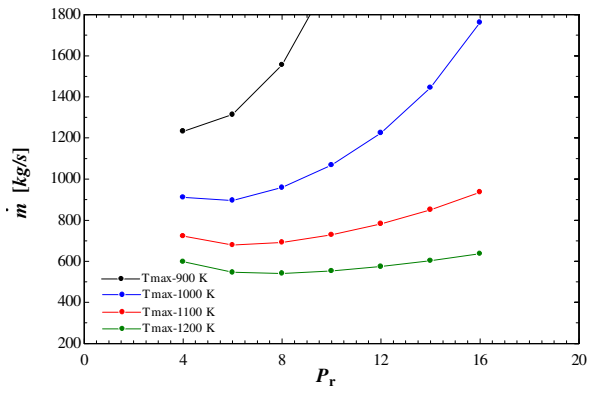

(a)

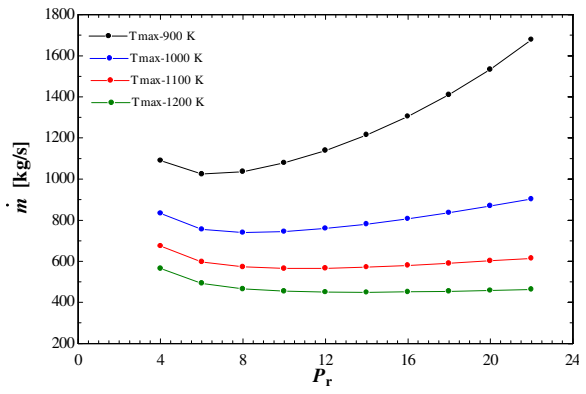

(b)

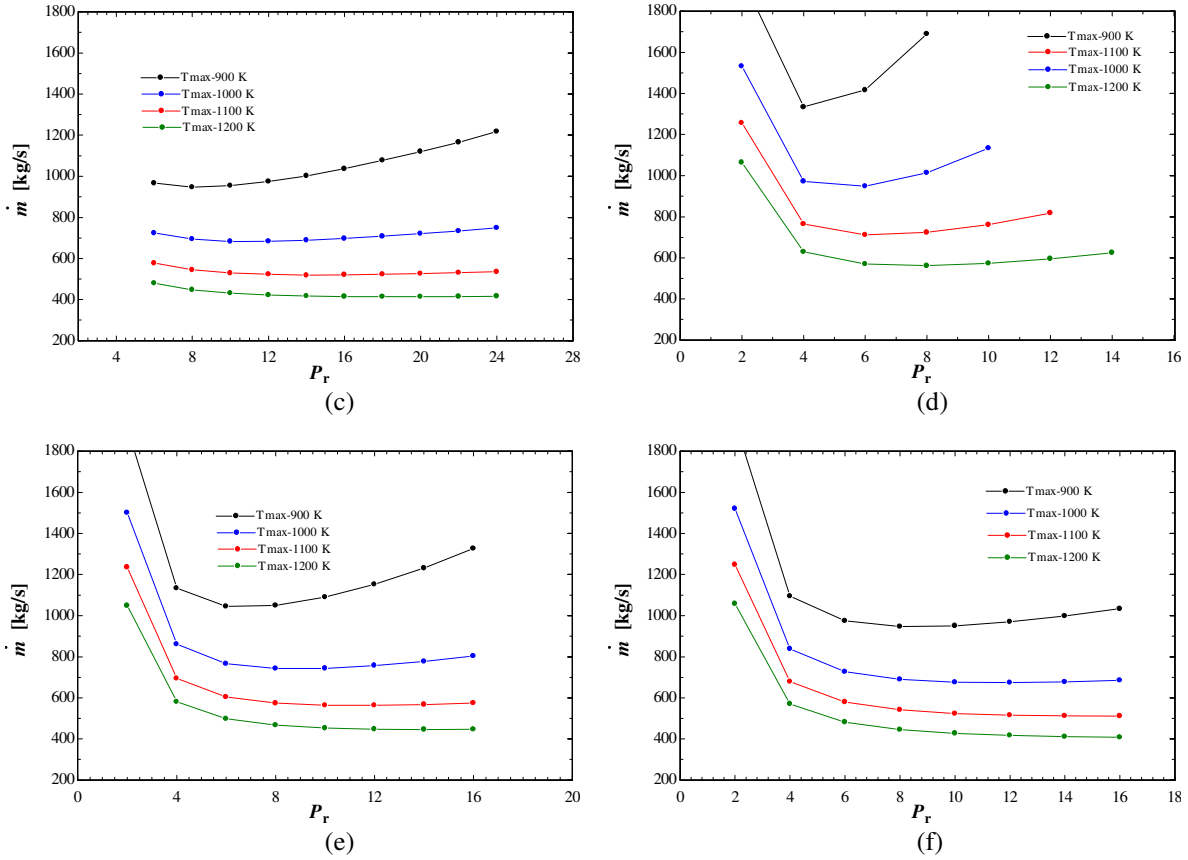

Figure 5.33: GT Mass-flow rate variation for different configurations: (a) Simple cycle, (b) Single-stage Intercooler, (c) Two-stage Intercooler, (d) Recuperator, (e) Single-stage Intercooler with Recuperator and (f) Two-stage Intercooler with Recuperator

The mass-flow rate for the simple cycle GT reduces with increasing peak cycle temperature. This happens due to increasing specific work by the working fluid. For a particular peak cycle temperature, the mass-flow rate initially decreases with pressure ratio then increases again driven by the change in net specific work. Table 5.2 shows the comparison of mass-flow rate at two different pressure ratios for a particular peak cycle temperature. The rate of increase is higher at lower peak cycle temperature while the mass-flow rate is relatively insensitive to pressure ratio change at higher peak cycle temperature.

This trend is repeated for all configurations. The configurations with recuperator show a higher mass-flow at lower pressure ratio and a greater variation in GT mass-flow with change in pressure ratio for all peak cycle temperatures.

GT Thermal Power Input

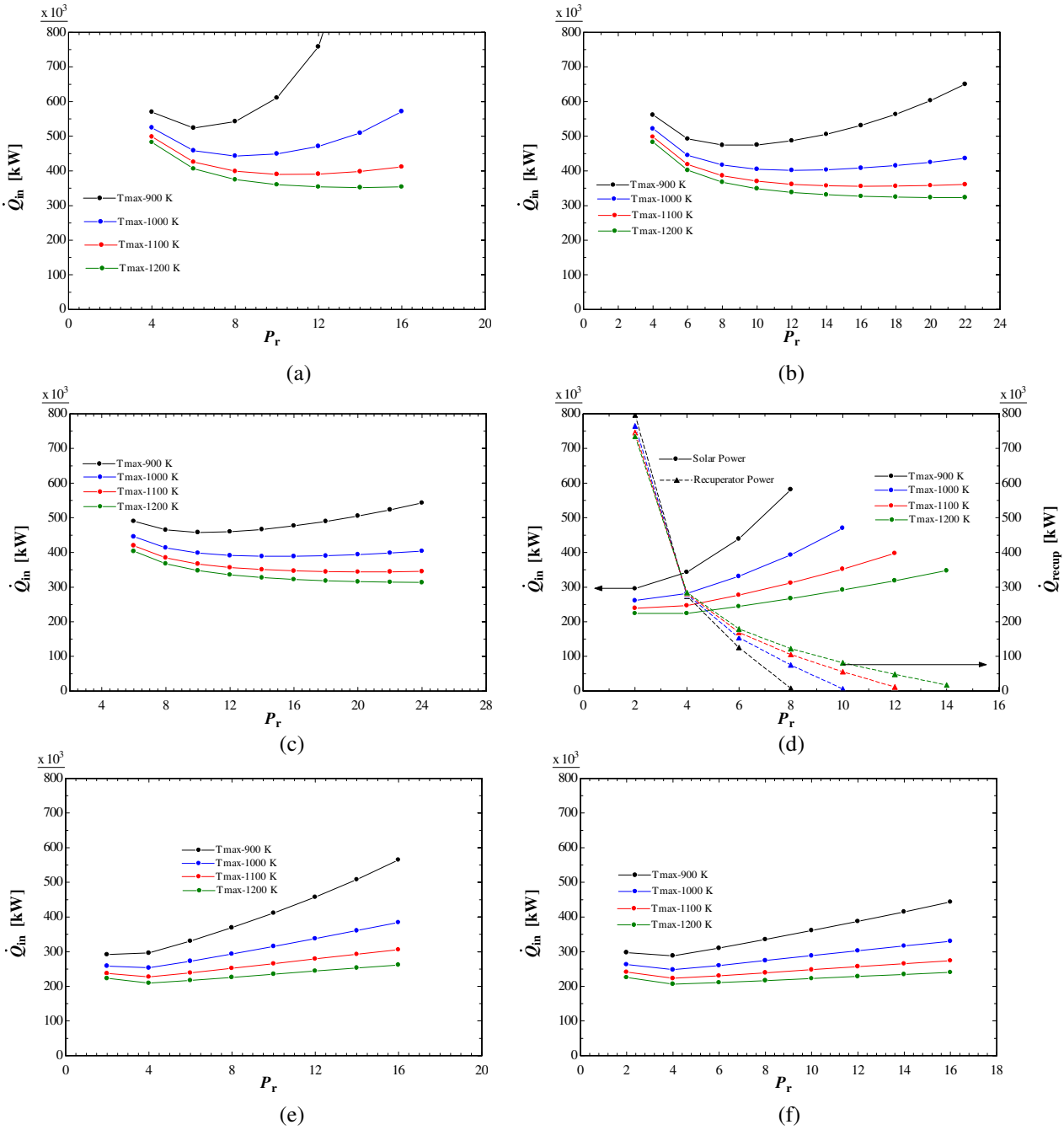

Figure 5.34: GT Thermal Power Input variation for different configurations: (a) Simple cycle, (b) Single-stage Intercooler, (c) Two-stage Intercooler, (d) Recuperator, (e) Single-stage Intercooler with Recuperator and (f) Two-stage Intercooler with Recuperator

The required thermal power input is the inverse of the GT system efficiency for a rated design power output. This required thermal power input determines the size of the solar collector field and the size of the receiver system.

For a simple cycle GT, at higher pressure ratio and peak cycle temperature, the required thermal power input reduces. The variation is more sensitive to change in peak cycle temperature.

For systems with intercooler-only augmentation (Figure 5.34b and 5.34c), the required thermal power input reduces significantly for lower peak cycle temperature. For systems with recuperator (Figure 5.34d, 5.34e and 5.34f), the required thermal power input drops significantly at low pressure ratio in keeping with the high GT efficiency at the same operating conditions.

Solar Collector System Area

The heliostat field area and the receiver surface area are determined based on the required thermal power input. The power from heliostat field does not vary linearly with field area overall, but for the limited range of variation of field area for the configurations considered; this variation is observed to be linear (SAM, 2011).

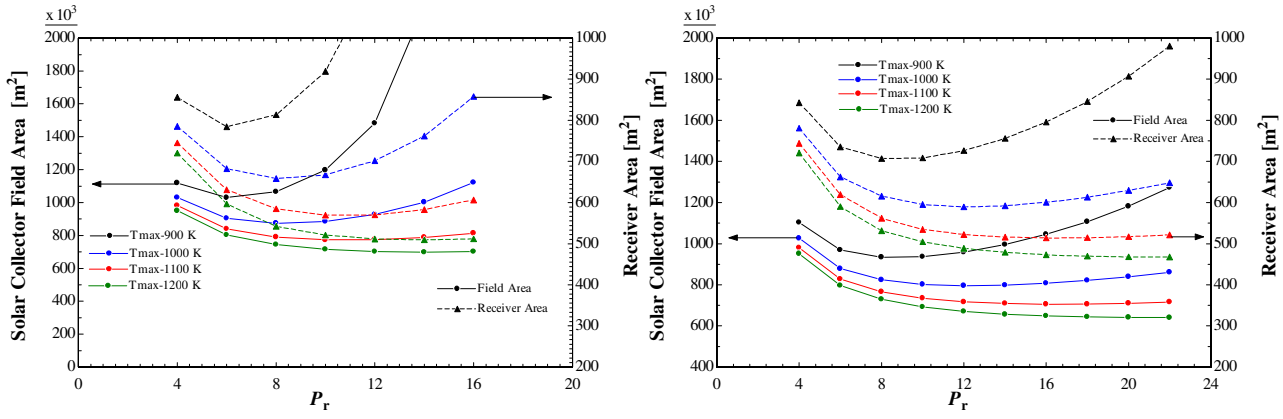

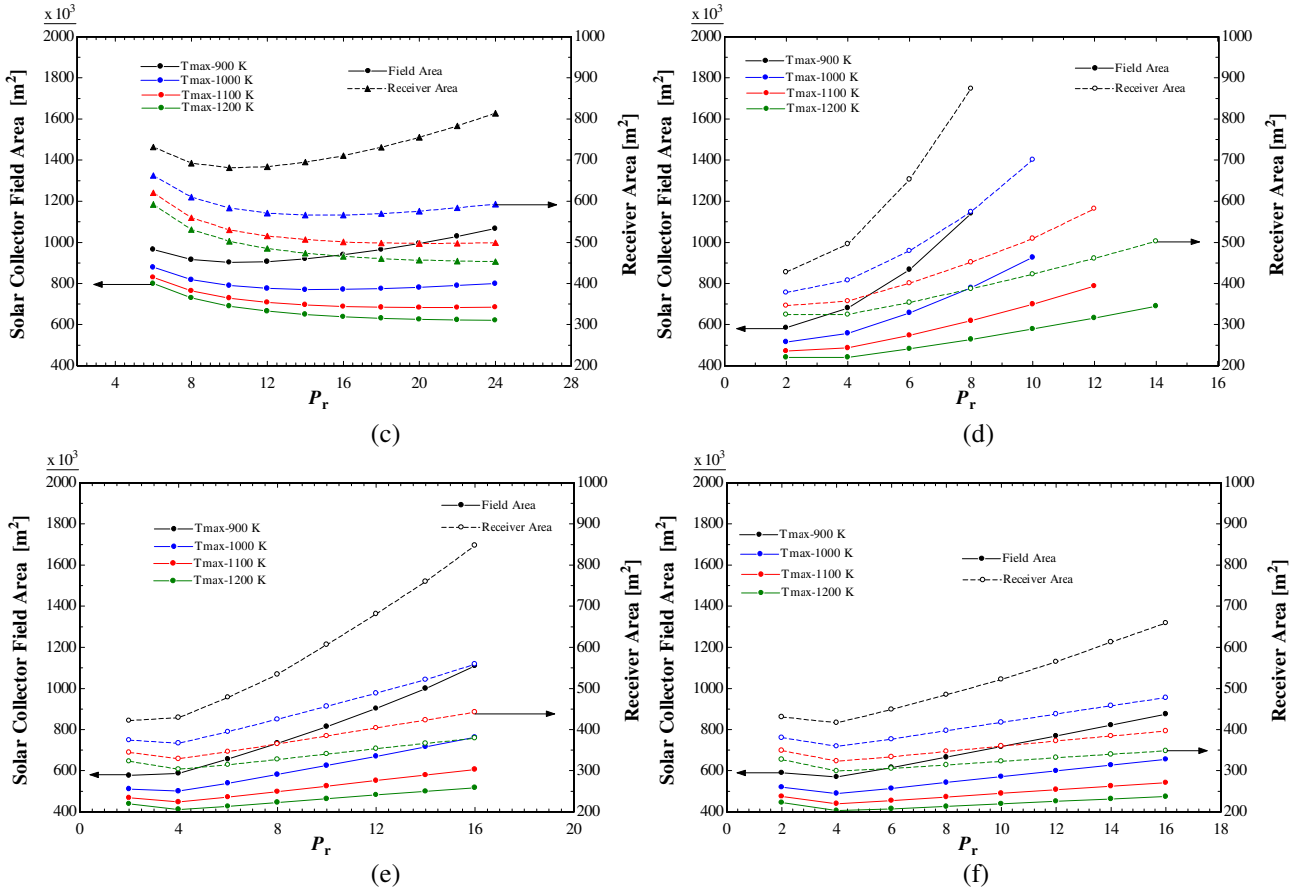

Figure 5.35: Solar Collector System Area variation for different configurations: (a) Simple cycle, (b) Single-stage Intercooler, (c) Two-stage Intercooler, (d) Recuperator, (e) Single-stage Intercooler with Recuperator and (f) Two-stage Intercooler with Recuperator

The heliostat field area varies from about 0.7 sq. km. for simple cycle GT to 0.4 sq. km. for the recuperator with two-stage intercooler system for the best operating conditions in the respective configurations. The receiver surface area varies between 500 sq. m and 200 sq. m for the same configurations.

Incident Solar Radiation and Energy to Receiver

The energy from incident solar radiation depends on the area of heliostat field. The energy ranges between 1800 GWh for the simple cycle and 1000 GWh for two-stage intercooler with recuperator. A part of the incident solar energy is lost due to the inefficiencies of the heliostat field as described in the system modeling chapter (Chapter 3) and the remaining energy reaches the receiver system as reflected solar radiation.

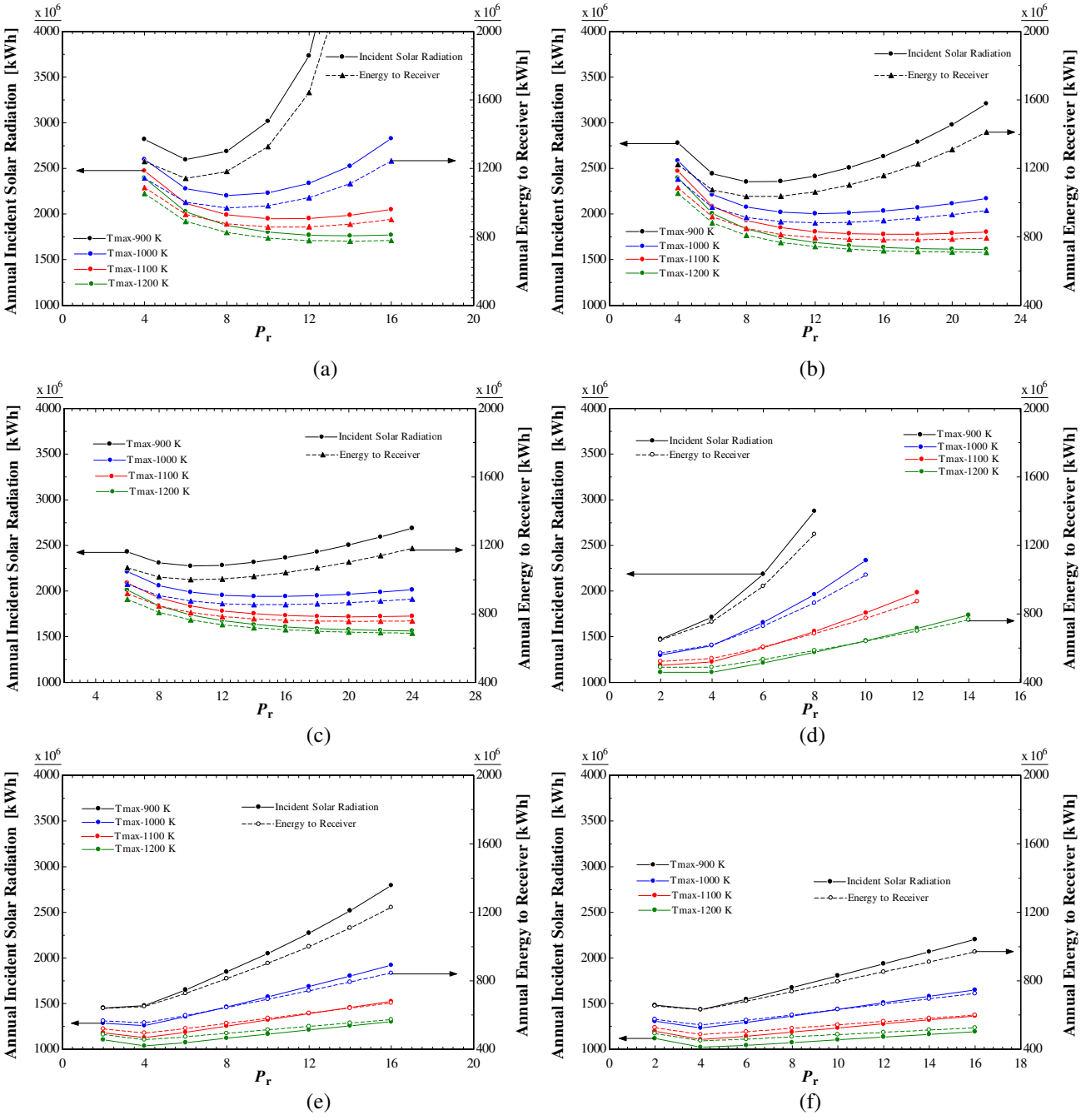

Figure 5.36: Incident Solar Energy and Energy to Receiver variation for different configurations: (a) *Simple cycle*, (b) *Single-stage Intercooler*, (c) *Two-stage Intercooler*, (d) *Recuperator,* (e) *Single-stage Intercooler with Recuperator and* (f) *Two-stage Intercooler with Recuperator*

This fraction is demonstrated to be relatively constant for the range of field area and operating conditions in system modeling chapter. On the basis of this fact, the energy to

the receiver system ranges between 800 GWh and 450 GWh. The trends for both the parameters match the trend for solar collector system area.

Receiver Efficiency

The performance of the receiver system is very crucial to the determination of the overall power-plant system performance. This is because the GT system's thermodynamic performance improves with increase in peak cycle temperature but the receiver system's performance reduces with increase in peak cycle temperature. To increase the peak cycle temperature, the receiver system has to raise the temperature of the HTF (heat transfer fluid). This heightened HTF temperature increases the losses from the receiver system due to convection and radiation.

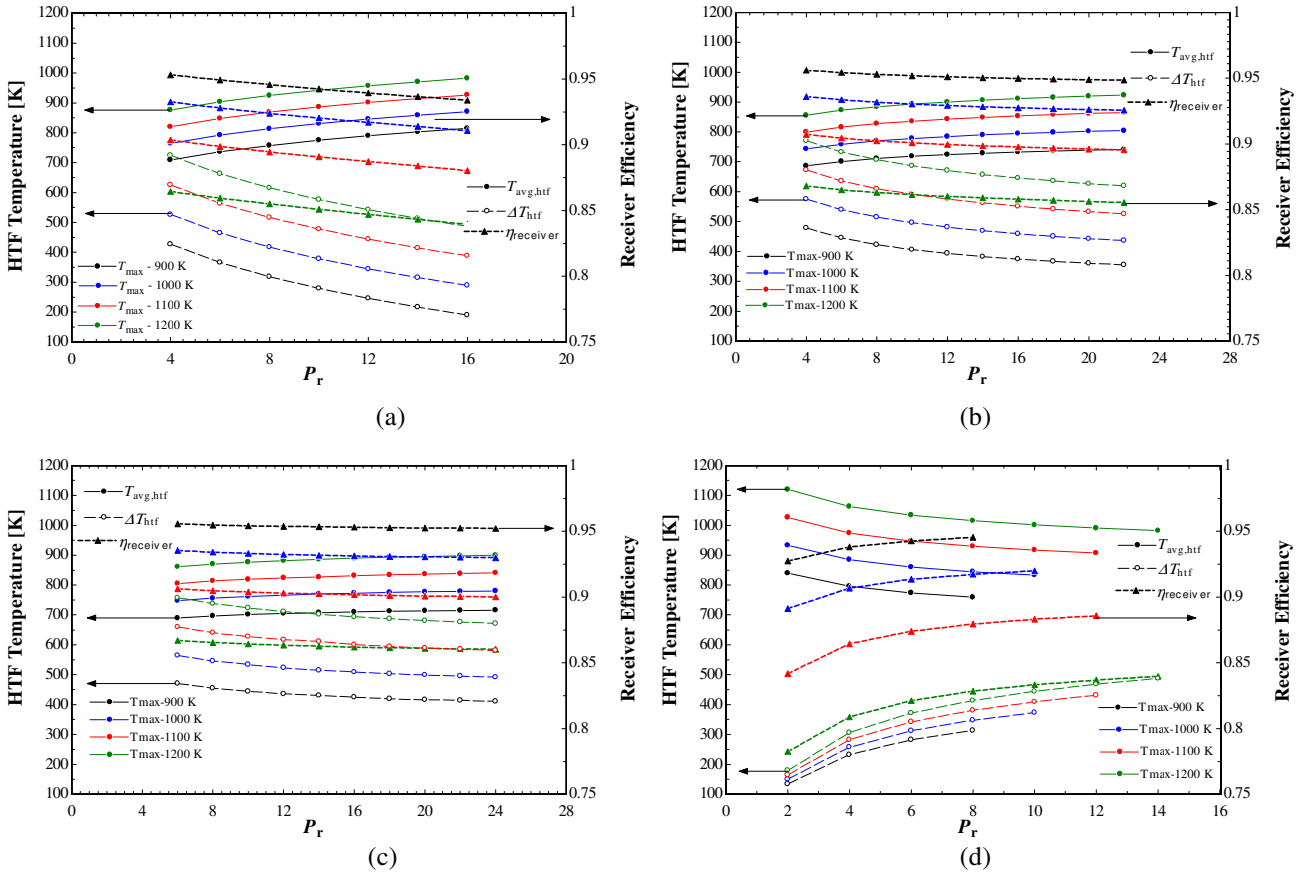

(a) (b)

(c) (d)

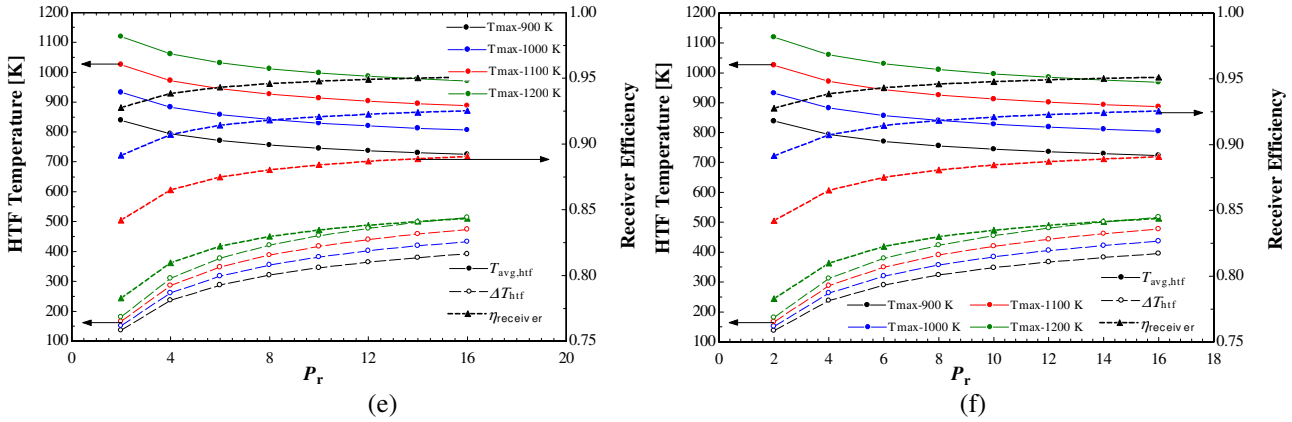

Figure 5.37: Receiver Efficiency variation for different configurations: (a) Simple cycle, (b) Single-stage Intercooler, (c) Two-stage Intercooler, (d) Recuperator, (e) Single-stage Intercooler with Recuperator and (f) Two-stage Intercooler with Recuperator

The receiver efficiency is observed to reduce with increasing peak cycle temperature for all configurations as the losses increase with the receiver operation at higher temperature. The receiver efficiency also changes with variation in HTF temperature rise, where in the receiver efficiency increases with higher HTF temperature rise.

Since the simple cycle and the intercooler-only systems (Figure 5.37a, 5.37b and 5.37c) have lower average HTF temperature, the receiver efficiency is higher for these configurations. Between these three configurations, the two-stage intercooler configuration's receiver efficiency is the least sensitive to change in system pressure ratio.

For the configurations with recuperator (Figure 5.37d, 5.37e and 5.37f), the HTF inlet temperature is high increasing the average HTF inlet temperature significantly and reducing the receiver efficiency. This reduction in receiver efficiency is more pronounced at higher peak cycle temperature which reduces the advantage of augmenting a recuperator into the GT system.

Energy to Power-block and Annual Electricity Generation

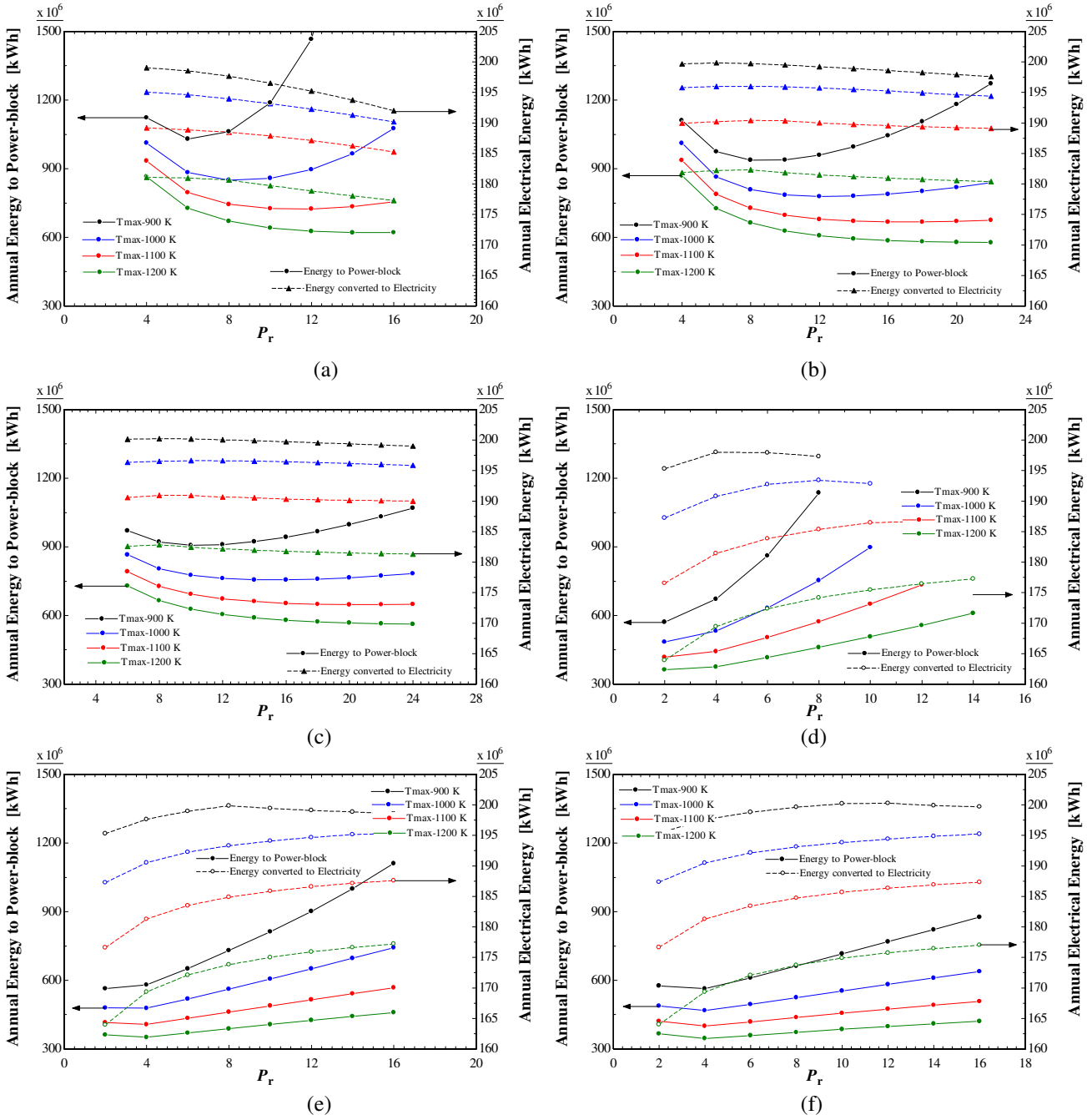

Figure 5.38: Energy to Power-block and Annual Electricity Generation variation for different configurations: (a) *Simple cycle*, (b) *Single-stage Intercooler*, (c) *Two-stage Intercooler*, (d) *Recuperator,* (e) *Single-stage Intercooler with Recuperator and* (f) *Two-stage Intercooler with Recuperator*

The energy to power-block (i.e. the GT system) shows the effect of receiver performance loss. This energy ranges between 650 GWh for simple cycle to 350 GWh for two-stage intercooler with recuperator. The annual electricity generation is then calculated based on the GT efficiency. Ideally, as the solar field area is determined on the basis of GT efficiency, the energy conversion should be same for all configurations. However, the energy conversion varies with configuration. It reduces with increase in peak cycle temperature. This is due to reduction in receiver efficiency for higher temperature operation.

The intercooler-only systems (Figure 5.38b and 5.38c) result in the highest electricity generation for all configurations. This is achieved at high pressure ratio. The recuperator configurations (Figure 5.38d, 5.38e and 5.38f) show high electricity generation at high pressure ratio but at low pressure ratio where the GT efficiency is relatively high for these configurations, the electricity generation rate is the lowest.

Overall System Efficiency

The overall system efficiency is a good representation of the power-plant system performance. It shows the combined effect of all the sub-systems in the power-plant.

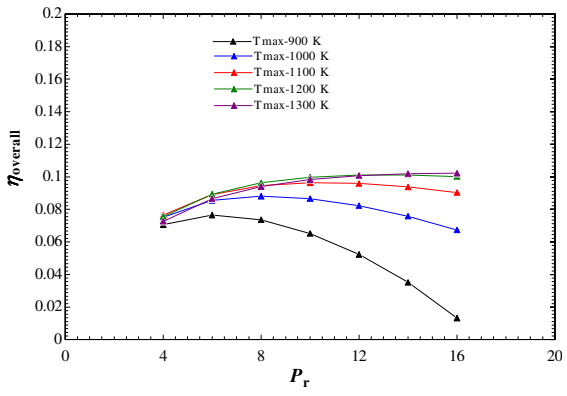

(a)

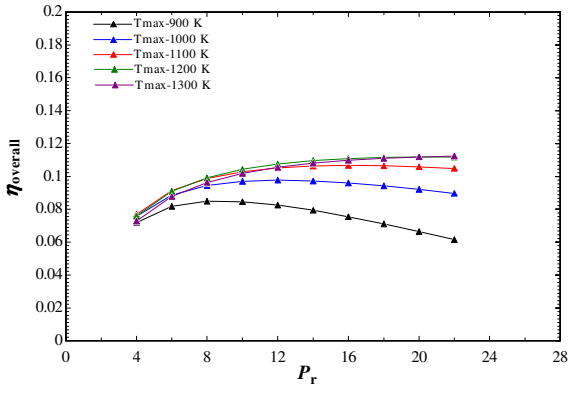

(b)

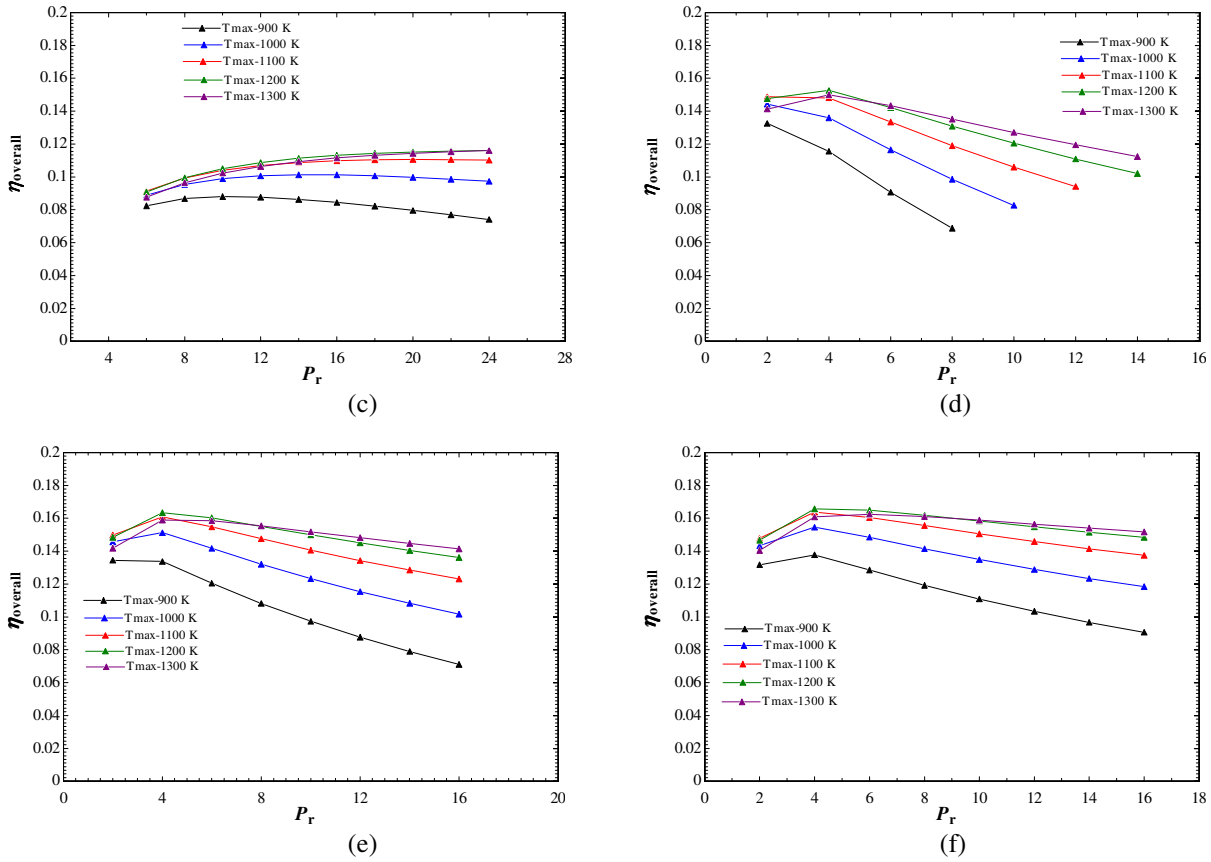

Figure 5.39: Overall System Efficiency variation for different configurations: (a) Simple cycle, (b) Single-stage Intercooler, (c) Two-stage Intercooler, (d) Recuperator, (e) Single-stage Intercooler with Recuperator and (f) Two-stage Intercooler with Recuperator

It clearly demonstrates the effect of augmenting the GT system with intercooler and recuperator where the simple cycle (Figure 5.39a) has a peak overall efficiency of about 10%, the intercooler only system (Figure 5.39b and 5.39c) improve this efficiency to about 12%, the recuperator only (Figure 5.39d) achieves about 15.5% and recuperator with intercooler (Figure 5.39e and 5.39f) achieve a high value of about 16.5%.

Solar Collector System Cost

The solar collector system has the largest share in the capital expenditure on the power-plant. The share ranges from 70% to 80% between all configurations. The solar collector system cost is very much representative of the thermal power input trend as the cost

varies proportionately with heliostat field area and receiver surface area. For the most economical system in each configuration, the solar collector system cost varies between 1800 $/kW and 1050 $/kW.

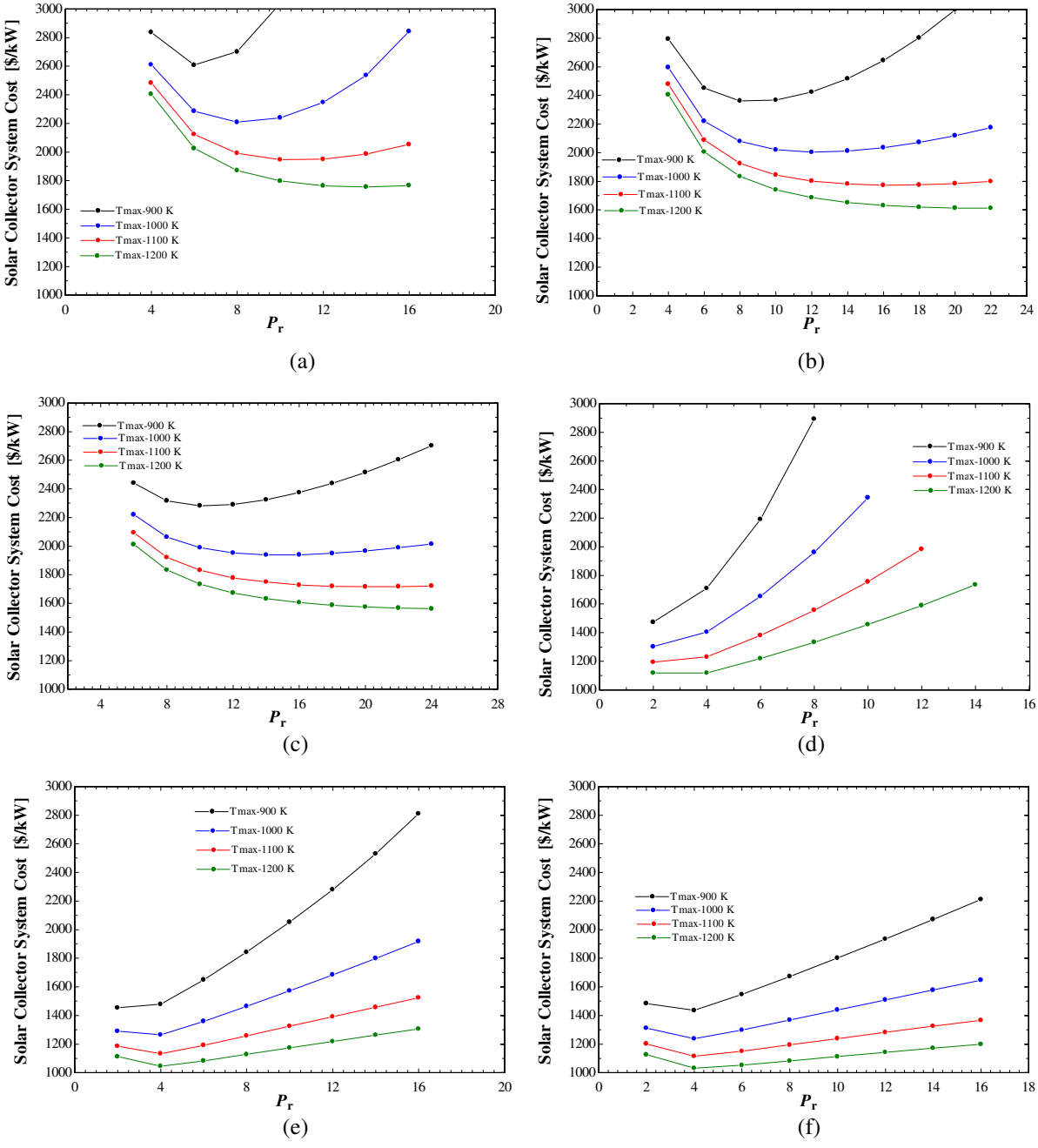

Figure 5.40: Solar Collector System Cost variation for different configurations: (a) Simple cycle, (b) Single-stage Intercooler, (c) Two-stage Intercooler, (d) Recuperator, (e) Single-stage Intercooler with Recuperator and (f) Two-stage Intercooler with Recuperator

Gas Turbine Cost

The GT has the next highest expense share from the power-plant cost. The GT system cost depends largely on the mass-flow rate of air through the system and partly on the pressure ratio. The GT cost reduces with increase in peak cycle temperature for all configurations as the GT mass-flow reduces with it. The simple cycle and intercooler-only system (Figure 5.41a, 5.41b and 5.41c) show a linear variation of GT cost with pressure ratio where the GT cost increases with higher pressure ratio. For the recuperator augmented systems (Figure 5.41d, 5.41e and 5.41f), the GT cost initially reduces then increases with increase in system pressure ratio following the trend for GT mass-flow.

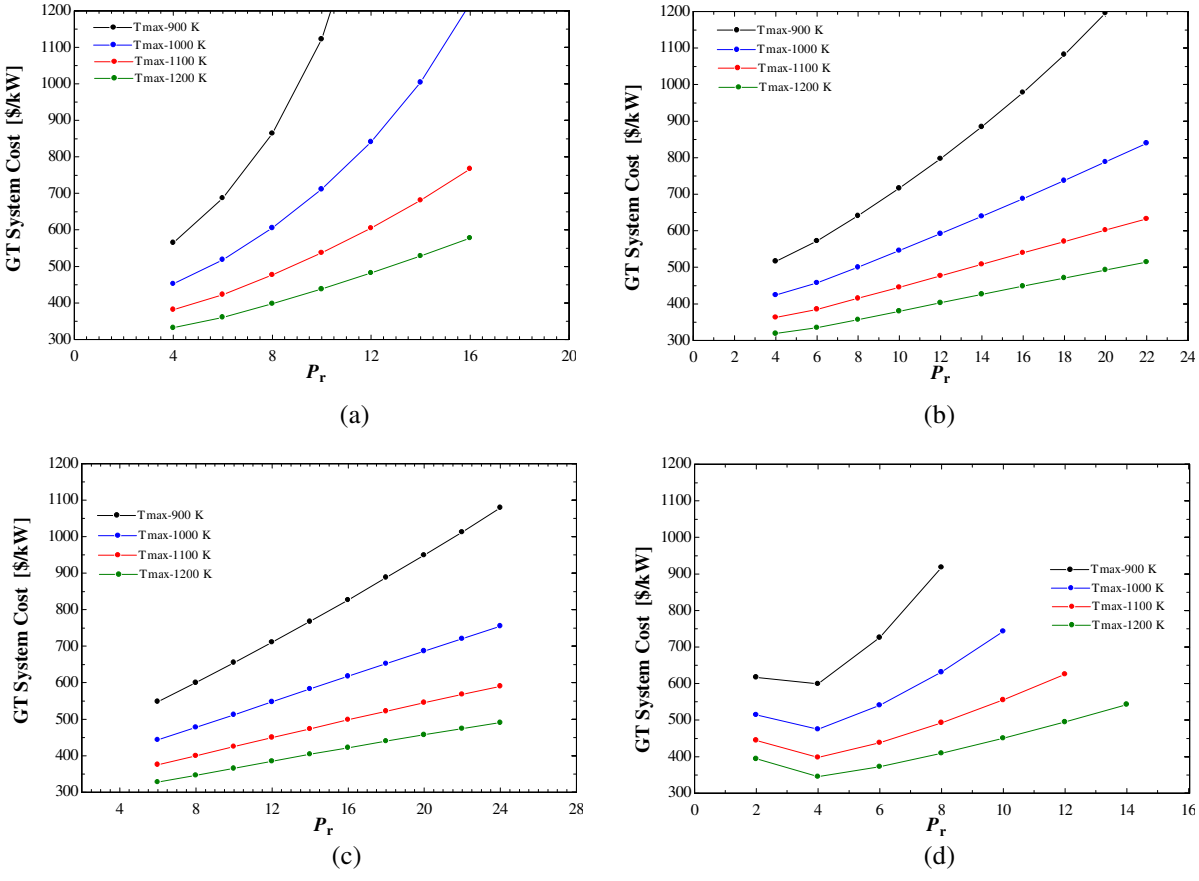

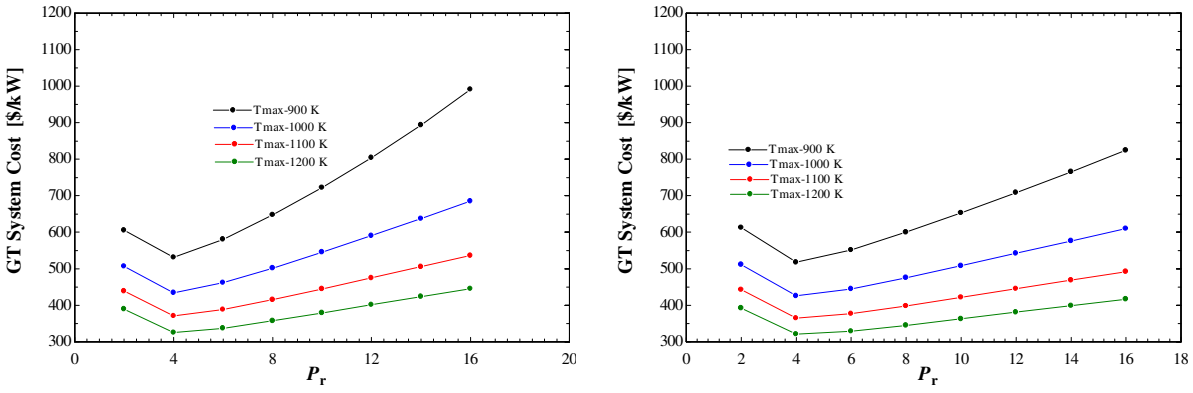

Figure 5.41: GT Cost variation for different configurations: (a) Simple cycle, (b) Single-stage Intercooler, (c) Two-stage Intercooler, (d) Recuperator, (e) Single-stage Intercooler with Recuperator and (f) Two-stage Intercooler with Recuperator

Heat-exchanger Cost

The heat-exchangers in the power-plant account for the lowest share in the cost of the power-plant. However, this is the only cost component to show maximum variation among different configurations. This is because the augmentations done on the GT system, namely intercooler and recuperator are basically heat-exchangers. So, for different configurations, the number of heat exchangers varies and for each heat-exchanger, the cost depends on the heat-exchanger surface area. The heat-exchanger present in all the configurations is the solar heat-exchanger which extracts the heat from HTF. The intercooler is a smaller heat-exchanger based on the heat transfer requirement at compression stage. The recuperator with air on both sides as the working fluid and the amount of heat transfer, nets the highest share in the heat-exchanger cost.

The heat-exchanger accounts for up to 3% of the power-plant cost. The simple cycle and intercooler-only systems (Figure 5.42a, 5.42b and 5.42c) have the lowest heat-exchanger cost for the most economical systems in each configuration. The recuperator augmented systems (Figure 5.42d, 5.42e and 5.42f) have higher heat exchanger cost due to presence of the recuperator.

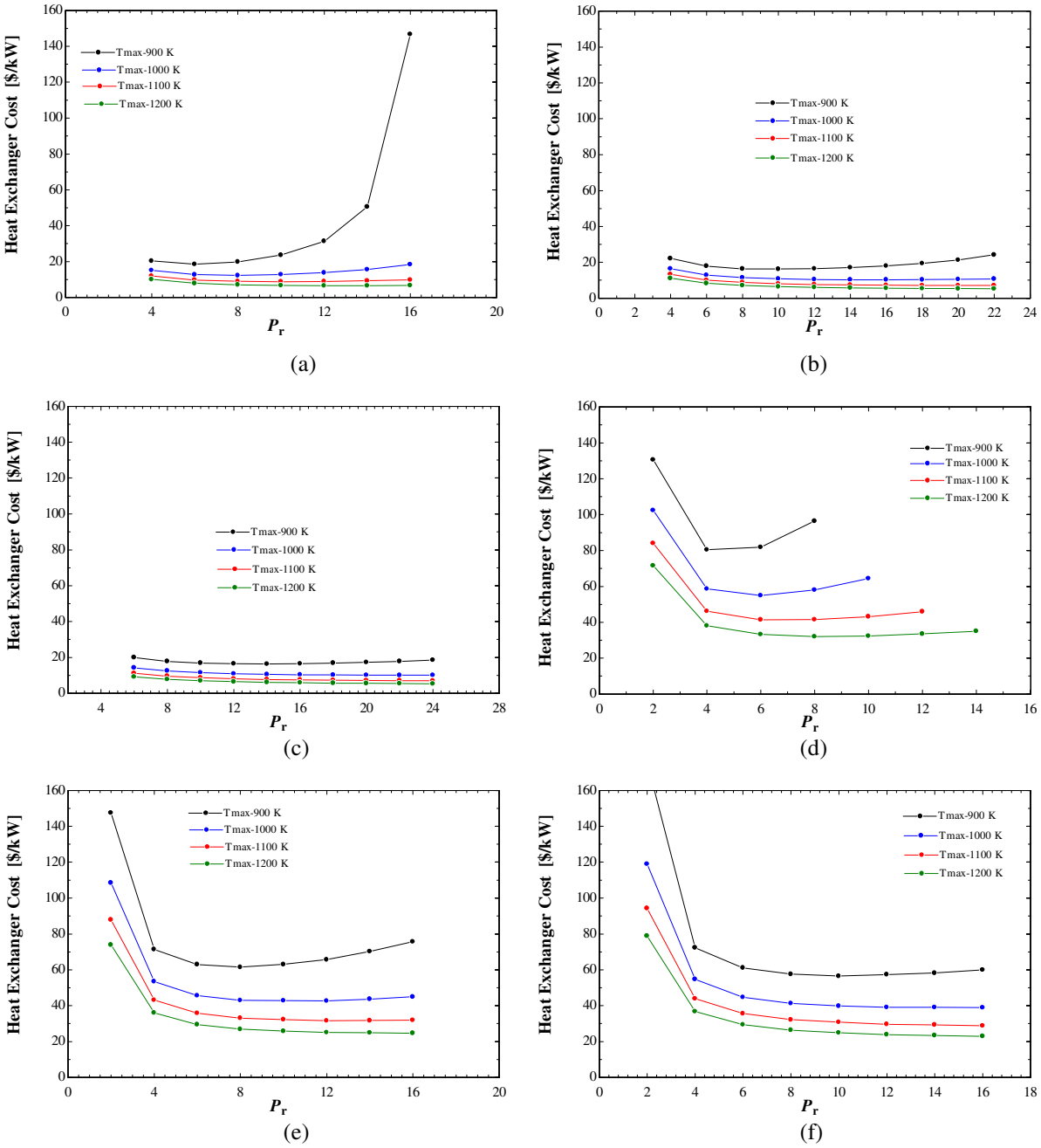

Figure 5.42: Heat-exchanger Cost variation for different configurations: (a) Simple cycle, (b) Single-stage Intercooler, (c) Two-stage Intercooler, (d) Recuperator, (e) Single-stage Intercooler with Recuperator and (f) Two-stage Intercooler with Recuperator

Power-plant Cost

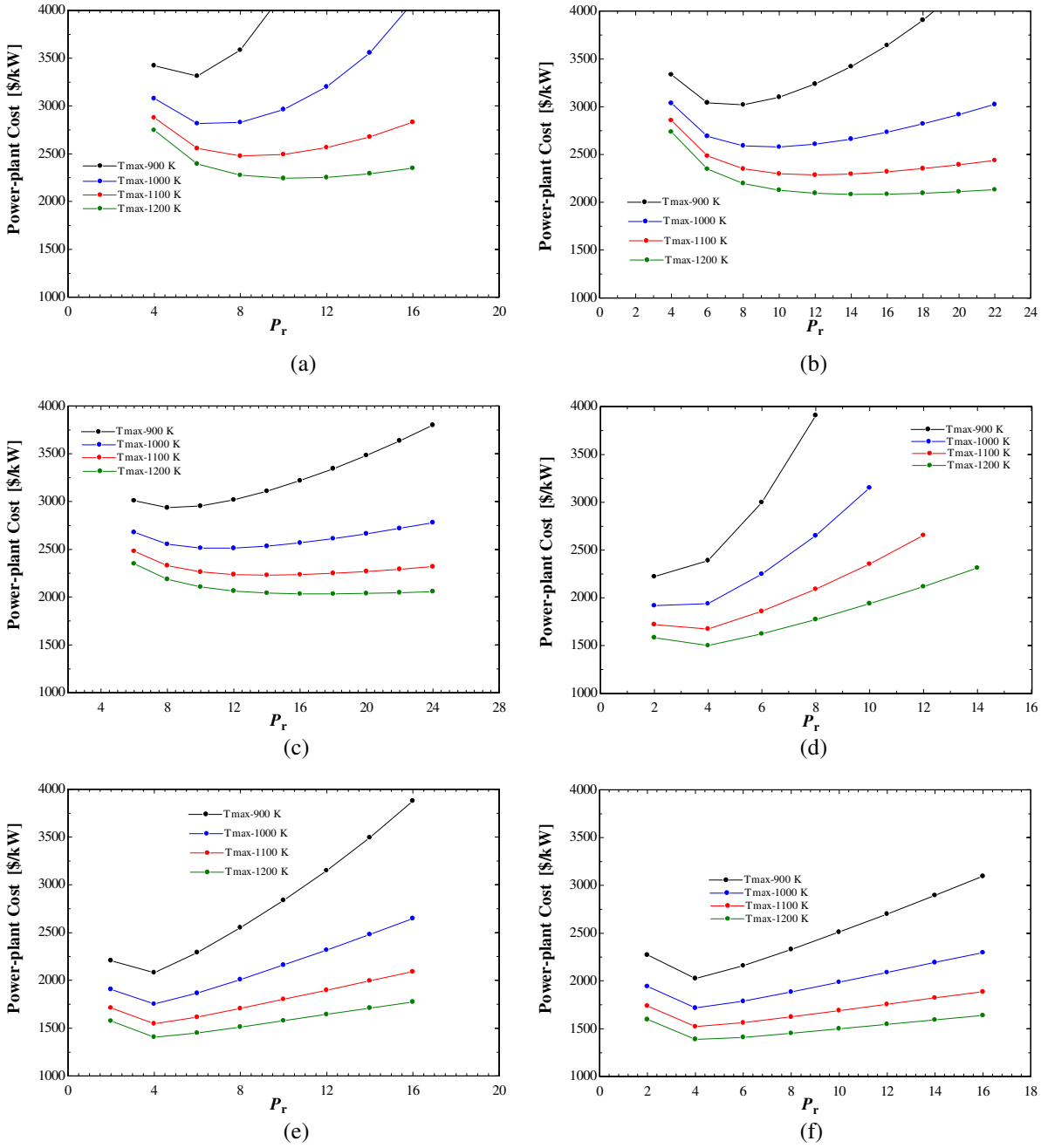

Figure 5.43: Power-plant Cost variation for different configurations: (a) Simple cycle, (b) Single-stage Intercooler, (c) Two-stage Intercooler, (d) Recuperator, (e) Single-stage Intercooler with Recuperator and (f) Two-stage Intercooler with Recuperator

As the solar collector system has the highest share in the cost of the power-plant, the power-plant cost shows a favorable trend for the configurations with recuperator which had the highest GT efficiency leading to a smaller solar collector system.

Annualized Life-cycle Cost

The annualized life-cycle cost is the yearly cost incurred on the operation of power-plant for the planning period based on the total power-plant cost discounted for the future and considering the inflation for the said period. It also incorporates the annual O&M cost to calculate the yearly expense incurred on the operation of the power-plant.

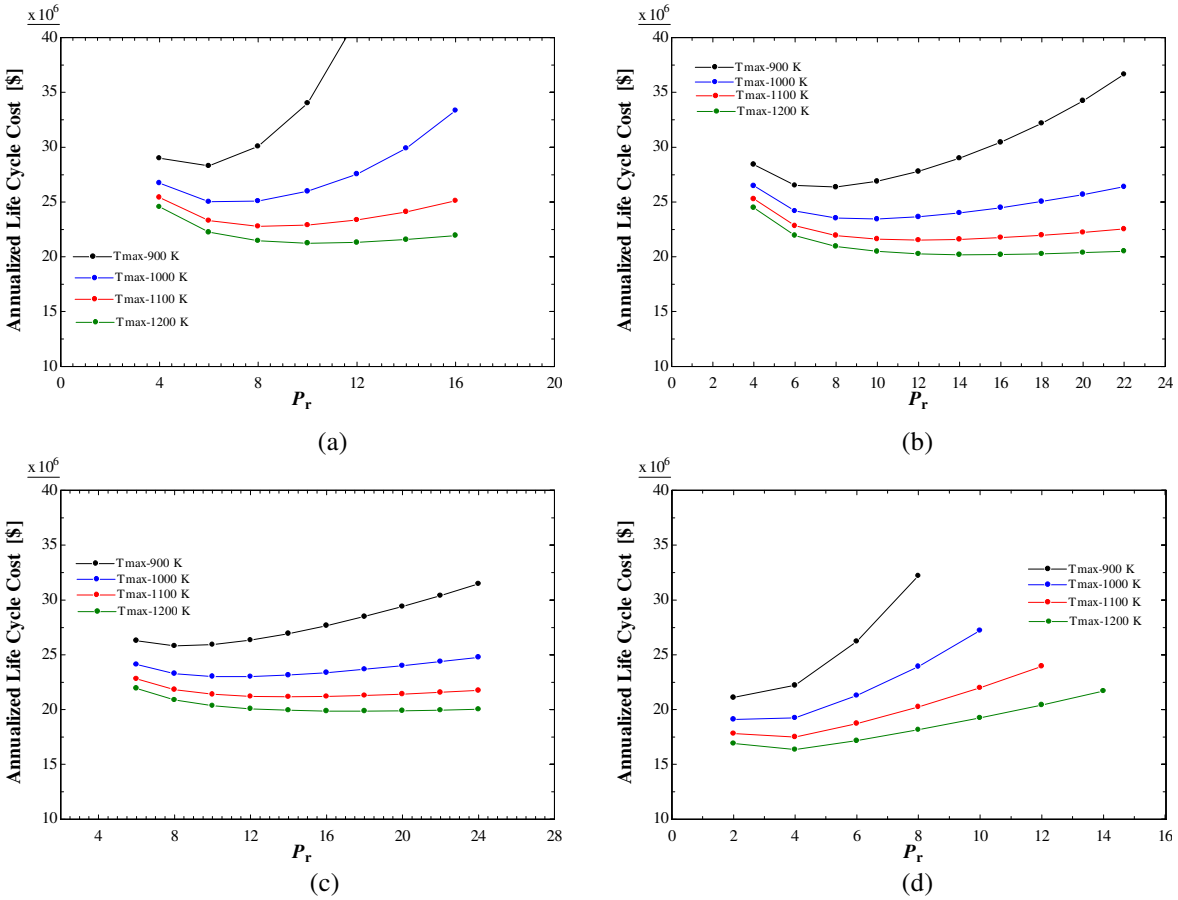

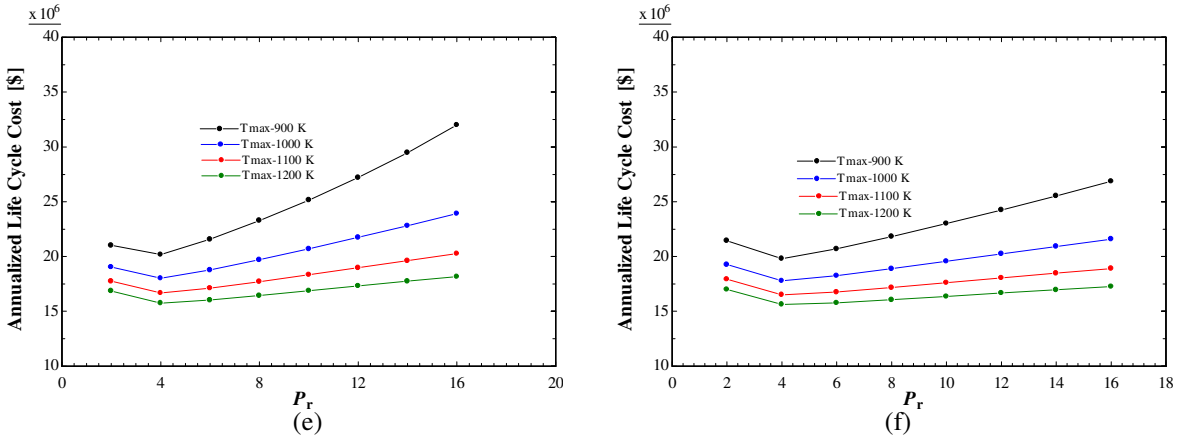

Figure 5.44: Annualized Life-cycle Cost variation for different configurations: (a) Simple cycle, (b) Single-stage Intercooler, (c) Two-stage Intercooler, (d) Recuperator, (e) Single-stage Intercooler with Recuperator and (f) Two-stage Intercooler with Recuperator

The simple cycle configuration costs $ 21 million yearly. The intercooler-only systems (Figure 5.44b and 5.44c) bring this cost down to $ 20 million. However, the recuperator augmented systems bring this cost down to $16.5 million.

Unit Cost of Electricity

The unit cost of electricity depends on two major factors, the annual cost of the power-plant and the annual electricity generation. The combined effect of these factors is seen in the trends for unit cost of electricity for each configuration.

For all configurations, the unit cost of electricity initially reduces with increase in peak cycle temperature and then it increases. This trend is accounted for by the reduction in receiver performance with increase in peak cycle temperature. The optimum peak cycle temperature for simple cycle and intercooler-only systems (Figure 5.45a, 5.45b and 5.45c) is 1200 K. For the recuperator augmented systems (Figure 5.45d, 5.45e and 5.45f), the peak cycle temperature comes down to 1100 K.

For the simple cycle and intercooler-only systems, the unit cost of electricity is high at low pressure ratio and then it reduces at higher pressure ratio. While for the recuperator

augmented systems, the unit cost initially drops to a minimum at lower pressure ratio then it rises again with increasing pressure ratio.

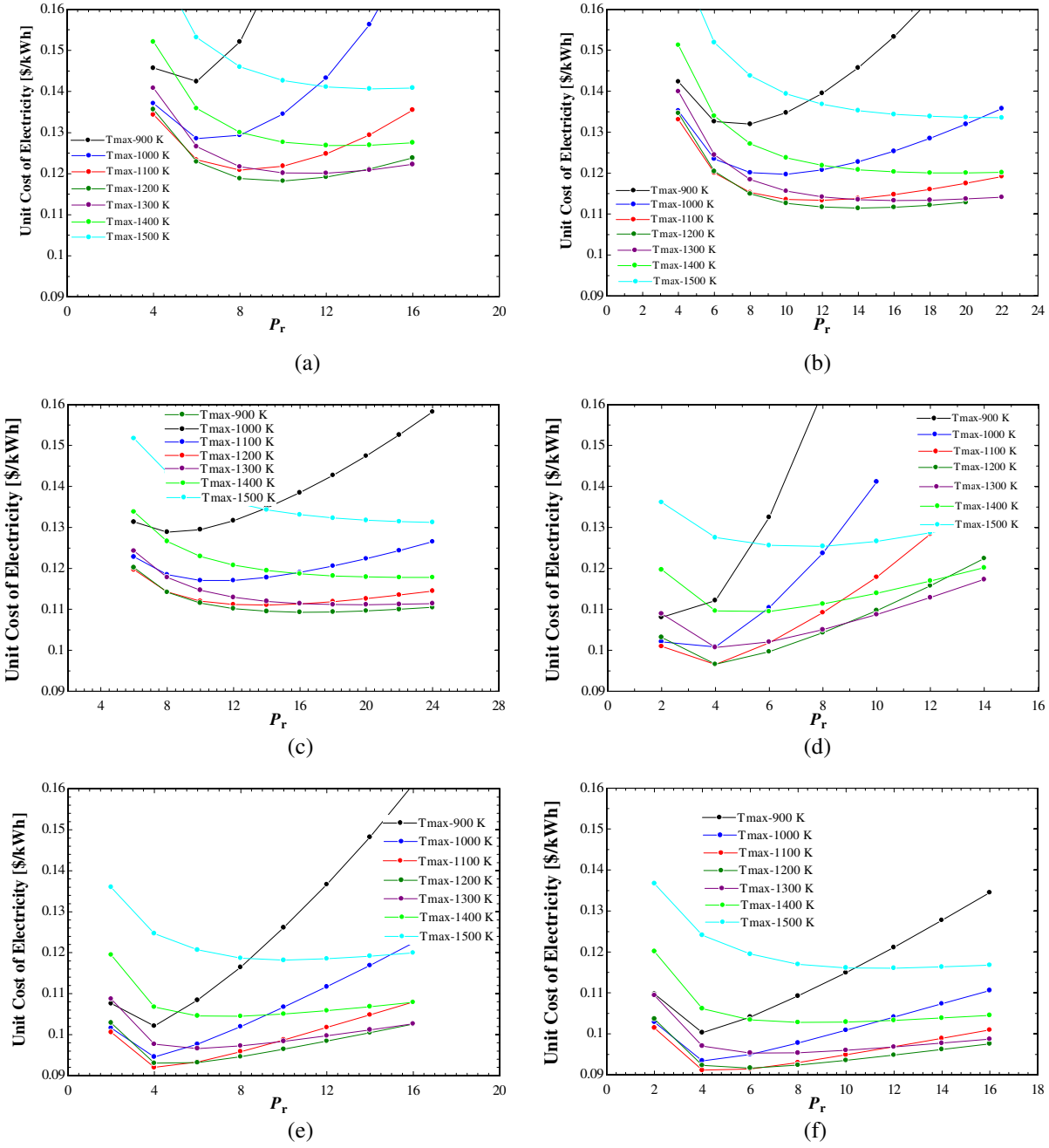

Figure 5.45: Unit Cost of Electricity variation for different configurations: (a) Simple cycle, (b) Single-stage Intercooler, (c) Two-stage Intercooler, (d) Recuperator, (e) Single-stage Intercooler with Recuperator and (f) Two-stage Intercooler with Recuperator

The unit cost of the most economical system for each configuration ranged from 12 cent/kWh for the simple cycle to about 9 cents/kWh for the two-stage intercooler with recuperator configuration.

Summary of System Design for Performance

The HTSGT system was assessed for many design configurations that can be implemented. The typical component performance parameters are listed below. The gas turbine cycle is able to reach efficiencies of above 40% with reasonable sub-system level efficiencies and pressure-losses.

The following tables enlist the improvement in system performance from a simple cycle to addition of intercooler followed by recuperator. The intercooler and the recuperator do act together to improve the HTSGT system performance significantly.

Table 5.5: GT system parameters for peak power plant economy for each configuration

System Configuration	Pressure Ratio	Peak Cycle Temperature	Mass-flow rate	Effective Temperature of Heat Input	Effective Temperature of Heat Rejection	Thermal Power Input	GT Efficiency	Annual Energy Conversion	GT Cost
	[-]	[K]	[kg/s]	[K]	[K]	[MW]	[%]	[GWh]	[$/kW]
Simple Cycle	10	1200	553	875	495	360	28	180	438
Intercooler-1 Stage	14	1200	449	826	448	331	30.5	181	426
Intercooler-2 Stage	16	1200	415	802	430	322	31.4	182	422
Recuperator	4	1100	764	936	387	246	41	181	398
Recuperator + Intercooler-1 Stage	4	1100	694	934	350	227	44.5	181	371
Recuperator + Intercooler-2 Stage	4	1100	679	933	340	223	45.2	181	365

GT Performance

The highest GT efficiency among the assessed configurations is attained with a 2-stage intercooler and recuperator system. The Intercooler improves GT efficiency for a given peak cycle temperature and allows for higher efficiency by increasing pressure ratio. The recuperator requires a lower pressure ratio for performance but improves the GT efficiency drastically. GT cost varies from 438 $/kW for simple cycle to 345 $/kW for recuperated system. Table 5.5 shows the best parameters for the GT system for each configuration.

Solar Collector System Performance

The solar collector system which includes the heliostat field and the central receiver shows a reduction in cost from 1797 $/kW for simple cycle to 1115 $/kW for the two-stage intercooler with recuperator configuration. The heliostat field and receiver area are inversely dependent on the GT efficiency which increases from simple cycle to two-stage intercooler configuration. Another interesting observation is that the receiver efficiency also increases from simple cycle to augmented configurations. The intercooled systems have higher receiver efficiency than the recuperated and intercooled system. This happens because of lower average HTF temperature for intercooled system configurations due to intercooling. Table 5.6 shows the solar collector system parameters for each configuration.

Table 5.6: Solar collector system parameters for peak power plant economy for each configuration

System Configuration	Pressure Ratio	Peak Cycle Temperature	Incident Solar Radiation	Energy to Receiver	Receiver Efficiency	Energy to Power-block	GT Efficiency	Annual Energy Conversion	Solar Collector System Cost
	[-]	[K]	[GWh]	[GWh]	[%]	[GWh]	[%]	[GWh]	[$/kW]
Simple Cycle	10	1200	1802	793	85.1	641	28	180	1797
Intercooler-1 Stage	14	1200	1654	728	85.9	594	30.5	181	1651
Intercooler-2 Stage	16	1200	1608	707	86.2	579	31.4	182	1605
Recuperator	4	1100	1226	539	86.4	443	41	181	1230
Recuperator + Intercooler-1 Stage	4	1100	1127	496	86.5	407	44.5	181	1133
Recuperator + Intercooler-2 Stage	4	1100	1107	487	86.5	400	45.2	181	1115

Power plant Performance

Table 5.7 shows the overall power plant performance for each configuration. The overall efficiency of power plant improves from 10% of incident solar radiation converted to electricity to 16.4% for the two-stage intercooler with recuperator system. The augmentation of recuperator increases the overall efficiency significantly.

Solar collector system and GT system costs show a decrease with augmentation of intercooler and recuperator but the heat exchanger cost rises with augmentation of

recuperator as the surface area requirement for the recuperator is higher due to air as the working fluid for the recuperator.

The power plant capital expense reduces from 2242 $/kW for simple cycle system to 1523 $/kW for the two-stage intercooler with recuperator system. The operations and maintenance (O&M) cost is same for all configurations as the value is fixed based on rated system power. In reality, with improved system performance for augmented configurations which reduce the size of the power plant for the same rated capacity, the O & M cost will be lower compared to simple cycle.

The annualized life-cycle cost reduces from 21.2 MM$/year for simple cycle configuration to 16.5 MM$/year for the two-stage intercooler with recuperator configuration. The annual energy conversion to electricity is at 180 GWh for simple cycle configuration. It increases for intercooled systems due to increase in receiver efficiency. For recuperator only configuration, the receiver efficiency is lower than simple cycle configuration due to higher average HTF temperature due to recuperation. This causes the energy conversion to drop below simple cycle configuration's energy conversion. For the recuperated configurations with intercooling, the peak cycle temperature is lower which improves the receiver efficiency.

The unit cost of electricity reduces from 11.8 cents/kWh to 9.1 cents/kWh from simple cycle configuration to two-stage intercooler with recuperator configuration.

The best configuration is the two-stage intercooler with recuperator which has the highest GT efficiency leading to lowest capital cost.

Table 5.7: Power plant system parameters for peak power plant economy for each configuration

System Configuration	Pressure Ratio	Peak Cycle Temperature	Receiver Efficiency	GT Efficiency	Overall Efficiency	Solar Collector System Cost	GT Cost	Heat Exchanger Cost	Power plant Cost	O & M Cost	Annualized Life-cycle Cost	Annual Energy Conversion	Cost of Unit Electricity
	[-]	[K]	[%]	[%]	[%]	[$/kW]	[$/kW]	[$/kW]	[$/kW]	[MM$/yr]	[MM$/yr]	[GWh]	[cents/kWh]
Simple Cycle	10	1200	85.1	28	10	1797	438	7	2242	6.5	21.2	180	11.8
Intercooler-1 Stage	14	1200	85.9	30.5	11	1651	426	6	2083	6.5	20.2	181	11.1
Intercooler-2 Stage	16	1200	86.2	31.4	11.3	1605	422	6	2034	6.5	20	182	10.9
Recuperator	4	1100	86.4	41	14.8	1230	398	46	1674	6.5	17.5	181	9.6
Recuperator + Intercooler-1 Stage	4	1100	86.5	44.5	16.1	1133	371	43	1547	6.5	16.7	181	9.2
Recuperator + Intercooler-2 Stage	4	1100	86.5	45.2	16.4	1115	365	44	1523	6.5	16.5	181	9.1

Cost Sensitivity Analysis

There are many parameters which have been assumed constant for system performance assessment for all configurations based on certain stated assumptions. However, these assumptions can change leading to a change in the values of the assumed constants. In this section, we assess the sensitivity of the performance for the best configuration i.e. two-stage intercooler with recuperator configuration to variation in these parameters individually.

GT compressor efficiency

The GT compressor(s) efficiency has been assumed to be 86% based on GE's 6FA GT compressor performance. Figure 5.46 shows the variation in unit cost of electricity with compressor efficiency.

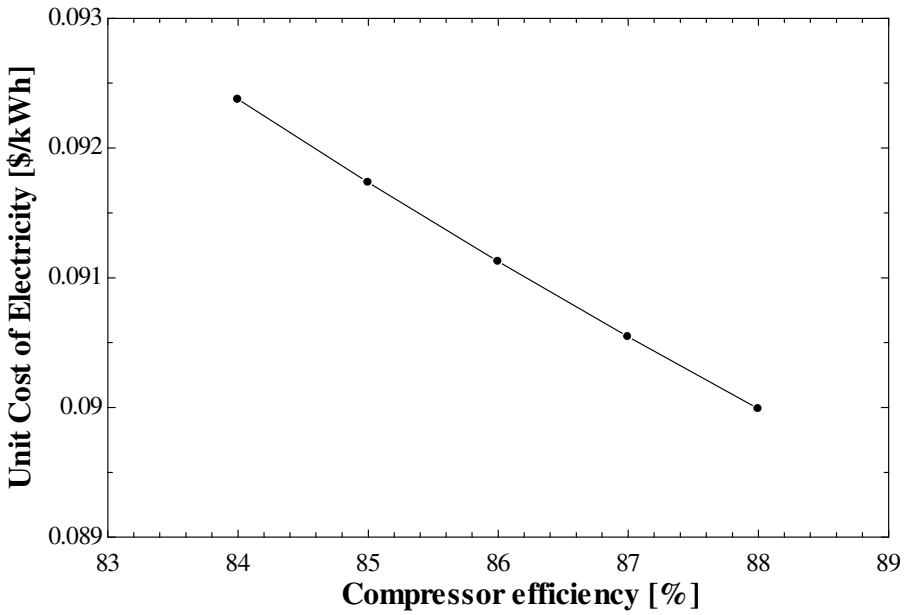

Figure 5.46: Sensitivity of unit cost of electricity to compressor efficiency - Two-stage Intercooler with Recuperator

The unit cost of electricity reduces with increase in GT compressor efficiency and the unit cost of electricity is 9.0 cents/kWh for a compressor efficiency of 88%.

GT turbine efficiency

The GT turbine efficiency has been assumed to be 85% based on GE's 6FA GT turbine performance. Figure 5.47 shows the variation in unit cost of electricity with turbine efficiency.

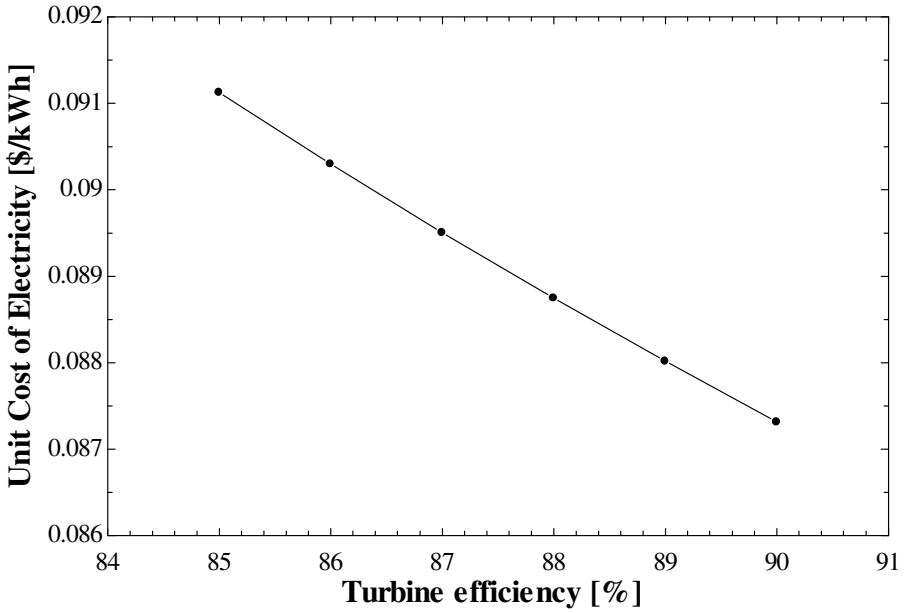

Figure 5.47: Sensitivity of unit cost of electricity to turbine efficiency - Two-stage Intercooler with Recuperator

The unit cost of electricity reduces with increase in GT turbine efficiency and the unit cost of electricity is 8.7 cents/kWh for a turbine efficiency of 90%.

Heat exchanger effectiveness

The heat exchanger effectiveness has been assumed to be 95% based on MPBR heat exchanger design study. Figure 5.48 shows the variation in unit cost of electricity with heat exchanger effectiveness. The unit cost of electricity increases with decrease in heat exchanger effectiveness from 95%.

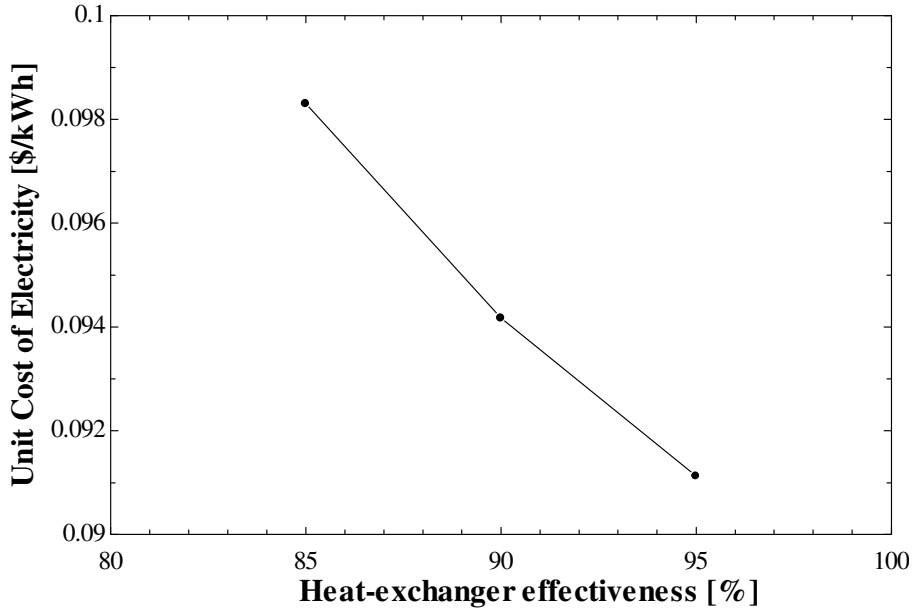

Figure 5.48: Sensitivity of unit cost of electricity to heat exchanger effectiveness - Two-stage Intercooler with Recuperator

Heat exchanger pressure loss

The heat exchanger pressure loss has been assumed to be 2% based on MPBR heat exchanger design study. Figure 5.49 shows the variation in unit cost of electricity with heat exchanger pressure loss.

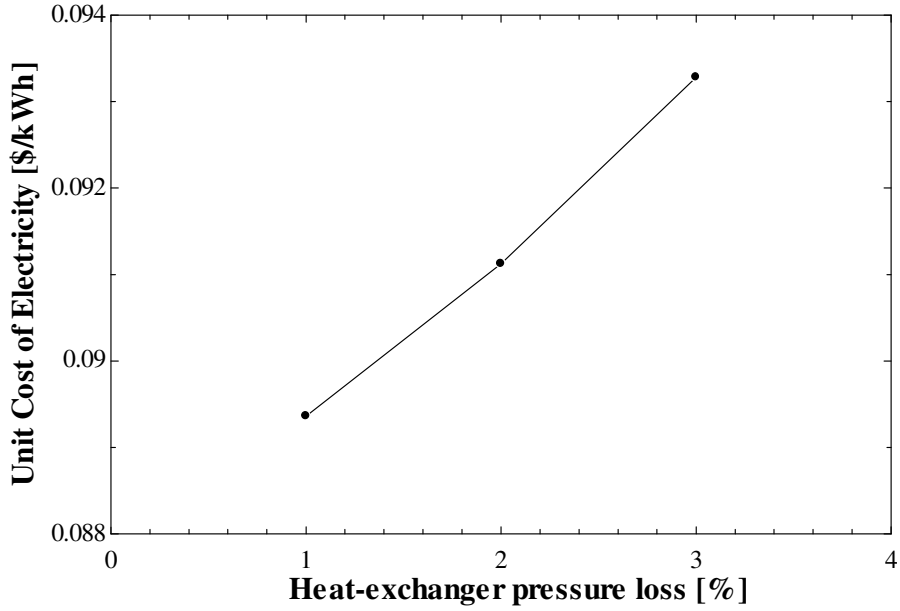

Figure 5.49: Sensitivity of unit cost of electricity to heat exchanger pressure loss- Two-stage Intercooler with Recuperator

The unit cost of electricity increases with increase in heat exchanger pressure loss. So, the lowest unit cost of electricity is 8.9 cents/kWh for 1% pressure loss. The heat exchanger cost increases due to tighter tolerance on pressure loss, but the overall performance increases, resulting in reduction of unit cost of electricity.

Solar multiple

Solar multiple is the ratio of input thermal power capacity to design thermal power. The solar multiple for a system without thermal storage should be at 1. With thermal storage, the excess thermal energy from the field is stored for post daylight operation of the plant. However, the extra field area will also improve the capacity factor of the plant. This assessment is to determine the improvement in energy cost by increasing the solar multiple. Figure 5.50 shows the variation in unit cost of electricity with solar multiple.

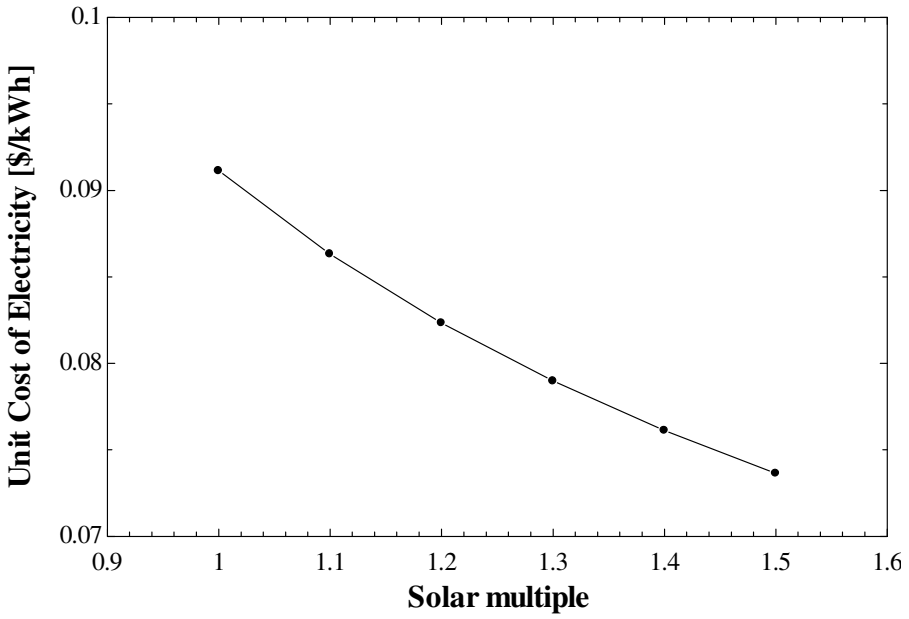

Figure 5.50: Sensitivity of unit cost of electricity to solar multiple - Two-stage Intercooler with Recuperator

For this assessment, solar multiple is used in sizing the solar collector system and determining the solar energy incident on the field, which assumes all energy from the field, is being directed to the power-block, which might not happen in reality if there is

excess power input than rated capacity of the GT system. Also, the heliostat field efficiency will drop with increase in field size, which is not accommodated in the calculations. So the cost estimate for higher solar multiple has to be considered with the caution as the energy cost prediction is lower than reality. The unit cost of electricity reduces with increase in solar multiple and for a solar multiple of 1.5 the unit cost of electricity is 7.4 cents/kWh.

Asset discount rate

The discount rate has been assumed to be 7.5% for the power plant. Figure 5.51 shows the variation in unit cost of electricity with change in discount rate.

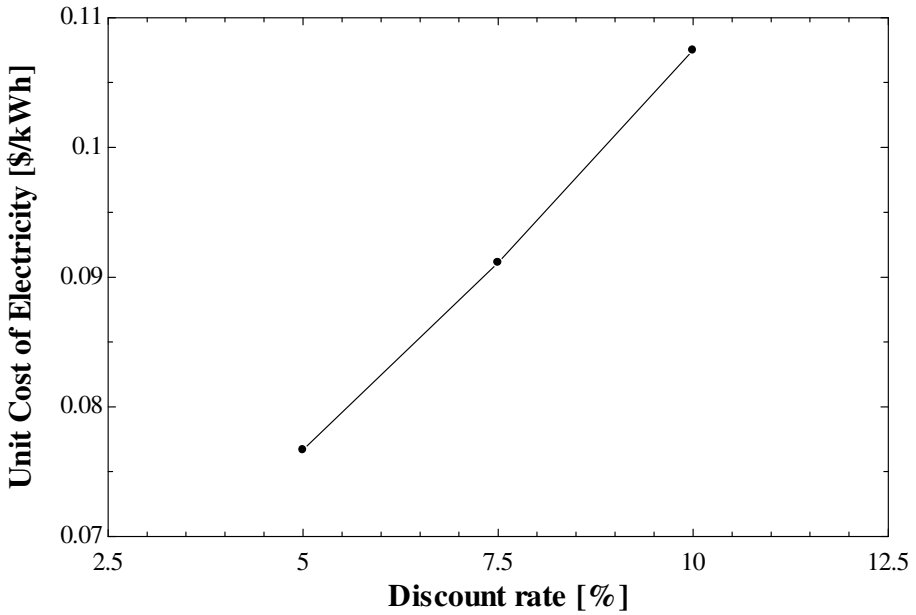

Figure 5.51: Sensitivity of unit cost of electricity to discount rate - Two-stage Intercooler with Recuperator

The unit cost of electricity reduces with decrease in discount rate and the unit cost of electricity is 7.7 cents/kWh for a discount rate of 5%. The unit cost of electricity is very sensitive to changes in discount rate.

Planning period

The planning period (also known as economic life) has been assumed to be 30 years for the power plant. Figure 5.52 shows the variation in unit cost of electricity with change in discount rate.

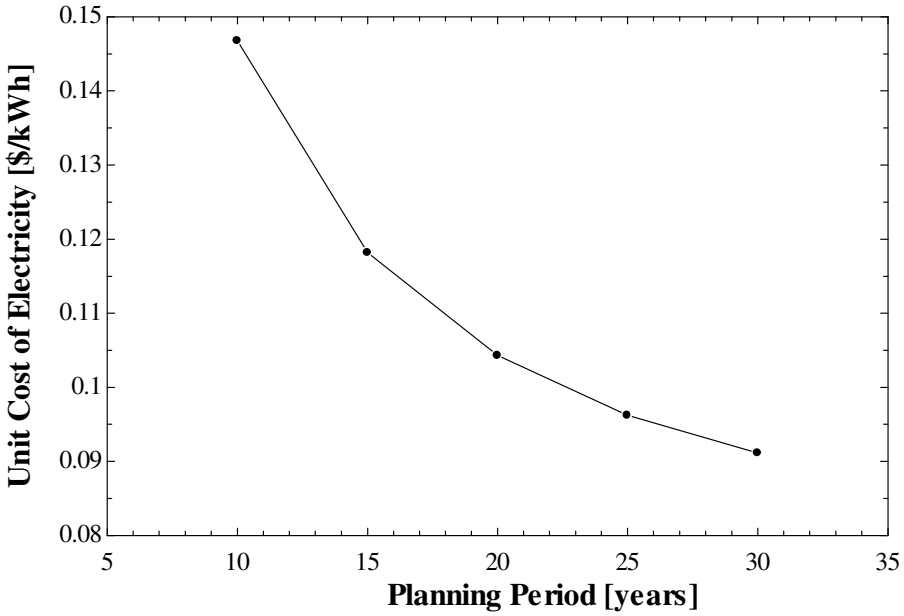

Figure 5.52: Sensitivity of unit cost of electricity to planning period - Two-stage Intercooler with Recuperator

The unit cost of electricity reduces with increase in economic life and for a planning period of 30 years, the unit cost of electricity is 9.1 cents/kWh, same as the base case. The unit cost of electricity initially drops rapidly then gradually with increase in economic life. The unit cost of electricity is again very sensitive to change in planning period and so plays a major role in determining accurate unit cost.

Comparison with Helium based Brayton Cycle

As reviewed in the MPBR study, helium based Brayton cycle is the preferred cycle for nuclear power generation system to extract heat from the gas reactor. Brayton cycle allows for a higher reactor core outlet temperature compared to Rankine cycle, while helium acts as an inert working fluid best suited for the radioactive environment. Helium also has higher specific heat and thermal conductivity which improves its heat transfer characteristics significantly compared to air resulting in smaller gas turbine and heat-exchanger surface area and achieving higher effectiveness for the heat exchanger for the same cost compared to air. Also, the closed loop cycle required for helium based gas turbine system can be utilized to operate the system at higher pressure resulting in a more compact gas turbine (Chunyun, 2003). So it is imperative to make an assessment of the helium based gas turbine system operating in closed loop and compare its performance with the air based gas turbine system operating in both open cycle and closed loop cycle as a feasible option for a solar gas turbine system.

This assessment was done on the optimum configuration obtained for the HTSGT system, i.e. gas turbine system with two stage intercooler and recuperator. Figure 5.53 shows the comparison of the unit cost of electricity for air and helium based gas turbine systems, both operating at 100 kPa (atmospheric pressure) and 2000 kPa at compressor inlet. The higher operating pressure was chosen based on the assessment for MPBR system (Chunyun, 2003).

The system performances for both the working fluids are not too different as seen in Figure 5.53. For both working fluids, the system operating at higher pressure yields a lower unit cost of electricity. However, between the two working fluids, the air based gas turbine system performs more economically at corresponding operating conditions than the helium based system. This is due to the higher overall efficiency for the air based

system. Table 5.8 lists the system level parameters for all the four configurations depicted above.

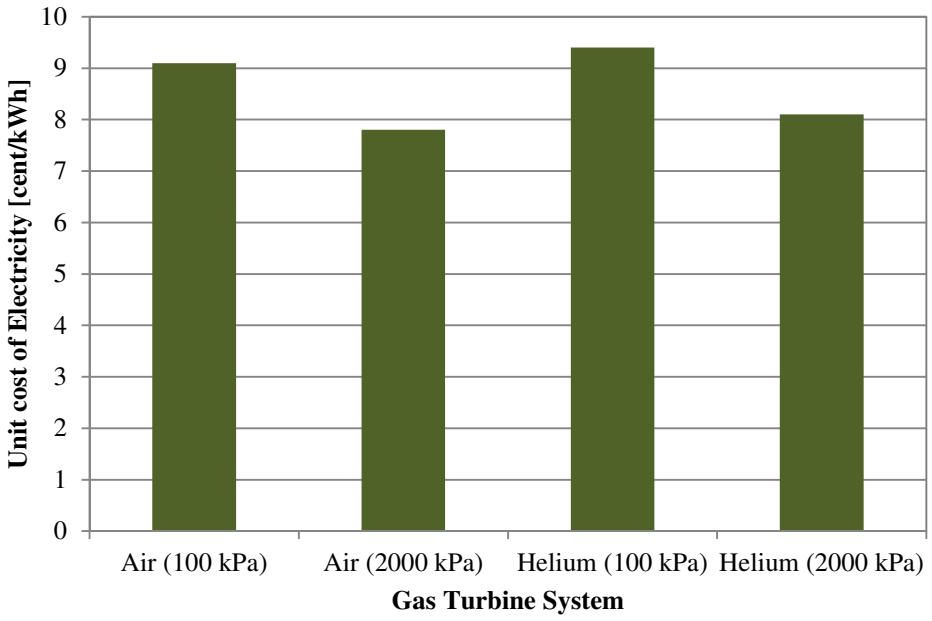

Figure 5.53: Unit cost of electricity for Air and Helium based Gas Turbine systems

The helium based systems have smaller heat exchangers as expected resulting in a lower heat exchanger cost. However, it does not show a significant difference in gas turbine system cost. The gas turbine system performance for the helium based system is lower compared to the air based system at comparable peak cycle temperature. This happens due to higher specific heat for helium which yields lower cycle efficiency with a recuperated configuration. The major cost for the power plant system is the solar collector system which depends mainly on the gas turbine system performance. This reduces the impact of reduction in the gas turbine system cost for the high operating pressure systems on the unit cost of electricity. One more important point to note is that the GT system cost implements the cost model developed based on air based GT systems, so it does not account for the increase in number of stages in the helium based GT system for both compressor and turbine sub-systems. This is due to the fact that owing to higher

heat capacity of the helium gas, the work imparted or extracted at a single stage of the turbo-machine (compressor or turbine) is small and raises the enthalpy of helium by smaller quanta. This necessitates an increase in number of stages in a helium based GT system. This fact is verified by the estimate of helium based turbo-machine cost in MPBR study (Chunyun, 2003) which is higher than the estimate calculated in the present study. Overall, the helium based system does not show too high an impact on unit cost of electricity over the air based HTSGT system.

Table 5.8: Power plant system parameters for Air and Helium based configurations

Powerplant Parameters	Unit	Working Fluid			
		Air (100 kPa)	Air (2000 kPa)	Helium (100 kPa)	Helium (2000 kPa)
Tin	[K]	300	300	300	300
Pin	[kPa]	100	2000	100	2000
Tmax	[K]	1100	1100	1200	1100
Pressure ratio	[-]	4	4	4	4
GT Efficiency	[%]	45.2	45.2	45.2	40.8
Receiver Efficiency	[%]	86.5	86.5	83.2	88.2
Overall Efficiency	[%]	16.4	16.4	15.7	15
Annual Electricity	[GWh]	181	181	174	185
Solar Collector System cost	[$/kW]	1110	1110	1120	1240
GT cost	[$/kW]	365	40.5	377	48.2
Heat-exchanger cost	[$/kW]	44.0	11.0	16.0	7.3
Powerplant cost	[$/kW]	1520	1170	1510	1290
Annualized Life cycle cost	[Million $]	16.5	14.2	16.4	15
Unit cost of Electricity	[cent/kWh]	9.1	7.8	9.4	8.1

The improvement in heat exchanger performance is shown in detail in Table 5.9 for the recuperator for each configuration.

Table 5.9: Recuperator Heat-exchanger parameters for Air and Helium based configurations

		Working Fluid							
Hx Parameters	**Unit**	**Air at NTP**		**Compressed Air**		**Helium at NTP**		**Compressed Helium**	
		Cold	**Hot**	**Cold**	**Hot**	**Cold**	**Hot**	**Cold**	**Hot**
Tin	**[K]**	359	833	360	833	383	780	384	715
Pin	**[kPa]**	400	102	8000	2041	400	102	8000	2041
Tout	**[K]**	812	383	812	384	760	403	699	401
Mdot	**[kg/s]**	679		679		98		119	
DP/P	**[kPa]**	0.005	0.02	0.006	0.02	0.005	0.02	0.006	0.02
Re	**[-]**	529	255	10200	4900	162	78	3050	1470
Nu	**[-]**	8.6	5.4	64.0	39.0	4.4	4.1	28.0	17.0
h	**[W/m^2-K]**	547	311	4100	2260	1470	1220	8940	4900
A	**[m^2]**	51000	104000	10800	21900	16300	32900	6660	13500
η_{fin}	**[%]**	88	77	54	38	74	44	38	22
$\eta_{overall}$	**[%]**	91	81	66	47	81	48	54	28
U	**[W/m2-K]**	252	124	1200	590	592	293	1760	872
UA	**[kW/K]**	12900		12900		9660		11700	
NTU	**[-]**	18.1		18.2		19		19	
Qdot	**[MW]**	322		321		192		194	
Cost	**[$Million]**	2.85		0.6		0.9		0.37	

Conclusion

The air based HTSGT system emerges as a viable option for power generation using solar energy. The unit cost of electricity for the system at 9 cent/kWh is much better than the current operating cost for the Rankine cycle based systems and comparable to the projected operating costs for some of the future solar power generation systems. The helium based Brayton cycle compares well with the air based system but does not give a significant improvement in the system performance. There are other factors at a disadvantage for the helium based system like the helium gas being lighter, which makes the gas prone to leakage which requires an additional investment in making the system leak proof. Supercritical Carbon di-oxide based gas turbine systems are also being proposed as a viable power generation system for harnessing solar energy similar to helium based system with improved gas turbine performance at high operating pressure, but the corrosive nature of CO_2 is one of the main challenges that needs to be addressed along with leakage (Chunyun, 2003).

Another advantage of the air based system operating in open cycle is that it can be combined with a gas fired combustion system to augment the system performance and perform as a hybrid system to generate power. It will enhance the capacity factor of the system. This configuration can be incorporated with gas turbine system like GE-10 (Figure 5.54) with a silo combustor. The working fluid can be by-passed to the solar heat exchanger and then passed through the combustor for further raising the temperature of the working fluid.

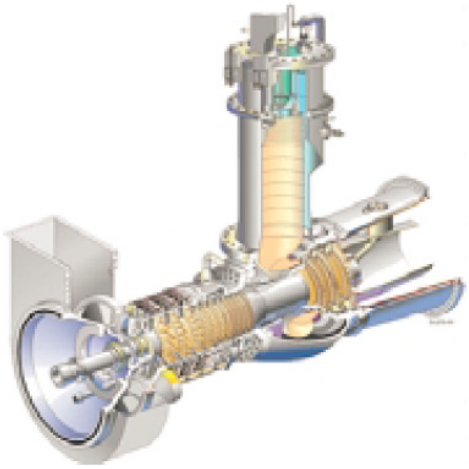

Figure 5.54: GE-10 Gas turbine system (Source: www.ge.com)

The proposed HTSGT system is a preliminary design and needs further investigation in detail to realize a working design, but at this stage it presents itself as a promising option to harness solar energy for power generation.

CHAPTER 6

LORENTZ CYCLE GAS TURBINE

Introduction

An ideal Brayton cycle operating between given maximum and minimum cycle temperatures will have a thermal efficiency lower than Carnot cycle operating between the same temperatures. In the previous chapter, intercooling and regeneration (recuperation) processes were augmented into the Brayton cycle to improve the thermal efficiency of the gas turbine (GT).

There are thermodynamic cycles which under specific conditions match the Carnot cycle efficiency, like the Ericsson cycle and Stirling cycle (Nag, 2005). The Ericsson cycle comprises of two isothermal processes with two isobaric processes. Figure 1 shows the temperature-entropy plot for the Ericsson cycle. The Ericsson cycle efficiency with ideal regeneration ($Q_{2\text{-}3} = Q_{4\text{-}1}$) achieves Carnot efficiency.

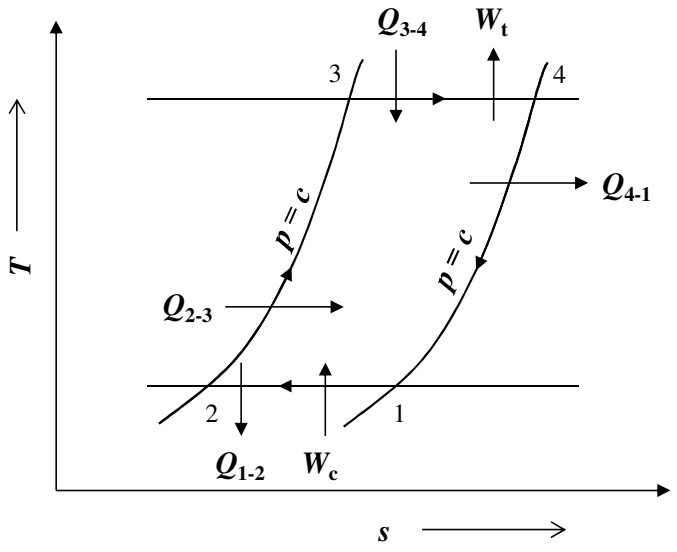

Figure 6.1: Ericsson Cycle

However, it is difficult to achieve a perfect isothermal condition in a GT, but with a heat source and sink of finite heat capacity, a gliding temperature compression and expansion

process is achievable. This modified Ericsson cycle is called the Lorentz (or Lorenz) cycle.

The Lorentz cycle has been attributed to H. Lorenz by Zeuner in his book on thermodynamics (Zeuner, 1907). The cycle developed by Lorentz had two adiabatic processes and two polytropic processes. In recent years other authors and researchers, notably Alefeld and Rademacher have recognized the benefits of gliding temperature cycles (Alefeld et. al, 1993), which may be correctly called Lorenz cycles or alternatively identified as Lorentz cycles by Lee and Kim (1992). They show that the Lorentz cycle has higher second law efficiency than Carnot cycle for a heat source of finite heat capacity rates. The compression and expansion processes are adiabatic while heat addition and rejection processes are gliding temperature processes.

Lorentz Cycle

The Lorentz cycle proposed in this study has two isobaric and two polytropic (gliding temperature) processes. Figure 2 shows the proposed cycle with the individual process steps.

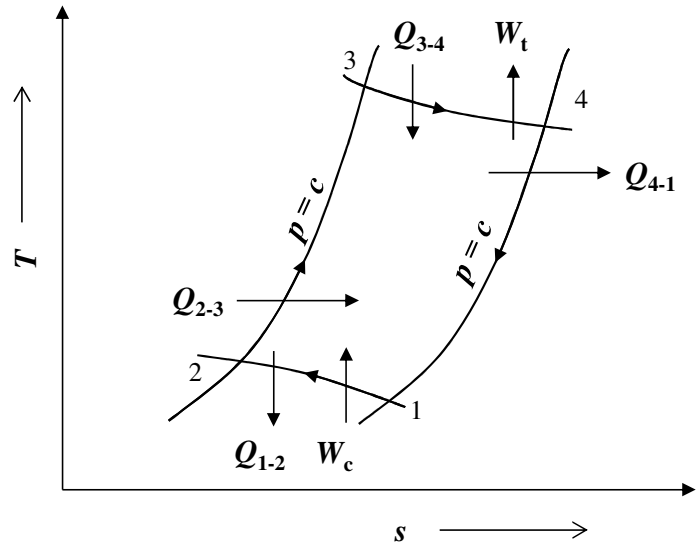

Figure 6.2: Proposed Lorentz Cycle

The cycle is initiated at station 1 with the polytropic compression process. Work W_c is imparted to the working fluid and heat $Q_{1\text{-}2}$ is extracted from it. Between station 2 and station 3, heat $Q_{2\text{-}3}$ is added to the working fluid at constant pressure. The next process is polytropic expansion between stations 3 and 4 with heat addition $Q_{3\text{-}4}$ and work extraction W_t. The final process that completes the cycle is isobaric heat extraction $Q_{4\text{-}1}$ which brings the working fluid from station 4 back to station 1. This cycle is applicable on a standard GT with modifications and the GT thus modified is called the Lorentz Cycle Gas Turbine (LCGT).

A closer look at Figure 2 will reveal that the gliding temperature compression process is very similar to the adiabatic compression followed by intercooling in multiple stages. Similarly, the polytropic expansion process is likened to adiabatic expansion with reheating in multiple stages. The temperature gliding results from the heat transfer for both compression and expansion processes happening between the working fluid and sources of finite heat capacity rate. The details of the sources will be described in the coming sections. The advantage of this cycle is that with recuperation, the effective temperatures of heat addition and heat extraction are very close to the maximum and minimum cycle temperatures respectively. This implies that the thermal efficiency of the cycle will be very close to the Carnot efficiency than the standard GT operating between the same temperatures.

This chapter attempts to explore the possibility of implementing a Lorentz cycle gas turbine with a feasible economy of performance. The next sections will describe the conceptual assessment of the LCGT system and discuss the feasibility of its implementation.

Lorentz Cycle Implementation

The standard GT operates an open air Brayton cycle. The heat addition is achieved in a combustion stage after compression in an axial compressor. The working fluid with elevated temperature expands through the axial turbine generating work. The working fluid is exhausted into the atmosphere after passing through the turbine. For the LCGT, the standard GT needs to be augmented. The prevalent practice is to install external sub-systems like intercooler and reheater and split the GT into multiple stages of compressors and turbines (Cengel, 1998). These external sub-systems are heat-exchangers to provide heat to or extract from an external source outside the GT. The disadvantage of this approach is that the overall system becomes complicated and bulky with multiple sub-systems.

To avoid these shortcomings, LCGT system proposed in this study makes use of the compressor and turbine stage wall surfaces to simultaneously act as heat transfer surfaces. For the compression process, the heat sink fluid is circulated through the internal passages formed in the stator blades. This fluid extracts the heat from the working fluid and cools it while the heat-sink fluid temperature rises. The process is repeated for all the stages of the axial compressor giving rise to the temperature glide. For the expansion process, the heating fluid (HTF from solar collector system) is passed through the passages formed inside the nozzle blades. This acts to heat the working fluid passing through the turbine stages while the heating fluid cools down. The exhaust gas from the turbine is passed through a recuperator to heat the working fluid at the exit of the compressor. The fluid at the exit of the coldside of recuperator is heated using the HTF to achieve the turbine inlet temperature. Thus the entire process is completed to generate power using LCGT.

LCGT Model

To assess the LCGT system, representation of the compression and expansion process in the LCGT system model as described in the previous section is critical. To fulfill this requirement, the compressor and turbine models are developed in detail. The flow through individual rows of stator and rotor blades for the compressor stage and through individual nozzle and blade rows in turbine stage is modeled respectively. The next sections describe the modeling details for the compressor and turbine stages. Following the details of compressor and turbine stage models, the heat exchanger model is described. This model essentially simulates the heat transfer across the wall surfaces of compressor and turbine stage.

Compressor row-by-row model

The row-by-row compressor model is an effective simple tool based on basic principles and empirical data to perform the thermodynamic and fluid-mechanical assessment of the compressor sub-system in a greater detail. The system is sub-divided into individual stages comprising the rotor and stator portions for each stage. The aero-thermodynamic model is evaluated for each stage to generate the state of working fluid for the next stage. The model predicts performance of a compressor stage based on stage aerodynamic parameters and the corresponding losses using correlations based on cascade and axial compressor test data (Dixon, 2005). The distinctive feature of the model is that it solves for the performance of individual rotor and stator rows in a stage with separate calculations for aerodynamic performance and losses to obtained better predictions than stage level model. The model designs and assesses the compressor system for a given mass-flow and pressure rise and can be used to optimize the system for efficiency. The following section describes the model in detail.

EES Model

The EES model was developed to design a compressor system that generated a specified overall pressure-ratio for the given mass-flow rate and achieve optimum system efficiency based on stage design variables. The model is useful for both designing and analyzing a system and also has provisions to incorporate heat transfer across compressor stage.

The EES model developed implements a modular approach to estimate the performance of the entire compressor section. The compressor system calculations are performed sequentially in a procedure, wherein individual stage calculations are performed iteratively, with the output from each stage calculation supplied as input to the next stage's calculation. The individual stage calculation is performed in a sub-program, where the system design is represented as system of equations and solved simultaneously to generate the output.

In EES, a procedure and a sub-program are two different programming constructs that are made available to serve distinct purposes. A regular computer program is a set of instructions executed sequentially to achieve a definite output. The execution is procedural in nature with the instructions executed later having no bearing on the instructions before them. This is the characteristic of a procedure defined in EES.

In real life problem solving, like designing a system, there are a set of physical and empirical relations between design parameters and all these parameters are inter-related to form a set of equations, which when solved together as a system, yields the desired output to determine the unknown parameters. Such a system cannot be solved procedurally as any design parameter can have a bearing on the value of another design parameter, which sometimes in turn determines the value of the original design parameter forming what is known as an implicit relationship.

A sub-program in EES is an effective and sophisticated way of dealing with implicit relationships inherent in the system of equations for e.g. the heat transfer for the intra stage cooling in the turbo-machine wherein the temperature drop and the heat transfer rate are inter-dependent. These implicit relations need an iterative procedure in a procedural programming format. But with EES, these relations can be separately represented in an EES sub-program and solved as system of equations whereas the part of the design, which can be derived sequentially, can be put down in EES procedures, thus effectively modularizing the model.

The set of equations have been represented in a block diagram to understand the process flow as shown in Figure 6.1. The individual compressor stage comprises of the rotor and the stator section. The working fluid enters the rotor section at a particular velocity and based on the aerodynamic design of the rotor blade row and the rotor speed, gets accelerated downstream to a different velocity. The rotor blades impart kinetic energy to the fluid, which tends to increase the flow speed and also causes rise in pressure. This flow then enters the stator blade row, which acts as diffuser and decelerates the flow while increasing its static pressure further. The model assumes a 'normal' compressor stage for which the absolute velocities and flow direction are same in the stage exit as in the inlet. This is a fair assumption as this is a design point calculation.

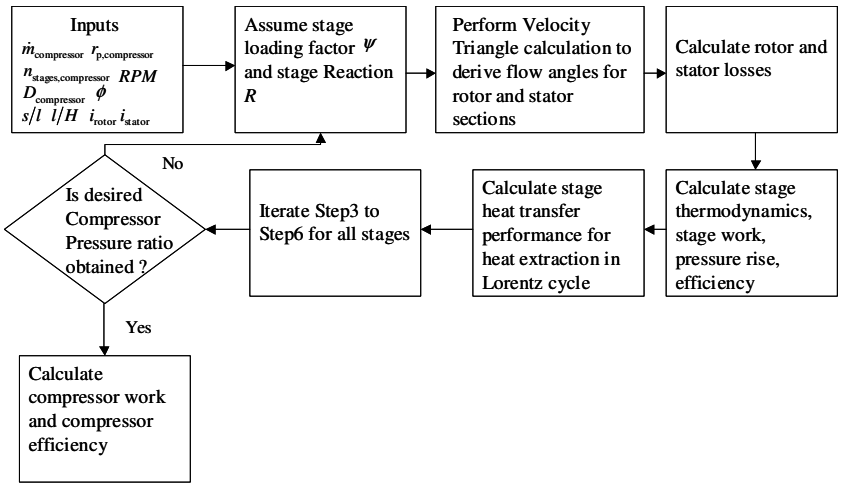

Figure 6.3: Process Flow for Individual Compressor Stage Calculation

List of Symbols

The variables used in the model are listed below

Variable	Description
$\dot{m}_{comp}$	Compressor mass flowrate
$r_{p,comp}$	Overall compressor pressure ratio
D_{comp}	Compressor mean-line diameter
n_{stg}	Number of compressor stages
RPM	Compressor shaft rotations per minute
ϕ	Stage flow coefficient
ψ	Stage loading factor
R	Stage reaction
s	Blade pitch
l	Blade chord length
H	Blade height
U	Blade speed
C	Absolute flow speed
W	Flow speed relative to blade speed
α	Absolute flow angle
β	Relative flow angle
h	Specific enthalpy
p	Flow static pressure
ρ	Flow density
η	Stage efficiency
λ	Work done factor

Compressor Model

The basic compressor design assessment begins with assessing the fluid-mechanics based on the 2-D cascade blade design and the system level flow parameters. The model requires the compressor mass-flow $\dot{m}_{comp}$, overall pressure ratio $r_{p,comp}$, RPM, mean compressor diameter D_{comp}, number of stages n_{stg}, stage flow coefficient ϕ, blade mean space-chord ratio *s/l*, blade mean aspect ratio *l/H* as inputs. In the next step the stage loading factor ψ and stage reaction *R* are assumed to start the calculations. The velocity triangle calculations are performed to establish the flow velocities across the rotor and stator blades and the flow angles.

The next step is to determine the stage level parameters like stage work, stage loss parameters, stage efficiency and stage pressure rise. This leads to determining the stage thermodynamics to completely determine the state of fluid at the exit of the stage. This procedure needs to be repeated for all the stages to arrive at the performance estimate of entire compressor system. This process is repeated for different values of stage loading factor and reaction till the desired compressor pressure rise is achieved. The other option to design and assess the system is to assume the blade angles and calculate the stage level parameters like loading factor and reaction. The advantage of assuming the stage loading factor and stage reaction over blade angles is that the design is always in the valid range of performance and iterations do not terminate abruptly in EES. With the blade angles as inputs, certain combinations of different blade angles take the design beyond the performance envelope and it is very difficult to iterate on and optimize the design in an automated fashion or perform parametric studies of academic interest. The following sections describe the formulation for each of the above stated aspects of the compressor design.

Velocity Triangle Calculations

The velocity diagram for the compressor stage establishes the aerodynamic behavior of the fluid and subsequently the stage thermodynamics. The velocity triangle is depicted in Figure 2. The flow from a previous stage has a velocity C_1 and direction α_1; subtracting the blade-speed U gives the inlet relative velocity W_1 at angle β_1 (the axial direction is the reference for all angles). In the Reference Frame of rotor blades, the flow is turned to the direction β_2 at outlet with a relative velocity W_2. By adding the blade speed U to W_2 we get the absolute velocity from the rotor, C_2 at angle α_2. The stator blades deflect the flow towards the axis with velocity C_3 at angle α_3. For the normal repeating stage in a multistage compressor, C_3 is equal to C_1 and α_3 is equal to α_1.

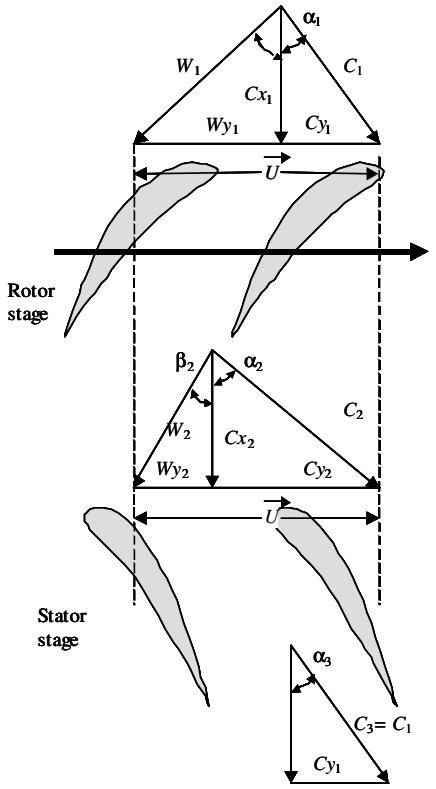

Figure 6.4: Compressor Stage Velocity Triangles

Thermodynamics of Compressor Stage

The steady flow energy equation (assuming adiabatic flow) and momentum equation imply the specific work done by the rotor on the fluid to be calculated as:

$$\Delta W = \dot{W}_{\mathrm{p}} / \dot{m} = h_{02} - h_{01} = U\left(C_{\mathrm{y}2} - C_{\mathrm{y}1}\right) \tag{6.1}$$

For axial machines where there is no radial shift of the streamlines across the rotor (i.e. $U_1 = U_2$) then:

$$h_1 + \frac{1}{2}w_1^2 = h_2 + \frac{1}{2}w_2^2 \tag{6.2}$$

Across the stator, h_0 is constant, and

$$h_2 + \frac{1}{2}c_2^2 = h_3 + \frac{1}{2}c_3^2 \tag{6.3}$$

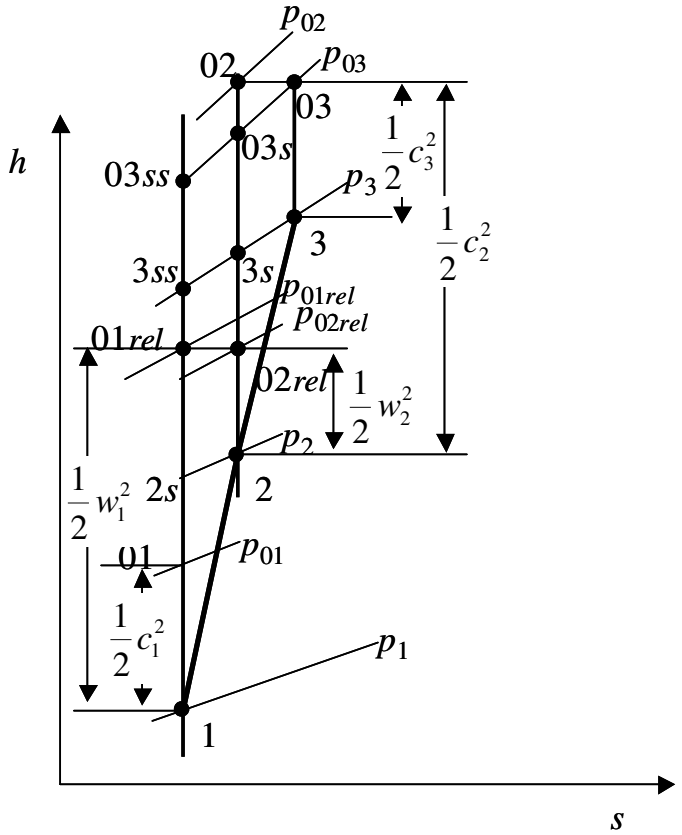

Figure 6.5: Thermodynamics of an axial compressor stage

These relations describing the thermodynamics of a compressor stage are depicted in Figure 6.5.

Stage Parameters - Compressor

Some important compressor stage parameters are represented that strongly affect the design and off-design performance characteristics.

Flow Coefficient

It is the ratio of average axial velocity of flow in the compressor stage to blade speed

$$\phi = \frac{c_x}{U} \tag{6.4}$$

Stage Loading Factor

It is the ratio of specific compressor work to square of blade speed

$$\psi = \frac{w_{comp}}{U^2} \tag{6.5}$$

The stage loading factor is representative of the amount of work performed by each stage on the working fluid. Ideally, this parameter should be large to reduce the number of stages, but in reality, it is limited to ~0.4 to avoid flow separation on the blade surface.

Stage Reaction Ratio

For incompressible and reversible flow, it is the ratio of static pressure rise in rotor to static pressure rise in stage, but a more general definition that covers compressible and irreversible flow is the ratio of enthalpy rise in rotor to enthalpy rise in stage given by

$$R = \frac{h_2 - h_1}{h_3 - h_1} \tag{6.6}$$

From Eq. 6.2 and simplifying further

$$R = \frac{w_1^2 - w_2^2}{2U\left(c_{y2} - c_{y1}\right)} = \frac{w_{y1}^2 - w_{y2}^2}{2U\left(c_{y2} - c_{y1}\right)} = \frac{w_{y1} + w_{y2}}{2U} \tag{6.7}$$

So, from Figure 6.2

$$R = \left(\frac{c_x}{U}\right)\tan\beta_m \tag{6.8}$$

where

$$\tan\beta_m = \frac{1}{2}\left(\tan\beta_1 + \tan\beta_2\right) \tag{6.9}$$

Compressor Stage Loss Relationships and Efficiency

From eqns. 6.1 and 6.3 the actual work performed by the rotor on unit mass of fluid is $W_{stg} = h_{03} - h_{01}$. The minimum work required to attain the same final stagnation pressure as the real process is

$$\begin{aligned} W_{stg,min} &= \left(h_{03ss} - h_{01}\right) \\ &= \left(h_{03} - h_{01}\right) - \left(h_{03s} - h_{03ss}\right) - \left(h_{03} - h_{03s}\right) \end{aligned} \tag{6.10}$$

Simplifying by approximating $\Delta h = T\Delta s$ for a constant pressure and referring to Figure 6.5

$$W_{stg,min} = W_{stg} - \left(\frac{T_{03}}{T_2}\right)\left(h_2 - h_{2s}\right) - \left(\frac{T_{03}}{T_3}\right)\left(h_3 - h_{3s}\right) \tag{6.11}$$

The temperature rise in a compressor stage is relatively small compared to absolute temperature and so Eq. 6.11 can be approximated to

$$W_{stg,min} = W_{stg} - \left(h_2 - h_{2s}\right) - \left(h_3 - h_{3s}\right) \tag{6.12}$$

The enthalpy losses in the stator can be expressed as

$$h_3 - h_2 = \frac{1}{2}\left(c_2^2 - c_3^2\right) \tag{6.13}$$

As $h_{03} = h_{02}$ and $p_0 = p + 1/2\,\rho c^2$ for incompressible fluid, Eq. 6.13 can be written as

$$h_3 - h_2 = \left[\left(p_{02} - p_2\right) - \left(p_{03} - p_3\right)\right]/\rho \tag{6.14}$$

From Figure 6.5, using the relation $\Delta h = (1/\rho)\Delta p$,

$$h_{3s} - h_2 = \left(p_3 - p_2\right)/\rho \tag{6.15}$$

Subtracting Eq. 6.15 from 6.14,

$$h_3 - h_{3s} = \left(p_{03} - p_{02}\right)/\rho = \frac{\Delta p_{0,\mathrm{str}}}{\rho} \tag{6.16}$$

Similarly for rotor section,

$$h_2 - h_{2s} = \left(p_{01\mathrm{rel}} - p_{02\mathrm{rel}}\right)/\rho = \frac{\Delta p_{0,\mathrm{rtr}}}{\rho} \tag{6.17}$$

The total-to-total stage efficiency is then given by

$$\eta_{\mathrm{tt}} = \frac{W_{\mathrm{stg,min}}}{W_{\mathrm{stg}}} = 1 - \frac{\left(h_2 - h_{2s}\right) + \left(h_3 - h_{3s}\right)}{\left(h_{03} - h_{01}\right)} = 1 - \frac{\Delta p_{0,\mathrm{rtr}} + \Delta p_{0,\mathrm{str}}}{\rho\left(h_{03} - h_{01}\right)} \tag{6.18}$$

where $\Delta p_{0,\mathrm{rtr}}$ and $\Delta p_{0,\mathrm{str}}$ are the total stagnation pressure losses across rotor and stator sections in the stage respectively.

Estimation of compressor stage efficiency

The efficiency of a turbo-machine is one of the most sought after parameters in its design. The prediction of efficiency of a system depends on accurately estimating the losses in the turbo-machine stage. During the 1940's and 50's a lot of effort was put in understanding these loss mechanisms through research and testing on 2D cascades as well as real machines and empirical data was generated to develop correlations for predicting these losses (David, 2011). These correlations were extensively used through the 60's and 70's till more advanced techniques of experimenting and analyzing the

losses came into existence. However, the correlations developed by researchers in the 40's and 50's like Howell (1945), Ainley (1951) and Carter (1948) etc. predict the turbo-machine performance to within ± 2 % accuracy (Denton, 1993) which is an acceptable range for the current effort. This section describes the broad category of losses in the axial compressor and how these losses are modeled based on the correlations mentioned above. Compressor stage losses can be classified into three broad categories (Howell, 1945)

1) Profile losses on blade surfaces
2) Skin friction losses on the annulus walls
3) Secondary losses (all losses not included in 1 and 2)

For compressor stage these losses are represented by the overall drag coefficient derived as

$$\begin{aligned} C_{\mathrm{D}} &= C_{\mathrm{Dp}} + C_{\mathrm{Da}} + C_{\mathrm{Ds}} \\ &= C_{\mathrm{Dp}} + 0.02\, s/H + 0.018 C_{\mathrm{L}}^2 \end{aligned} \tag{6.19}$$

This derivation is based on empirical values for compressor cascades (Howell,1945) where

$$C_{\mathrm{Dp}} = \frac{s}{l}\left(\frac{\Delta p_0}{\frac{1}{2}\rho w_1^2}\right)\frac{\cos^3\beta_{\mathrm{m}}}{\cos^2\beta_1}$$

and

$$\mathrm{C_L} = 2(s/l)\cos\beta_{\mathrm{m}}(\tan\beta_1 - \tan\beta_2) \tag{6.20}$$

The profile loss coefficient is estimated based on Figure 4 for different angles of incidence.

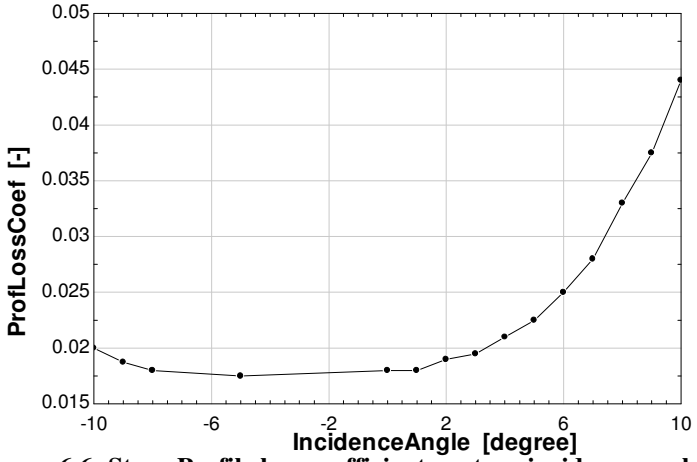

Figure 6.6: Stage Profile loss coefficient vs stage incidence angle

In multi-stage axial compressors, the wall boundary layers thicken through first few stages and axial velocity profile rises increasing energy losses due to friction towards the mid-section. This reduces the work done by the stage as the root and tip sections also incur losses due to stalling and tip leakage. This loss could be accommodated in the stage stagnation enthalpy rise as (Howell, 1945)

$$h_{03} - h_{01} = \lambda U\left(c_{y2} - c_{y1}\right) \tag{6.21}$$

where λ is the *work done factor*. For multi-stage compressor the recommended value for λ is 0.86 (Howell, 1945).

The stage total-to-total efficiency can now be estimated based on the determination of loss coefficients. From Eq. 6.4, 6.5, 6.18, 6.19 and 6.20

$$\begin{aligned}\eta_{tt} &= 1 - \frac{\Delta p_{0,rtr} + \Delta p_{0,str}}{\rho\left(h_{03} - h_{01}\right)} = 1 - \frac{\Delta p_{0,rtr} + \Delta p_{0,str}}{\rho\psi U^2} \\ &= 1 - \frac{\left(\Delta p_{0,rtr} + \Delta p_{0,str}\right) \Big/ \left(\frac{1}{2}\rho c_x^2\right)}{2\psi/\phi^2}\end{aligned} \tag{6.22}$$

Simplifying further and defining new terms

$$\eta_{tt} = 1 - \frac{\left(\zeta_{rtr} + \zeta_{str}\right)\phi^2}{2\psi} \tag{6.23}$$

where ζ_{rtr} and ζ_{str} are the overall total pressure loss coefficients for the rotor and stator sections respectively and $\zeta = (l/s) C_D \sec^3 \alpha_m$

Stage Pressure Rise

Pressure rise in a real stage with irreversible losses can be estimated based on the stage efficiency as follows

$$\eta_{tt} = \frac{\Delta h_{isen}}{\Delta h_{real}} \tag{6.24}$$

For isentropic process $\Delta h = (1/\rho)\Delta p$, so

$$\eta_{tt} = \frac{(1/\rho)\Delta p}{\Delta h_{real}} \tag{6.25}$$

Rearranging terms

$$\Delta p = \eta_{tt} \rho \Delta h_{real} = \eta_{tt} \rho \psi U^2 \tag{6.26}$$

The estimation of the stage pressure rise concludes the stage level calculations. This process is repeated for all stages in the compressor to arrive at an overall pressure rise. If the desired overall pressure rise is not achieved, the stage loading factor and the reaction ratio is altered and the entire process is repeated till we achieve our desired design condition.

The schematic of such a multi-stage axial compressor is shown in Figure 6.7.

EES Schematic

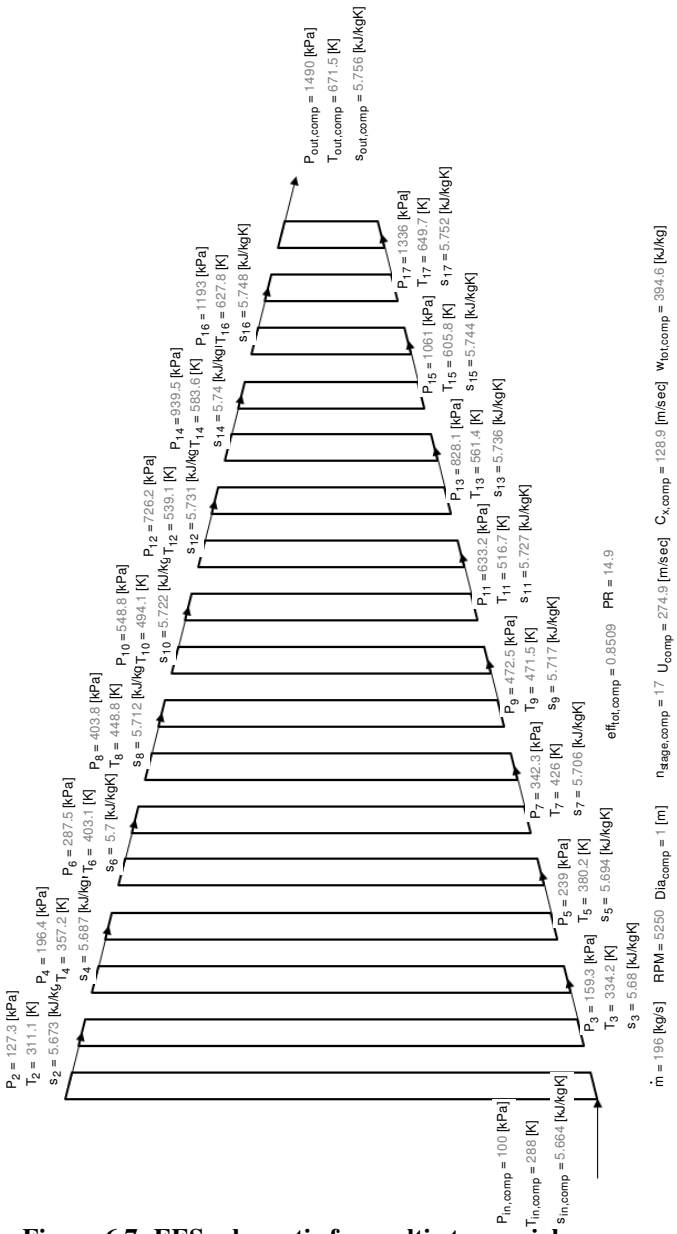

Figure 6.7: EES schematic for multi-stage axial compressor

The EES schematic shows the working fluid state at the inlet and outlet of the compressor and after every compressor stage and other relevant parameters.

T-s Diagram

The T-S diagram is shown in Figure 6.7 for the scenario shown in Figure 6.8.

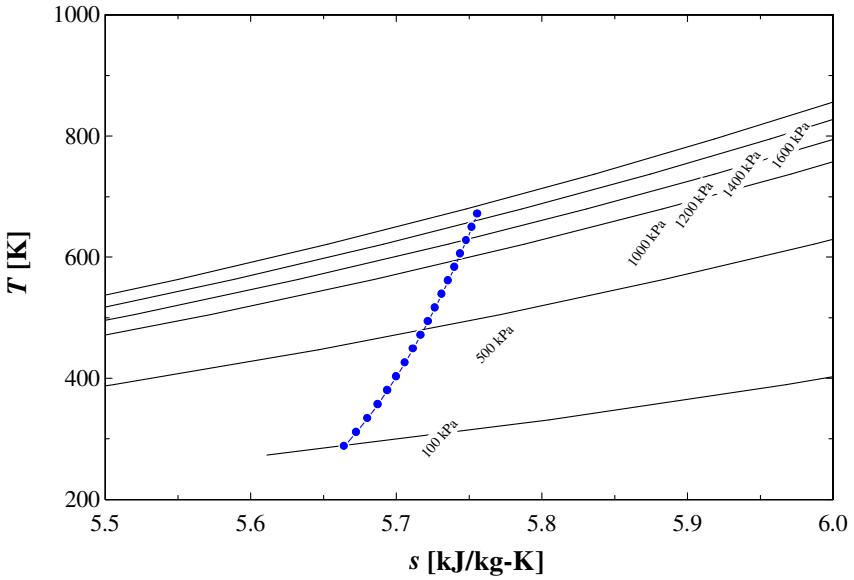

Figure 6.8: T-S Diagram for compressor

Velocity Diagram

The Velocity diagram is shown in Figure 6.9 for the same case.

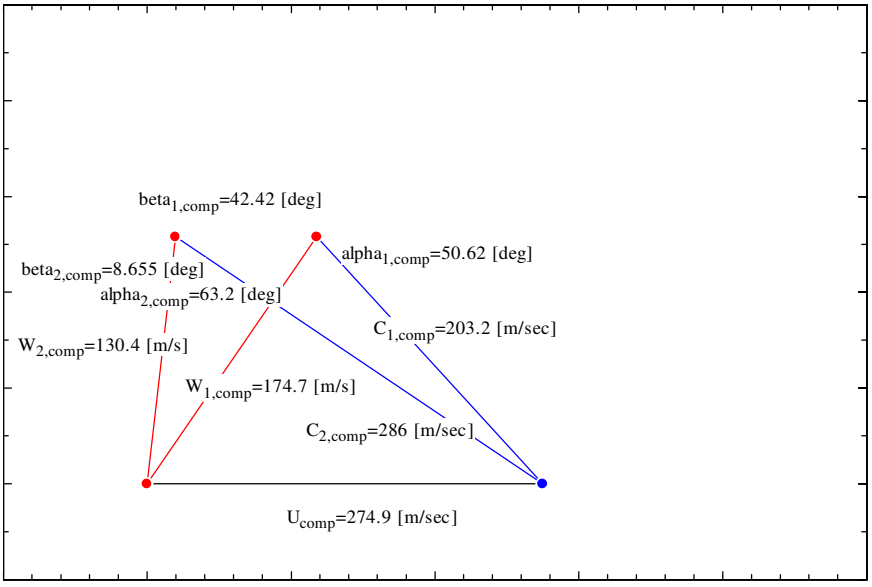

Figure 6.9: Compressor Stage Velocity Triangles

Comparison with Commercial Design

The model was validated with commercial designs (GE 6FA gas turbine compressor and GE LM2500+) to compare the model performance predictions with a real system. The following tables list the comparison.

Table 6.1: Compressor Performance Estimate- EES Model vs 6FA

Parameters	6FA(GE)	EES Model
Massflow (kg/s)	196	196
Pressure Ratio	14.9	15
Stages	17	17
Compressor efficiency	86%	85%

Table 6.2: Compressor Performance Estimate- EES Model vs LM2500+

Parameters	LM2500+(GE)	EES Model
Massflow (kg/s)	84.5	84.5
Pressure Ratio	23	23.01
Stages	17	17
Compressor Polytropic efficiency	91%	91.90%

The known system parameters were specified as inputs and the other model parameters were tuned to achieve the desired performance for the compressor system, which matches well with the commercial designs and shows the efficacy of the model in predicting axial compressor performance.

Turbine row-by-row model

The row-by-row turbine model is similar to the compressor row-by-row model in performing the thermodynamic and fluid-mechanical assessment of the turbine sub-system in a greater detail. The system is sub-divided into individual stages comprising the nozzle and rotor portions for each stage. The aero-thermodynamic model for each stage is evaluated to generate the state of working fluid for the next stage. The model predicts performance of a turbine stage based on stage aerodynamic parameters and the corresponding losses using well-established and validated 2D cascade correlations as well as stage level thermodynamics. The model solves for the performance of individual nozzle and rotor rows in a stage with separate calculations for aerodynamic performance and losses to obtained better predictions than stage level model. The model designs and assesses the turbine system for a given mass-flow and pressure drop and can be used to optimize the system for optimum efficiency. The following section describes the model in detail.

EES Model

The turbine model is similar to the compressor model. The set of equations have been represented in a block diagram to understand the process flow as shown in Figure 1. The individual turbine stage comprises of the nozzle and the rotor section. The working fluid enters the nozzle section at a particular velocity and based on the aerodynamic design of the turbine nozzle row, gets accelerated downstream to a different velocity. The nozzle converts the pressure in the flow to kinetic energy, which tends to increase the flow speed and reduce static pressure. This flow then enters the turbine rotor row, which converts the energy in the flow to work. The model assumes a ‘normal’ turbine stage for which the absolute velocities and flow direction are same in the stage exit as in the inlet. This is a fair assumption as this is a design point calculation.

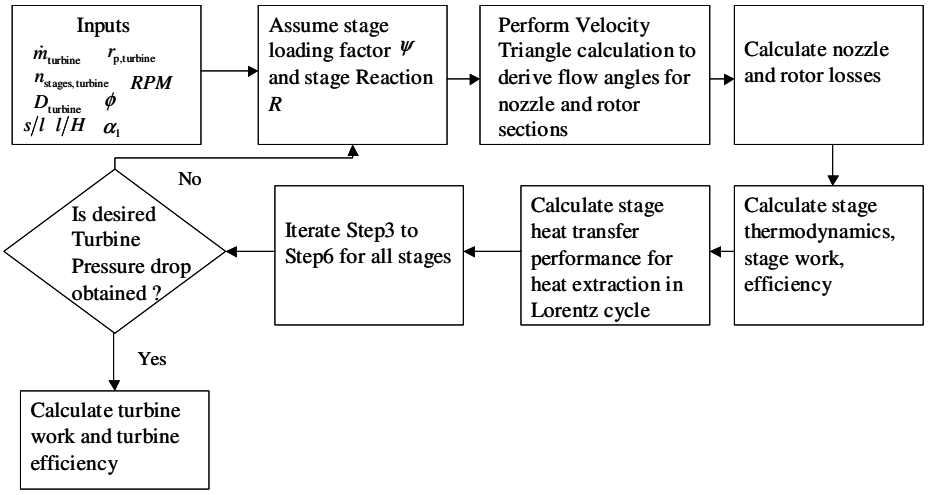

Figure 6.10: Process Flow for Individual Turbine Stage Calculation

List of Symbols

The variables used in the model are listed below

Variable	Description
$\dot{m}_{turbine}$	Turbine mass flowrate
$r_{p,turbine}$	Overall turbine pressure ratio
$D_{turbine}$	Turbine mean-line diameter
n_{stages}	Number of turbine stages
RPM	Turbine shaft rotations per minute
ϕ	Stage flow coefficient
ψ	Stage loading factor
R	Stage reaction
s	Blade pitch
l	Blade chord length
H	Blade height
U	Blade speed
C	Absolute flow speed
W	Flow speed relative to blade speed
α	Absolute flow angle
β	Relative flow angle
h	Specific enthalpy
p	Flow static pressure
ρ	Flow density
η	Stage efficiency
λ	Work done factor

Turbine Model

The basic turbine design assessment begins with assessing the fluid-mechanics based on the 2-D cascade blade design and the system level flow parameters. The model requires the turbine mass-flow $\dot{m}_{\text{turb}}$, overall pressure ratio $r_{\text{p,turb}}$, RPM, mean turbine diameter D_{turb}, number of stages n_{stg}, stage flow coefficient ϕ, blade mean space-chord ratio *s/l*, blade mean aspect ratio *l/H* as inputs. In the next step the stage loading factor ψ and stage reaction *R* are assumed to start the calculations. The velocity triangle calculations are performed to establish the flow velocities across the rotor and stator blades and the flow angles. The next step is to determine the stage level parameters like stage work, stage loss parameters, stage efficiency and stage pressure drop. This leads to determining the stage thermodynamics to completely determine the state of fluid at the exit of the stage. This procedure needs to be repeated for all the stages to arrive at the performance estimate of entire turbine system. This process is repeated for different values of stage loading factor and reaction till the desired turbine pressure drop is achieved. The other option to design and assess the system is to assume the blade geometry and calculate the stage level parameters like loading factor and reaction. The advantage of assuming the stage loading factor and stage reaction over blade geometry is that the design is always in the valid range of performance and iterations do not terminate abruptly in EES. With the blade geometry as inputs, certain combinations of different blade parameters take the design beyond the performance envelope and it is very difficult to iterate on and optimize the design in an automated fashion or perform parametric studies of academic interest. The following sections describe the formulation for each of the above stated aspects of the turbine design.

Velocity Triangle Calculations

The velocity diagram for the turbine stage establishes the aerodynamic behavior of the fluid and subsequently the stage thermodynamics. The velocity triangle is depicted in Figure 2. The flow from a previous stage has a velocity C_1 and direction α_1; the flow accelerates through the nozzle section to achieve a velocity C_2; subtracting the blade speed U gives the inlet relative velocity W_2 at angle β_2 (the axial direction is the reference for all angles). In the Reference Frame of rotor blades, the flow is turned to the direction β_3 at outlet with a relative velocity W_3. By adding the blade speed U to W_3 we get the absolute velocity from the rotor, C_3 at angle α_3. For the normal repeating stage in a multistage turbine, C_3 is equal to C_1 and α_3 is equal to α_1.

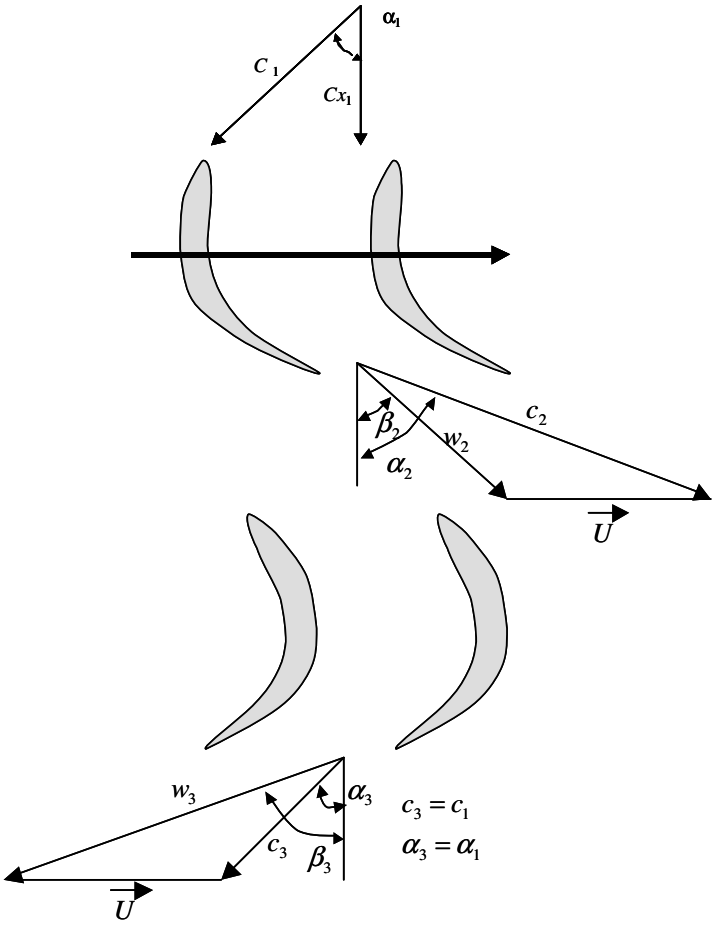

Figure 6.11: Turbine Stage Velocity Triangles

Thermodynamics of Turbine Stage

The steady flow energy equation (assuming adiabatic flow) and momentum equation imply the specific work done by the fluid on the rotor to be calculated as:

$$\Delta W = \dot{W}_{\mathrm{p}} / \dot{m} = h_{01} - h_{03} = U\left(C_{\mathrm{y}2} + C_{\mathrm{y}3}\right) \tag{6.27}$$

Across the nozzle, h_0 is constant, and

$$\begin{aligned} & h_{01} = h_{02} \\ & \text{or} \\ & h_1 + \frac{1}{2}c_1^2 = h_2 + \frac{1}{2}c_2^2 \end{aligned} \tag{6.28}$$

Across the rotor section, the fluid works on the blades to transfer energy. The change in enthalpy of the fluid is equal to the work done:

$$\begin{aligned} & h_{02} - h_{03} = \Delta W \\ & \left(h_2 - h_3\right) + \frac{1}{2}\left(c_{\mathrm{y}2}^2 - c_{\mathrm{y}3}^2\right) = U\left(c_{\mathrm{y}2} + c_{\mathrm{y}3}\right) \end{aligned} \tag{6.29}$$

Simplifying further

$$\left(h_2 - h_3\right) + \frac{1}{2}\left(c_{\mathrm{y}2} + c_{\mathrm{y}3}\right)\left[\left(c_{\mathrm{y}2} - U\right) - \left(c_{\mathrm{y}3} + U\right)\right] = 0 \tag{6.30}$$

For axial machines, it is assumed that there is no radial shift of the streamlines across the rotor (i.e. $U_1 = U_2$) or that the rotor speed is constant through the stage. In such a case the flow velocities relative to the rotor blade speed is given by:

$$\begin{aligned} & c_{\mathrm{y}2} - U = w_{\mathrm{y}2} \\ & c_{\mathrm{y}3} + U = w_{\mathrm{y}3} \end{aligned} \tag{6.31}$$

From Eq. 6.30 and 6.31

$$h_2 + \frac{1}{2}w_2^2 = h_3 + \frac{1}{2}w_3^2 \tag{6.32}$$

These relations describing the thermodynamics of a turbine stage are depicted in Figure 6.12. These relations are used in the later section to develop the model for calculating the stage efficiency.

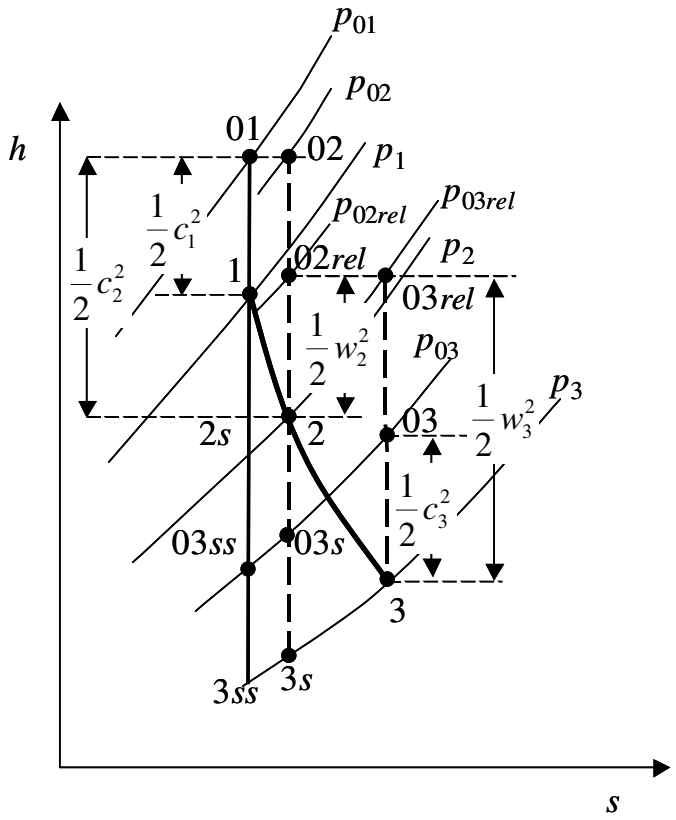

Figure 6.12: Thermodynamics of an axial turbine stage

The next step is to define some more stage level parameters, which will be used to develop the turbine stage efficiency model. These higher level parameters simplify the representation of flow physics in a stage and help in interpreting the turbine design better.

Stage Parameters - Turbine

Some important turbine stage parameters are represented that strongly affect the design and off-design performance characteristics.

Flow Coefficient

It is the ratio of average axial velocity of flow in the turbine stage to blade speed

$$\phi = \frac{c_x}{U} \tag{6.33}$$

Stage Loading Factor

It is the ratio of specific turbine work to square of blade speed

$$\psi = \frac{w_{turb}}{U^2} \tag{6.34}$$

The stage loading factor is representative of the amount of work performed by the fluid on each stage. Ideally, this parameter should be large to reduce the number of stages, it is found to be in the range of ~0.5 to ~1.5.

Stage Reaction Ratio

For incompressible and reversible flow, it is the ratio of static pressure rise in the rotor to static pressure rise in stage, but a more general definition that covers compressible and irreversible flow is the ratio of enthalpy rise in rotor to enthalpy rise in stage given by

$$R = \frac{h_2 - h_3}{h_1 - h_3} \tag{6.35}$$

From Eq. 6.32 and simplifying further

$$R = \frac{w_3^2 - w_2^2}{2U\left(c_{y2} + c_{y3}\right)} = \frac{w_{y3}^2 - w_{y2}^2}{2U\left(c_{y2} + c_{y3}\right)} = \frac{w_{y3} - w_{y2}}{2U} \tag{6.36}$$

So, from Figure 6.11

$$R = \left(\frac{c_x}{2U}\right)\left(\tan\beta_3 - \tan\beta_2\right) \tag{6.37}$$

Turbine Stage Loss Relationships and Efficiency

The total to total efficiency of a turbine stage is defined as

$$\eta_{tt} = \frac{W_{stage}}{W_{stage,ideal}} = \frac{h_{01} - h_{03}}{h_{01} - h_{03ss}} \tag{6.38}$$

For the normal stage assumption

$$\eta_{tt} = \frac{h_1 - h_3}{h_1 - h_{3ss}} \tag{6.39}$$

From Fig. 6.12, Eq. 6.39 can be represented as

$$\eta_{tt} = \frac{h_1 - h_3}{(h_1 - h_3) + (h_3 - h_{3s}) + (h_{3s} - h_{3ss})} \tag{6.40}$$

Again from Figure 6.12,

$$s_{3s} - s_{3ss} = s_2 - s_{2s} = \Delta s \tag{6.41}$$

Also, at constant pressure

$$\Delta h = T \cdot \Delta s \tag{6.42}$$

From Eq. 6.41 and 6.42

$$\frac{(h_{3s} - h_{3ss})}{T_{3ss}} = \Delta s = \frac{(h_2 - h_{2s})}{T_{2s}} \tag{6.43}$$

or

$$h_{3s} - h_{3ss} = (T_{3ss}/T_{2s})(h_2 - h_{2s}) \tag{6.44}$$

So replacing the third term in the denominator of Equation 6.40 from 6.44

$$\eta_{tt} = \frac{h_1 - h_3}{(h_1 - h_3) + (h_3 - h_{3s}) + (h_2 - h_{2s}) \cdot T_{3ss}/T_{2s}} \tag{6.45}$$

The numerator and the first term in the denominator represent the turbine work. The second term in the denominator represents the loss in the rotor section and the third term in the denominator represents the loss in the nozzle section. The loss in the nozzle section for the flow is represented in terms of a loss coefficient as

$$h_2 - h_{2s} = \frac{1}{2} c_2^2 \zeta_N \tag{6.46}$$

Where c2 is the nozzle exit velocity and ζ_N represents the loss coefficient. Similarly, the loss in the rotor section for the flow is represented as

$$h_3 - h_{3s} = \frac{1}{2} w_3^2 \zeta_R \tag{6.47}$$

From 6.45, 6.46 and 6.47, the total-to-total stage efficiency is then given by

$$\eta_{tt} = \left[1 + \frac{\zeta_N c_2^2 T_{3ss}/T_{2s} + \zeta_R w_3^2}{2(h_1 - h_3)} \right]^{-1} \tag{6.48}$$

The losses in the individual rows (nozzle and rotor) in a stage can be also defined as

$$\frac{h_1 - h_2}{h_1 - h_{2s}} = \eta_N \tag{6.49}$$

and

$$\frac{h_1 - h_3}{h_1 - h_{3s}} = \eta_R \tag{6.50}$$

So, Equation 6.45 can be also represented as

$$\eta_{tt} = \frac{1}{1 + \frac{(h_3 - h_{3s})}{(h_1 - h_3)} + \frac{(h_2 - h_{2s})}{(h_1 - h_3)} \cdot T_{3ss}/T_{2s}} \tag{6.51}$$

Rearranging further and using Equation 6.49 and 6.50

$$\eta_{tt} = \frac{1}{\frac{1}{\eta_R} + \left(\frac{1}{\eta_N} - 1\right)\frac{(h_1 - h_2)}{(h_1 - h_3)} \cdot T_{3ss}/T_{2s}} \tag{6.52}$$

Estimation of turbine stage efficiency

For the preliminary design of a gas turbine stage, it is necessary to estimate and model the loss mechanisms in the stage and derive the stage efficiency. One of the first methods to predict the turbine stage efficiency was to derive the blade row losses based on the overall turbine efficiency of a wide range of turbines (Soderberg, 1949). Another approach was to determine the profile loss coefficients for both impulse and reaction blades against flow deflection and blade pitch-cord ratio (Ainley, 1951). Profile loss for intermediate blading was derived from the combination of impulse and reaction profile loss equations. There are many other methods available for predicting the axial turbine stage efficiency (David, 2011). However the blade row loss model gives turbine efficiencies to within 3 % error over a wide range of Reynolds number and blade aspect ratio (Dixon, 2005). The blade row loss model was developed based on a lot of data assembled on various types of turbines. The model assumes the nominal design point with Reynolds number of 100000 and blade aspect ratio (*b/H*) of 3. The nominal loss coefficient is then only a function of the fluid deflection angle for a given blade thickness-chord ratio (*t/l*). An analytical expression for this function at a blade thickness-chord ratio of 0.2 is given by

$$\zeta^* = 0.04 + 0.06\left(\frac{\varepsilon}{100}\right)^2 \tag{6.53}$$

This expression fits the data well for the deflection angles below 120^o.

Now, if the blade aspect ratio is other than 3, the nominal loss coefficient is corrected as

$$\begin{aligned} 1+\zeta_1 &= (1+\zeta^*)(0.993+0.021b/H) \text{ for nozzles} \\ 1+\zeta_1 &= (1+\zeta^*)(0.975+0.075b/H) \text{ for rotors} \end{aligned} \tag{6.54}$$

where ζ_1 is the loss coefficient at Re = 100,000, b is the blade cord and H is the blade height.

A further correction to the loss coefficient is made if the Reynolds number is different from 100,000. The Reynolds number is based on the nozzle exit velocity C_2 and the hydraulic diameter D_h at the throat section.

$$\mathrm{Re} = \rho_2 c_2 D_\mathrm{h} / \mu \tag{6.55}$$

The correction is

$$\zeta_2 = \left(\frac{100000}{\mathrm{Re}}\right)^{\frac{1}{4}} \zeta_1 \tag{6.56}$$

Based on Equation 6.46 and 6.49, the nozzle loss coefficient can be correlated to the nozzle row efficiency as

$$\eta_\mathrm{N} = \frac{1}{1+\dfrac{c_2^2 \zeta_\mathrm{N}}{2(h_1 - h_2)}} \tag{6.57}$$

And from Equation 6.47 and 6.50, rotor loss coefficient can be correlated to rotor efficiency as

$$\eta_\mathrm{R} = \frac{1}{1+\dfrac{w_3^2 \zeta_\mathrm{R}}{2(h_1 - h_3)}} \tag{6.58}$$

The tip leakage loss can be incorporated in the rotor row efficiency based on the loss model by Kacker and Okapuu for unshrouded blades (Ning, 2000)

$$\eta_R = \eta_{R,0} \cdot \left(1 - 0.93 \cdot \left(\frac{r_{tip}}{r_{mean}} \right) \cdot \frac{1}{H \cdot \cos(\alpha_3)} \cdot t_{tip} \right) \tag{6.59}$$

here $\eta_{R,0}$ is the base rotor efficiency without any tip clearance, r_{tip} is the tip radius and t_{tip} is the tip clearance. There are other losses like end-wall losses, cooling losses etc. which have not been considered in this study.

EES Schematic

The EES schematic is shown in Figure 6.13 for a representative scenario

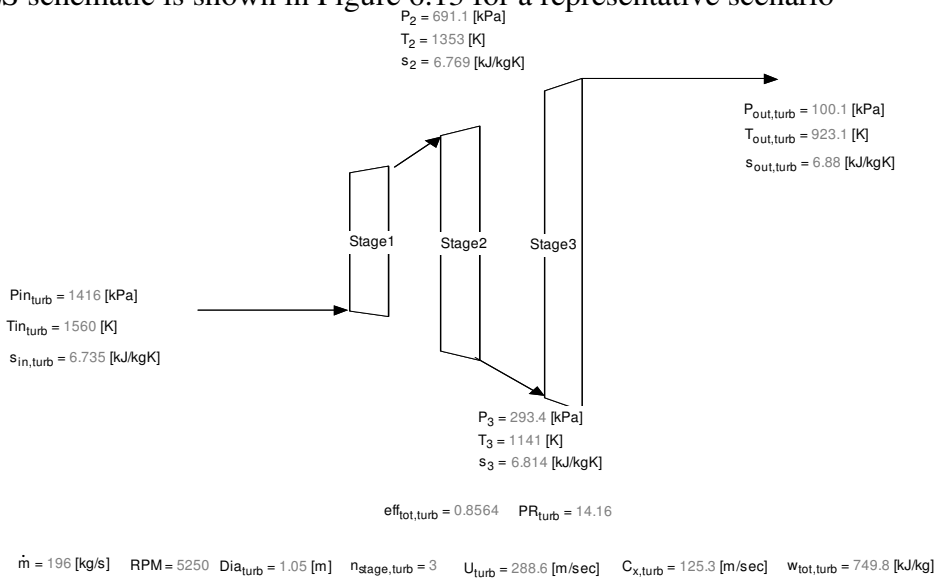

Figure 6.13: EES schematic

The schematic shows the state of working fluid through all the stages of the turbine and the stage level parameters.

T-S Diagram

The T-S diagram for the above scenario is shown in Figure 6.14.

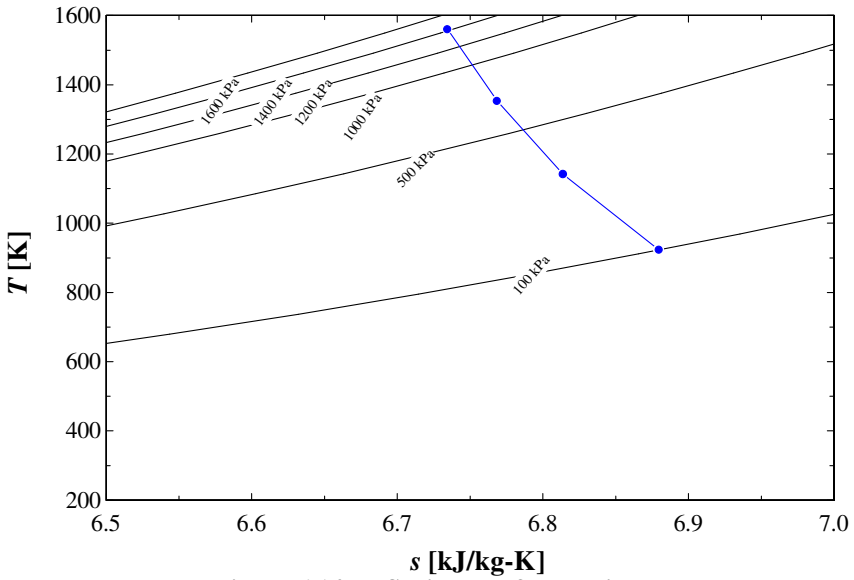

Figure 6.14: T-S Diagram for turbine

Comparison with Commercial Design

The model was validated with commercial design of GE 6FA gas turbine to compare the model performance predictions with a real system at its design point. The following tables list the comparison.

Table 6.3: Turbine Performance Estimate- EES Model vs 6FA

Parameters	6FA(GE)	EES Model
Massflow (kg/s)	196	196
Pressure Ratio	14.9	14.9
Stages	3	3
Compressor efficiency	85%	86%

Validation of Gas Turbine model

The models for the compressor and turbine stage are put together to form a unified gas turbine system model. This model can predict the overall GT performance and can be used to assess the performance of the proposed LCGT system with the augmentation of the heat transfer model. In this section, the simple cycle GT model is validated with commercial products for performance. The model is compared against GE 6FA and 7FA GTs for overall GT performance (Jay, 1996). Tables 6.4 and 6.5 represent the model inputs and the result for the 6FA and 7FA GT systems respectively.

Table 6.4: GT Performance Estimate- EES Model vs 6FA

Parameters	6FA	EES Model
Airflow [kg/s]	196	196
Pressure ratio	14.9	14.9
Turbine Inlet Temperature [K]	1560	1560
RPM	5250	5250
Exhaust Temperature [K]	870	923
Output [MW]	70.1	69.6
Efficiency [%]	34.2	34.6

The model predictions are in close agreement to the actual design for the 6FA. This is acceptable for a preliminary design assessment for a GT system. Figure 6.15 shows the overall GT thermodynamic cycle for the 6FA.

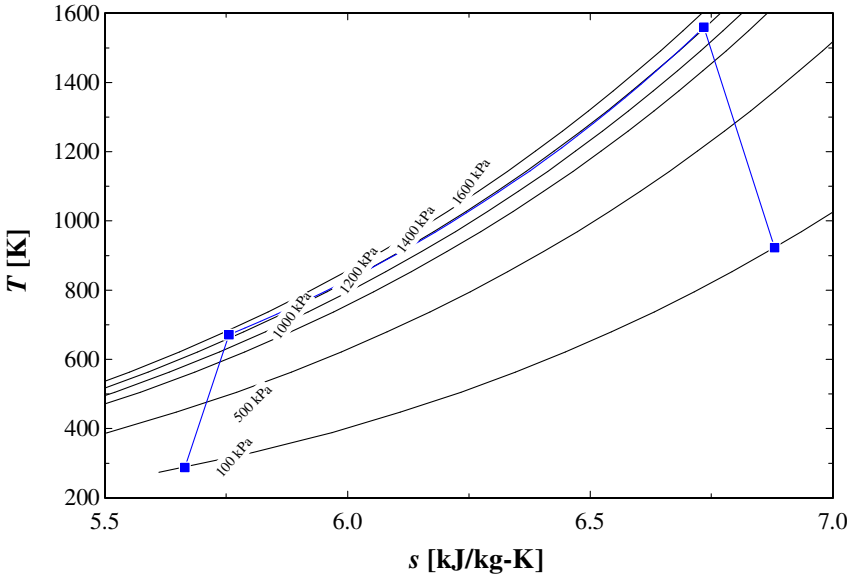

Figure 6.15: T-S Diagram for 6FA GT model

Table 6.5: GT Performance Estimate- EES Model vs 7FA

Parameters	7FA	EES Model
Airflow [kg/s]	432	432
Pressure ratio	14.8	14.8
Turbine Inlet Temperature [K]	1560	1560
RPM	3600	3600
Exhaust Temperature [K]	867	905
Output [MW]	167.8	166.2
Efficiency [%]	36.2	37.2

Similar to the 6FA model, the 7FA model also predicts the GT performance in close agreement to the actual 7FA GT. Figure 6.16 shows the thermodynamic cycle for the 7FA EES model.

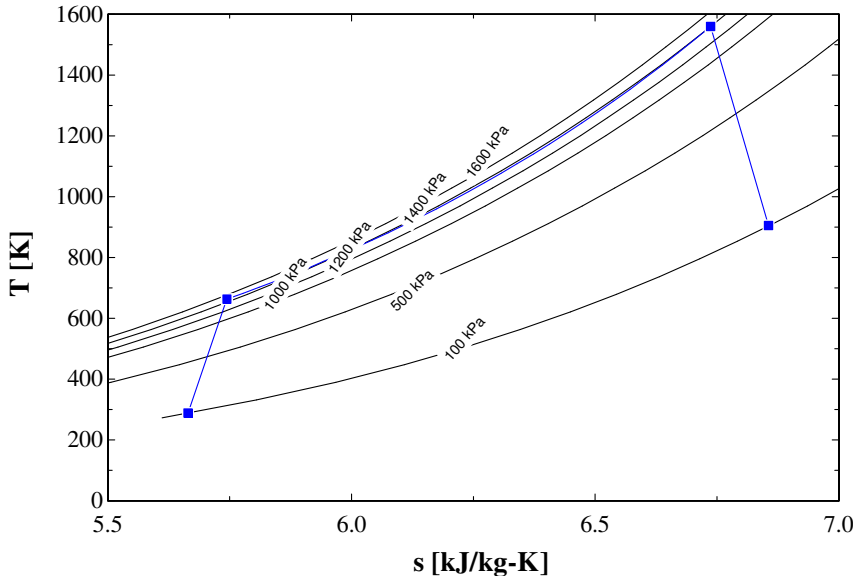

Figure 6.16: T-S Diagram for 7FA GT model

Heat exchanger model

After the model for normal stage calculation, the next step is to model the heat transfer across the walls of compressor and turbine stage. The compressor and turbine wall surfaces exposed to the GT working fluid have significantly large surface area. To affect heat transfer across the wall surface, the inner core of the blades need to have passages formed inside them. These inner passages will carry a heat transfer fluid to either impart or extract heat across the surface.

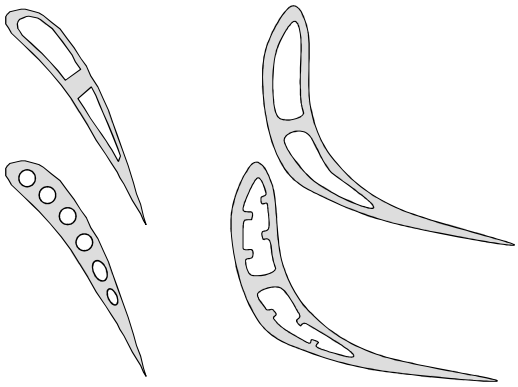

Figure 6.17: Probable designs for internal passages in compressor and turbine stages

The compressor and turbine stages' primary purpose is to compress the air and extract work from expansion of hot gases respectively. So, with the compressor and turbine stages acting as heat-exchangers, generation of heat in the process of compression and removal of heat through compressor wall surfaces will happen simultaneously. Similarly for the turbine stages, cooling due to expansion and heat addition from wall surfaces will happen together.

To represent this phenomenon in the model, the heat transfer calculations are performed after stage calculations. The exit temperature from normal stage calculations is taken as the inlet temperature for the hot side in case of compressor stage and cold side for the turbine stage respectively. Based on the fluid properties of working fluid and the corresponding fluid on the other side, flow conditions and geometry of the stage, the heat transfer across the stage is calculated. The flow conditions and geometry of the stage are considered at mean stage diameter. The working fluid temperature after consideration of stage heat transfer is considered as the stage exit temperature.

EES Model

The heat-exchanger model developed for this assessment is based on heat-exchange for a flow through pipe across the pipe wall surface. The equations shown below are for the

compressor stage heat-exchanger calculation. The turbine stage model is also the same with calculation based on flow and geometry details corresponding to the turbine stage.

Geometry calculations

For given blade dimensions (blade height *h*, blade cord *l* and blade pitch *s*), the stage parameters that can be determined are given in Table 6.6

Table 6.6: Stage Geometric Parameters

Stage Parameter	Expression
Blade span, spanbld	$2 \cdot l$
Number of blades, nbld	$\pi \cdot D_{\text{mean}} / span_{\text{bld}}$ computed to nearest integer
Stage area, Astg	$h \cdot span_{\text{bld}} \cdot n_{\text{bld}}$

Heat-transfer coefficient calculation

The heat transfer model developed for this study is a simple representation of the flow geometry and heat transfer mechanism (namely heat transfer across a pipe surface) using the Dittus-Boelter correlation for heat transfer assessment. This approach is easily applicable for internal passages created in the compressor and turbine vanes. However, for the air-side flow through the compressor and turbine stages, use of Dittus-Boelter correlation is questionable. To justify the use of the Dittus-Boelter correlation for heat transfer calculation, past literature review is carried out followed by assessment of different correlations to verify the applicability. The fluid properties (at rotor row exit temperature, T_2), namely density ρ, viscosity μ, thermal conductivity *k* and Prandtl number Pr, are the known quantities utilized for the calculation.

An assessment of heat transfer and flow structure in a rectangular channel with wing type vortex generator was carried out experimentally. The experiment results for the reference

case (i.e. rectangular channel with no vortex generators) were compared against standard correlations to validate the test set-up (Isak et al., 1998). Specifically, the friction factor and average Nusselt number from the study were compared against Petukov's friction factor formula and Dittus-Boelter correlation for Nusselt number

$$f = \left(0.79 \ln \mathrm{Re} - 1.64\right)^{-2} \tag{6.60}$$

$$\mathrm{Nu}_{\mathrm{avg}} = 0.023 \cdot \mathrm{Re}^{0.8} \cdot \mathrm{Pr}^{\mathrm{n}} \tag{6.61}$$

where n = 0.3 for heating flow and n = 0.4 for cooling flow

Re is the Reynolds number for the flow, which was calculated for a rectangular channel of dimensions *a* and *b* as

$$\mathrm{Re} = \frac{2ab}{(a+b)} \cdot \frac{v}{\nu} = \frac{D_{\mathrm{h}} \cdot v}{\nu} \tag{6.62}$$

where D_{h} is the hydraulic diameter.

The results showed a very good match between the experiment results for the reference case and the correlations for friction factor and Nusselt number calculation.

Another study on computer based simulation of forced turbulent convection in a rectangular channel showed a very good correspondence between the numerical calculation and Dittus-Boelter correlation (Rivas et al., 2012).

Figure 6.18 shows the comparison of Dittus-Boelter correlation and Gnielinski correlation for a range of Reynolds number.

The Gnielinski correlation is given by

$$\mathrm{Nu} = \frac{(f/8)(\mathrm{Re} - 1000)\mathrm{Pr}}{1 + 12.7(f/8)^{1/2}\left(\mathrm{Pr}^{2/3} - 1\right)} \tag{6.63}$$

where f is calculated using Eq. 6.60. The predicted Nusselt numbers from both correlations are almost identical over the entire range of Reynolds number.

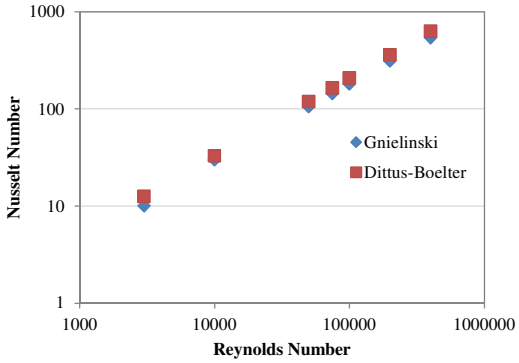

Figure 6.18: Comparison of Dittus-Boelter and Gnielinski correlation

The heat-transfer coefficient calculations for compressor stage heat transfer on air-side based on Dittus-Boelter correlation (Incropera, 2005) are given in Table 6.7.

Table 6.7: Stage Heat-transfer Parameters

Flow Parameters	Expression
Hydraulic diameter, D_h	$\frac{2 \cdot h \cdot s \cdot \cos(\alpha_2)}{(s \cdot \cos(\alpha_2) + h)}$
Reynolds number, Re	$\frac{\rho \cdot C_2 \cdot D_h}{\mu}$
Nusselt number, Nu	$0.023 \cdot \mathrm{Re}^{0.8} \cdot \mathrm{Pr}^{0.3}$
Heat transfer coefficient, *htc*	$\frac{\mathrm{Nu} \cdot k}{D_h}$

A similar set of calculations are performed for the inner passages of the blade. Water is the cooling fluid. The heat-transfer area for the blade inner passages is assumed to be half the stage area to represent the shortage of flow area for the inner passage. The actual inner passage area will depend on the passage design and can also have a greater area ratio than half of stage area. Figure 6.17 shows a set of probable passage designs to affect heat-exchange across the stages.

For the sake of simplicity again, the inner passage hydraulic diameter is assumed to be constant.

The thermal conductance of the hot side of the compressor stage is given by

$$UA_{\mathrm{h}} = htc_{\mathrm{h}} \cdot A_{\mathrm{stg,h}} \tag{6.64}$$

The thermal conductance of the cold side (inner passage) of the compressor stage is given by

$$UA_{\mathrm{c}} = htc_{\mathrm{c}} \cdot A_{\mathrm{stg,c}} \tag{6.65}$$

The thermal conductance for the wall material is given by

$$R_{\mathrm{w,bld}} = \frac{t_{\mathrm{bld}}}{k_{\mathrm{bld}} \cdot A_{\mathrm{stg,c}}} \tag{6.66}$$

The overall thermal conductance for the stage is then given by

$$UA_{\mathrm{stg}} = \frac{1}{\frac{1}{UA_{\mathrm{h}}} + R_{\mathrm{w,bld}} + \frac{1}{UA_{\mathrm{c}}}} \tag{6.67}$$

The stage heat-transfer is then given by

$$Q_{\mathrm{hx,stg}} = UA_{\mathrm{stg}} \cdot LMTD_{\mathrm{stg}} \tag{6.68}$$

where $LMTD_{\mathrm{stg}}$ is the log mean temperature difference for the stage, calculated as

$$LMTD_{\mathrm{stg}} = \frac{\Delta T_{\mathrm{in}} - \Delta T_{\mathrm{out}}}{\ln\left(\frac{\Delta T_{\mathrm{in}}}{\Delta T_{\mathrm{out}}}\right)} \tag{6.69}$$

ΔT_{in} is the temperature difference between the hot and cold fluids before heat transfer is affected and ΔT_{out} is the temperature difference between hot and cold fluids after heat transfer. ΔT_{in} is a known quantity while ΔT_{out} depends on the heat transfer across the stage. Since Equation 6.68 and 6.69 are interdependent, they are solved iteratively to arrive at the stage heat transfer.

A brief mention should be made here regarding the variation in treatment of heat transfer between heat-exchanger calculations for plate-fin heat exchanger and the heat transfer across compressor and turbine stages being carried out in the present section. The main reason for this difference is the lack of geometric details on the air-side as well as the design of internal passages. This lack of detail should be kept in mind while interpreting the results from the current section wherein a greater uncertainty about the predictions is bound to occur.

LCGT with recuperator

Model

The LCGT model calculates the performance of the entire system based on the given inputs for the system configuration. The compressor and turbine model solve for the row-by-row performance along with the heat transfer calculations. The LCGT model is also augmented with the receiver model and the cost models utilized in the HTSGT system as described in the system modeling chapter (Chapter 3).

The LCGT model is run for a range of GT pressure ratio and peak cycle temperature to determine the optimum configuration which gives the best economy.

The LCGT system is designed for a 100 MW output using the power tower system and a recuperator. The external heat exchangers have an effectiveness of 95% and 2% pressure loss. The compressor and turbine efficiencies are determined using the respective row-by-row models. The compressor model inputs are listed in Table 6.8

Table 6.8: Compressor Model Inputs

Blade pitch, s	0.25H
Blade cord, l	0.3H
Rotor incidence angle, i_{rot}	10 deg.
Stator incidence angle, i_{stat}	5 deg.
Number of stages, $n_{stg,comp}$	6

The compressor mean diameter, D_{comp} and first stage blade height, H are determine based on the system mass flow. This is done to reduce the sensitivity of the stage flow profile to variation in system mass flow. Both the parameters above vary with the square root of mass flow rate.

Table 6.9: Turbine Model Inputs

Nozzle blade cord, b_{nzl}	0.6H
Rotor blade cord, b_{rot}	0.65H
Rotor tip clearance, t_{rot}	0.013H
Number of turbine stages, n_{stg}	3

The turbine model inputs are listed in Table 6.9. Like the compressor, the turbine mean diameter and first stage blade height is dependent on the mass flow of the system. The stage geometric parameters for both compressor and turbine are nominal values in the range of applicability of the cascade correlations used and can be varied to optimize the system performance.

The GT cost model is augmented with an additional factor, namely the Lorentz cycle cost factor k_{lc} multiplied with the GT cost obtained from the HTSGT cost model.

$$C_{\mathrm{lcgt}} = k_{\mathrm{lc}} \cdot C_{\mathrm{htsgt}} \tag{6.70}$$

The factor represents the rise in GT cost to accommodate the cost of manufacturing the stages of the compressor and turbine with internal passages and the additional system configuration changes required to affect heat exchange. This factor will depend on the design of the internal passage and how the fluids are routed internally. It is beyond the scope of a conceptual assessment of the proposed system to determine this factor with accuracy. However, a sensitivity of the system performance to a range of values for this factor will demonstrate its impact at the system level. The nominal value for the factor is considered as 1.5.

Results

The LCGT system is assessed for a range of pressure ratios and peak cycle temperatures. The LCGT mass-flow is altered to achieve the machine output in the range of 90 to 100 MW. Figure 6.19 shows the variation in GT efficiency, receiver efficiency and the overall power plant efficiency for all the configurations considered.

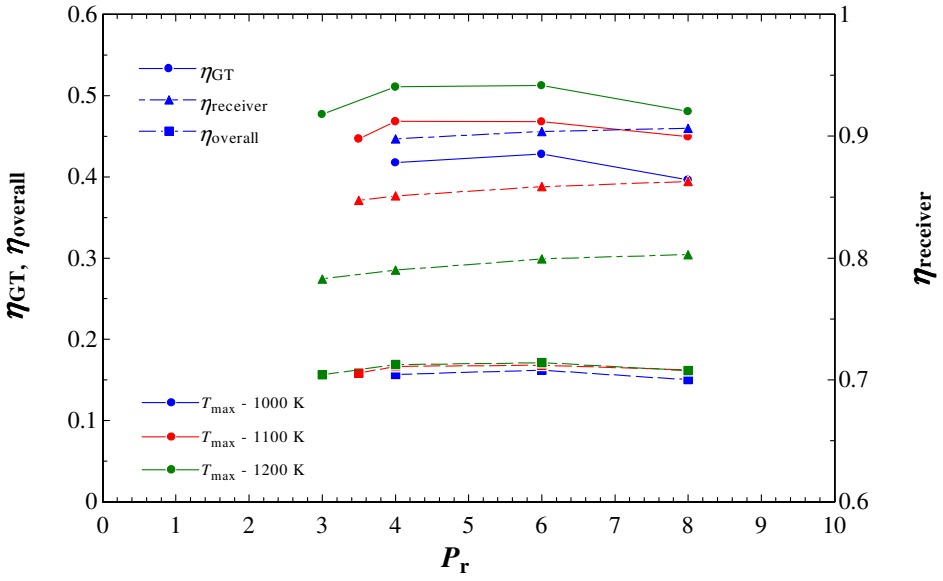

Figure 6.19: System efficiency variation with pressure ratio and temperature-LCGT

The peak GT efficiency for a particular peak cycle temperature occurs at the pressure ratio of 4 and 6. The GT efficiency increases with increase in peak cycle temperature. The trend is similar to a recuperated system but the efficiency does not reduce drastically with pressure ratio as in a recuperated system. The receiver efficiency reduces with increasing peak cycle temperature and reducing pressure ratio. This is due to increase in average HTF temperature with increase in peak cycle temperature or reduction in pressure ratio. The overall system efficiency shows similar trend as the GT efficiency for a particular peak cycle temperature. However, the overall efficiency increases initially with peak cycle temperature but the efficiency curve for 1200 K almost overlaps the curve for 1100 K showing a peak for the temperature.

The system efficiency dictates the cost of the system. Figure 6.20 shows the power plant cost for the configurations assessed.

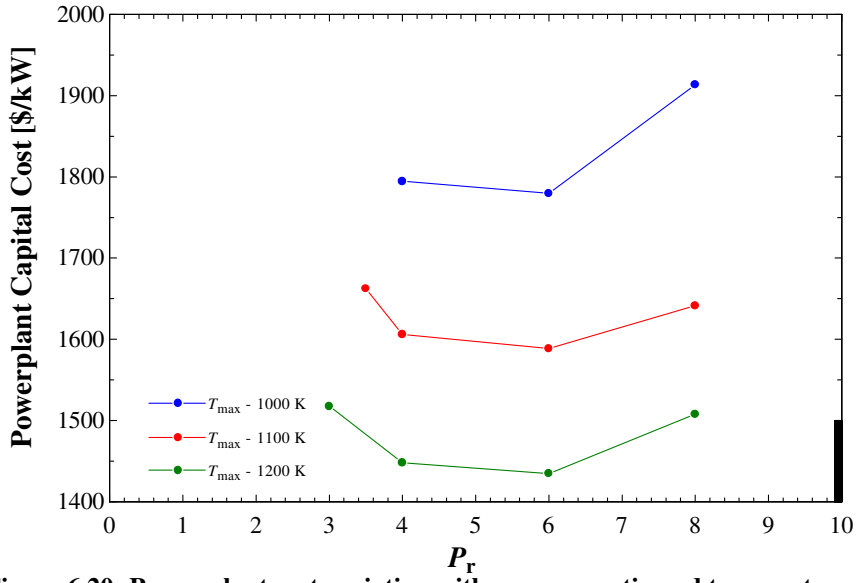

Figure 6.20: Power plant cost variation with pressure ratio and temperature-LCGT

The power plant cost reduces with increase in peak cycle temperature. For a particular peak cycle temperature, the pressure ratio of 6 achieves the lowest system cost. However, this is not the complete representation of the system performance. The unit cost of electricity which accounts for the amount of energy conversion achieved for a particular configuration is the real indicator of a system's effectiveness. Figure 6.21 shows the unit cost of electricity for the configurations.

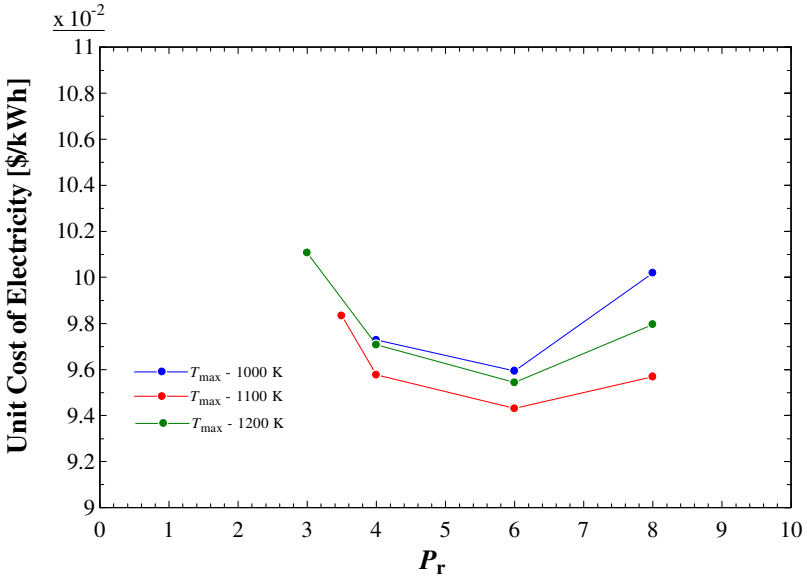

Figure 6.21: Unit cost of electricity variation with pressure ratio and temperature-LCGT

The figure above shows that the optimum unit cost of electricity is achieved at pressure ratio of 6 and a peak cycle temperature of 1100 K. The unit cost of electricity increases in either direction of changing temperature and pressure ratio. An interesting observation is the proximity of the optimum point for LCGT system to the optimum point for the HTSGT system which is at pressure ratio of 4 and peak cycle temperature of 1100 K. The minimum unit cost achieved is 9.4 cent/kWh which is very close to the HTSGT system economy.

Figure 6.22 shows the T-s diagram for the optimum system configuration.

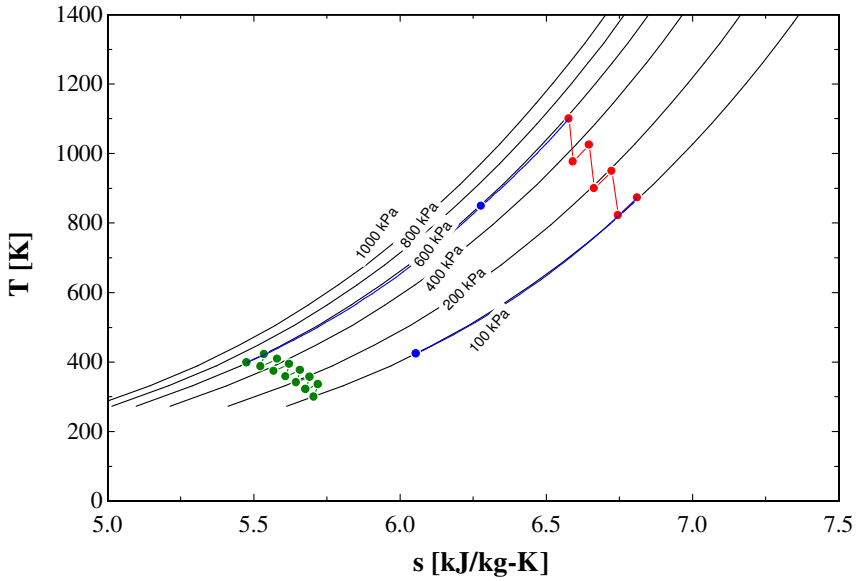

Figure 6.22: T-s diagram for the optimum LCGT configuration

The effect of heat transfer across the compressor and turbine stages is observed to achieve the effect of a gliding temperature cycle. The recuperator reduces the heat input required for a specified work out from the solar collector system, improving the GT efficiency. Table 6.10 represents the system parameters for the optimum configuration

Table 6.10: LCGT Optimum Configuration Parameters

Pressure ratio, P_r	6
Peak cycle temperature, T_{max} [K]	1100
Rated Output, $\dot{W}_{grid}$ [MW]	100
GT efficiency, η_{GT} [%]	46.8
Compressor efficiency, η_{comp} [%]	94
Turbine efficiency, η_{turb} [%]	96
Receiver efficiency, η_{rec} [%]	85.8
Overall efficiency, $\eta_{overall}$ [%]	16.8
Design Thermal power input, Q_{dsgn} [MW]	217
Solar collector system cost, $C_{SC,tot}$ [$/kW]	1080
GT system cost, C_{GT} [$/kW]	492
Heat exchanger cost, C_{Hx} [$/kW]	19
Power plant cost, $C_{PP,tot}$ [$/kW]	1589
Annualized Life cycle cost [Million $]	17
Annual electricity generation [GWh]	181
Unit cost of electricity [cent/kW]	9.4

The heat transfer calculations for the compressor and turbine stages are presented in Table 6.11

Table 6.11: LCGT Optimum Configuration Stage Heat transfer Parameters

Compressor (stage# 17-Air side)	
A_{stg} [m^2]	2.2
Htc [W/m^2-K]	2660
UA_{stg} [W/K]	4600
LMTD [K]	2.5
Turbine (stage# 3-Air side)	
A_{stg} [m^2]	39.2
Htc [W/m^2-K]	1088
UA_{stg} [W/K]	20100
LMTD [K]	1.34

Lorentz Cost Factor

Figure 6.23 shows the sensitivity of the unit cost of electricity to the Lorentz cost factor. The unit cost changes significantly with change in the Lorentz cost factor. This implies a careful consideration while designing the internal passages to keep the change in cost at a minimum.

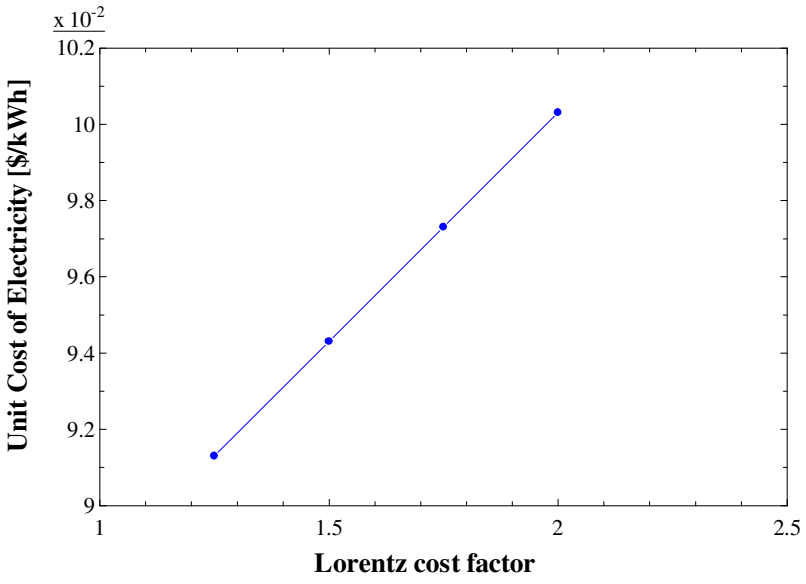

Figure 6.23: Sensitivity of unit cost of electricity to Lorentz cost factor

Conclusion

The LCGT system presents itself as a feasible option for harnessing solar energy to generate power. The GT efficiency achieved with an open air cycle is comparable to the HTSGT system. The LCGT system can also be compared to dish/Stirling systems where in the design can be leveraged to smaller scales without losing out on the system performance. With a more detailed design and assessment of the proposed heat exchange system within the compressor and turbine stages, better system efficiency can be achieved to improve the economy of the power plant.

CHAPTER 7

CONCLUSIONS AND FUTURE WORK

This Chapter will present conclusions from the present study that have been drawn based on the foregoing thermodynamic and economic evaluation of the performance of the gas cycles for solar thermal power generation systems. In addition, this chapter will include a brief discussion on possible directions to extend this study.

Conclusions

The thermodynamic and economic design for a 100 MW solar thermal power generation system implementing gas turbine has been characterized in this study through a system evaluation of three selected gas power cycles.

The main design constraints imposed on the cycles were based on the practical limitations of the particular design configuration. In addition, for individual sub-systems and components, the performance parameters were based on available performance data or established guidelines. On the basis of the results of the parametric evaluation of the three cycles considered, the study draws the following conclusions:

1. The gas cycles using a gas turbine offer a feasible option to generate electricity based on solar energy.

2. The CGT system at a peak efficiency of 28% does not meet the requirement for generating solar power at an economical rate at the peak cycle temperature of 750 K compared to current power generation technology operating for a parabolic trough solar collector system.

3. The HTSGT system gives the most economical system at 9.1 cent/kWh for unit cost of electricity and an overall system efficiency of 16.5%.

4. The optimum HTSGT configuration is a basic gas turbine with two intercoolers, three compressors and a recuperator operating at a peak cycle temperature of 1100 K and an overall pressure ratio of 4 with a GT efficiency of 45.2%.

5. The LCGT system has the maximum overall efficiency of 16.8% and the minimum unit cost of electricity at 9.4 cent/kWh.

6. The optimum LCGT configuration operates at a peak cycle temperature of 1100 K and an overall pressure ratio of 6 with a GT efficiency of 46.8%.

Future Work

The present effort was a basic investigation into the applicability of gas cycles in the solar thermal power generation. Development of more detailed component models and system optimization to capture the dynamic behavior of the system will improve the understanding of the system and improve confidence in the applicability of the technology. The cost models can incorporate higher order details of the cost of each system and component to achieve a more representative cost of electricity generation.

The HTSGT and LCGT system in combination with a gas/oil fired combustion system can enhance the system flexibility and improve the capacity factor. Incorporation of TES will improve the system capacity factor and improve the overall system efficiency. These augmentations to the system can also be studied to arrive at the optimum configuration.

APPENDIX A: EES CODES FOR VARIOUS MODELS

Power plant Model – GT with 2 stage Intercooler and Recuperator

```
//Model Begins

i_lpcomp_in = 1
i_ic1_in = 2
i_ipcomp_in = 3
i_ic2_in = 4
i_hpcomp_in = 5
i_recup_cold_in = 6
i_solarhx_in = 7
i_turb_in = 8
 i_recup_hot_in = 9
i_exh_in = 10


working_fluid$ = 'AIR'

T[i_lpcomp_in]=300
P[i_lpcomp_in]=100 [kPa]

T_0_K=T[i_lpcomp_in]
h_0 = enthalpy(working_fluid$,T=T[i_lpcomp_in])
s_0=entropy(working_fluid$,T=T[i_lpcomp_in],P=P[i_lpcomp_in])
rho_0=density(working_fluid$,T=T[i_lpcomp_in],P=P[i_lpcomp_in])
Q_gt = m_dot/rho_0
hp = rp/(lp*ip)

W_dot_grid=100000 [kW]

Eta_c=0.86
Eta_t=0.85
eff_hx = 0.95
eff_gen=0.99
ploss=0.02

ploss_IC1=ploss
ploss_IC2=ploss
ploss_recup=ploss

"Coolant-Water"
P_water = 500 [kPa]
T_water = 300 [K]
ploss_w = 0.8

"Heating-HTF"
P_HTF = 500 [kPa]
ploss_HTF = 0.8

"!LP Compression"

h[i_lpcomp_in]=enthalpy(working_fluid$,T=T[i_lpcomp_in])
s[i_lpcomp_in]=entropy(working_fluid$,T=T[i_lpcomp_in],P=P[i_lpcomp_in])
v1=volume(working_fluid$,T=T[i_lpcomp_in],P=P[i_lpcomp_in])
s2s=s[i_lpcomp_in]
h2s=enthalpy(working_fluid$,P=P[i_ic1_in],s=s2s)
v2s=volume(working_fluid$,P=P[i_ic1_in],s=s2s)
T2s=temperature(working_fluid$,v=v2s,P=P[i_ic1_in])
Eta_c=(h[i_lpcomp_in]-h2s)/(h[i_lpcomp_in]-h[i_ic1_in])"Definition of compressor
efficiency"

P[i_ic1_in]=lp*P[i_lpcomp_in]
s[i_ic1_in]=entropy(working_fluid$,P=P[i_ic1_in],H=h[i_ic1_in])
v2=volume(working_fluid$,P=P[i_ic1_in],s=s[i_ic1_in])
T[i_ic1_in]=temperature(working_fluid$,P=P[i_ic1_in],v=v2)
h[i_ic1_in]=W_c_lp+ h[i_lpcomp_in]                    "compressor work"
```

```
 "!InterCooler-1"

"Coolant"
eff_hx_IC1=eff_hx

fluid_cold_IC1$ = 'Water'
TL_in_IC1 = T_water
fluid_hot_IC1$ = 'AIR'
TH_in_IC1 = T[i_ic1_in]
PH_in_IC1 = P[i_ic1_in]
PC_in_IC1 = P_water { bars of water pressure}
m_dot_cold_IC1 = 500 [kg/s]
ploss_h_IC1=ploss_IC1
ploss_c_IC1=ploss_w
call HXer(eff_hx_IC1,
ploss_h_IC1,ploss_c_IC1,TL_in_IC1,TH_in_IC1,PH_in_IC1,PC_in_IC1,fluid_hot_IC1$,fluid_cold
_IC1$ ,m_dot,m_dot_cold_IC1,1 :
hx_area_IC1,hx_cost_IC1,ploss_h_actual_IC1,ploss_c_actual_IC1,TL_out_IC1,TH_out_IC1 )

Pressure_rise = P_water
flow_velocity = 30 [m/s]
Pump_RPM = 3600

P[i_ipcomp_in]=P[i_ic1_in]*(1-ploss_IC1)
call ICHXer(eff_hx_IC1, T[i_lpcomp_in],T[i_ic1_in] : T[i_ipcomp_in] )
s[i_ipcomp_in]=entropy(working_fluid$,T=T[i_ipcomp_in],P=P[i_ipcomp_in])
h[i_ipcomp_in]=enthalpy(working_fluid$,T=T[i_ipcomp_in])

T_eff_IC1=(h[i_ipcomp_in]-h[i_ic1_in])/((s[i_ipcomp_in]-s[i_ic1_in]))

"!IP Compression"
v3=volume(working_fluid$,T=T[i_ipcomp_in],P=P[i_ipcomp_in])
P[i_ic2_in]=ip*P[i_ipcomp_in]/(1-ploss_IC1)
s4s=s[i_ipcomp_in]
h4s=enthalpy(working_fluid$,P=P[i_ic2_in],s=s4s)
v4s=volume(working_fluid$,P=P[i_ic2_in],s=s4s)
T4s=temperature(working_fluid$,v=v4s,P=P[i_ic2_in])
Eta_c=(h[i_ipcomp_in]-h4s)/(h[i_ipcomp_in]-h[i_ic2_in])"Definition of compressor
efficiency"

s[i_ic2_in]=entropy(working_fluid$,P=P[i_ic2_in],H=h[i_ic2_in])
v4=volume(working_fluid$,P=P[i_ic2_in],s=s[i_ic2_in])
T[i_ic2_in]=temperature(working_fluid$,P=P[i_ic2_in],v=v4)
h[i_ic2_in]=W_c_ip+ h[i_ipcomp_in]                    "compressor work"

"!InterCooler-2"

"Coolant"
eff_hx_IC2=eff_hx

fluid_cold_IC2$ = 'Water'
TL_in_IC2 = T_water
fluid_hot_IC2$ = 'Air'
TH_in_IC2 = T[i_ic2_in]
PH_in_IC2 = P[i_ic2_in]
PC_in_IC2 = P_water { bars of water pressure}
m_dot_cold_IC2 = 500 [kg/s]
ploss_h_IC2=ploss_IC2
ploss_c_IC2= ploss_w
call HXer(eff_hx_IC2,
ploss_h_IC2,ploss_c_IC2,TL_in_IC2,TH_in_IC2,PH_in_IC2,PC_in_IC2,fluid_hot_IC2$,fluid_cold
_IC2$ ,m_dot,m_dot_cold_IC2,1 :
hx_area_IC2,hx_cost_IC2,ploss_h_actual_IC2,ploss_c_actual_IC2,TL_out_IC2,TH_out_IC2 )
P[i_hpcomp_in]=P[i_ic2_in]*(1-ploss_IC2)
call ICHXer(eff_hx_IC2, T[i_lpcomp_in],T[i_ic2_in] : T[i_hpcomp_in] )
s[i_hpcomp_in]=entropy(working_fluid$,T=T[i_hpcomp_in],P=P[i_hpcomp_in])
h[i_hpcomp_in]=enthalpy(working_fluid$,T=T[i_hpcomp_in])

T_eff_IC2=(h[i_hpcomp_in]-h[i_ic2_in])/(s[i_hpcomp_in]-s[i_ic2_in])
```

```
"!HP Compression"
v5=volume(working_fluid$,T=T[i_hpcomp_in],P=P[i_hpcomp_in])
P[i_recup_cold_in]=hp*P[i_hpcomp_in]/(1-ploss_IC2)
s6s=s[i_hpcomp_in]
h6s=enthalpy(working_fluid$,P=P[i_recup_cold_in],s=s6s)
v6s=volume(working_fluid$,P=P[i_recup_cold_in],s=s6s)
T6s=temperature(working_fluid$,v=v6s,P=P[i_recup_cold_in])
Eta_c=(h[i_hpcomp_in]-h6s)/(h[i_hpcomp_in]-h[i_recup_cold_in])"Definition of compressor
efficiency"

s[i_recup_cold_in]=entropy(working_fluid$,P=P[i_recup_cold_in],H=h[i_recup_cold_in])
v6=volume(working_fluid$,P=P[i_recup_cold_in],s=s[i_recup_cold_in])
T[i_recup_cold_in]=temperature(working_fluid$,P=P[i_recup_cold_in],v=v6)
h[i_recup_cold_in]=W_c_hp+ h[i_hpcomp_in]           "compressor work"

w_c = w_c_lp + w_c_ip + w_c_hp

"!Combustion"

"Heating-HTF"
eff_hx_solar=eff_hx

fluid_cold_solar$ = 'Air'
TL_in_solar = T[i_solarhx_in]
fluid_hot_solar$ = 'HTF'
TH_in_solar =(Tmax-T[i_solarhx_in])/eff_hx_solar+T[i_solarhx_in]
PH_in_solar = P_HTF
PC_in_solar = P[i_solarhx_in]
call HTF_flow(eff_hx_solar,
TL_in_solar,TH_in_solar,PH_in_solar,PC_in_solar,fluid_cold_solar$,m_dot : m_dot_hot_solar
)
ploss_h_solar=ploss_HTF
ploss_c_solar= ploss
call HXer(eff_hx_solar,
ploss_h_solar,ploss_c_solar,TL_in_solar,TH_in_solar,PH_in_solar,PC_in_solar,fluid_hot_sol
ar$,fluid_cold_solar$ ,m_dot_hot_solar,m_dot,1 :
hx_area_solar,hx_cost_solar,ploss_h_actual_solar,ploss_c_actual_solar,TL_out_solar,TH_out
_solar )
flow_velocity_solar = 10 [m/s]

P[i_turb_in]=P[i_solarhx_in]*(1-ploss)
T[i_turb_in]=Tmax
h[i_turb_in]=enthalpy(working_fluid$,T=T[i_turb_in])
s[i_turb_in]=entropy(working_fluid$,P=P[i_turb_in],T=T[i_turb_in])
v8=volume(working_fluid$,P=P[i_turb_in],T=T[i_turb_in])
h[i_turb_in]=q_in+h[i_solarhx_in]                   "Combustion Heat Input"

"!Expansion"
P[i_lpcomp_in]=P[i_recup_hot_in]*(1-ploss_recup)
s9s=s[i_turb_in]
h9s=enthalpy(working_fluid$,P=P[i_recup_hot_in],s=s9s)
v9s=volume(working_fluid$,P=P[i_recup_hot_in],s=s9s)
T9s=temperature(working_fluid$,P=P[i_recup_hot_in],v=v9s)
w_t_s=h[i_turb_in] - h9s                            "isentropic turbine work"
w_t=w_t_s*Eta_t
h[i_turb_in]=h[i_recup_hot_in]+W_t                  "Turbine Work"
v9=volume(working_fluid$,P=P[i_recup_hot_in],h=h[i_recup_hot_in])
 s[i_recup_hot_in]=entropy(working_fluid$,P=P[i_recup_hot_in],h=h[i_recup_hot_in])
T[i_recup_hot_in]=temperature(working_fluid$,P=P[i_recup_hot_in],v=v9)

"!Recuperator"
"Coolant"
"Option-1 : Air to Air"
eff_hx_recup=eff_hx

fluid_cold_recup$ = 'AIR'
TL_in_recup = T[i_recup_cold_in]
 fluid_hot_recup$ = 'AIR'
TH_in_recup = T[i_recup_hot_in]
PH_in_recup = P[i_recup_hot_in]
PC_in_recup = P[i_recup_cold_in]
```

```
ploss_h_recup=ploss_recup
ploss_c_recup= ploss_recup
call HXer(eff_hx_recup,
ploss_h_recup,ploss_c_recup,TL_in_recup,TH_in_recup,PH_in_recup,PC_in_recup,fluid_hot_rec
up$,fluid_cold_recup$ ,m_dot,m_dot,1 :
hx_area_recup,hx_cost_recup,ploss_h_actual_recup,ploss_c_actual_recup,TL_out_recup,TH_out
_recup )

P[i_solarhx_in] = P[i_recup_cold_in]*(1-ploss_recup)
call REGENHXer(eff_hx_recup, T[i_recup_cold_in],T[i_recup_hot_in] : T[i_solarhx_in] )
h[i_solarhx_in]=enthalpy(working_fluid$,T=T[i_solarhx_in])
h7s = h[i_solarhx_in]
s[i_solarhx_in] = entropy(working_fluid$,T=T[i_solarhx_in], P=P[i_solarhx_in])
s7s = s[i_solarhx_in]
q_ex_rec=h[i_solarhx_in]-h[i_recup_cold_in]

P[i_exh_in] = P[i_lpcomp_in]
h[i_exh_in]=h[i_recup_hot_in]-q_ex_rec
T[i_exh_in]=Temperature(working_fluid$,H=h[i_exh_in])
 s[i_exh_in]=entropy(working_fluid$,T=T[i_exh_in],P=P[i_exh_in])
h10s=h[i_exh_in]
s10s=s[i_exh_in]

"!CoolOff"
q_exh + h[i_lpcomp_in]=h[i_exh_in]                    "Heat Rejection"

"!Cycle Statistics"
w_net=w_t - w_c

"work per mass of compressor Air"
w_grid=w_net*eff_gen

"size the system and components"
m_dot=W_dot_grid/w_grid

"compressor"
W_dot_comp = m_dot*w_c

"turbine"
W_dot_turb = m_dot*w_t

W_dot_net = m_dot*w_net

"intercooler"
Q_dot_IC1=m_dot*(h[i_ic1_in]-h[i_ipcomp_in])
Eq_dot_IC1=Q_dot_IC1*(1-T_0_K/T_eff_IC1)

Q_dot_IC2=m_dot*(h[i_ic2_in]-h[i_hpcomp_in])
Eq_dot_IC2=Q_dot_IC2*(1-T_0_K/T_eff_IC2)

Q_dot_IC = Q_dot_IC1 + Q_dot_IC2
Eq_dot_IC = Eq_dot_IC1 + Eq_dot_IC2

"Heat-Exchanger"
Q_dot_in = m_dot*q_in
Eq_dot_HX_H = Q_dot_in*(1-T_0_K/T_H_eff)
Eq_dot_HX = Q_dot_in*(1-T_0_K/Tmax)

"recuperator"
Q_dot_recup = m_dot*q_ex_rec
T_L_rec=(h[i_recup_cold_in]-h[i_solarhx_in])/(s[i_recup_cold_in]-s[i_solarhx_in])
T_H_rec=(h[i_recup_hot_in]-h[i_exh_in])/(s[i_recup_hot_in]-s[i_exh_in])
Eq_dot_L_recup=Q_dot_recup*(1-T_0_K/T_L_rec)
Eq_dot_H_recup=Q_dot_recup*(1-T_0_K/T_H_rec)

"exhaust"
Q_dot_exh = m_dot*q_exh
T_eff_exh=(h[i_exh_in]-h[i_lpcomp_in])/(s[i_exh_in]-s[i_lpcomp_in])

"calculate the overall effective  temps"
Q_dot_out=Q_dot_IC + Q_dot_exh
```

```
S_dot_Q_out=Q_dot_IC1/T_eff_IC1 + Q_dot_IC2/T_eff_IC2 + Q_dot_exh/T_eff_exh
T_L_eff=Q_dot_out/S_dot_Q_out
T_H_eff=(h[i_turb_in]-h[i_solarhx_in])/(s[i_turb_in]-s[i_solarhx_in])
eta_Carnot=1-T_L_eff/T_H_eff

"Overall Energy Balance"
H_dot[i_lpcomp_in] = m_dot*h[i_lpcomp_in]
H_dot[i_ic1_in] = m_dot*h[i_ic1_in]
H_dot[i_ipcomp_in] = m_dot*h[i_ipcomp_in]
H_dot[i_ic2_in] = m_dot*h[i_ic2_in]
H_dot[i_hpcomp_in] = m_dot*h[i_hpcomp_in]
H_dot[i_recup_cold_in] = m_dot*h[i_recup_cold_in]
H_dot[i_solarhx_in] = m_dot*h[i_solarhx_in]
H_dot[i_turb_in] = m_dot*h[i_turb_in]
H_dot[i_recup_hot_in] = m_dot*h[i_recup_hot_in]
H_dot[i_exh_in] = m_dot*h[i_exh_in]

Ex_dot[i_lpcomp_in] = m_dot*((h[i_lpcomp_in]-h_0)-T_0_K*(s[i_lpcomp_in]-s_0))
Ex_dot[i_ic1_in] = m_dot*((h[i_ic1_in]-h_0)-T_0_K*(s[i_ic1_in]-s_0))
Ex_dot[i_ipcomp_in] = m_dot*((h[i_ipcomp_in]-h_0)-T_0_K*(s[i_ipcomp_in]-s_0))
Ex_dot[i_ic2_in] = m_dot*((h[i_ic2_in]-h_0)-T_0_K*(s[i_ic2_in]-s_0))
Ex_dot[i_hpcomp_in] = m_dot*((h[i_hpcomp_in]-h_0)-T_0_K*(s[i_hpcomp_in]-s_0))
Ex_dot[i_recup_cold_in] = m_dot*((h[i_recup_cold_in]-h_0)-T_0_K*(s[i_recup_cold_in]-s_0))
Ex_dot[i_solarhx_in] = m_dot*((h[i_solarhx_in]-h_0)-T_0_K*(s[i_solarhx_in]-s_0))
Ex_dot[i_turb_in] = m_dot*((h[i_turb_in]-h_0)-T_0_K*(s[i_turb_in]-s_0))
Ex_dot[i_recup_hot_in] = m_dot*((h[i_recup_hot_in]-h_0)-T_0_K*(s[i_recup_hot_in]-s_0))
Ex_dot[i_exh_in] = m_dot*((h[i_exh_in]-h_0)-T_0_K*(s[i_exh_in]-s_0))

"component energy analysis"
E_acc_comp = H_dot[i_lpcomp_in]+W_dot_comp-H_dot[i_recup_cold_in]-Q_dot_IC
E_acc_recup = H_dot[i_recup_cold_in] + H_dot[i_recup_hot_in] - H_dot[i_solarhx_in] -
H_dot[i_exh_in]
E_acc_HX = H_dot[i_solarhx_in] + Q_dot_in - H_dot[i_turb_in]
E_acc_turb = H_dot[i_turb_in] - W_dot_turb - H_dot[i_recup_hot_in]

"Exergy Analysis"
I_dot_HX = Ex_dot[i_solarhx_in] + Eq_dot_HX_H - Ex_dot[i_turb_in]
I_dot_HX_H = Eq_dot_HX_H - Eq_dot_HX
I_dot_recup = Ex_dot[i_recup_cold_in] + Ex_dot[i_recup_hot_in] - Ex_dot[i_solarhx_in] -
Ex_dot[i_exh_in]
I_dot_turb = Ex_dot[i_turb_in] - W_dot_turb - Ex_dot[i_recup_hot_in]
I_dot_comp = Ex_dot[i_lpcomp_in]+W_dot_comp-Ex_dot[i_recup_cold_in]-Eq_dot_IC
I_dot_IC=Ex_dot[i_ic1_in]-Ex_dot[i_ipcomp_in]+Ex_dot[i_ic2_in]-Ex_dot[i_hpcomp_in]-
Eq_dot_IC

I_dot_total = I_dot_comp + I_dot_recup + I_dot_HX + I_dot_turb+I_dot_IC

"Efficiencies"

eta_energy = W_dot_net/Q_dot_in

eta_exergy = (1-T_L_eff/T_H_eff)-(T_L_eff*I_dot_total)/(T_0_K*Q_dot_in)

//Cost Analysis
solar_multiple=1.0
Q_design = solar_multiple*Q_dot_in
tower_ref_cost = 901500
tower_coeff = 0.01298
tower_height= interpolate(tower_height,Qin,height_tower,Qin=Q_design)
tower_cost = tower_ref_cost*EXP(tower_coeff*tower_height)
tower_cap = tower_cost / W_dot_grid
receiver_ref_area = 1110
receiver_ref_cost = 59148900
receiver_coeff = 0.7
receiver_area= interpolate(Rec_area,Qin,area_rec,Qin=Q_design)
receiver_cost = receiver_ref_cost*(receiver_area/receiver_ref_area)
receiver_cap = receiver_cost / W_dot_grid
field_unit_cost = 201
field_area= interpolate(Field_area,Qin,area_field,Qin=Q_design)
field_cost = field_unit_cost*field_area
field_cap = field_cost / W_dot_grid
```

```
solar_collector_cap = tower_cap + receiver_cap + field_cap

gt_cap_0 = 227

m_dot_base = 200 [kg/s]
P_base = 100 [kPa]
T_base = 300 [K]
R_base = 287
R_fluid = 287

gt_cap =
gt_cap_0*(((m_dot*T_0_K*R_fluid/P[i_lpcomp_in])/(m_dot_base*T_base*R_base/P_base))^0.734*
(rp/12.7)^0.366)

hx_IC1_cap=hx_cost_IC1*1e6/W_dot_grid
 hx_IC2_cap=hx_cost_IC2*1e6/W_dot_grid
hx_recup_cap=hx_cost_recup*1e6/W_dot_grid
hx_solar_cap=hx_cost_solar*1e6/W_dot_grid

hx_priceindex_ratio = 1.47
hx_total_cap = hx_priceindex_ratio*(hx_IC1_cap+hx_IC2_cap+hx_recup_cap+hx_solar_cap)

pwrplnt_total_cap=hx_total_cap+gt_cap+solar_collector_cap

drate=0.075                    "MARR for general econ analysis"
irate=0.025                    "inflation rate for fuel"
npds=30               "planning period for general econ analysis"

irate2=0.0
// LCCF for annualized cost
call LCCFP(drate,irate,npds:USPWF)

LCC_tot=pwrplnt_total_cap*W_dot_grid

Cost_annual=LCC_tot/USPWF

E_incsolar_annual = interpolate(Incident_solar_energy,Qin,E_solar_annual,Qin=Q_design)
eta_SF = 0.44
alpha_receiver = 0.95
E_SF_annual = eta_SF*E_incsolar_annual
Tavg_htf = (TH_in_solar+TH_out_solar)/2
DeltaT_htf=(TH_in_solar-TH_out_solar)
eta_receiver =
interpolate2D(receff,Thot,Tcold,eta_receiver,Thot=TH_in_solar,Tcold=TH_out_solar,70)
E_powerblock_annual = eta_receiver*E_SF_annual*alpha_receiver
W_annual = E_powerblock_annual*eta_energy
eta_overall = W_annual/E_incsolar_annual

OM_Annual = 65*W_dot_grid

Cost_Annual_tot = Cost_annual + OM_Annual

Cost_unit=Cost_annual_tot/W_annual
```

Heat-exchanger Model

```
PROCEDURE HXer(eff_hx,
ploss_h_req,ploss_c_req,TL_in,TH_in,PH_in,PC_in,fluid_hot$,fluid_cold$,m_dot_hot,m_dot_co
ld,hx_type : hx_area,hx_cost,ploss_h,ploss_c,TL_out,TH_out )
"HTF Properties"
rho_HTF=2020 [kg/m^3]
Cp_HTF=1.89 [kJ/kg-K]
mu_HTF=rho_HTF*1.4e-6
Prnl_HTF=5.938
k_HTF=0.6 [W/m-K]

if (TL_in < TH_in) then

"Determine Minimum Fluid"
T_avg = (TH_in+TL_in)/2
```

```
if (isidealgas(fluid_cold$)) then
c_p_c_avg = SPECHEAT(fluid_cold$,T=T_avg)
else
c_p_c_avg = SPECHEAT(fluid_cold$,T=T_avg, P = PC_in)
endif
if (fluid_hot$='HTF') then
c_p_h_avg = INTERPOLATE('Salt (60% NaNO3-40% KNO3)','T','C',T=T_avg)
else
if (isidealgas(fluid_hot$)) then
c_p_h_avg =  SPECHEAT(fluid_hot$,T=T_avg)
else
c_p_h_avg =  SPECHEAT(fluid_hot$,T=T_avg, P = PH_in)
endif
endif
C_c_test = m_dot_cold*c_p_c_avg
C_h_test = m_dot_hot*c_p_h_avg
C_min_test = MIN(C_c_test , C_h_test)
rev = 1

if( (C_c_test <= C_h_test) and (rev > 0)) then

40: TL_out = TL_in+eff_hx*(TH_in-TL_in)
T_cold_avg = (TL_in+TL_out)/2
if (isidealgas(fluid_cold$)) then
c_p_c = SPECHEAT(fluid_cold$,T=T_cold_avg)
else
c_p_c = SPECHEAT(fluid_cold$,T=T_cold_avg, P = PC_in)
endif
C_c = m_dot_cold*c_p_c
q_c = C_c*(TL_out-TL_in)
TH_out = TH_in-C_min_test*eff_hx*(TH_in-TL_in)/C_h_test
TH_out_itr = TH_out
Repeat
T_hot_avg = (TH_in+TH_out_itr)/2
if (fluid_hot$='HTF') then
c_p_h = INTERPOLATE('Salt (60% NaNO3-40% KNO3)','T','C',T=T_hot_avg)
else
if (isidealgas(fluid_hot$)) then
c_p_h = SPECHEAT(fluid_hot$,T=T_hot_avg)
   else
c_p_h = SPECHEAT(fluid_hot$,T=T_hot_avg, P=PH_in)
endif
endif
C_h = m_dot_hot*c_p_h
q_h = C_h*(TH_in-TH_out_itr)
diff_q = abs(q_h - q_c)
TH_out = TH_out_itr
TH_out_itr = (q_h - q_c)/C_h+TH_out
until (diff_q < 1)
 min_fluid$ = fluid_cold$
endif

if ((C_h_test <= C_c_test) and (rev>0)) then

50: TH_out = TH_in-eff_hx*(TH_in-TL_in)
T_hot_avg = (TH_in+TH_out)/2
if (fluid_hot$='HTF') then
c_p_h = INTERPOLATE('Salt (60% NaNO3-40% KNO3)','T','C',T=T_hot_avg)
else
if (isidealgas(fluid_hot$)) then
c_p_h = SPECHEAT(fluid_hot$,T=T_hot_avg)
else
c_p_h = SPECHEAT(fluid_hot$,T=T_hot_avg, P=PH_in)
endif
endif
C_h = m_dot_hot*c_p_h
q_h = C_h*(TH_in-TH_out)
TL_out = TL_in+C_min_test*eff_hx*(TH_in-TL_in)/C_c_test
TL_out_itr = TL_out
Repeat
T_cold_avg = (TL_in+TL_out_itr)/2
```

```
if (isidealgas(fluid_cold$)) then
c_p_c = SPECHEAT(fluid_cold$,T=T_cold_avg)
else
c_p_c = SPECHEAT(fluid_cold$,T=T_cold_avg, P = PC_in)
endif
C_c = m_dot_cold*c_p_c
q_c = C_c*(TL_out_itr-TL_in)
diff_q = abs(q_h - q_c)
TL_out = TL_out_itr
TL_out_itr = (q_h - q_c)/C_c+TL_out
until (diff_q < 1)
min_fluid$ = fluid_hot$
endif
if(((C_c_test-C_h_test)*(C_c-C_h) < 0) and (min_fluid$ = fluid_hot$) and (rev>0)) then
rev = 0
goto 40
endif
if(((C_c_test-C_h_test)*(C_c-C_h) < 0) and (min_fluid$ = fluid_cold$) and (rev>0)) then
rev = 0
goto 50
endif


C_min = MIN(C_c,C_h)
C_max = MAX(C_c,C_h)

"HXer core details - Ref. Chunyun Wang"
module_series = 1
module_parallel = 1
module_series_min = 1
module_parallel_min = 1
volume_hx_min = 100000
ploss_c_min = 1
ploss_h_min = 1
series_itr_done = 0
mp_last =100000
mp_2ndlast=100000
ms_step = 1
itr=0
step_limit = 0.05
Repeat
diff_hx = 0.1
eff_hx_calc = 0
ploss_h = 1
ploss_c = 1
mp_step = 100
itr_done = 0
Repeat

core_length = 0.561
core_width = 0.762
core_height = 1.5
plate_spacing =0.00165
fin_spacing=1/45*0.0254
fin_thickness=0.000076
parting_plate_thickness=0.00038
n_plate_c = 1
n_plate_h =2

plate_spacing_c =plate_spacing*n_plate_c
plate_spacing_h =plate_spacing*n_plate_h

beta_c = 4685
beta_h = 4734

d_e_c=4*1.761e-4 *(1+(n_plate_c-1)*.15)
d_e_h=4*1.743e-4*(1+(n_plate_h-1)*.15)

alpha_c =
plate_spacing_c/((n_plate_c+n_plate_h)*plate_spacing+2*parting_plate_thickness)*beta_c
```

```
alpha_h =
plate_spacing_h/((n_plate_c+n_plate_h)*plate_spacing+2*parting_plate_thickness)*beta_h

sigma_c = alpha_c*d_e_c/4
sigma_h = alpha_h*d_e_h/4

fin_area_ratio = 2*plate_spacing/(2*plate_spacing+2*fin_spacing)

"HX volume"
volume_hx = core_length*core_width*core_height*module_series*module_parallel

"Frontal Area"
A_f=core_width*core_height*module_parallel

"Free flow Area"
A_c = sigma_c*A_f
A_h = sigma_h*A_f

"Surface Area"
S_c = alpha_c*volume_hx
S_h = alpha_h*volume_hx

"Mass velocity"
G_c = m_dot_cold/A_c
G_h = m_dot_hot/A_h
if (isidealgas(fluid_cold$)) then
mu_c = viscosity(fluid_cold$, T=T_cold_avg)

cond_c = conductivity(fluid_cold$, T=T_cold_avg)

c_p_c = SPECHEAT(fluid_cold$, T=T_cold_avg)

prndtl_c = PRANDTL(fluid_cold$, T=T_cold_avg)
else
mu_c = viscosity(fluid_cold$, T=T_cold_avg, P = PC_in)

cond_c = conductivity(fluid_cold$, T=T_cold_avg, P = PC_in)

c_p_c = SPECHEAT(fluid_cold$, T=T_cold_avg, P = PC_in)

prndtl_c = PRANDTL(fluid_cold$, T=T_cold_avg, P = PC_in)
endif
if (fluid_hot$='HTF') then
mu_h = INTERPOLATE('Salt (60% NaNO3-40% KNO3)','T','mu',T=T_hot_avg)
cond_h = INTERPOLATE('Salt (60% NaNO3-40% KNO3)','T','k',T=T_hot_avg)
c_p_h = INTERPOLATE('Salt (60% NaNO3-40% KNO3)','T','C',T=T_hot_avg)
prndtl_h = c_p_h*1000*mu_h/cond_h
else
if (isidealgas(fluid_hot$)) then
mu_h = viscosity(fluid_hot$, T=T_hot_avg)

cond_h = conductivity(fluid_hot$, T=T_hot_avg)

c_p_h = SPECHEAT(fluid_hot$, T=T_hot_avg)

prndtl_h = PRANDTL(fluid_hot$, T=T_hot_avg)
else
mu_h = viscosity(fluid_hot$, T=T_hot_avg,P=PH_in)

cond_h = conductivity(fluid_hot$, T=T_hot_avg,P=PH_in)

c_p_h = SPECHEAT(fluid_hot$, T=T_hot_avg,P=PH_in)

prndtl_h = PRANDTL(fluid_hot$, T=T_hot_avg,P=PH_in)
endif
endif
"Reynolds number"
Re_c = G_c*d_e_c/mu_c
Re_h = G_h*d_e_h/mu_h

"Friction factor - Wavy Fin 11.44-3/8W Ref: Kays &London"
```

```
ar = (fin_spacing-fin_thickness)/(plate_spacing-fin_thickness)
f_lam_c =  24/Re_c*(1-1.3553*ar+1.9467*ar^2-1.7012*ar^3+0.9564*ar^4-0.2537*ar^5)
f_kl_c = 10^(-0.4025*log10(Re_c)-0.8774+1)
m_friction=1.76
f_c = (f_lam_c^m_friction+f_kl_c^m_friction)^(1/m_friction)

f_lam_h =  24/Re_h*(1-1.3553*ar+1.9467*ar^2-1.7012*ar^3+0.9564*ar^4-0.2537*ar^5)
f_kl_h = 10^(-0.4025*log10(Re_h)-0.8774+1)
f_h = (f_lam_h^m_friction+f_kl_h^m_friction)^(1/m_friction)

"Colbourn factor - Wavy Fin 11.44-3/8W Ref: Kays &London"

Nu_lam_c =  7.541*(1-2.61*ar+4.97*ar^2-5.119*ar^3+2.702*ar^4-0.548*ar^5)
H_lam_c = Nu_lam_c*cond_c/d_e_c
St_lam_c = H_lam_c/(G_c*c_p_c*1000)
j_lam_c = St_lam_c*prndtl_c^0.667

j_kl_c = 10^(-0.3201*log10(Re_c)-1.866+1)
m_colburn=6.2
j_c = (j_lam_c^m_colburn+j_kl_c^m_colburn)^(1/m_colburn)
H_c = j_c*G_c*c_p_c*1000/prndtl_c^0.667
St_c = H_c/(G_c*c_p_c*1000)
Nu_c = H_c*d_e_c/cond_c


Nu_lam_h =  7.541*(1-2.61*ar+4.97*ar^2-5.119*ar^3+2.702*ar^4-0.548*ar^5)
H_lam_h = Nu_lam_h*cond_h/d_e_h
St_lam_h = H_lam_h/(G_h*c_p_h*1000)
j_lam_h = St_lam_h*prndtl_h^0.667

j_kl_h = 10^(-0.3201*log10(Re_h)-1.866+1)
j_h = (j_lam_h^m_colburn+j_kl_h^m_colburn)^(1/m_colburn)
H_h = j_h*G_h*c_p_h*1000/prndtl_h^0.667
St_h = H_h/(G_h*c_p_h*1000)
Nu_h = H_h*d_e_h/cond_h



"Fin efficiency calculation - Single stack, even loading"
k_f = 24 [W/m-K]

m_f_h = (2*H_h/(k_f*fin_thickness))^0.5

Y_o_f_h = (2*H_h*k_f*fin_thickness)^0.5*core_length

m_s_h = (2*H_h/(k_f*parting_plate_thickness))^0.5

Y_o_s_h = (H_h*k_f*parting_plate_thickness/2)^0.5*core_length

if (n_plate_h > 1) then
fin_area_ratio_h = 2*plate_spacing_h/(2*plate_spacing_h+2*fin_spacing)

eta_f_h = TANH(m_f_h*plate_spacing_h/2)/(m_f_h*plate_spacing_h/2)

else
fin_area_ratio_h = 2*plate_spacing_h/(2*plate_spacing_h+2*fin_spacing)

eta_f_h = TANH(m_f_h*plate_spacing_h/2)/(m_f_h*plate_spacing_h/2)
endif
eta_o_h = 1-fin_area_ratio_h*(1-eta_f_h)

m_f_c = (2*H_c/(k_f*fin_thickness))^0.5

Y_o_f_c = (2*H_c*k_f*fin_thickness)^0.5*core_length

m_s_c = (2*H_c/(k_f*parting_plate_thickness))^0.5

Y_o_s_c = (H_c*k_f*parting_plate_thickness/2)^0.5*core_length

if (n_plate_c > 1)  then
fin_area_ratio_c = 2*plate_spacing_c/(2*plate_spacing_c+2*fin_spacing)
```

```
eta_f_c = TANH(m_f_c*plate_spacing_c/2)/(m_f_c*plate_spacing_c/2)

else
fin_area_ratio_c = 2*plate_spacing_c/(2*plate_spacing_c+2*fin_spacing)

eta_f_c = TANH(m_f_c*plate_spacing_c/2)/(m_f_c*plate_spacing_c/2)
endif
eta_o_c = 1-fin_area_ratio_c*(1-eta_f_c)

"Overall Heat Transferr Coefficient"

U_c = 1/(S_c/(S_h*eta_o_h*H_h)+1/(eta_o_c*H_c))

NTU = U_c*S_c/(C_min*1000)
R = C_min/C_max

if ( 1-R > 0.0001) then
eff_hx_calc = (1-exp(NTU*(R-1)))/ (1-R*exp(NTU*(R-1)))
else
eff_hx_calc = NTU/(1+NTU)
endif

diff_eff= abs(eff_hx - eff_hx_calc)

"Pressure-drop calculation"
"Hotside"
if (fluid_hot$='HTF') then
nu_H_in = 1/INTERPOLATE('Salt (60% NaNO3-40% KNO3)','T','rho',T=TH_in)
nu_H_out = 1/INTERPOLATE('Salt (60% NaNO3-40% KNO3)','T','rho',T=TH_out)
else
nu_H_in = VOLUME(fluid_hot$,P=PH_in,T=TH_in)
nu_H_out = VOLUME(fluid_hot$,P=PH_in,T=TH_out)
endif

nu_H_m = (nu_H_in+nu_H_out)/2

"Entrance and Exit Loss Coefficient Lookup"
if Re_H < 2000 then
K_c_h = INTERPOLATE(Kc_Laminar,sigma,K_c,sigma=sigma_h)
K_e_h = INTERPOLATE(Ke_Laminar,sigma,K_e,sigma=sigma_h)

else
K_c_h = INTERPOLATE2D(Kc_Turbulent,Re,sigma,K_c,Re=Re_H,sigma=sigma_h)
K_e_h = INTERPOLATE2D(Ke_Turbulent,Re,sigma,K_e,Re=Re_H,sigma=sigma_h)

endif


"Delta P = G^2*nu_1/(2*g_c)*(Phi_1+Phi_2+Phi_3-Phi_4)"
gc =9.81
Phi_1_h = 1 + K_c_h - sigma_h^2

Phi_2_h = 2*(nu_H_out/nu_H_in - 1)

Phi_3_h = f_h*S_h*nu_H_m/(A_h*nu_H_in)

Phi_4_h = (1 - sigma_h^2 - K_e_h)*nu_H_out/nu_H_in

DeltaP_h = G_h^2*nu_H_in/(2*gc)*(Phi_1_h+Phi_2_h+Phi_3_h-Phi_4_h)
ploss_h = DeltaP_h/(1000*PH_in)

"Coldside"
nu_C_in = VOLUME(fluid_cold$,P=PC_in,T=TL_in)
nu_C_out = VOLUME(fluid_cold$,P=PC_in,T=TL_out)

nu_C_m = (nu_C_in+nu_C_out)/2

"Entrance and Exit Loss Coefficient Lookup"
if Re_C < 2000 then
K_c_c = INTERPOLATE(Kc_Laminar,sigma,K_c,sigma=sigma_c)
```

```
K_e_c = INTERPOLATE(Ke_Laminar,sigma,K_e,sigma=sigma_c)

else
K_c_c = INTERPOLATE2D(Kc_Turbulent,Re,sigma,K_c,Re=Re_C,sigma=sigma_c)
K_e_c = INTERPOLATE2D(Ke_Turbulent,Re,sigma,K_e,Re=Re_C,sigma=sigma_c)

endif

"Delta P = G^2*nu_1/(2*g_c)*(Phi_1+Phi_2+Phi_3-Phi_4)"
Phi_1_c = 1 + K_c_c - sigma_c^2

Phi_2_c = 2*(nu_C_out/nu_C_in - 1)

Phi_3_c = f_c*S_c*nu_C_m/(A_c*nu_C_in)

Phi_4_c = (1 - sigma_c^2 - K_e_c)*nu_C_out/nu_C_in

DeltaP_c = G_c^2*nu_C_in/(2*gc)*(Phi_1_c+Phi_2_c+Phi_3_c-Phi_4_c)
ploss_c = DeltaP_c/(1000*PC_in)

if ((eff_hx_calc < eff_hx) or ((ploss_c > ploss_c_req) or (ploss_h > ploss_h_req))) then
module_parallel = module_parallel + mp_step
else
if (mp_step > step_limit)  then
module_parallel = module_parallel - 0.9*mp_step
mp_step = mp_step/10
else
itr_done = 1
endif
endif


until (itr_done > 0)
if (volume_hx < volume_hx_min) then
hx_area = S_c + S_h
hx_volume = volume_hx
core_volume = 1.3*hx_volume

hx_weight = 2358.8 * core_volume
hx_cost = hx_weight *0.00001668
volume_hx_min = volume_hx
module_series_min = module_series
module_parallel_min = module_parallel
ploss_h_min = ploss_h
ploss_c_min = ploss_c

L_c_min = core_length*module_series_min/sigma_c
L_h_min = core_length*module_series_min/sigma_h

Re_c_min = Re_c
Re_h_min = Re_h

H_c_min = H_c
H_h_min = H_h

j_c_min = j_c
j_h_min = j_h
f_c_min = f_c
f_h_min = f_h
Nu_c_min = Nu_c
Nu_h_min = Nu_h


A_c_min = A_c
A_h_min = A_h

S_c_min = S_c
S_h_min = S_h

dhyd_c_min = 4*A_c_min*L_c_min/S_c_min
dhyd_h_min = 4*A_h_min*L_h_min/S_h_min
```

```
fin_area_ratio_h_min = fin_area_ratio_h
fin_area_ratio_c_min = fin_area_ratio_c

eta_f_c_min = eta_f_c
eta_f_h_min = eta_f_h

eta_o_c_min = eta_o_c
eta_o_h_min = eta_o_h

U_c_min = 1/(S_c/(S_h*eta_o_h*H_h)+1/(eta_o_c*H_c))
U_h_min = 1/(S_h/(S_c*eta_o_c*H_c)+1/(eta_o_h*H_h))

NTU_min = NTU
R_min = R

endif
if (mp_last <= module_parallel) then
if (ms_step > step_limit) then
module_series = module_series - 2*ms_step
ms_step = ms_step/10
mp_last = mp_2ndlast
else
series_itr_done = 1
endif
else

mp_2ndlast = mp_last
mp_last = module_parallel
endif

itr = itr+1
mp[itr] = module_parallel
ms[itr] = module_series

module_series = module_series + ms_step
module_parallel = 1

msstp[itr] = ms_step
ms2[itr] = module_series

until (series_itr_done > 0)
else
min_fluid$ = 'unreal'
 hx_area = 0
hx_cost = 0
ploss_h_min = ploss_h_req
ploss_c_min = ploss_c_req
TL_out = TL_in
TH_out = TH_in

endif

end
```

Receiver Model

```
Procedure tempsky(T_amb,P_amb,rh,hour:T_sky)
T_dp = dewpoint(AirH2O,T= T_amb,P=P_amb,R=rh/100)
T_sky = T_amb*(0.711+0.0056*T_dp+0.000073*T_dp^2+0.013*cos((180-hour*15)*PI/180))^0.25
end

Procedure PipeFlow(Re_inner,Pr_inner,LoverD,relRough:Nusselt_t,f)
f = 1/(0.790*ln(Re_inner)-1.64)^2
Nusselt_t = (f/8)*(Re_inner-1000)*Pr_inner/(1+12.7*(f/8)^0.5*(Pr_inner^0.667 - 1))
```

```
end

Procedure Nusselt_FC(ksD,Re_for:Nu)
if (ksD = 0) then
   Nu = 0.3 + 0.488*Re_for^0.5*(1+(Re_for/28200)^0.625)^0.8
else
   if (ksD <= 7.5e-4) then
      if ( Re_for <= 7.0e5) then
         Nu = 0.3 + 0.488*Re_for^0.5*(1+(Re_for/28200)^0.625)^0.8
      else
         if (Re_for >= 2.2e7) then
            Nu = 0.0455*Re_for^0.81
         else
            Nu = 0.00257*Re_for^0.98
         endif
      endif
   else
      if ( (ksD > 7.5e-4) and (ksD <= 3.0e-3)) then
         if ( Re_for <= 1.8e5) then
            Nu = 0.3 + 0.488*Re_for^0.5*(1+(Re_for/28200)^0.625)^0.8
         else
            if (Re_for >= 4.0e6) then
               Nu = 0.0455*Re_for^0.81
            else
               Nu = 0.0135*Re_for^0.89
            endif
         endif
      else
         if ( (ksD > 3.0e-3) and (ksD <= 9.0e-3)) then
            if ( Re_for <= 1.0e5) then
               Nu = 0.3 + 0.488*Re_for^0.5*(1+(Re_for/28200)^0.625)^0.8
            else
               Nu = 0.0455*Re_for^0.81
            endif
         else
            Nu = 0.0455*Re_for^0.81
         endif
      endif
   endif
endif


end



Procedure
Rec_eff(T_salt_hot,T_salt_cold,azimuth,zenith,dni,field_eff,T_atm,P_amb,rh,V_wind,hour:et
a_therm,q_inc_sum,q_conv_sum,q_rad_sum,q_abs_sum,m_dot_salt_tot)
{
V_wind = 3
T_salt_hot = 2400
T_salt_cold = 600
azimuth = 61.8
zenith = 80
I_bn = 950
field_eff = 0.44
T_atm = 15 [C]
P_amb = 100 [kPa]
}
N_panels = 24
nlines = 2
D_out = 40
th_tu = 1.25
H_rec = 17.78
D_rec = 13.33
THT = 194.44
grav = 9.81

//Receiver dimensions, parameters
```

```
D_tube = D_out/1000 {Value in meters}
th_tube = th_tu/1000 {Thickness of the tube}
D_inner = D_tube - 2*th_tube {Diameter of each receiver tube}
D_in = D_inner*1000 {Inner diameter of the tube}
A_tube = pi*D_tube/2*H_rec {Outer area of each tube}
n_t = Floor((pi*D_rec)/(D_tube*N_panels)){The number of tubes per panel}
N_tube =n_t*N_panels {Number of tubes in the system}
A_receiver = pi*D_rec*H_rec {The area of the receiver exposed
to the ambient air, [S&K]}
A_rec_proj = D_tube*H_rec*N_tube {The projected area of the tubes}
T_amb = converttemp('C','K',T_atm) {Ambient temperature}
call  tempsky(T_amb,P_amb,rh,hour:T_sky)
//skytemp(T_amb,(T_dp+273.15),hour)!The effective sky temp [K]
A_node = pi*D_rec/N_panels*H_rec {The area of each node}
P_atm=P_amb {*myconvert('atm','Pa') !Ambient pressure, in [Pa]}
azi_adj = azimuth + 180 {By TRNSYS convention, the
azimuth angle is 0 at due south, negative to the east, and positive to
the west. The range is then -180 to 180. By the convention used here,
the azimuth is 0 at due north, and ranges clockwise from 0 to 360. This
adjusts.}
sigma = 5.670e-8 {[W/m^2-K^4] Stefan-Boltzmann constant}
epsilon = .88 {Emissivity: Taumoefolau, T. et al., 2004}
alpha_paint = 0.95

I_bn = dni /3.6

if(((zenith>85) or (I_bn<150)) or ((zenith=0) and (azimuth=0))) then
m_dot_salt_tot=0
eta_therm=0
W_dot_pump=0
q_conv_sum=0
q_rad_sum=0
q_inc_sum = 0
q_abs_sum = 0
T_s=0
Q_thermal=0
ey = -1
goto 100
endif

//Get flow pattern
//call flowPatterns(N_panels,flowtype,Flow_pattern,salt_out,nlines)
j=1
Repeat
if (j<=N_panels/2) then
   Flow_pattern[j]=j-1
else
   if (j>N_panels/2) then
       Flow_pattern[j]=j+1
   endif
endif

if (j=N_panels/4+1) then
   Flow_pattern[j]=3*N_panels/4+1
endif
if (j=3*N_panels/4) then
   Flow_pattern[j]=N_panels/4
endif
if (Flow_pattern[j]>24) then
   Flow_pattern[j]=0
endif

j=j+1
until (j >N_panels)

salt_out[1..2]=[N_panels/2,N_panels/2+1]
nlines = 2
j=1
Repeat

if (j/9 <= 1) then
```

```
   colname$ = concat$('f',chr$(j+48))
else
   colname$ = concat$('f',chr$(49))
   colname$ = concat$(colname$,chr$(j+38))
endif

array[j]= interpolate2D(flux,zenith,azimuth,colname$,zenith=zenith,azimuth=azi_adj)

flux_in[j]=array[j]/950*I_bn*field_eff
j=j+1
until (j >12)

{Translate to the number of panels, so each panel has its own linearly
interpolated flux value}

j=1
Repeat
Panel[j] = j {The position of each panel}
ppos[j]=(12/N_panels*(j-1)+6/N_panels)+1
flo[j]=floor(ppos[j])
ceil[j]=ceil(ppos[j])
ind[j]= (ppos[j]-flo[j])/(ceil[j]-flo[j])
if(ceil[j]>12) then
ceil[j]=1
endif
Psp_field[j]=ind[j]*(flux_in[ceil[j]]- flux_in[flo[j]])+flux_in[flo[j]] {Average area-
specific power for node}
P_field[j]=A_node*Psp_field[j]*alpha_paint {The power incident on each node}
j=j+1
until(j>N_panels)

//Guess values ---------------------------------------------------------

j=1
Repeat
T_sX[j] = 800 {Guess temperature for the surface nodes}
T_panel_outX[j] = 600 {Guess values for the fluid temp coming
out of the control volume}
T_panel_inX[j] = 600 {Guess values for the fluid temperature
coming into the control volume}
j=j+1
until(j>N_panels)

m_dot_saltX = 180/nlines {coolant mass flow rate guess value}
T_salt_hotX = 200 {Initial value for error calculation}
//---------------------------------------------------------------------------

qq=1
Repeat
if((qq>200) or (T_salt_hotX>400+T_salt_hot)) then
m_dot_salt_tot=0
eta_therm=0
W_dot_pump=0
q_abs_sum = 0
T_s=0
Q_thermal=0
ey = -2
goto 100
endif
err=(T_salt_hotX - T_salt_hot)/T_salt_hot
if(abs(err)<(1.0e-4)) then goto 50 {Check for convergence}
j=1
Repeat
T_s[j] = T_sX[j]
T_panel_out[j] = T_panel_outX[j]
T_panel_in[j] = T_panel_inX[j]
j=j+1
until(j>N_panels)


m_dot_salt = m_dot_saltX
```

```
j=1
Repeat
T_panel_ave[j] = (T_panel_in[j]+T_panel_out[j])/2 {The average
coolant temperature in each control volume}
T_film[j] = (T_s[j]+T_amb)/2
j=j+1
until(j>N_panels)

T_coolant_prop = (T_salt_hot + T_salt_cold)/2
T_s_ave = sum(T_s[i],i=1,N_panels)/N_panels

T_film_ave = (T_amb+T_salt_hot)/2

{Convection coefficient for external forced convection using S&K}
k_film = Conductivity(Air,T=T_film_ave) {Conductivity of the air}
mu_film = Viscosity('Air',T=T_film_ave) {Air Dynamic viscosity}
rho_film = Density('Air', T=T_film_ave, P=P_atm) {Density of the air}
c_p_film = specheat('Air',T=T_film_ave)*1000 {Spec.heat}
Re_for = rho_film*V_wind*D_rec/mu_film {Reynolds number}
ksD = (D_tube/2)/D_rec {The effective roughness of the cylinder}
call Nusselt_FC(ksD,Re_for:Nusselt_for) {Nusselt #}
h_for = Nusselt_for*k_film/D_rec {Heat transfer coefficient}

{Convection coefficient for external natural convection}
beta = volexpcoef('Air',T=T_amb) {Volumetric expansion coefficient}
nu_amb = Viscosity('Air',T=T_amb)/Density('Air',T=T_amb,P=P_atm) {Kinematic viscosity}
j=1
Repeat
{Grashof #}
Gr_nat[j] = grav*beta*(T_s[j]-T_amb)*H_rec**3/nu_amb**2
{Nusselt number}
Nusselt_nat[j] = .098*Gr_nat[j]**(1/3)*(T_s[j]/T_amb)**(-.14)
h_nat[j] = Nusselt_nat[j]*k_film/H_rec {Natural convection coef.}
j=j+1
until(j>N_panels)

{Mixed convection}
m=3.2

j=1
Repeat
h_mixed[j] = (h_for**m+h_nat[j]**m)**(1/m)
q_dot_conv[j] = h_mixed[j]*A_node*(T_s[j] - T_film[j]) {Convection}
j=j+1
until(j>N_panels)


{Radiation from the receiver}
{Calculate the radiation node by node}

j=1
Repeat
h_rad_amb[j] = sigma*epsilon*(T_s[j]**2+T_amb**2)*(T_s[j]+T_amb)
{The radiation coefficient for amb}
h_rad_sky[j] = sigma*epsilon*(T_s[j]**2+T_sky**2)*(T_s[j]+T_sky)
{The radiation coef. for sky}
q_dot_amb[j] = .5*h_rad_amb[j]*A_node*(T_s[j]-T_amb) {amb losses per node}
q_dot_sky[j] = .5*h_rad_sky[j]*A_node*(T_s[j] - T_sky) {sky losses per node}
j=j+1
until(j>N_panels)



{Calculate the losses from the surface}

j=1
Repeat
q_dot_rad[j] = q_dot_amb[j]+q_dot_sky[j] {Total rad.losses per node}
q_dot_loss[j] = q_dot_rad[j]+q_dot_conv[j] {Total losses per node}
j=j+1
```

```
until(j>N_panels)


q_loss_sum = sum(q_dot_loss[i],i=1,N_panels) {Receiver total losses}
q_conv_sum = sum(q_dot_conv[i],i=1,N_panels) {Receiver convection}
q_rad_sum = sum(q_dot_rad[i],i=1,N_panels) {Receiver radiation losses}

{Calculate the flux incident on the surface}

j=1
Repeat
q_dot_inc[j]=P_field[j]*1000
q_dot_abs[j] = q_dot_inc[j] - q_dot_loss[j] {The absorbed flux}
j=j+1
until(j>N_panels)


q_inc_sum = sum(q_dot_inc[i],i=1,N_panels) {The total power incident}
q_abs_sum = sum(q_dot_abs[i],i=1,N_panels) {The total power absorbed}

{Calculate the temperature drop across the receiver tube wall.. assume
a cylindrical thermal resistance}

j=1
Repeat
{The temperature at which the conductivity of the wall is evaluated}
T_wall[j] = (T_s[j] + T_panel_ave[j])/2
{The conductivity of the wall}
k_tube[j] = INTERPOLATE('Stainless_AISI316','T','k',T=T_wall[j])
{The thermal resistance of the wall}
R_tube_wall[j] = th_tube/(k_tube[j]*H_rec*D_rec*pi**2/2)
j=j+1
until(j>N_panels)

{Calculations for the inside of the tube}
C_p_coolant = INTERPOLATE('Salt (60% NaNO3-40% KNO3)','T','C',T=T_coolant_prop)*1000
{Specific heat of the coolant}
LoverD = H_rec/D_inner
RelRough = (1.5e-6)/D_inner {Relative roughness of the tubes.}
mu_coolant = INTERPOLATE('Salt (60% NaNO3-40% KNO3)','T','MU',T=T_coolant_prop)
k_coolant = INTERPOLATE('Salt (60% NaNO3-40% KNO3)','T','k',T=T_coolant_prop)
rho_coolant = INTERPOLATE('Salt (60% NaNO3-40% KNO3)','T','RHO',T=T_coolant_prop)
{Average velocity of the coolant through the receiver tubes.}
u_coolant = m_dot_salt/(n_t*rho_coolant*(D_inner/2)**2*pi)
{Reynolds number for internal flow}
Re_inner = rho_coolant*u_coolant*D_inner/mu_coolant
{Prandtl number for internal flow}
Pr_inner = C_p_coolant*mu_coolant/k_coolant
{The internal convection correlation. Petukhov, Gneilinski}
call PipeFlow(Re_inner,Pr_inner,LoverD,relRough:Nusselt_t,f)
if(Nusselt_t<=0) then
m_dot_salt_tot=0
eta_therm=0
W_dot_pump=0
q_abs_sum = 0
T_s=0
Q_thermal=0
ey = -3
goto 100
endif
{Convection coefficient between the inner tube wall and the coolant}
h_inner = Nusselt_t*k_coolant/D_inner
{The thermal resistance associated with this value}
R_conv_inner = 1/(h_inner*pi*D_inner/2*H_rec*n_t)

{Set up numerical flow grid}

j=1
Repeat
{The panel inlet temp is equal to the panel outlet temp from the
previous panel, according to the flow diagram}
```

```
if(Flow_pattern[j]<1) then
T_panel_inX[j] = T_salt_cold
else
T_panel_inX[j] = T_panel_out[Flow_pattern[j]]
endif
{The energy balance for each node}
T_panel_outX[j] = T_panel_in[j] + q_dot_abs[j]/(m_dot_salt*c_p_coolant)
{Calculate the surface temperature based on the absorbed heat}
T_sX[j]=T_panel_ave[j]+q_dot_abs[j]*(R_conv_inner+R_tube_wall[j])
j=j+1
until(j>N_panels)

T_salt_hotX = sum(T_panel_outX[salt_out[i]],i=1,nlines)/nlines
{Calculates the mixed outlet temperature of the salt}


eta_therm = q_abs_sum/q_inc_sum

{Final calculations}
m_dot_saltX = q_abs_sum/(nlines*C_p_coolant*(T_salt_hot-T_salt_cold))
{Do a check to make sure the mass flow rate is reasonable}
if(m_dot_saltX<5) then
m_dot_salt_tot=0
eta_therm=0
W_dot_pump=0
q_abs_sum = 0
T_s=0
Q_thermal=0
ey = -4
goto 100
endif

qq=qq+1
until(qq>201)

50: m_dot_salt_tot = m_dot_salt*nlines

L_e_45 = 16 {The equivalent length produced by the bends in the tubes.}
L_e_90 = 30
{Pressure drop across the tube, straight length}
DELTAP_tube = rho_coolant*(f*H_rec/D_inner*u_coolant**2/2)
{Pressure drop across 45 degree bends}
DELTAP_45 = rho_coolant*(f*L_e_45*u_coolant**2/2)
{Pressure drop across 90 degree bends}
DELTAP_90 = rho_coolant*(f*L_e_90*u_coolant**2/2)
{Total pressure drop across the tube,(4)90-deg bends, (2)45-deg bends}
DELTAP = DELTAP_tube + 2*DELTAP_45 + 4*DELTAP_90
{The pressure drop from pumping up to the receiver}
DELTAP_THT = rho_coolant*THT*grav
{The net pressure drop across the receiver panels}
DELTAP_net = DELTAP*N_panels/nlines+DELTAP_THT
Pres_D = DELTAP_net/1e6
{The energy required by the pump to move coolant through the receiver}
eta_pump = 0.8 {Assumption}
W_dot_pump = DELTAP_net*u_coolant*pi*D_inner**2/4*n_t/eta_pump
{Calculate the thermal output of the tower}
Q_thermal = m_dot_salt_tot*C_p_coolant*(T_salt_hot - T_salt_cold)

100: exitcode = -1

dummy2 = 0

end

//model begins here.............................

P_amb = 100 [kPa]

T_salt_hot = 900
T_salt_cold = 600
{
```

```
V_wind = 3
azimuth = 61.8
zenith = 80
dni = 950
field_eff = 0.44
T_atm = 15 [C]
rh = 0.4
hour = 15
T_wet=300 [K]
hel_power = 0 [kW]
}

call
Rec_eff(T_salt_hot,T_salt_cold,azimuth,zenith,dni,field_eff,T_atm,P_amb,rh,V_wind,hour:et
a_therm,q_inc_sum,q_conv_sum,q_rad_sum,q_abs_sum,m_dot_salt_tot)
```

REFERENCES

Ainley, D. G. and Mathieson, G. C. R, A Method of Performance Estimation for Axial-Flow Turbines British Aeronautical Research Council, R&M 2974, 1951

Alan Goodrich, Ted James, and Michael Woodhouse, Residential, Commercial, and Utility-Scale Photovoltaic (PV) System Prices in the United States: Current Drivers and Cost-Reduction Opportunities – NREL, 2012

Alefeld, G. and R. Rademacher, Heat Conversion Systems, CRC Press, Boca Raton, Fl, 1993

Allan D. Kraus, Abdul Aziz, James Welty, Extended Surface Heat Transfer– John Wiley and Sons, 2001

Angela M Patnode, Simulation and Performance Evaluation of Parabolic Trough Solar Power Plants– University of Wisconsin-Madison, 2006

Anthony Lopez, Billy Roberts, Donna Heimiller, Nate Blair, and Gian Porro, U.S. Renewable Energy Technical Potentials: A GIS-Based Analysis – NREL, 2012

Awad M. and Muzychka Y., Models for Pressure Drop and Heat Transfer in Air Cooled Compact Wavy Fin Heat Exchangers, Journal of Enhanced Heat Transfer, 2011

Carter, A.D.S, Three dimensional flow theories for axial compressors and turbines, Proceedings of Instn. Mech. Engrs., 1948

Charles W. Forsberg, Per F. Peterson, and Haihua Zhao, High-Temperature Liquid-Fluoride-Salt Closed-Brayton-Cycle Solar Power Towers, Journal of Solar Energy Engineering, May 2007, Vol. 129

Charles W. Forseberg et al, High Temperature Liquid Fluoride Salt Closed Brayton Cycle Solar Power Towers–Journal of Solar Energy Engineering, Vol. 129, May-2007

Christian Vetter, Hans-Joachim Wiemer, Dietmar Kuhn, Comparison of sub- and supercritical Organic Rankine Cycles for power generation from low-

temperature/low-enthalpy geothermal wells, considering specific net power output and efficiency, Applied Thermal Engineering, 51 (2013), 871-879

Chunyun Wang, Design, Analysis and Optimization of the Power Conversion System for the Modular Pebble Bed Reactor System–MIT, 2003

CM Meyer, From troughs to triumphs: SEGS and gas, Energize, 2008

Colin F. McDonald and David Gordon Wilson, The Utilization of Recuperated and Regenerated Engine Cycles for High-Efficiency Gas Turbines in the 21st Century, Applied Thermal Engineering Vol. 16, Nos 8/9, pp. 635-453, 1996

Craig E. Tyner, Solar Two: A Molten Salt Power Tower Demonstration– Sandia National Laboratories, 1995

Craig Turchi, Mark Mehos, Clifford K. Ho and Gregory J. Kolb, Current and Future Costs for Parabolic Trough and Power Tower Systems in the US Market, Presented at SolarPACES 2010, Perpignan, France, September 21-24, 2010

Cutler Cleveland, The Encyclopedia of Earth, 2008

D. Y. Goswami, J. F. Kreider and F. Kreith, Principles of Solar Engineering , Philadelphia: Taylor & Francis, 2 ed., 2000

D. Yogi Goswami and Feng Xu, Analysis of a New Thermodynamic Cycle for Combined Power and Cooling Using Low and Mid Temperature Solar Collectors, Journal of Solar Energy Engineering, May 1999, Vol. 121

Daniel Walravena, Ben Laenenb, William D'haeseleer, Comparison of Thermodynamic Cycles for Power Production from Low-Temperature Geothermal Heat Sources, Energy Conversion and Management, 2012

David K. Hall, Performance Limits of Axial Turbomachine Stages, MIT, Feb 2011

Denton, J. D, Loss mechanisms in Turbomachinery, ASME, 93-GT-435, 1993

Dirk Pauschert, Study of Equipment Prices in the Power Sector, ESMAP Technical Paper 122/09, 2009

DoE, “Energy Sources - Solar”, http://www.energy.gov/energysources/solar.htm (Accessed November 03, 2011)

DoE, “High-Concentration, Low-Cost Parabolic Trough System for Baseload CSP” http://www1.eere.energy.gov/solar/sunshot/csp_baseload_skyfuel.html, 2012 (Accessed Mar, 2013)

Elysia J. Sheu, Alexander Mitsos, Ahmad A. Eter, Esmail M. A. Mokheimer, Mohamed A. Habib and Amro Al-Qutub, A Review of Hybrid Solar–Fossil Fuel Power Generation Systems and Performance Metrics, Journal of Solar Energy Engineering, November 2012, Vol. 134

Energy Information Administration – Electricity-Detailed State Data http://www.eia.gov/electricity/data/state/(Accessed November, 2012)

Energy Information Administration – International Energy Outlook-2010 Report #:DOE/EIA-0484(2010), 2010

Environment News Service, “Utility-Scale Solar Plant Goes Online in Nevada” http://www.ens-newswire.com/ens/jun2007/2007-06-05-09.asp#anchor2, 2007 (Accessed Mar, 2013)

Frank P. Incropera and David P. De Witt, Fundamentals of Heat and Mass Transfer, John Wiley and Sons, 2005

G.A. Rivas, E.C. Garcia and M. Assato, Forced Turbulent Heat Convection in a Rectangular Duct with Non-Uniform Wall Temperature, Intech, 2012

Garg & Prakash, Solar Energy: Fundamentals and Applications, 2006

Gregory J. Kolb, Clifford K. Ho, Thomas R. Mancini, and Jesse A. Gary, Rich Crowley and Paul Quinlan, Power Tower Technology Roadmap and Cost Reduction Plan , SANDIA, 2011

Howell, A. R., Fluid Dynamics of Axial Compressors, Proceedings of Instn. Mech. Engrs.153, 1945

Hugo Ahlenius, UNEP/GRID-Arendal – NASA. 2008. NASA Surface meteorology and Solar Energy (SSE) Release 6.0 Data Set, Clear Sky Insolation Incident On A Horizontal Surface. http://eosweb.larc.nasa.gov/sse/ (Accessed April 24, 2008)

Huijuan Chen, D. Yogi Goswami and Elias K. Stefanakos, A review of thermodynamic cycles and working fluids for the conversion oflow-grade heat, Renewable and Sustainable Energy Reviews, 2010

I. Hischier, P. Leumann and A. Steinfeld, Experimental and Numerical Analyses of a Pressurized Air Receiver for Solar-Driven Gas Turbines, Journal of Solar Energy Engineering, May 2012, Vol. 134

Isak Kotcioglu, Teoman Ayhan, Hayati Olgun, Betul Ayhan, Heat Transfer and Flow Structure in a Rectangular Channel With Wing-Type Vortex Generator, Journal of Engg. And Environmental Science, 1998

J. Ramachandran and M.C. Conway, MS6001FA – An Advanced-Technology 70-MW Class 50/60... Hz Gas Turbine– John Wiley and Sons, 2001

James Mason and Vasilis Fthenakis, A Solar Grand Plan Scientific American, 2007

James Spelling, Bjorn Laumert and Torsten Fransson, A Thermoeconomic Study of Low-Temperature Intercooled-Recuperated Cycles for Pure-Solar Gas-Turbine Applications, Journal of Solar Energy Engineering, November 2012, Vol. 134

John Graham-Cumming, The Geek Atlas: 128 Places Where Science and Technology Come Alive – O'Reilly Media, 2009

John Perlin, From Space to Earth: The Story of Solar Electricity– AATEC Publications, 1999

John Pye, Compact Linear Fresnel Reflector-ANU, 2011

Kearney, D., Assessment of a Molten Salt Heat Transfer Fluid in a Parabolic Trough Solar Field, Submission to JSEE April 2002

Ken Butti and John Perlin, A Golden Thread: 2500 years of solar architecture and technology, 1980

Kistler, B.L., A User's Manual for DELSOL3: A Computer Code for Calculating the Optical Performance and Optimal System Design for Solar Thermal Central Receiver Plants, Sandia National Labs, Albuquerque, NM. SAND86-8018, 1986

Kyle Kitzmiller and Fletcher Miller, Thermodynamic Cycles for a Small Particle Heat Exchange Receiver Used in Concentrating Solar Power Plants, Journal of Solar Energy Engineering, August 2011, Vol. 133

L. Stoddard, J. Abiecunas, and R. O'Connell, Economic, Energy, and Environmental Benefits of Concentrating Solar Power in California, Black & Veatch, NREL, 2006

Leonard D. Jaffe, A Review of Test Results on Solar Thermal Power Modules With Dish-Mounted Stirling and Brayton Cycle Engines, Journal of Solar Energy Engineering, November 1988, Vol. 110

Marc Godin, Stirling Engines Overview –PTAC Distributed Power Generation and Energy Efficiency Forum, 2005

Michael J. Wagner, Simulation and Predictive Performance Modeling of Utility-Scale Central Receiver System Power Plants– University of Wisconsin-Madison, 2008

Miriam makhyoun, Rich Crowley and Paul Quinlan, Levelized Cost ofSolar Photovoltaics in North Carolina – NCSEA, 2012

Nag, Engineering Thermodynamics, Tata Mc-Graw Hill, 2005

Nathan P. Siegel, Clifford K. Ho, Siri S. Khalsa and Gregory J. Kolb, Development and Evaluation of a Prototype Solid Particle Receiver: On-Sun Testing and Model Validation, Journal of Solar Energy Engineering, May 2010, Vol. 132

Ning Wei, Significance of Loss Models in Aerothermodynamic Simulation for Axial Turbines, Royal Institute of Technology, 2000

NREL, "High-Performance Photovoltaics" http://www.nrel.gov/pv/high_performance_pv.html, (Accessed Jan, 2013)

P. Gang, L. Jing, J. Jie, Analysis of low temperature solar thermal electric generation using regenerative organic Rankine Cycle, Applied Thermal Engineering 30, 2010

Patrick O'Grady, "SES, Tessera debut new solar plant in Peoria" http://www.bizjournals.com/phoenix/stories/2010/01/18/daily87.html, 2010 (Accessed Mar, 2013)

Peterson, F., Liquid-salt cooled Advanced High Temperature Reactors, Department of Nuclear Engineering, University of California, Berkeley, GoNERI Seminar, December 11, 2008

R. Chacartegui, D. Sánchez, J.M. Muñoz de Escalona, T. Sánchez, Alternative ORC bottoming cycles for combined cycle power plants, Applied Energy 86, 2009

R. H. Goddard, A New Invention to Harness the Sun, Popular Science, 1929

Ramon Ferreiro Garcia, Efficiency enhancement of combined cycles by suitable working fluids and operating conditions, Applied Thermal Engineering, 42 (2012), 25-33

Rene I. Olivares, Chunlin Chen and Steven Wright, The Thermal Stability of Molten Lithium–Sodium–Potassium Carbonate and the Influence of Additives on the Melting Point, Journal of Solar Energy Engg., 2012

Reuters, "Global solar power capacity grew 44 pct in 2009", http://www.reuters.com/article/2010/03/30/us-energy-solar-idUSTRE62T3AQ20100330 (Accessed August 12, 2010)

Rick Le Blanc, "The Case for Concentrating Solar Power", http://www.helioscsp.com/noticia.php?id_not=428 (Accessed June, 2011)

Robert Cable, Solar Trough Generation - The California Experience, Presented at ASES FORUM, Washington DC, 2001

S.L. Dixon, Fluid Mechanics and Thermodynamics of Turbomachinary– Elsevier Butterworth-Heinemann, 2005

Sahil Popli, Peter Rodgers, Valerie Eveloy, Gas turbine efficiency enhancement using waste heat powered absorption chillers in the oil and gas industry, Applied Thermal Engineering, 50 (2013), 918-931

Sargent and Lundy, Assessment of parabolic Trough and Power Tower Solar Technology Cost and Performance Forecasts – NREL, 2003

SEIA, "Photovoltaic (Solar Electric)" http://www.seia.org/policy/solar-technology/photovoltaic-solar-electric, (Accessed November 03, 2012)

Soderberg, C. R, Unpublished notes, Gas Turbine Laboratory, Massachusetts Institute of Technology (quoted in reference [Dixon, 1989]), 1949

SolarMillenium, Parabolic Trough Power Plants-Andasol 1 to 3 –2008

Solarpaces, "Parabolic Trough System", http://www.solarpaces.org/CSP_Technology/csp_technology.htm (Accessed on January, 2013)

Spanish News, "Abengoa Solar puts its PS20 solar tower into operation" http://www.spanishnews.es/20090428-abengoa-solar-puts-its-ps20-solar-tower-into-operation/id=352/, 2009 (Accessed Mar, 2013)

Stefano Giuliano, Reiner Buck and Santiago Eguiguren, Analysis of Solar-Thermal Power Plants With Thermal Energy Storage and Solar-Hybrid Operation Strategy, Journal of Solar Energy Engineering, August 2011, Vol. 133

Suzanne E. Price and J. Rhett Mayor, Analysis Of Solar-Thermal Power Cycles For Distributed Power Generation, Proceedings of the ASME 2009 3rd International Conference of Energy Sustainability, July 19-23, 2009, San Francisco, California, USA

Suzanne E. Price, A Consideration of Cycle Selection For Meso-Scale Distributed Solar-Thermal Power, Georgia Institute of Technology, August 2009

Suzanne Price, Thermodynamic Design and Comparative Analysis of Rankine, ORC, and Kalina Cycles for Low-Cost, Meso-scale Power Generation Systems, Proceedings of Energy Sustainability 2008, August 10-14, 2008, Jacksonville, Florida USA

Thomas Mancini, Peter Heller and Barry Butler, Dish-Stirling Systems: An Overview of Development and Status, Journal of Solar Energy Engineering, May 2003, Vol. 125

Thomas W. Africa, The Classical World, 1975

Uri Fisher, Chemi Sugarmen, Arik Ring and Joseph Sinai, Gas Turbine ‘‘Solarization’’-Modifications for Solar/Fuel Hybrid Operation, Journal of Solar Energy Engineering, August 2004, Vol. 126

W.M. Kays, A.L. London, Compact Heat exchangers– Mc Graw Hill, 1984

Won-Yong Lee And Sang-Soo Kim, The Maximum Power From a Finite Reservoir For a Lorentz Cycle, Energy,Vol. 17, pp. 275-281, 1992

X. R. Zhang, H. Yamaguchi, K. Fujima, M. Enomoto and N. Sawada, Theoretical analysis of a thermodynamic cycle for power and heat production using super-critical carbon dioxide, Energy, 32 (2007), 591-599

Y. A. Cengel, and M. A. Boles, Thermodynamics: An Engineering Approach, Boston: McGraw Hill, 4 ed., 2002

Y. Wu, N. Ren, T. Wang and C. Ma, Experimental Study on Optimized Composition of Mixed Carbonate Salt for Sensible Heat Storage in Solar Thermal Power Plant, Solar Energy, 85(9), pp. 1957–1966, 2011

Yongping Yang, Qin Yan, Rongrong Zhai, Abbas Kouzani, Eric Hub, An efficient way to use medium-or-low temperature solar heat for power generation e integration into conventional power plant, Applied Thermal Engineering, 31 (2011), 157-162

You Ying, Eric J. Hu, Thermodynamic advantages of using solar energy in the regenerative Rankine power plant, Applied Thermal Engineering, 19 (1999), 1173-1180

Yousef S. H. Najjar and Mahmoud S. Zaamout, Comparative Performance Of Closed Cycle Gas Turbine Engine With Heat Recovery Using Different Gases, Heat Recovery Systems & CHP Vol. 12, No. 6, pp. 489-495, 1992

Yousef S.H. Najjar, Gas turbine cogeneration systems: a review of some novel cycles, Applied Thermal Engineering, 20 (2000), 179-197

Zeuner, Gustav, Technical Thermodynamics, 1907